DTU Library

Combining Gas Bearing and Smart Material Technologies for Improved Machine Performance Theory and Experiment

Nielsen, Bo Bjerregaard

Link back to DTU Orbit

DTU

Combining Gas Bearing and Smart Material Technologies for Improved Machine Performance Theory and Experiment

PhD Thesis

$$(EIv'')'' = q - \rho A\ddot{v}$$

$$\Delta \int_a^b \varepsilon \, \theta \, \sqrt{17} \, \Omega \, f \, \infty \, + \, \{2.718 \, \chi^2 \, \sum$$

Bo Bjerregaard Nielsen
DCAMM Special Report No. S221
July 2016

DTU Mechanical Engineering
Department of Mechanical Engineering

Combining Gas Bearing and Smart Material Technologies for Improved Machine Performance

Theory and Experiment

Bo Bjerregaard Nielsen

English title of the thesis:
Combining Gas Bearing and Smart Material Technologies for Improved Machine Performance
– Theory and Experiment

Afhandlingens danske titel:
Kombination af luftleje og smart materiale teknologierne til forbedring af maskiners ydeevne
– Teori og eksperiment

PhD Student:
Bo Bjerregaard Nielsen
bobjni@mek.dtu.dk
ORCID: 0000-0003-0748-4426

Supervisor:
Ilmar Ferreira Santos
ifs@mek.dtu.dk
ORCID: 0000-0002-8441-5523

Summary (English)

According to industry leaders, the world is on the verge of the fourth industrial revolution in which the Internet of Things and cyber-physical systems are central concepts. Where the previous industrial revolution evolved around electronics, IT and automated production on machine level, Industry 4.0 will enable a much stronger interaction between all of these technical achievements, from factory level all the way down to the individual machine elements. This can be exemplified by its the impact on machine maintenance. Nowadays, to avoid unwanted machine stops, maintenance cycles are scheduled based on the principle of the weakest link, e.g., the minimum expected lifetime of any machine element. In the future individual machine elements will not only send information about their performance, they will also be able to compensate for "wear and tear" or adapt to new operating conditions autonomously in coordination with adjacent machine elements. This requires mechatronic machine elements, which combine traditional passive mechanical components with sensors, actuators, electronics and computer algorithms, which thereby become "self-acting" machine elements, e.g. the piezoelectric air foil bearing (PAFB).

One way of supporting a rotor running at higher speed is by using air foil bearing (AFB). An AFB utilizes the aerodynamic pressure created by the relative velocity difference between the rotor and the bearing surface. In an AFB the bearing surface is flexible and is made up by a thin top foil and a bump foil placed between the top foil and bearing housing. The PAFB combines the traditional AFB with piezoelectric material incorporated into the top foil. This creates a link between the mechanical domain of the traditional machine element and the electrical domain, i.e., ultimately a computer. The thesis deals with the development of the PAFB, and gives three main contributions: the design of a multifunctional test facility; the development of a state-of-the-art mathematical model of the PAFB and AFB; and interpretation of numerical results contributing to the understanding of both AFBs' and PAFBs' static and dynamic behaviours. The facility is designed to experimentally study the PAFB and its sub-systems. This allows for validation of mathematical models and gain of further knowledge of the PAFB's static and dynamic behaviour. The mathematical models, based on the finite element method (FEM), are created as a combination of AFB models and models of piezoelectric material and their constitutive equations. The model includes journal, air film, piezoelectric top foil (PTF), bump foil and electrical circuit. It takes non-linear effects resulting from the aerodynamic pressure into account allowing for a separation of the top foil and bump foil. Numerical results obtained with a sub-model of the PTF shows good agreement with experiments, while simulations of a passive PAFB closely resembles results obtained with a non-linear AFB model known from literature.

A numerical investigation shows that rotor-bearing sub-harmonic vibrations associated with large journal unbalance can be eliminated when the top foil is only partly supported by the bump foil, i.e., "shallow pocket" effect. The aerodynamic forces are significantly affected by the deformations of the PTF caused by the piezoelectric material due to an electrical potential difference (EPD) imposed between the electrodes. It is possible to increase the aerodynamic forces, and thereby the bearing load capacity, by a factor of two. The future steps in the development of PAFB are the design of feedback control laws and the experimental validation of a fully-controlled PAFB aided by the designed test facility and mathematical model derived in the thesis.

Resumé (Dansk)

Ifølge industriens ledere står verden på dørtærsklen til den fjerde industrielle revolution, hvor "Internet of Things" og "cyber-physical systems" vil være centrale elementer. Hvor den forrige industrielle revolution var centreret omkring elektronik, IT og automatiseret produktion på maskinniveau, vil "Industry 4.0" resultere i en stærkere interaktion mellem alle disse teknologiske fremskridt, fra fabriksniveau helt ned til maskinelementniveau. Dette kan eksemplificeres ved dets indvirkning på maskinvedligeholdelsen. I dag undgås uhensigtsmæssige produktionsstop ved at planlægge vedligeholdelse efter princippet om "det svageste led", det vil sige at den korteste levetid dikterer vedligeholdelsescyklussen. I fremtiden vil individuelle maskinelementer ikke kun nøjes med at sende informationer om deres tilstand, men de vil også kunne kompensere for slid eller i samspil med andre maskinelementer kunne tilpasse sig selvstændigt til en ændret driftssituation. Dette nødvendiggør mekatroniske maskinelementer, som igennem en kombination af traditionelle maskinelementer, sensorer, aktuatorer, elektronik og computeralgoritmer udgør intelligente maskinelementer, som for eksempel det piezoelektriske folieluftleje (PAFB).

En mulighed for understøtning af en rotor som roterer med høj hastighed er bølgefolieluftlejer (AFB). Et AFB benytter det aerodynamiske lufttryk som dannes på grund af den relative hastighedsforskel mellem rotoren og lejeoverfladen. I et AFB er lejeoverfladen fleksibel og opbygget af en tynd topfolie og en bølgefolie, der er placeret mellem topfolien og lejehuset. Et PAFB kombinerer det passive AFB med piezoelektriske materialer inkorporeret i lejets topfolie. Dette skaber en sammenhæng imellem det mekaniske domæne i det traditionelle maskinelement og det elektroniske domæne, hvilket i sidste ende er en computer. Afhandlingen omhandler udviklingen af et PAFB, og har tre primære bidrag: design af en fleksibel testopstilling; udvikling af en "state-of-the-art" matematisk model af PAFB'er og AFB'er; og præsentation af numeriske resultater som bidraget til forståelsen af den statiske og dynamiske ydeevne af både AFB'er og PAFB'er. Formålet med testopstillingen er at foretage eksperimentelle studier af et PAFB og dettes delsystemer. Dette muliggør eksperimentel validering af den matematiske model samt indsamling af yderligere viden omkring et PAFB's statiske og dynamiske ydeevne. Den matematiske model, som er baseret på finite element metoden (FEM), er en kombination af en model af et AFB og en model af det piezoelektriske materiale og dettes konstitutive ligninger. Modellen inkluderer en stiv rotor, luftfilm, piezoelektrisk topfolie (PTF), bølgefolie og elektriske kredsløb. Modellen tager højde for de ikke-lineære effekter fra det aerodynamiske tryk, samtidig med at den tillader at topfolien og bølgefolien ikke er i mekanisk kontakt. Numeriske resultater beregnet med en PTF sub-model stemmer overens med eksperimentelle målinger, ligesom simuleringer af et

passivt PAFB stemmer overens med resultater fra en ikke-lineær model af et AFB som er beskrevet i litteraturen.

En numerisk undersøgelse viser at de subharmoniske vibrationer i et AFB, som skyldes en stor masseubalance, kan elimineres, når bølgefolien kun delvist understøtter topfolien. Dette sker på grund af "shallow pocket" effekten. De aerodynamiske kræfter afhænger i høj grad af PTF deformationer, der skabes af det piezoelektriske materiale, som følge af forskellen mellem de elektriske potentialer (EPD) på elektroderne. Det er muligt at øge de aerodynamiske kræfter og dermed lejets bæreevne med en faktor to. De kommende tiltag i udviklingen af et PAFB er design af "feedback" regulering samt eksperimentel validering af et fuldt regulerbart PAFB ved hjælp af den konstruerede testopstilling og den matematiske model udledt i denne afhandling.

Preface

This thesis is submitted as a partial fulfilment of the requirements for obtaining the Danish PhD degree. The project was supervised by professor, Dr.-Ing, Dr.-Tech. Ilmar F. Santos and carried out at the Section of Solid Mechanics (FAM), Department of Mechanical Engineering (MEK), Technical University of Denmark (DTU) from February 2013 to July 2016. A part of the research was carried out at the Federal University of Rio de Janeiro (UFRJ) from November to December 2015 under the supervision of professor Marcelo A. Savi. Funding for the project has been provided by MEK and by a grant from The Danish Council for Independent Research (DFF), Technology and Production Sciences (FTP), Ministry of Higher Education and Science.

I would like to start out by expressing my gratitude toward my supervisor Ilmar F. Santos. I greatly appreciate having you as my supervisor and I have cherished the times we spent together on and off the project. But mostly, I feel honoured that you took me on as your PhD student, and let me work independently on my own project. After I received my master's degree in mechanical engineering I was eager to continue our collaboration together within the framework of a PhD project. Fortunately, the opportunity presented itself only a couple of years later, and I was happy to once again getting the chance to work with you. Thank you for believing in me.

A special thanks is directed toward Alejandro C. Varela and Andreas J. Voigt for all our scientific discussions, general conversations and coffee breaks at the stairs outside building 404. As the saying goes: "When you share a problem, you cut it in half, and when you share a joy, you double it", so thank you both for being there. Also, Jon S. Larsen deserves to be thanked. You have answered all my questions regarding the practical application of AFBs, just as you paved the way on AFBs within the research group, thereby making it easier for me and my project. I would also like to say thank you to present and former fellow PhD students, office mates, members of the "lunch club" and other colleges at FAM, Alejandro de M. Tehada, Cesar A. L. L. da Fonseca, Christian K. Christiansen, Fabian G. P. Vasques, Geraldo F. de S. Rebouças, Jonas Lauridsen, Jorge G. Salazar, Konstantinos Poulios, Martin F. Jørgensen, Niels S. Jensen, Nikolaj A. Dagnæs-Hansen og Søren Enemark.

Valuable assistance was provided by Martin S. Nielsen during the last part of the project. Your dedication during the experimental work was very much appreciated, just as your good mood and high working moral. I would also like to say thank you to Sebastian von Osmanski for your time during the finalisation of this thesis. Your knowledge within the field of AFBs is already at an impressive level, and I am sure that you will be more than capable of further developing the PAFB technology.

On a more personal note, I would like to express my gratitude toward Marina C. dos Santos for the help and guided tours through Rio de Janeiro during my external

research stay. Both Camilla and I really appreciated your kindness and hospitality. Also thanks to Marcelo A. Savi for inviting me to UFRJ. It was a great experience for me and one of the highlights of the PhD project.

Finally, I would like to thank friends and family. You are the ones who have supported me before, during and hopefully also after the PhD project. Thank you for inviting me to various social activities during these past three and a half years and giving me a chance to occupy my mind with something besides work. But most of all, I would like to express my gratitude towards Camilla, who especially throughout the last four months since our son was born, has been carrying all the heavy burdens thereby giving me a chance to finish up my PhD project. Thank you so much.

Kgs. Lyngby, 31 July 2016
Bo Bjerregaard Nielsen

Appended publications

Nielsen, B. B., M. S. Nielsen and I. F. Santos (2016). 'A layered shell containing patches of piezoelectric fibers and interdigitated electrodes: Finite element modeling and experimental validation'. *Journal of Intelligent Material Systems and Structures*. DOI: 10.1177/1045389X16642537.

Nielsen, B. B. and I. F. Santos (2017). 'Transient and steady state behaviour of elasto–aerodynamic air foil bearings, considering bump foil compliance and top foil inertia and flexibility: A numerical investigation'. *Proceedings of the Institution of Mechanical Engineers, Part J: Journal of Engineering Tribology*. DOI: 10.1177/1350650117689985.

Contents

Abbreviations and nomenclature

This nomenclature covers the thesis. The nomenclatures of the appended publications may differ.

Due to the three different physical domains in the mathematical model and the multiple numbers of components in the PAFB, the nomenclature used in this thesis differs some what from what is traditionally used in literature. A given variables is identified by a combination of character and subscript. The character describes the physical variable, while the subscript is given by the component, e.g., the thickness of the air film is h_a, while the thickness of the top foil is h_t and the top foil radial deflection is δ_t.

Abbreviations

AFC	Active fibre composite
AFB	Air foil bearing
DoF	Degree of freedom
DTU	Technical University of Denmark
EPD	Electric potential difference
FEM	Finite element method
FRF	Frequency response function
IC	Initial condition
IDE	Interdigitated electrode
MFC	Macro fibre composite
PAFB	Piezoelectric air foil bearing
PTF	Piezoelectric top foil
RAB	Rigid air bearing
SEFM	Simple elastic foundation model
THUNDER	Thin layer unimorph driver
3D	Three spatial dimensions

Latin symbols

A	Area $\left[\text{m}^2\right]$
$[A]$	State matrix
$[B]$	Dimensionless derivative matrix [-]
c	Radial clearance $[\text{m}]$

C Capacitance [F]

$[C]$ Constitutive matrix $\left[\text{Pa}^{-1}\right]$

d Distributed viscous damping $\left[\frac{\text{N}}{\text{s}\cdot\text{m}^3}\right]$

$\{D\}$ Electric displacement $\left[\frac{\text{C}}{\text{m}^2}\right]$

$[d]$ Piezoelectric constant $\left[\frac{\text{m}^2}{\text{C}}\right]$

$[D]$ Damping matrix $\left[\frac{\text{kg}}{\text{s}}\right]$ or $\left[\frac{\text{kg}\cdot\text{m}}{\text{s}}\right]$

E Young's modulus [Pa]

$\{E\}$ Electrical field $\left[\frac{\text{V}}{\text{m}}\right]$

$[e]$ Inverse piezoelectric constant $\left[\frac{\text{C}}{\text{m}^2}\right]$

$F, \{F\}$ Force or load [N]

H Electric Enthalpy [J]

$\{J\}$ Jacobian vector

k Distributed stiffness $\left[\frac{\text{N}}{\text{m}^3}\right]$

$[K]$ Stiffness matrix $\left[\frac{\text{N}}{\text{m}}\right]$ or [N]

h Radial thickness [m]

L Lagrangian [J]

l_b Half bump length [m]

l Length [m]

m Mass [kg]

$[M]$ Mass matrix [kg] or $[\text{kg}\cdot\text{m}]$

$[N]$ Shape function matrix [-]

p Pressure [Pa]

p_A Ambient pressure [Pa]

Q Electric charge [C]

q Generalised Coordinates

r Bearing radius [m]

R Electrical resistance [Ω]

$\{R\}$ Residual vector [-]

S_b Bump foil pitch [m]

t Time [s]

T Kinematic Energy [J]

$[T]$ Transformation matrix [-]

$\{u\}$ Deflection in global coordinates [m]

U_c Controllable voltage source [V]

U Internal Energy [J]

v Surface velocity $\left[\frac{\text{m}}{\text{s}}\right]$

$\{v\}$ State space vector in global coordinates [m] and $\left[\frac{\text{m}}{\text{s}}\right]$, $\{v\} = \{\{u\}, \{\dot{u}\}\}^\text{T}$

V Volume $\left[\text{m}^3\right]$

$\{V\}$ Local cosine coordinate vector [-]

$[V]$ Mode shape matrix, i.e., each column is a mode shape vector [-]

w Width [m]

$\{W\}$ Static load [N]

$x, y, z, \{x\}$ Location in global coordinates [m]

Greek symbols

α_{b}	Bump foil compliance $\left[\frac{1}{\mathrm{Pa}}\right]$
$\alpha_{\mathrm{t},i}, \beta_{\mathrm{t},i}$	Rotations in the top foil [-]
β_{b}	Loss factor for hysteresis damping [-]
$\delta_{(\ )}$	Radial deflection [m]
δ	Infinitesimal variation [-]
Δ	Difference [-]
$\{\varepsilon\}$	Mechanical strain [-]
$[\epsilon], [\eta]$	Electric permittivity $\left[\frac{\mathrm{F}}{\mathrm{m}}\right]$
κ	Correction factor [-]
$\Lambda, \{\Lambda\}$	Bearing number [-], $\Lambda = \frac{6\mu\Omega}{p_{\mathrm{A}}}\left(\frac{r}{c}\right)^2$, $\{\Lambda\} = \{\Lambda, 0\}^{\mathrm{T}}$
μ	Absolute viscosity $[\mathrm{Pa} \cdot \mathrm{s}]$
$[\mu]$	Local in-plane coordinate axis [-], $[\mu_i] = [-\{V_{2i}\}, \{V_{1i}\}]$
$\nabla, \{\nabla\}, [\partial]$	Spatial gradient $\left[\frac{1}{\mathrm{m}}\right]$
ν	Poisson's ratio [-]
Ω	Rotor angular velocity $\left[\frac{1}{\mathrm{s}}\right]$
ϕ	Electric potential [V]
ψ_{a}	Combined state variable for the air film $[\mathrm{Pa} \cdot \mathrm{m}]$, $\psi_{\mathrm{a}} = p_{\mathrm{a}} h_{\mathrm{a}}$
ρ	Density $\left[\frac{\mathrm{kg}}{\mathrm{m}^3}\right]$
$\{\sigma\}$	Mechanical stress [Pa]
θ	Circumferential angle [-]

Sub- and superscripts

$\hat{(\ )}$	Reduced matrix or vector
$\tilde{(\ )}$	Dimensionless variables
$\dot{(\ )}, \ddot{(\ )}$	First and second time derivative
$(\ )^*$	Evaluated at integration point
$(\ )_{\mathrm{a}}$	Air film
$(\ )_{\mathrm{b}}$	Bump foil
$(\ )_{\mathrm{c}}$	Electrical circuit
$(\ )_{\mathrm{e}}$	Electrode
$(\ )_e$	Element
$(\ )_{\mathrm{ee}}$	Coupling between electrical potential and charge
$(\ )_{\mathrm{eu}}$	Coupling between electrical potential and force
$(\ )_i$	Nodal counter
$(\ )_m$	Midpoint
$(\ )_{\mathrm{MFC}}$	MFC patch
$(\ )_\phi$	Electrical potential
$(\ )_{\mathrm{r}}$	Journal or rotor
$(\ )_{\mathrm{rb}}$	Removed bump foil
$(\ )_s$	Starting point
$(\ )_{\mathrm{t}}$	Top foil

$(\ )_{\mathrm{u}}$	Displacement
$(\ )_{\mathrm{uu}}$	Coupling between displacement and force
$(\ )_{\mathrm{ub}}$	Mass unbalance
$(\ )^{\mathrm{T}}$	Transposed matrix or vector

Nondimensionalisation

$\tilde{p}$	Pressure, $\tilde{p} = \frac{p}{p_A}$
$\tilde{h}$	Air film thickness, $\tilde{h} = \frac{h}{c}$
$\tilde{t}$	Time, $\tilde{t} = \Omega t$
$[\tilde{M}]$	Mass, $[\tilde{M}] = \frac{\Omega^2 c}{p_A r^2}[M]$
$[\tilde{D}]$	Damping, $[\tilde{D}] = \frac{\Omega c}{p_A r^2}[M]$
$[\tilde{K}]$	Stiffness, $[\tilde{K}] = \frac{c}{p_A r^2}[K]$
$\{\tilde{F}\}$	Load, $\{\tilde{F}\} = \frac{1}{p_A r^2}\{F\}$

Colour codes in sketches of air bearings

————	Bump foil or supported top foil
————	Top foil or unsupported top foil
————	Piezoelectric patch or MFC patch
————	Air film
————	Journal or rotor

Chapter 1

Introduction

1.1 Background

The wheel is considered by some to be the most important invention of all time. The uniqueness of the wheel is its ability to transfer reaction forces between rotating and stationary objects, and as such the bearing is the essential part of this inversion. Ever since ancient times, bearings have played a vital role for mankind, allowing us to create carriages, watermills, steam and combustion engines and data drives. In the present day and age, bearings can be divided into four types: solid lubricated plain bearings (e.g., bushings); elastohydrodynamic lubricated bearings (e.g., ball bearings); magnetic bearings (e.g., active electromagnetic bearings); and fluid film lubricated bearings (i.e., gas bearing). Each type has its own advantages and disadvantages, and one's choice of bearing depends on application, performance and cost.

A fluid film bearing uses a lubricant to fully separate two surfaces moving at different velocities. This type of bearing can be subdivided into four subtypes based on the lubricant used: liquid or gas, and the lubrication regime: dynamic or static. Generally speaking, fluid film bearings using a liquid lubricant are installed in heavy machinery where the rotation speed ranges from less than 100 rpm to around 10,000 rpm. In contrast, fluid film bearings using gas as the lubricant are found in smaller equipment and machinery. The weight of the shaft supported by a gas bearing ranges from a couple of grams up to 50 kg, while rotational speeds ranges from 5,000 rpm to in excess of 500,000 rpm.

Static fluid film bearings utilizes external pressurisation to support the rotor, i.e., the high pressure from the static lubrication forms the pressure profile in the bearing. The dynamic fluid film bearing utilizes a combination of a wedge formed in the fluid film and a relative velocity between the rotating and stationary parts to create the pressure profile. In this case, the geometry and dynamics of the rotor-bearing system enables the support of the rotation shaft, i.e., the bearing is self-acting. A bearing of the last type using gas a lubricant is an aerodynamic bearing, also called a gas or air bearing. The bearing type is used in the medical (see Pierart 2016), aeronautical (see Agrawal 1997) and food and water treatment (see Larsen 2015) industries; it is also commonly used in compressors/blowers providing "clean" air (see Walton II et al. 2007). There are many advantages of using aerodynamic bearings, such as the ones listed below.

- **Low friction between the stationary and rotating parts.** The friction forces in a fluid depend on its viscosity, and the viscosities of gases are generally much lower than those of liquids. In addition, the friction forces in a gas film are much lower than the dynamic friction in an elastohydrodynamic or solid lubricated bearing.

- **Lubricant is ample and clean.** If the bearing is used in a compressor, the medium transported can be used for lubrication. For other applications air can easily be used.

- **Reliable operation under extreme temperatures.** All components used in an air bearing can be made out of metal, which has a great geometric stability at high and low temperatures.

- **Simple mechanical design.** Few components are used in an air bearing, which are made of either solids or foils.

- **Self-acting during operation.** The aerodynamic pressure is self-preserving if the operational conditions are kept constant, hence it requires no external supply of any type.

However, aerodynamic bearings also have drawbacks in comparison to other bearing types. These disadvantages are listed below.

- **Demanding manufacturing requirements.** Because of the low viscosity of the gases, the distance between the bearing surface and rotor surface, i.e., the bearing clearance, must be very small in order to create a sufficient aerodynamic pressure. A small change in the bearing clearance has a great influence on the bearing performance, hence the tolerances for the components are very fine.

- **Sensitive to misalignments.** The fine tolerances within an air bearing translates in to a requirement of precise alignment of air bearings supporting a rotor. A slight offset of two air bearings in the radial direction will affect the bearing clearance in both bearings due to the radial location of the rotor.

- **Low load-carrying capacity.** This is due to the low viscosity of gases, which a high rotational speed cannot compensate for.

- **Poor damping characteristics.** Due to low viscosity of gases, the friction forces in the air film are low, implying a low dissipation of energy, and thus low level of damping.

- **Limited number of start/stop cycles.** Every time the rotor start or stop the aerodynamic pressure in the bearing will be too low to carry its load. This will resulted in mechanical contact between the surfaces of the bearing and rotor, hence wearing them down.

The initial air bearings were inspired by hydrodynamic bearings, which have rigid bearing surfaces. However, due to the drawbacks listed above, air bearings with rigid bearing surfaces, i.e., rigid air bearing (RAB), are primarily used for small scale rotating systems such as dentist drills ect. where it is possible to manufacture both bearings in

the same machine set-up. For large scale systems, where RABs have proven insufficient, air foil bearings (AFBs) are used in stead. The AFB is a further development of the RAB, in which the bearing surfaces are flexible, and commonly made up of foils, hence the name. Although the AFB is mechanically more complex than the RAB, it is less sensitive to misalignments, while having better damping characteristics, higher onset speed of instability and can carry a higher load at comparable minimum air film thickness. In the continued effort to improve the performance of rotor-bearing systems utilizing aerodynamic bearings three different approaches have been pursued: 1) improving the flexible support structure of the AFB; 2) combining the aerodynamic bearing with other bearing types, thereby creating a hybrid bearing; and 3) enabling a dynamic adjustment of the bearing performance during operation based on measurements, hence making the bearing active or "smart". It is in this context that the piezoelectric air foil bearing (PAFB) making up the ultimate objective of the present PhD thesis.

The piezoelectric air foil bearing

The PAFB resembles the AFB in most ways, as seen from the sketch of the PAFB shown in figure 1.1. They both have one or more flexible top foils supported in the radial direction by flexible bump foils and they both utilize the aerodynamic principle to support a rotating shaft. However, the PAFB incorporates one or more piezoelectric patches placed on the outside of the top foil, hence turning it into a piezoelectric top foil (PTF). The piezoelectric patch provides a coupling between the mechanical strain and stress of the top foil with the electrical potential and charge in the electrical circuit connected to the electrodes of the piezoelectric patch.

There are no limitations on the location or size of a piezoelectric patch in the PTF. This results in great flexibility for tailoring the properties of the PAFB to a given set of operational conditions. The bump foil is removed from the areas of the PTF where the piezoelectric patches are located, i.e., the PTF is partly supported. This is to prevent the piezoelectric patches from being damaged by the localised support pressures and rubbing found in the contact points between the bump foil and the PTF due to radial support and relative sliding between the PTF and bump foil.

When a piezoelectric patch is neither connected to an electrical circuit, nor is short-circuited, the properties of the PAFB perform similarly to those of an AFB. However, when the electrodes on the piezoelectric patch is connected to an electrical circuit the PAFB possess a coupling between the electrical and mechanical domains. The effects of the coupling are depicted by the three states of the PTF shown in figure 1.2: (a) initial shape; (b) inward deflected; and (c) outward deflected. When the PTF deflects an electrical potential difference (EPD) is generates between the electrodes on the piezoelectric patch, enabling a flow of electrical charge in the circuit, i.e., the coupling from mechanical to electrical domains. The direction of the flow depends on the deflection of the PTF. Vice versa, an EPD imposed between the electrodes of the piezoelectric patch generates a load on the PTF causing it to deflect, i.e., the coupling from electrical to mechanical domain. The advantages gained by using an PAFB instead of an AFB are listed below.

- **Ability to modify the aerodynamic pressure.** This will allow for higher onset speed of instability, better damping characteristics and increased load capacity.

(a) View along the axial direction

(b) Radial view towards the bearing centre of the piezoelectric top foils.
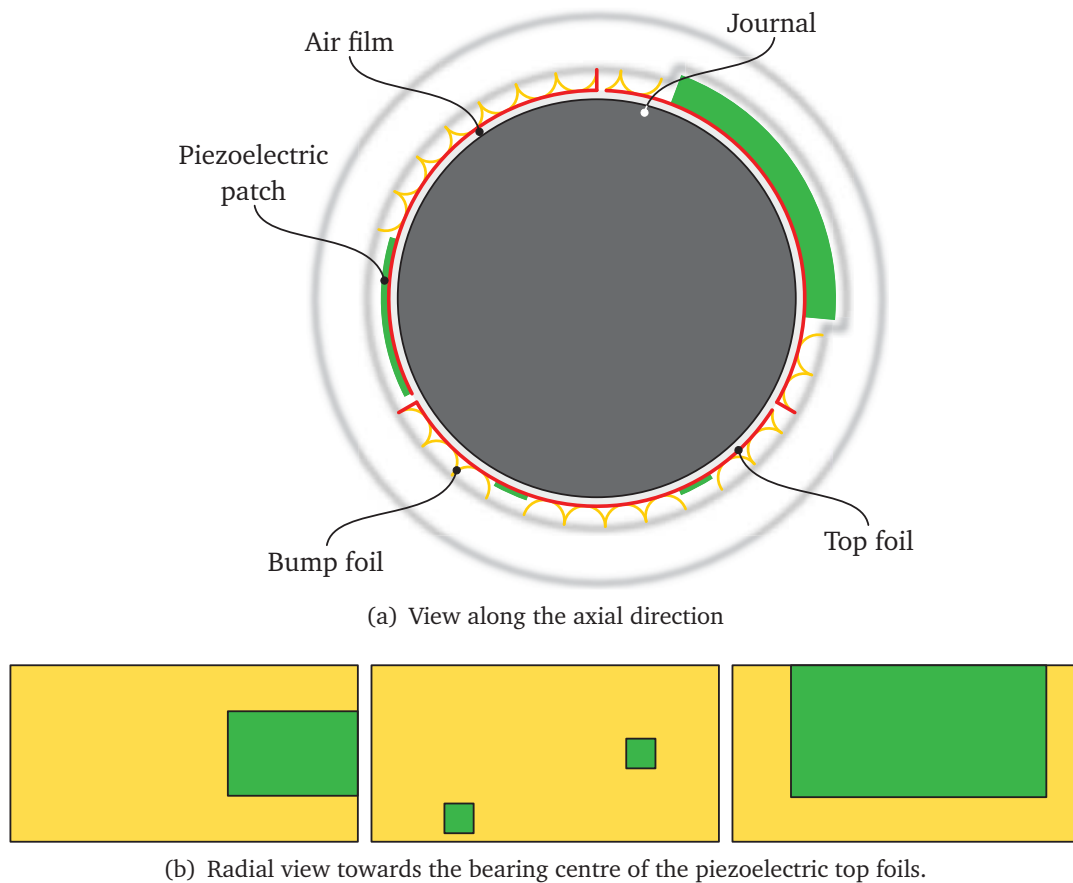
Figure 1.1: Sketch of a piezoelectric air foil bearing (PAFB) with three piezoelectric top foils (PTFs). Each top foil may incorporate multiple piezoelectric patches or none at all. The bump foil supporting the top foil is removed from the areas there the piezoelectric patches are located to ensure the support pressure at the contact points does not damage the patches.

- **Monitoring capabilities.** By measuring the electrical charge flowing in the electrical circuit connected to the electrodes on the piezoelectric patch, the movement of the PTF can be recorded, and thereby the performance of the PAFB.

The drawbacks of the PAFB are listed below.

- **Higher sensitivity to operating temperature.** The Curie temperature of the piezoelectric materials sets the upper limit for the operational temperature range.

- **More complex design.** A layered top foil including a piezoelectric patch with electrodes, an electrical circuit and a connection between the electrodes and the electric circuit.

1.2   State of the art literature study

The PAFB is a new addition to the subgroup of aerodynamic bearings, in which a piezoelectric patch is incorporated into the well-known AFB in order to create an active aerodynamic bearing, as described above. The presentation of the current state of the

(a) Unloaded or initial state of the PTF

(b) Inward deflected state of the PTF

(c) Outward deflected state of the PTF
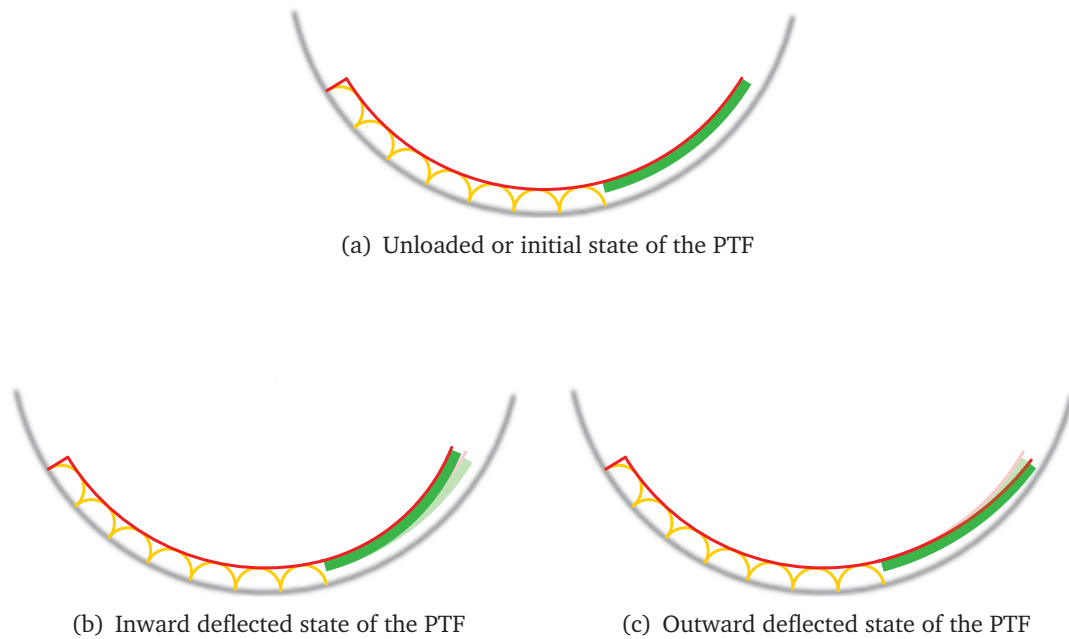
Figure 1.2: Sketch of initial state and two deformed states of an PTF with one piezoelectric patch. The PTF deformation can be caused by an EPD applied to the piezoelectric patch, while the EPD can be caused by a deformation of the PTF.

art will therefore focus, on the developments within the field of piezoelectric patches, as well as AFBs and other air bearing types aiming to enhance the bearing performance, including active bearings.

Piezoelectric patches

The study of piezoelectric material for sensors and actuators dates back to at least the fifties, e.g., Thurston (1953). However, the development of piezoelectric patches originates in the nineties according to Bryant (2007).

The initial flexible piezoelectric patch was the thin layer unimorph driver (THUNDER) developed by NASA. This patch consists of a thin piezoelectric sheet covered by electrodes on each side, as depicted in figure 1.3(a). Two versions of THUNDER patches exist, distinguishing themselves from one another by the mode they utilize, i.e., the extension mode, polarised in the thickness direction, and the shear mode, polarised in the in-plane direction. When an EPD is applied to the electrodes of an extension mode THUNDER patch, it will expand in the direction of the thickness and contract in the both of the in-plane directions. An EPD applied to a shear mode THUNDER patch will cause it to shear.

A further development of piezoelectric patches made by NASA was named the macro fibre composite (MFC), of which a sketch is shown in figure 1.3(b). Here, the piezoelectric layer has been exchanged with regular piezoelectric fibres, isolated from each other, and with two pairs of interdigitated electrodes (IDEs) placed on both sides. The design of the MFC originates from the active fibre composite (AFC) presented by Hagood and Bent (1993) and Hagood et al. (1993). The use of IDEs instead of full

Piezoelectric material   Piezoelectric material

Electrodes   Isolation material   Isolation material   Electrodes
        (a) THUNDER patch.   (b) MFC patch.
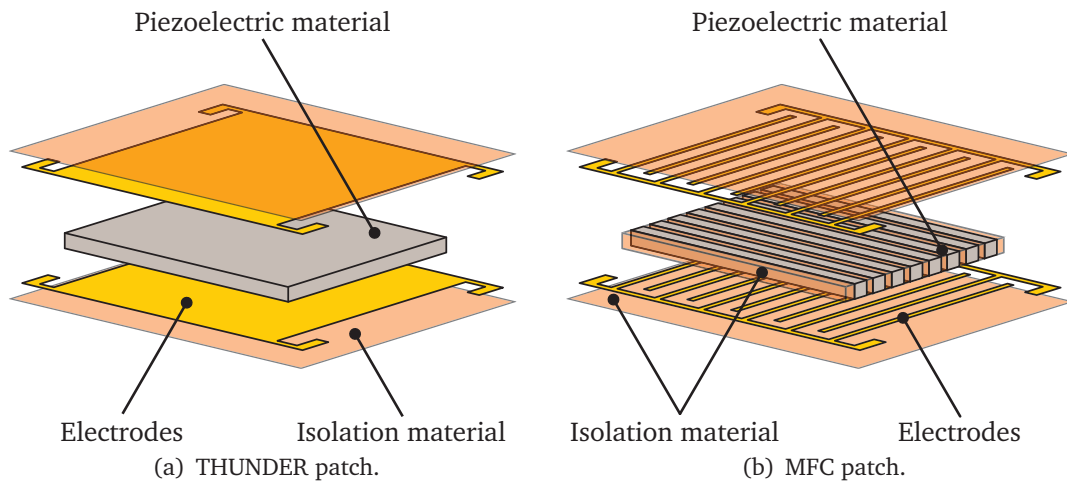
Figure 1.3: Two types of piezoelectric patches: the thin layer unimorph driver (THUNDER) and the macro fibre composite (MFC).

surface electrodes changes the direction of the electrical field caused by an EPD between the electrodes enabling an alignment of the electrical field and piezoelectric fibres. The EPD applied to the IDEs causes an asymmetric deflection of the MFC, i.e., a large expansion in the fibre direction and a smaller contraction perpendicular to the fibres. The orientation of the fibres can be used to tailor the response of the host structure. This enables the primary expansion of the MFC to be aligned with the circumferential direction of the PTF and thereby the air film wedge, which is of great importance for the aerodynamic pressure. Hence, MFC patches are used in the PAFB.

Modelling of piezoelectric patches

Modelling of piezoelectric patches is treated extensively in the literature, although the objectives of the research vary. At least three different objectives can be identified: 1) analytical and numerical models of structures incorporating the THUNDER patches; 2) models of the MFC unit cell; and 3) numerical models of structures with MFC patches.

The first group of mathematical models followed the development of the patches, hence in the late eighties and early nineties linear models were presented for structures with THUNDER patches of the extension mode type, e.g., Tzou and Gadre (1989) and Tzou and Tseng (1991). Subsequent mathematical models included different types of shear deformation theory, e.g., a first order model by Balamurugan and Narayanan (2001) and Suleman and Venkayya (1995), a higher order model by Balamurugan and Narayanan (2009) and Samanta et al. (1996), and a zigzag model by Tzou and Ye (1996) and Yasin and Kapuria (2013). Mathematical models for the shear mode THUNDER patch have been presented by, e.g., Benjeddou et al. (1997, 1999), Kapuria and Hagedorn (2007) and Trindade et al. (2001). These models were developed for layered beams, plates and shells containing piezoelectric patches and include either one or two spatial dimensions.

During the period in which the mathematical models for the THUNDER patches became increasingly sophisticated, further developments within piezoelectric patches resulted in the AFC and MFC patches, as already described. The greater structural

complexity of the AFC and MFC patches in comparison with the THUNDER patch, have made the structures of the AFC and MFC patches an object for investigation. The primary focus of this research has been numerical validation of analytical models for material averaging/homogenisation and correction factor for the non-uniform electrical field due to the IDEs (see Bent and Hagood 1997; Biscani et al. 2011; Deraemaeker et al. 2009; Nasser et al. 2011, 2008; Park and Kim 2005). These structural models make up the second group. The third and last group contains 3D structural models of beams incorporating AFC or MFC patches, e.g., Bilgen et al. (2010), Brockmann and Lammering (2006), Guennam and Luccioni (2006, 2009) and Nguyen and Kornmann (2006).

Air foil bearings

Air foil bearings have two sources of non-linearities affecting their performance: the air film between the rotor and top foil, and the mechanical contact between the top foil, bump foil and bearing sleeve or housing. The first source of non-linear effect, the air film, is a general concern for fluid film bearings. This was originally described by Reynolds (1886) for a thin film of liquid, but the governing equation bearing his name, the Reynolds equation, is also valid for a thin air film, as shown by Harrison (1913). The second source of non-linearity, the mechanical contact, is due to the design of the AFB, and relates to two phenomena: 1) dry friction between the bump foil and the adjacent structures, and 2) mechanical impact between the top foil and bump foil. Although these sources of non-linearity are not found in other types of fluid film bearings, they are among the most commonly encountered non-linearity in mechanical engineering and therefore well known in literature.

Some of the first researchers to develop theoretical models for the RAB, migrated from the field of hydrodynamic bearings with their experience of linearising the hydrodynamic forces. And as Albert Einstein allegedly said, "Everything should be as simple as it can be, but not simpler", they linearised the aerodynamic forces turning them into static loads and spring and damper coefficients as was common for hydrodynamic bearings (see Lund 1968; Lund 1964) in order to calculate the dynamic performance of the air bearings.

With the development of the AFB the second source of non-linearities arose. In the late seventies and early eighties some of the first experimental and numerical results for AFBs were published in the literature by Heshmat et al. (1982, 1983a,b) and Walowit and Anno (1975). These authors made an important contribution to the linear modelling of the bump foil in an AFB through the introduction of the simple elastic foundation model (SEFM). In this model, the bump foil is represented as a pattern of unconnected springs supporting the air film between the rotor and top foil. This was later expanded to include the hysteresis losses due to the friction forces via equivalent viscous damping (see Heshmat and Ku 1994; Ku 1994). The linearised aerodynamic forces and the SEFM have since then been used extensively in the literature, (see Kim and San Andrés 2008; Larsen and Santos 2013; Peng and Carpino 1993). Most of these models exclude the effects from the top foil, with the reasoning that its contribution to the structural stiffness is negligible in comparison to the bump foil. In fact, Heshmat et al. (1983b) assumed the top foil would be rigid enough to prevent sagging between bumps, but so soft that the deflection would only depend on localised loading. Many of the authors that have included the top foil structure in the AFB model along with the

SEFM have done so in order to study the effects from top foil sagging on the equilibrium position of the journal and the dynamic coefficients (see Carpino and Talmage 2003; Larsen and Santos 2014; San Andrés and Kim 2007, 2009; Temis et al. 2011; Xu et al. 2013, 2011).

The results steaming from the linearised AFB models show good agreement with experimental measurement when the rotor unbalance or perturbation from equilibrium position is small (see Larsen et al. 2015a; San Andrés et al. 2007). Experimental measurements of rotors supported by AFBs do, however, contain sub-harmonic vibrations in their responses (see Heshmat 1994). These vibrations are related to the non-linear sources in the AFB, and as the level of unbalance and perturbation increase so too do their influence, potentially causing bearing failure (see San Andrés et al. 2015).

Arghir et al. (2006) compared linear and non-linear results of a journal supported by an RAB. They showed the error caused by the linearisation increases for higher excitation amplitude. Bonello and Pham (2014) and Pham and Bonello (2013) introduced an efficient computational method for transient simulations of the compressible Reynolds equation. The method allows the governing equations to be solved simultaneously, and it was used by Larsen and Santos (2015) in combination with the SEFM to simulate the steady state response of a rotor supported by two AFB. The main sub-harmonic vibrations measured experimentally were predicted by the numerical simulations.

Enhanced performance of air foil bearings

In the continuing efforts to improve the performance of aerodynamic bearings, three general approaches are found in literature: 1) development of better mathematical models of the AFB in order to push the limits of the technology; 2) research into alternative top foil supports in order to improve the mechanical properties of the support structures and thereby the AFB; and 3) switching to an active bearing set-up, making it possible to compensate for the shortcomings of present-day AFBs.

The first approach, pursuing enhanced performance by means of mathematical modelling, largely focuses on the bump foil. As such, the aim is to replace the SEFM with a model that includes the dry friction forces at the contact points (see Hoffmann et al. 2015b; Le Lez et al. 2009; Lee et al. 2009). The focus of the second approach is on replacing the bump foil structure with another passive support structure. The alternative structures found in literature include protuberant foil (see Chen et al. 2015; Yu et al. 2011), helical springs (see Song and Kim 2007) and metal meshes (see San Andrés and Chirathadam 2013) including meshes made out of shape memory alloys (see Ertas et al. 2009b; Ma et al. 2015). While these two approaches have yielded important insights into various aspects of the AFB, neither of them have resulted in any significant performance improvements, with the exception of placing shims between the bump foil and bearing housing at strategically chosen locations along the circumference of the AFB (see Hoffmann et al. 2015b; San Andrés and Norsworthy 2015). In sharp contrast to these two approaches stands the third one, as described in the following paragraph.

Controllable fluid film bearings

The third approach take issue with the active bearings. Among the first publications on controllable air bearings are Horikawa et al. (1992, 1989) and Shimokohbe et al.

(1991). The active bearing consists of four tilting pads, each with a piezoelectric stack actuator behind them. The active aerodynamic bearing supports a vertically placed rigid journal. Although the rotational speed of the journal is low, i.e., 750 to 1,000 rpm, the position of the journal can be controlled within 25 nm.

Many similar active bearing designs are found in the literature and they vary with respect to type of actuator, fluid, and bearing segments. Qiu et al. (2003) also presented an aerodynamic tilting pad bearing with piezoelectric stack actuators, while Mizumoto et al. (2010) and Pipeleers et al. (2009) have shown results from circular aerodynamic bearings with flexible bearing segments controlled by piezoelectric stack actuators. Similar hydrodynamic bearings have been presented in the literature (see Deckler et al. 2004; Rylander et al. 1995; Santos 1995; Sun and Krodkiewski 2000; Wu et al. 2007), although other types of actuators have been used in some of the cases. In al these bearing designs the aerodynamic forces are controlled by changing the thickness of the air film.

Another method for creating an active fluid film bearing has been presented by Mizumoto et al. (1996). A piezoelectric actuator is used to control the size of the orifice area in an aerostatic bearing, hence the restricted flow limits the bearing support pressure. This type of active control on the bearing performance has also been used in an active tilting pad bearing, although servo valves were used to control the supply flows. Bearings combining the hydrodynamic and hydrostatic properties have been studied (see Haugaard 2010; Salazar and Santos 2015; Santos 2010; Santos and Russo 1998; Varela 2013). The principle has also been used in a combined aerodynamic and aerostatic bearing, i.e., an active RAB with piezoelectric actuators restricting the supply flows. This has been investigated by Morosi (2011), Pierart (2016), Santos (2010) and Theisen et al. (2016). A similar set-up has been studied by San Andrés and Ryu (2008), where the bearing used flexure pivot tilting pads instead of a rigid bearing surface.

While the aforementioned active air bearings have all shown significant improvements in their performance when compared to their passive counterparts, none of them are AFBs. Braun et al. (1995) presents an AFB with a polymeric elastic bed supporting the top foil and piezoelectric stack actuators affecting the bed. A similar version, although without the polymeric elastic bed, has been patented by Lee et al. (2003), where the top foil is directly supported by the piezoelectric actuators. No clear improvements of active AFB performance have been presented in the literature.

1.3 Objectives and original contributions of the project

The objectives at the onset of the PhD project was a theoretical and experimental investigation of the feasibility of applying "smart materials" to increase the payload, to suppress vibrations and to reduce energy consumption of rotation machines supported by gas-lubricated bearings. These objectives were to be achieved via smart materials coupled to compliant surfaces of an air bearing controlled by an embedded intelligence. The specific objectives are listed below.

- **Mathematical model of an air bearing.** Create a model an air bearing considering compressible fluid and compliant surfaces based on Modified Reynolds Equation, i.e., model an AFB.

- **Mathematical model of a smart material.** Create a multi-physical model of a smart material and a compliant bearing surface which are coupling via the materials constitutive equations, i.e., model the PTF. The constitutive equations may depended on input parameters, such as strain-stress relationship, temperature, magnetic flux density, current, voltage, chemical composition among others.

- **Design and construct a test facility.** Design a dedicated test rig, in which several strategies for controllable gas bearings connected to smart materials can be tested.

- **Validation of the mathematical multi-physical models.** Validation of the mathematical models and evaluation of the performance improvements toward enhancing of bearing load capacity, dynamic stability and reduction of energy losses.

In the context of the state of the art and the objectives of the PhD project, both described above, the main original contribution of this PhD study is presented in the two appended papers and this thesis, i.e., the mathematical model of the PAFB, and the material in the chapter concerning the numerical results. The contributions below are presented in chronological order.

Publication P1, Nielsen et al. (2016). In this paper the electro-mechanical finite element used to model the dynamic performance of the PTF is presented. The developed element is based on an 8-node serendipity isoparametric layered shell element developed by Panda and Natarajan (1981), which is capable of modelling the static deflection of a double curved flexible shell. The new element are useful for modelling shell structures incorporating one or more MFC patches of the expansion type, i.e., utilizing the d_{33} piezoelectric constant. The governing equations are deduced from the Lagrange equation and the linear isothermal constitutive equation of a piezoelectric material. The electro-mechanical element utilizes first-order shear deformation theory, and the dead zones in the electrical field associated with IDEs are accounted for. Experimental results are used to validate the numerical simulations of the mode shapes and resonance frequencies of an PTF. The validation shows a sound agreement between theory and experiments.

Publication P2, Nielsen and Santos (2017). The paper presents a non-linear fluid-mechanical finite element model of an AFB. The air film is modelled with 8-node plane isoparametric elements, the top foil uses equivalent double curved elements and the bump foil is represented by a bilinear version of the SEFM. The model contains the non-linearities of the air film and allows the top foil and bump foil to separate due to the bilinear SEFM. All governing equations are coupled, enabling simultaneous time stepping. The numerical results presented in the paper show the dynamic response of a traditional AFB with a fully supported top foil and three cases of AFBs with a partly supported top foil. The responses of the AFBs are shown for small and large journal unbalance at various rotational speeds. The steady state response for a journal rotation at constant speed and with a small unbalance are trivial in all cases, hence a harmonic vibration. This is not the case at a larger journal unbalance. Here, the steady state response of the journal supported by the AFB with a fully supported top foil contains sub-harmonic vibrations, as expected and documented in literature. These sub-harmonic vibrations are, however, not visible in the steady state response for the journal supported by the AFB with the unsupported area of top foil located in the high pressure zone. By removing the bumps, the sub-harmonic vibrations are also

removed. This positive effect has been attributed to the shallow pocket forming in the unsupported area due to a large sagging of the top foil.

PhD thesis. In addition to the publications, this PhD thesis contains the following original contributions to the current research base.

The mathematical model of the PAFB, which is based on the AFB model presented in publication P2, and the PTF presented in publication P1. The governing equations of the PAFB are implicitly coupled and can be solved simultaneously in time. The IDEs of the MFC patch can be coupled with different types of electrical circuits enabling the MFC to be used as a actuator or a sensor.

Based on the finding in publication P2 where the sub-harmonic vibrations were eliminated, a parameter study is performed to investigate the relationship between the sub-harmonic vibrations and the size of the unsupported area. Results presented in the thesis indicated that the circumferential length of the unsupported area is of higher importances than the width, i.e., if the unsupported area extends more than 90°, the sub-harmonic vibrations will be eliminated.

In a numerical parameter study, where a MFC is used as an actuator, the change in the aerodynamic forces are presented in relation to: 1) the size of the MFC patch; 2) the location of a MFC patch and 3) the EPD applied to the IDEs. The study is conducted with a fixed journal, hence only the PTF is allowed to move. Varying these three parameters the forces acting on the PTF changes, hence the PTF deflects into a new equilibrium position with a corresponding change in the thickness of the air film and aerodynamic forces. The parameter study shows that it is possible to increase the aerodynamic forces with up to 139 %.

1.4   Structure of the thesis

The thesis consists of five chapters, one appendix chapter and two appended publications. The five chapters contain highlights from the publications and additional work and findings obtained during the PhD study, as indicated above. Hence the thesis is paper-based, although extensive additional work is included in the thesis.

Chapter 2 introduces the test facility designed as a partial fulfilment of the PhD project. The test facility was manufactured, assembled and is now located at the Department of Mechanical Engineering at the Technical University of Denmark. A thorough description of the test facility is given, including the inherent flexibility to vary the experimental set-up, i.e., test different air bearing designs and measure different parameters. A schematic validation plan for the mathematical model of the PAFB shows the capabilities and usefulness of the test facility.

Chapter 3 presents the mathematical model of the PAFB, hence a fusion of publication P1 and publication P2 as mentioned above. The presentation beginning with the RAB containing only the air film and is then expanded into the fully coupled fluid-electro-mechanical system of the PAFB. The chapter ends with the model being validated by parts, i.e., the PTF is experimentally validated (publication P1), while the passive part of the PAFB is validated by numerical simulations of an AFB (publication P2).

Chapter 4 deals with the numerical results generated by the mathematical model and is divided into two part, namely: 1) results from a passive AFB system; and 2) results from an active PAFB system. Of the first part is a discussion regarding direction of rotation in an AFB and its effects on the bearing performance. This is followed by

the parameter study based on the findings presented in publication P2, i.e., varying the size of the unsupported top foil area as described above. Hereafter, a calculation of the onset speed of instability for two types of AFB and a discussion of the results. The chapter ends with results from the second part, a parameter study of the change in the aerodynamic forces based on the size and location of a MFC patch also mentioned previously.

Chapter 5 contains the conclusion and treats the further aspects of the PAFB.

Chapter 2

On the design of the test facility for controllable air bearings

This chapter gives an introduction to the test facility designed, constructed and used in the initial effort to develop piezoelectric air foil bearings (PAFBs). The chapter begins with an outline of the general design requirements of, and considerations applied to, the test facility. A literature review gives an overview of test facilities used for studying air journal bearings. This is followed by a description of the four modules making up the test facility created at the Technical university of Denmark (DTU). The versatility of the manufactured test facility is highlighted with respect to experimental set-ups. The chapter ends with a description of the secondary makeshift test facility used for identifying the modal parameters of the piezoelectric top foil.

2.1 Test facilities presented in the literature

In the literature two different types of test facilities are presented for the experimental investigation of journal bearing dynamic performance: 1) a free-floating rigid or flexible rotor supported by two test bearings (see Balducchi et al. 2014; Belforte et al. 2006; Ertas et al. 2010; Howard 2009; Kim and San Andrés 2009; Morosi and Santos 2012; Rudloff et al. 2012; San Andrés et al. 2007); and 2) a free-floating test bearing supported by a rigidly rotating rotor, i.e., a rigid rotor supported by two bearings. Both types of test facilities are sketched in figure 2.1. The designed test facility is of the second type.

The second type of test facility utilizing the floating bearing strategy was initially presented by Glienicke (1966) and used to study hydrodynamic bearings. In the original design the test bearing was located mid-distance between the two support bearings, i.e., it was a centralized floating bearing. Test facilities for air journal bearings have since been designed following the same principles (see Ertas et al. 2009a; Heshmat et al. 1982; Lee et al. 2008). This design configuration has the advantage of being highly rigid and it is symmetric at the mid-distance, hence in the center of the test bearing. This supports the common assumption of axial symmetry utilized in bearing calculations in order to reduce computational effort (see Pierart and Santos 2015).

However, the symmetric test bearing location yields practical disadvantages. The
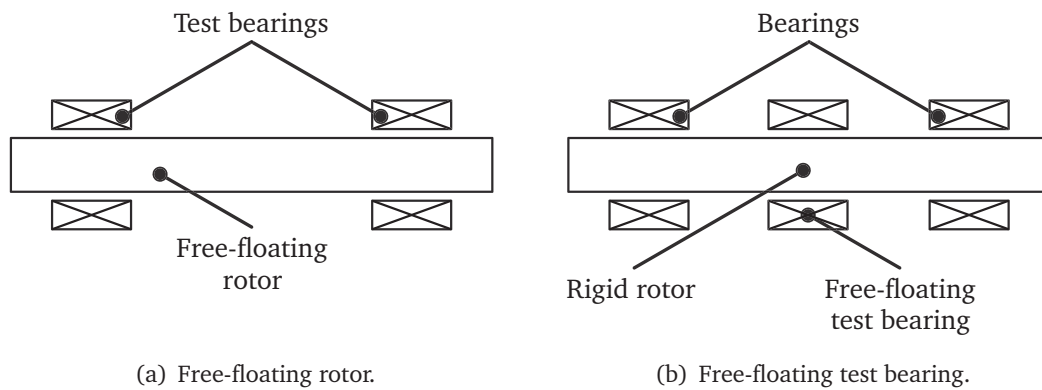
(a) Free-floating rotor.   (b) Free-floating test bearing.

Figure 2.1: The two types of test facilities found in the literature.

placement of the test bearing between the two support bearings makes it impossible to mount and dismount the test bearing without disassembling the test facility. This is impractical and may make it increasingly difficult to reproduce experimental data produced prior to the disassembly due to loss of alignment. In addition, the inner diameter of the support bearings sets the lower limit for the nominal test bearing size, since the test bearing must pass the land for one of the support bearings before it will be located at the mid-distance. These disadvantages may be overcome by dividing the test bearing or the rotor into multiple parts, although, this will only move the alignment issue to the assembly of the test bearing instead. Also, it limits the types of bearing that can be tested, since not all bearings can be divided into multiple pieces and still function as intended.

The alternative to placing the test bearing at mid-distance is to place it on the outside of the support bearings, i.e., an overhung free-floating test bearing. Test facilities utilizing this principle are also described in the literature (see Dellacorte 1998; Ruscitto et al. 1978; San Andrés et al. 2010a; San Andrés et al. 2010b). This configuration overcomes the difficulties of changing the test bearing without disassembling the test facility at the cost of symmetry and a comparable lower rigidity of the rotor. This has been described by Talukder and Stowell (2003), where the advantage of easy mounting and dismounting of the test bearing is highlighted. Due to the lower rigidity of the rotor the risk of it bending is higher, which results in an axially non-symmetric deflection of the rotor within the test bearing and a skewed distribution of aerodynamic pressure. To avoid these rotor deflection within the test bearing, the operational range of the "overhung free-floating test bearing" test facility must be below the first natural frequency and the rotor must be balanced.

A common problem for free-floating bearing designs is to restricting the test bearing from moving axially without affecting the bearing performance in radial direction. As indicated by the name "free-floating", the test bearing should ideally be floating on the air film, but due to unavoidable forces such as gravity and drag forces acting on the bearing surface, the axial movement of test bearing must be constrained. This is commonly done by connecting multiple stingers or wires to the test bearing. For centralised floating bearings the stringer or wires are placed circumferentially at the axial centre, orientated in the radial direction (see Ertas 2009). A sketch is provided in figure 2.2(a).
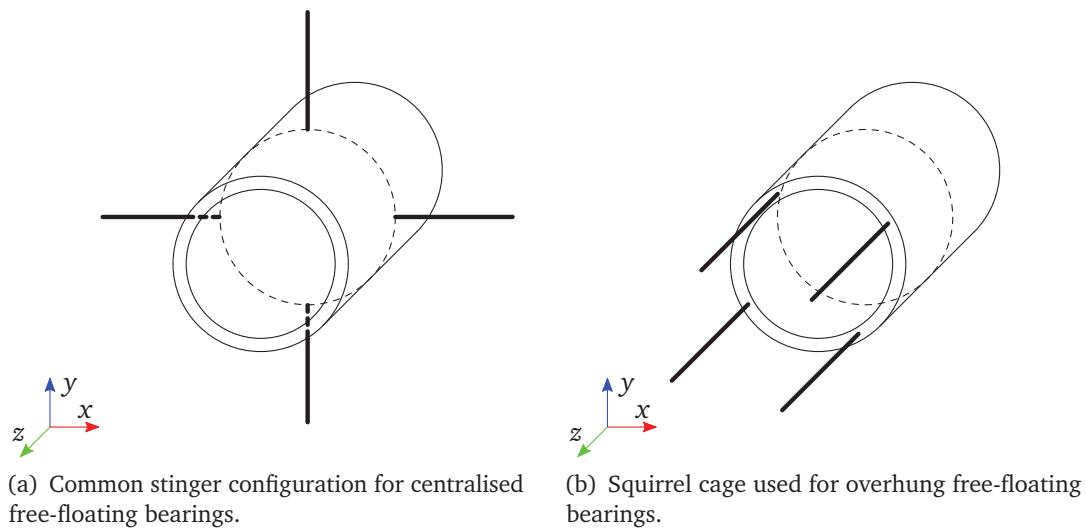
(a) Common stinger configuration for centralised free-floating bearings.

(b) Squirrel cage used for overhung free-floating bearings.

Figure 2.2: Two types of stinger placement used to constrain the unwanted motion of the test bearing.

A drawback of this types of confinement is that it affects all six degrees-of-freedom (DoFs) in the fixation point, e.g., a stinger preventing the test bearing from rotating due to drag forces will also limit the radial motion of the test bearing. This will affect the test bearing performance and as such it is not ideal. For overhung floating bearings a flexible squirrel cage is commonly used. In this method the stingers are orientated in an axial direction and placed along the circumference in one end of the test bearing, as seen in figure 2.2(b). This configuration also affects the radial motion of the test bearing, but due to the orientation of the stingers the effects from the high axial stiffness are eliminated at the expense of introducing an additional moment of inertia between two stingers placed on each side of the circumference (see Matta and Arghir 2012; Matta et al. 2010; San Andrés and Norsworthy 2015; San Andrés and Chirathadam 2011).

To obtain the dynamic characteristics of the test bearing, the air film must be perturbed. There exist two different techniques for exciting the air film: 1) shaking the rotor or 2) shaking the bearing house. The first resembles rotor-bearing systems found in industry where fixed bearings support a floating rotor, i.e., the movement of the rotor affects the air film. The second technique is commonly applied in floating bearing test facilities, since the rotor is rigidly supported by the two support bearings and is therefore, ideally, not able to move. However, the first technique has been used for floating bearing test facilities (see Bellabarba et al. 2005). In that case two active magnetic bearings were used to support the rigid rotor. This allowed for high-precision control of the linear placement and tilt of the rotor, and thereby the forces applied to the test bearing.

2.2   General design requirements and considerations

A rotor-bearing system with PAFB can be divided into the following subsystems: journal, air film, piezoelectric top foil and bump foil. The same subsystems are found

in the developed mathematical model of the journal-bearing system with PAFB and for this reason the validation will be performed in steps follow this division. Figure 2.3 shows the principle of the stepwise validation. Before the construction of the presented test facility two of the validation steps could be performed on existing test facilities at DTU, namely the validations of the "structural properties of bump foil" (see Larsen et al. 2014) and "rotor-bearing system properties" (see Larsen et al. 2015a). For this reason the presented test facility must be able to perform the remaining three experiments required to validate the mathematical model of the PAFB, namely: validating the "modal properties of piezoelectric top foil", the "aerodynamic effects" and the "PAFB properties".

By performing simple experiments the number of uncertainties are minimized since the design parameters are easier to control and monitor. This results in a higher quality of experimental data, giving better grounds for validating the mathematical model. The validation may also reveal limitations of the model, since these will be more obvious due to the high quality measurements. This should provide insights into the physics governing the subsystem and thereby an increased knowledge of the important parameters. This is the main reason for validating the mathematical models of the subsystems instead of only the system model itself.

Based on the objective of the PhD thesis requiring a test facility capable of investigating "several strategies for controllable gas bearings" and the validation requirements a "free-floating test bearing" test facility has been designed and constructed, as seen in figure 2.4. The test facility is designed with a vertical journal, as opposed to most test facilities found in the literature. This enables the test bearing to be mounted on top of an aerostatic thrust bearing, i.e., the test bearing floats on top of the air cushion. This eliminates the requirement of stingers, wires or a squirrel cage thereby avoiding the restrictions on radial motions that they introduce. The high-speed spindle can be moved in axial direction enabling an easy assembly of, and access to, the test bearing. The design results in a highly versatile test facility with the capability of being used for experimental investigations of many different types of air bearings and bearing sizes. The test facility also accommodates the mounting of a single top foil with a fixed clamped edge. This enables the study of the top foil interactions with the air film. Performing multiple experiments with different test bearings and top foil segments broadens validation range of the mathematical model, just as it can provide a better physical understanding of the design parameters influencing the bearing performance.

2.3 Overview of the test facility at the Technical University of Denmark

The test facility, seen in figure 2.4, has been designed with the capability to experimentally investigate top foil and air film interactions, as well as to assess the dynamic performance of air journal bearings.

The designed and constructed main test facility consists of fourth module modules. The four comes in two versions. The modules are: 1) frame structure and high-speed spindle; 2) motor drive, amplifiers and data acquisition system; 3) actuators and sensors; 4a) free-floating test bearing and rigid journal and 4b) clamped flexible test bearing segment and rigid journal. Components from the four modules are highlighted in figure 2.4. Modules (1) and (2) form the permanent part of the test facility, while modules (3) and (4) are designed as exchangeable parts making them easy to replace or modify
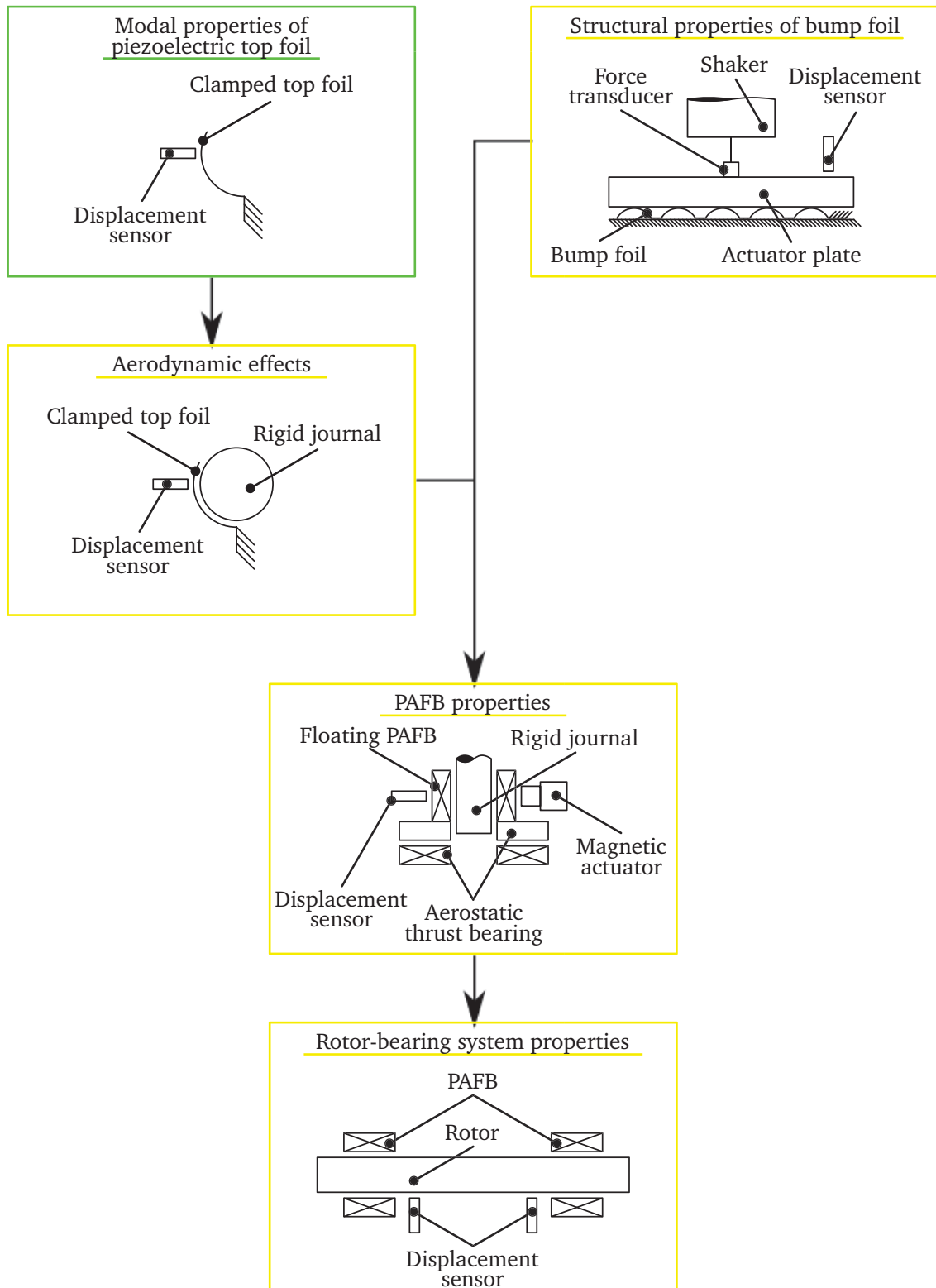
Figure 2.3: Stepwise validation of the mathematical model of an AFB and PAFB. The validation addressed in the PhD thesis is highlighted in green, while the future aspects of the research are marked in yellow.
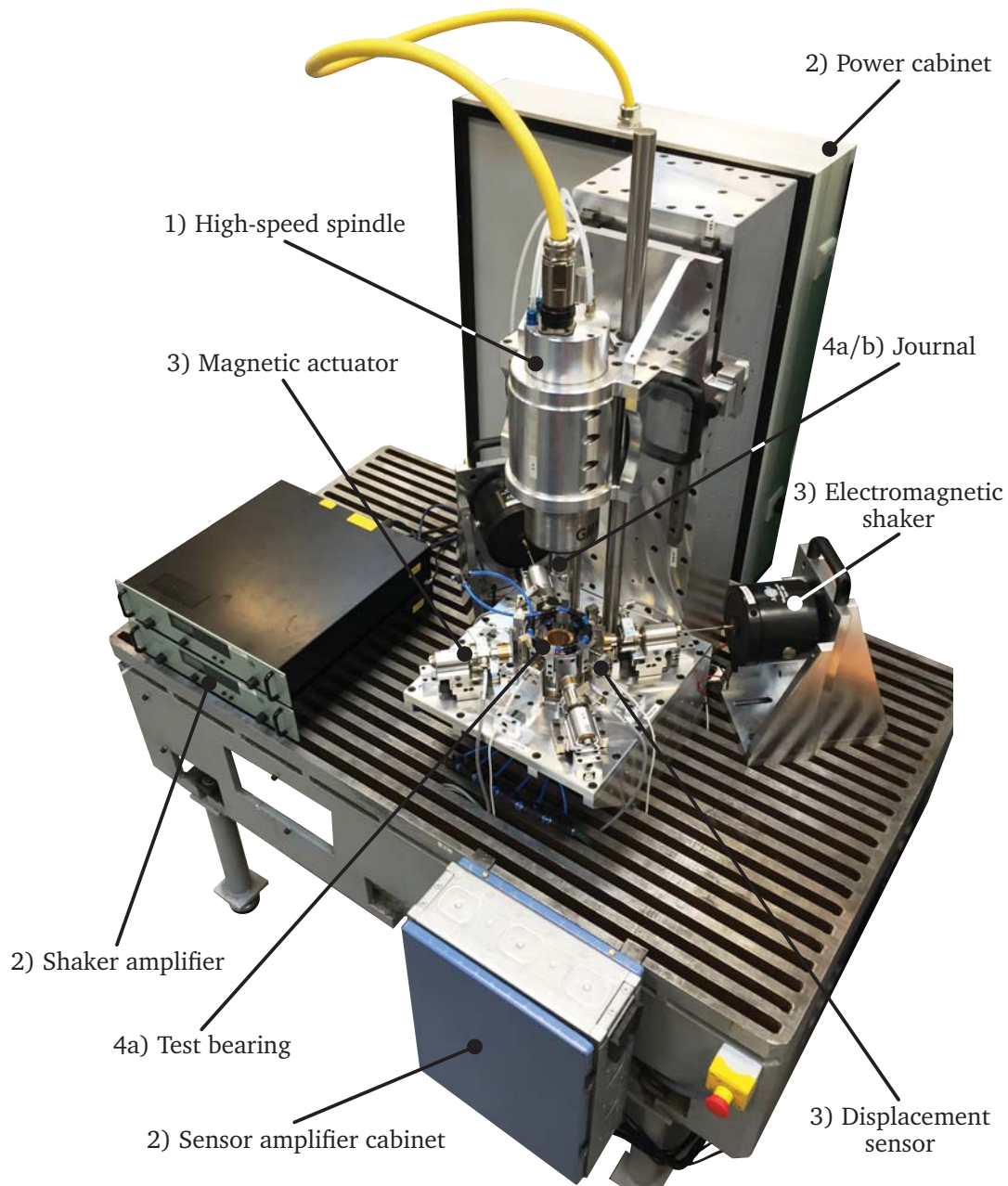
Figure 2.4: The test facility allows for experimental studies of the static and dynamic performance of an air journal bearing or the response of a single top foil segment. Four modules make up the test facility: 1) frame structure and high-speed spindle; 2) motor drive, amplifiers and data acquisition system; 3) actuators and sensors; 4a) floating test bearing and fixed journal and 4b) clamped flexible test bearing segment and fixed journal. Modules 4a and 4b are mutually exclusive.

Table 2.1: A list of the properties for the main test facility.

Description	Dimensions	Unit
Overall dimensions ($h \times w \times l$)	$922 \times 400 \times 685.5$	[mm]
Maximal rotational speed	45,000	[rpm]
Upper nominal size of test bearing ($d \times h$)	Ø105 × 100	[mm]
Shaker frequency range	0-10,000	[Hz]
Shaker frequency force	45	[N]
Displacement sensor range	0-2	[mm]

in order to accommodate the need for different experiments. The main properties of the test facility are listed in table 2.1. The four modules are presented below, along with their key components.

Module 1: Frame structure and high-speed spindle

A front view and section view of module 1 are shown in figure 2.5. The module consists of the frame structure made up by a tabletop (blue), frame and base structure (orange), high-speed spindle mounted in a guide structure (magenta), aerostatic thrust bearing (red) located in the tabletop and a spline-hub joint with a torque limiter (green) placed between the aerostatic bearing and the base structure.

The structure, in which the high-speed spindle is mounted, can be raised and lowered manually, assisted by the gas spring, along the linear guides and precision rods located in the tabletop, frame and base structure. This enables the journal to be moved axially and to be disengaged from the test bearing in a simple manner. The linear guides and precision rods ensure proper angular alignment of the high-speed spindle relative to the top part of the aerostatic thrust bearing. This is very important, since a misalignment between these components will result in a misalignment of the test bearing and journal thereby increase the risk of rotor-bearing contact at the bearing edges. Axially alignment of the test bearing and journal is ensured by the free radial movement of the test bearing, since the test bearing is free-floating due to the aerostatic thrust bearing it is mounted on.

The high-speed spindle is manufacture by GMN and is of the type HV-P 120 - 45000/18. It runs up to 45,000 rpm and is outfitted with a HSK C-40 tool interface at the bottom enabling an easy and fast replacement of the journal. The conical interface ensures a proper fastening of the journal, just as it maintaining the angular alignment when one journal is replaced by another one.

The test bearing is mounted on top of the aerostatic thrust bearing with four M3 bolts. A pattern of threaded holes, seen in figure 2.6(a), are placed on three aligned reference circles in order to accommodate for different test bearing sizes and. Depending on the diameter of the test bearing, at least one set of holes will be available for fastening. It is very important the bottom surface of the test bearing, which is connected to the aerostatic bearing, is perpendicular to the axial direction of the test bearing. This will ensure that a proper angular alignment of the test bearing and journal can be archived, according to the description above.

The floating test bearing is supported radially by the aerodynamic forces from air film located between the journal and the bearing surface. In axial direction, the test
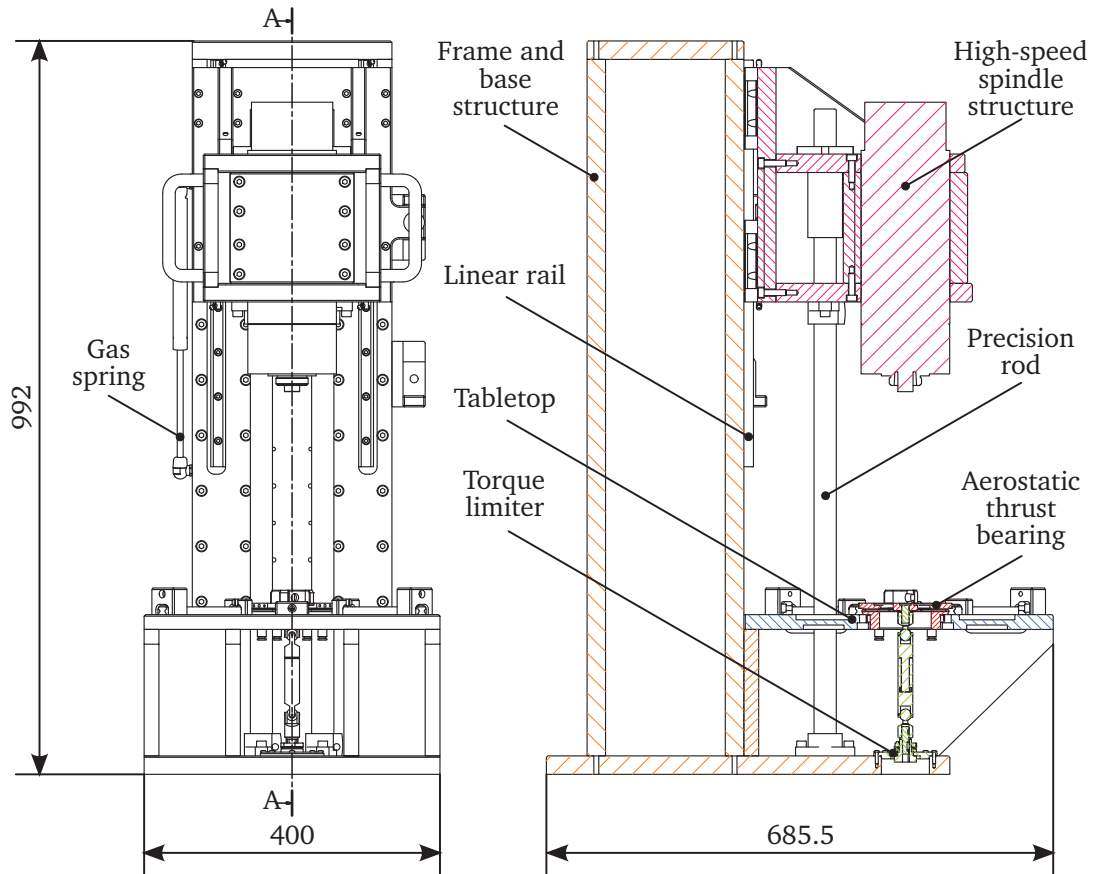
Figure 2.5: A section view of the frame structure and high-speed spindle module. The frame and base structure is hatched with orange, the magenta is the high-speed spindle and guide structure, the tabletop is blue, the red is the aerostatic thrust bearing and the green is the torque limiter and spline-hub joint.

bearing is supported by a combination of gravity and the lift provided by the aerostatic thrust bearing. This support in combination with the aerodynamic forces from the air film prevents tilting of the test bearing. A spline-hub joint connected to the aerostatic top part and a torque limiter ensures the test bearing will not rotate unless bearing failure occurs. In such case the torque transferred from the high-speed spindle through the journal and test bearing will surpass the loading level allowed by the torque limiter and the test bearing will therefore be able to rotate along with the journal.

Module 2: Motor drive, amplifiers and data acquisition system

The high-speed spindle is connected to a combined motor drive and frequency transformer (SIEB & MEYER, Drive System SD2S, type 0362146LF) via a high-frequency impedance and an EMC filer, all of which are placed in the power cabinet, see figure 2.7. The motor drive monitors and maintains the rotational speed of the high-speed spindle. When running at high speeds the spindle requires cooling just as the ceramic ball bearings are oil mist lubricated. This enables the ball bearings to perform as specified by the manufacturer thereby preventing them from being worn down quickly. The oil mist is supplied by the oil lubrication unit GMN Prelub GB 2, while the cooling unit

(a) The top part of the aerostatic thrust bearing. The
hole pattern is intended for mounting the test bearing.

(b) The tabletop.

Figure 2.6: Two of the key components in module 1, the top part of the aerostatic thrust bearing
and the tabletop. Magnetic actuators and eddy current displacement sensors are located on top
of the tabletop. These parts are key components of module 3.
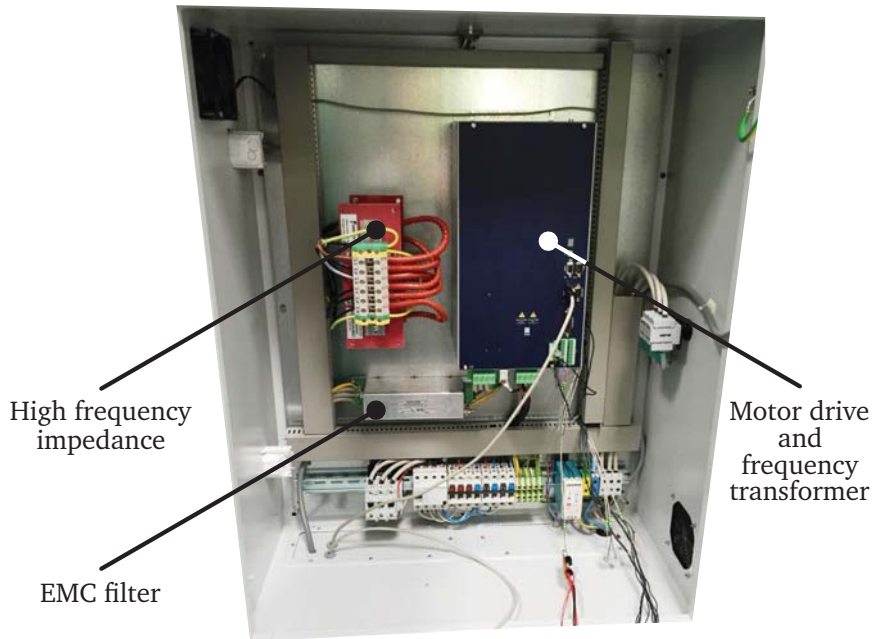
Figure 2.7: The power cabinet for the high-speed spindle.

(GMN Chillers K 3.9-T/2) keeps the spindle from overheating.

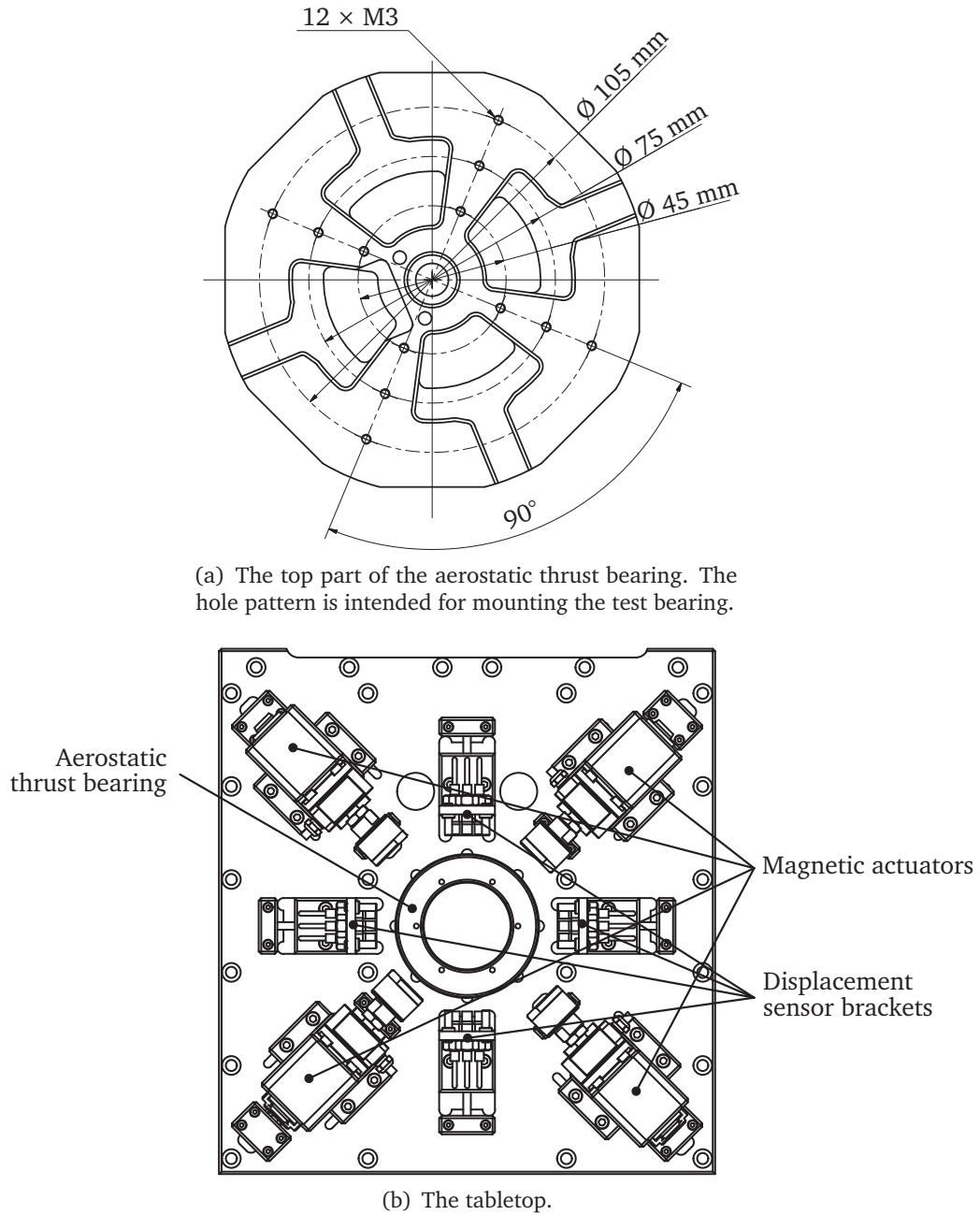The sensors and actuators used in the test facility, including the piezoelectric patches used in the PAFB, are all connected to a computer via a data acquisition and control system (dSpace DS 1103 R&D Controller Board). Amplification of the sensor and actuator signals are done by MEGGiTT IQS 450 (displacement sensors), HBM type AE101 (force transducers), B&K Power Amplifier, Type 2718 (shakers) and Smart Material High Voltage Amplifier HVA 1500/50-3 (MFC patches). All of the amplifiers are located in the sensor cabinet, see figure 2.8.

Module 3: Actuators and sensors

The main test facility is fitted with displacement sensors, force transducers, permanent magnets and shakers for measuring and actuating. Figure 2.6(b) shows the location of the magnetic actuators and the brackets for the displacement sensors. The four sensor brackets and four magnetic actuators are placed alternately next to each other around the aerostatic thrust bearing with an 45° angle between them. The magnetic actuators are mounted on top of linear rails, while the sensor brackets are placed in guide slots. This ensures precise alignment of the components with the centre of the aerostatic thrust bearing, i.e., the test bearing and journal.

The sensor brackets shown in figure 2.9(a) can hold three eddy current displacement sensors (MEGGiTT TQ 412). The safety pins protect the sensors from unintended impacting with the test bearing as it is floating on the aerostatic thrust bearing. The magnetic actuator, seen in figure 2.9(b), consists of a permanent neodym magnet placed in front of a strain gauge based force transducer (HBM type U2B). The advantage of using a strain gauge based force transducer, as opposed to a piezoelectric based transducer, is the ability of the former to measure both static and dynamic loads. The back side of the force transducer can be fixed in order to apply a static force to the test bearing, or

Power supplies

Amplifiers for
displacement
sensors

Amplifiers for
force transducers

Amplifiers for
shakers

Data acquisition
and control system

Amplifiers for
MFC ptaches
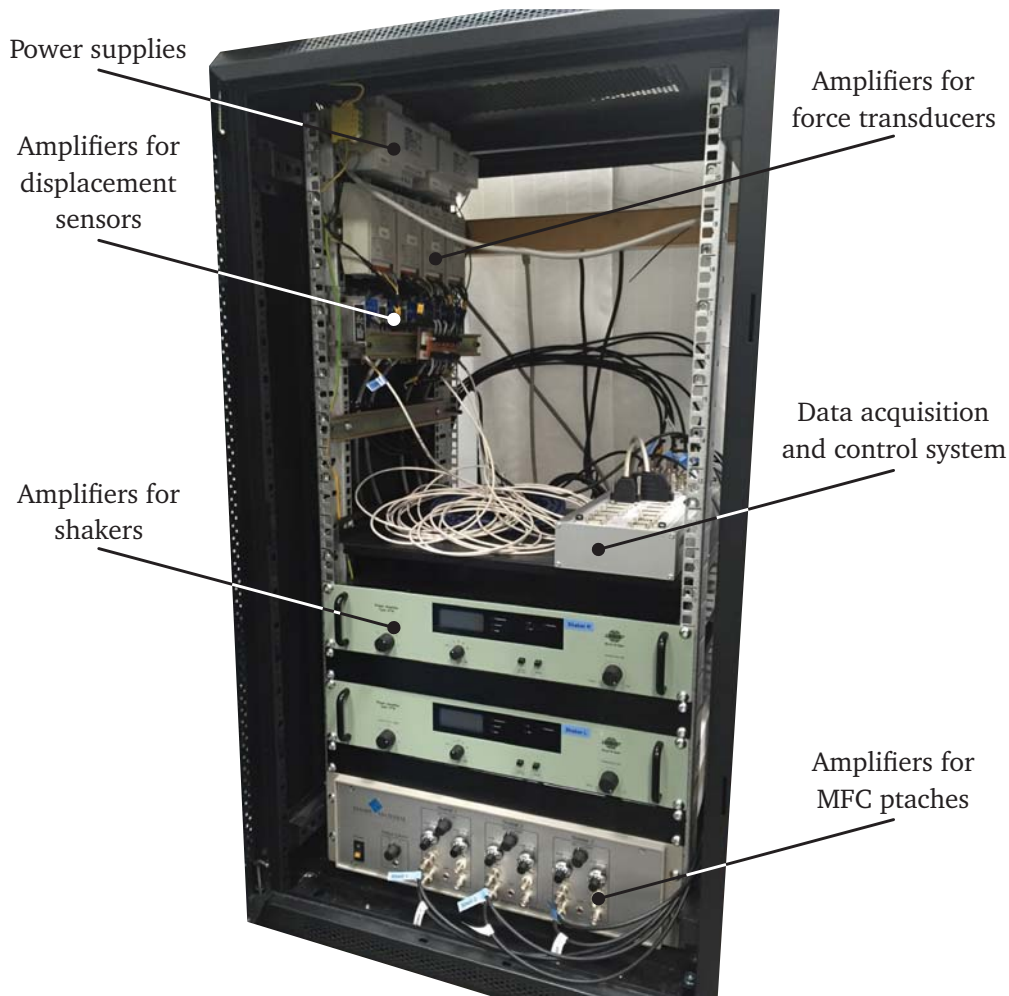
Figure 2.8: The amplifier cabinet. The design and layout was carried out by specialists.

it can be connected to an electromagnetic shaker (B & K Vibration Exciter - Type 4809) thereby providing a dynamic excitation.

In figure 2.10 the sensor and actuator locations are shown. The magnetic field from the magnet, pulls the curved actuator plate with a force dependent on the intensity of the magnetic field and the distance between the magnet and the actuator plate. The distance between a given magnet and plate can be adjusted by sliding the actuator along the linear rail, thereby changing the applied static force. The centre of each curved actuator plate are aligned with the centre of the aerostatic thrust bearing. This ensures the distance between the magnets and the surface of the plates are unaffected by an axial rotation of the aerostatic thrust bearing. The distance measured by the displacement sensors will, however, be affected by a rotation of the aerostatic thrust bearing. Such a rotation also rotates the test bearing and since the sensor plates are flat the linear distance between the outer placed displacement sensors and the sensor plate will differ, i.e., at one edge of the sensor plate will approach the sensor bracket, while at the other edge the sensor plate will move away. The sensor layout in the sensor bracket, shown in figure 2.9(a), is also capable of detecting a tilt of the test bearing by utilizing the same strategy.

(a) The sensor bracket.   (b) Magnetic actuator.
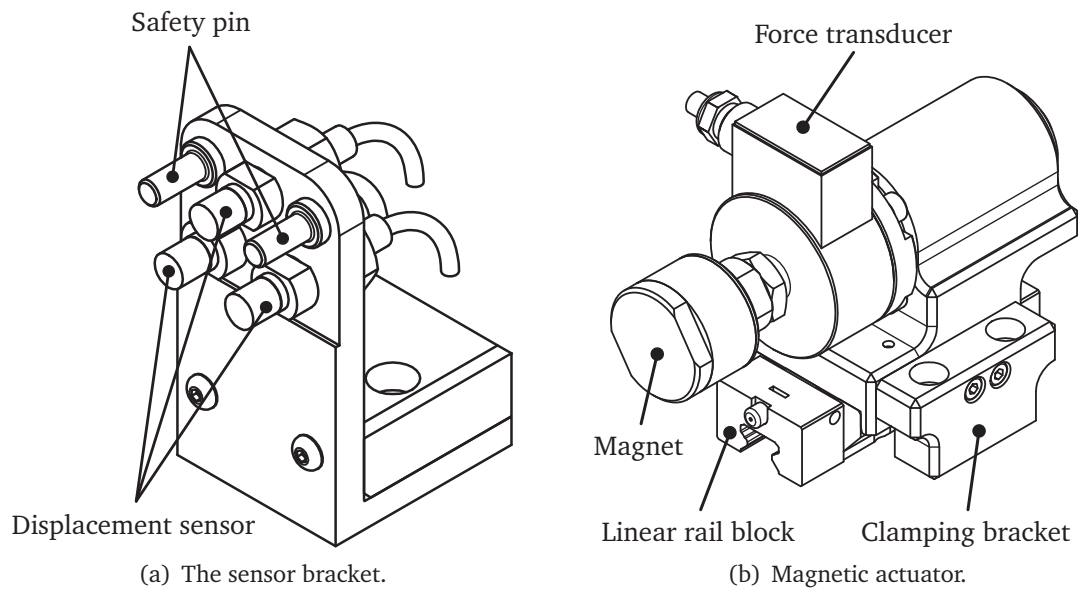
Figure 2.9: Sensor bracket and magnetic actuators on linear rail block.
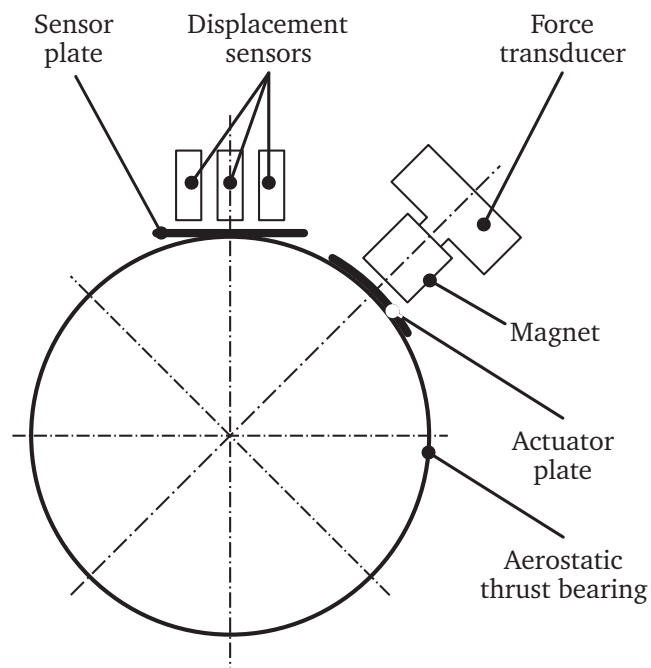
Figure 2.10: Placement of displacement sensors and magnetic actuators relative to the flat sensor and curved actuator plates. Both types of plates are mounted onto the top part of the aerostatic thrust bearing.
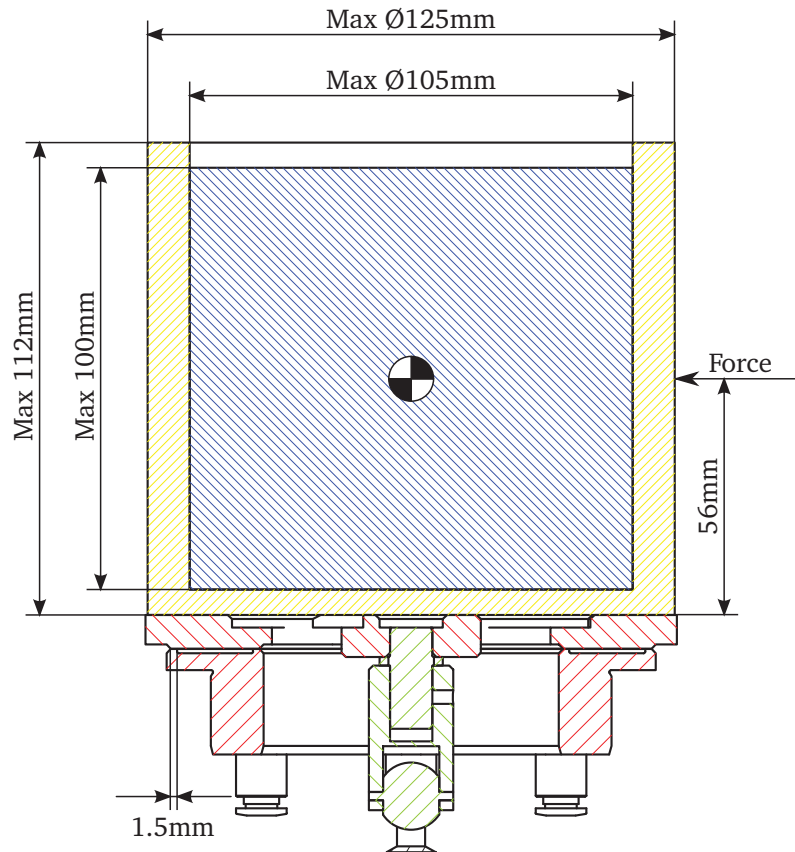
Figure 2.11: The design domain for the test bearing. The blue area marks the maximum size of the journal, while the yellow area is intended for the structural components of the test bearing. The overall geometric limit is Ø125 mm × 112 mm. The red area is the aerostatic thrust bearing and the green area is the spline-hub joint. These components are a part of module 1 and can be seen in figure 2.5.

Module 4a: Free-floating test bearing and rigid journal

The free-floating test bearing is mounted on top of the aerostatic thrust bearing, while the journal is rigidly connected to the high-speed spindle. It is important that the excitation and bearing forces, e.g., aerodynamic forces, are aligned with the combined centre of mass, including both test bearing and top part of the aerostatic bearing, in order to avoid the introduction of moments. This will keep the tilting of test bearing to a minimum, i.e., ensuring the bearing motions are isolated to the radial direction only. The location of the magnetic actuators are located at a distance of 56 mm above the top part of the aerostatic bearing, hence the centre of mass must also be located at this distance as indicated by figure 2.11. This may require an elevation of the test bearing from the aerostatic thrust bearing in order to align the aerodynamic forces with the magnetic actuators, just as additional masses may be required to change the location of the mass centre.

The design of the test facility imposes geometric restrictions on the test bearing, which are highlighted in figure 2.11. The size of the test bearing is limited by the physical space between the thrust bearing and the high-speed spindle as well as the radial size of the thrust bearing. These limitations result in an upper limit of Ø125 mm ×

112 mm for the outer dimensions of the test bearing. The upper nominal bearing size is Ø105 mm × 100 mm, since the outer boundaries of the test bearing must accommodate for bearing housing and bolt connection for fastening the test bearing to the top part of the aerostatic thrust bearing.

A sketch of the aerostatic test bearing mounted on top of the aerostatic thrust bearing is presented in figure 2.12. The test bearing measures Ø40 mm × 40 mm and it has six injection points located at the axial centre, evenly distributed around the circumference. The test bearing is elevated by the distance piece in order to aligned axial centre of the test bearing with the magnetic actuators (not shown in the figure) in line with the description above. Magnet and sensor plates are located on each side of the aerostatic thrust bearing top part, while additional masses are placed between the plates at the top. These masses are added in order to elevate the centre of mass to align it with the magnetic actuators and the centre of the test bearing as description above. Figure 2.13 shows the aerostatic test bearing mounted in the test facility.

Placing a floating test bearing in the test facility enables experimental investigations of the static and dynamic performance of the bearing. When only static forces is applied to the test bearing it is possible to measure, for instance, the locus curve as a function of rotational speed or static loading. By performing experiments where a specific excitation pattern is applied to the test bearing via the shakes, the associated dynamic response of the test bearing can be measured. The excitation pattern can simulate, among other things, a rotor with a mass unbalance affecting the test bearing.

Module 4b: Clamped flexible test bearing segment and rigid journal

The alternative to the floating test bearing is a clamped flexible test bearing segment. This module consists of a flexible top foil mounted in a testing bracket and placed on the linear rail via a pivot mount, hence it replaces a magnetic actuator in the test facility. Figure 2.14 shows the module placed in the test facility. The leading edge of the top foil is placed in the clamping mechanism without bump foil for support. A sensor bracket is placed behind the top foil, accommodating displacement sensors at various locations. The pivot mount and linear rail enables a modification of the air gap by changing the distance and inclination top foil relative to the journal.

The configuration of the test facility makes it possible to experimentally investigate the interactions between the top foil and the air film. The aerodynamic pressure generated due to the profile of the air film deforms the top foil which in turn changes the profile of the air film. The top foil deformations are measured by the displacement sensors located in the sensor bracket on the backside of the testing bracket. As an example, when no outside forces or excitations are applied to the top foil it is possible to find the onset speed of instability by increasing the rotational speed until self-excited vibrations are detected in the top foil. When outside forces or excitations are applied to the top foil, e.g. by a MFC patch, dynamic properties of the PTF can be investigated, such as the resonance frequencies of the air film.

The testing bracket can be removed from the test facility and mounted in a vice with the top foil remaining in the clamping mechanism (see figure 2.15). This eradicates the influence of the aerodynamic forces on the top foil, hence the top foil deflects freely. Furthermore, this configuration enables an experimental investigation of the modal parameters, i.e., resonance frequencies and mode shapes, which are used in the experimental validation of the mathematical model of the PTF.

Figure 2.12: Sketch of a ∅40 mm × 40 mm aerostatic test bearing.

High-speed spindle

Journal

Added mass

Aerostatic test bearing

Sensor bracket

Sensor plate

Displacement sensor

Magnet inside sleeve

Adjustment bolt

Magnetic actuator

Force transducer
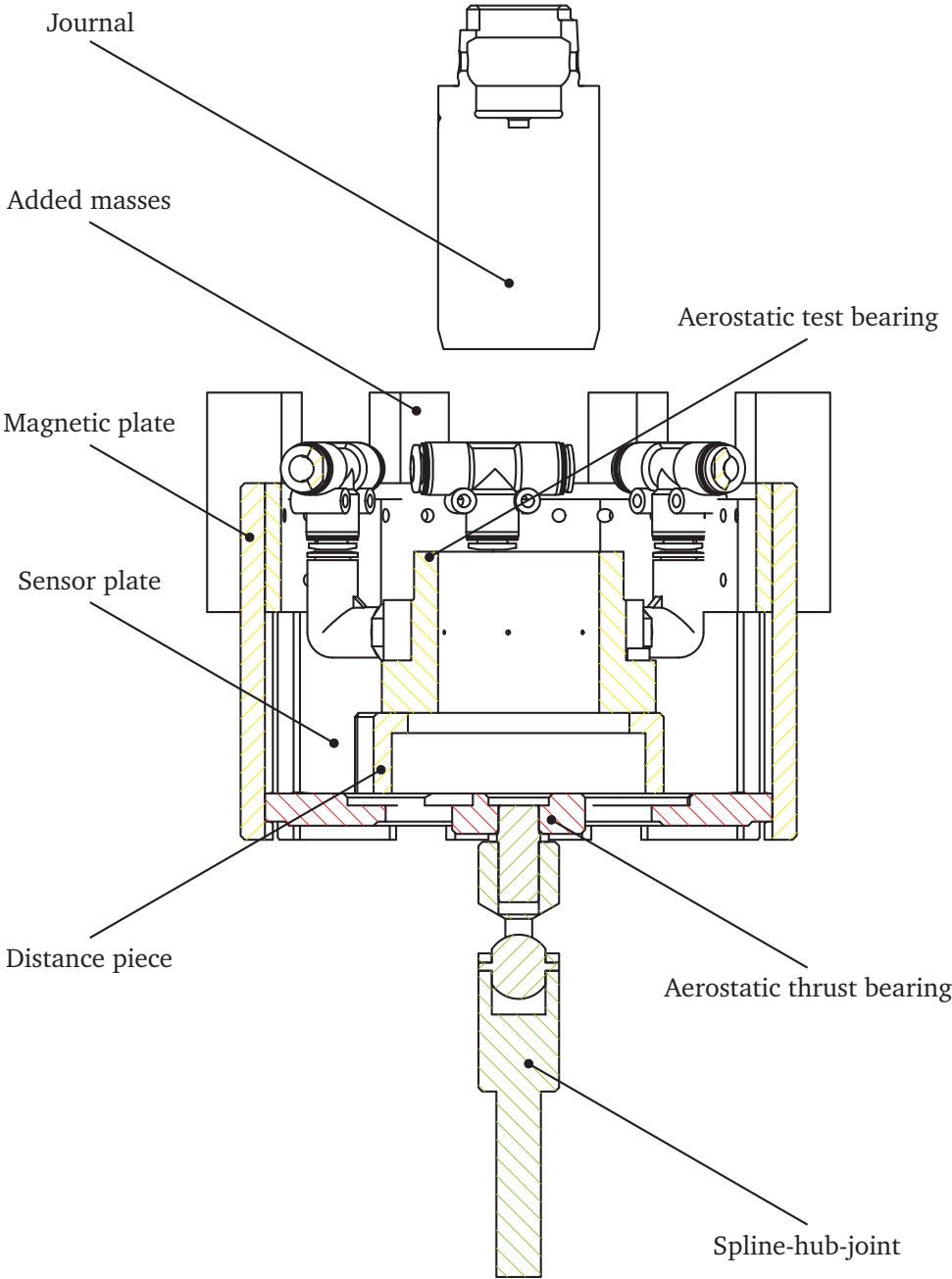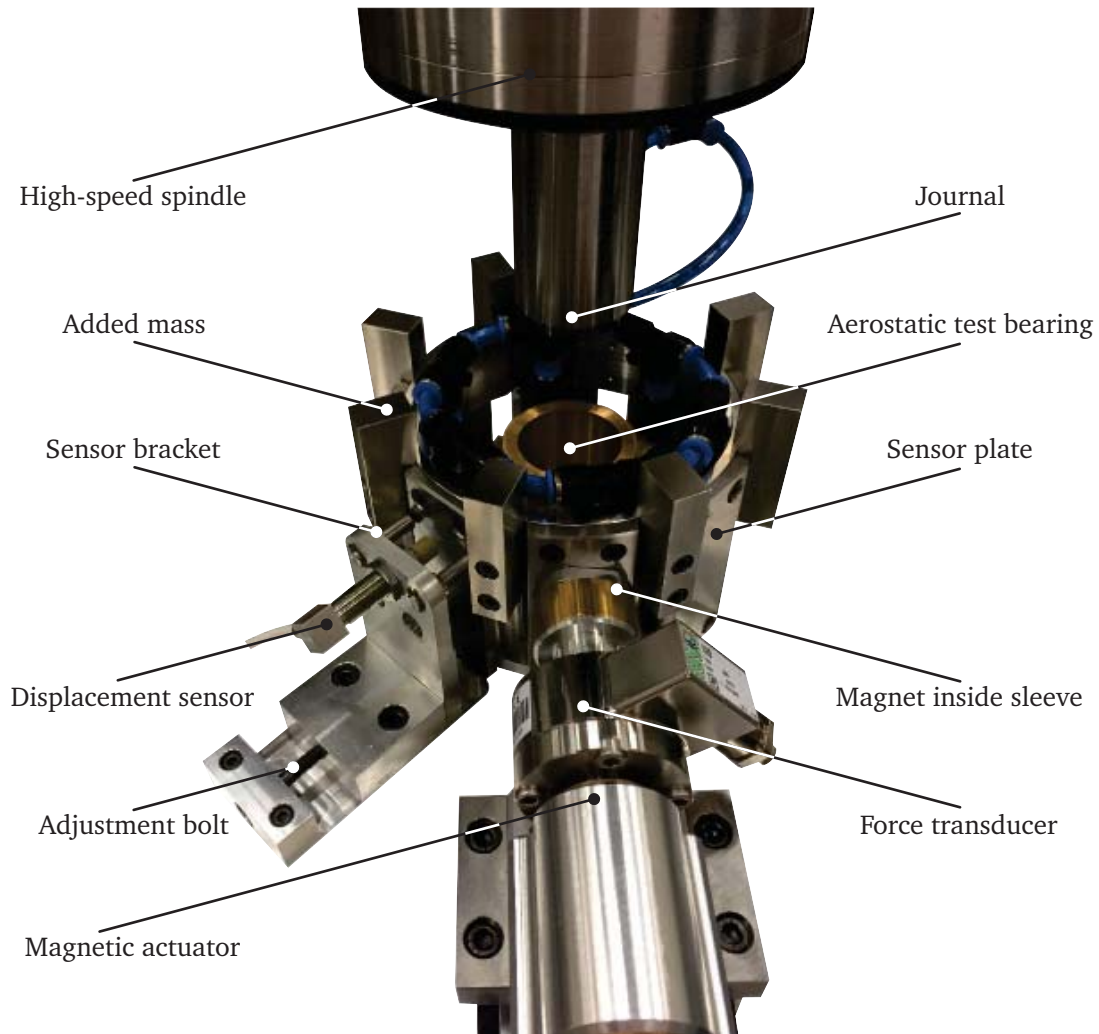
Figure 2.13: Photo of a Ø40 mm × 40 mm aerostatic test bearing mounted in the main test facility.

Only the testing bracket has been used for the experimental validation of the mathematical model of the piezoelectric air foil bearing. The submodel which is experimentally validated is the piezoelectric top foil model.

2.4   Conclusion

Although the test facility was designed and constructed with the aim of testing controllable air bearings, i.e. controllable AFB, this a goal has not yet been fully achieved. Nevertheless, preliminary tests were conducted using an aerostatic bearings (seen in figure 2.13). Results from these experiments are reported in the master thesis written by Grathwol (2015).

A second set of experiments was conducted with a PTF clamped in the testing bracket, while the testing bracket was mounted on the linear rail on the tabletop as seen in figure 2.14. The aim of the experimental investigation was to examined the coupling between an unsupported PTF and the aerodynamic pressure caused by a
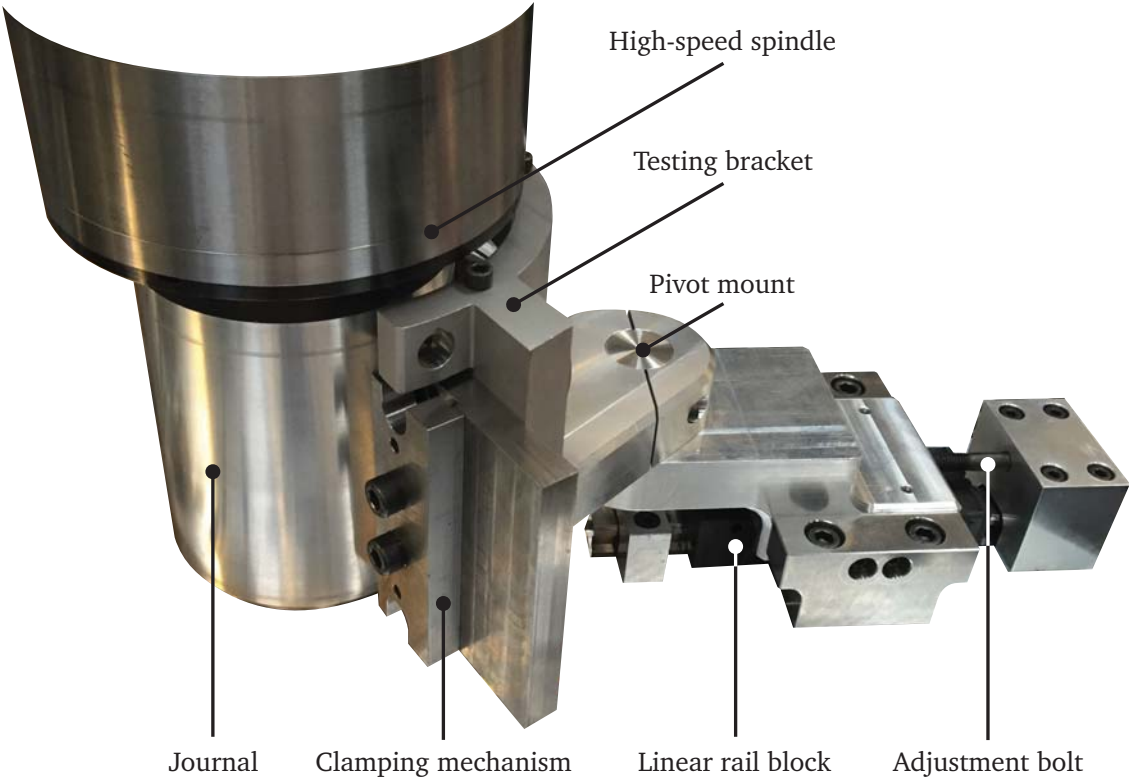
Figure 2.14: Top foil testing-bracket mounted in the main test facility.
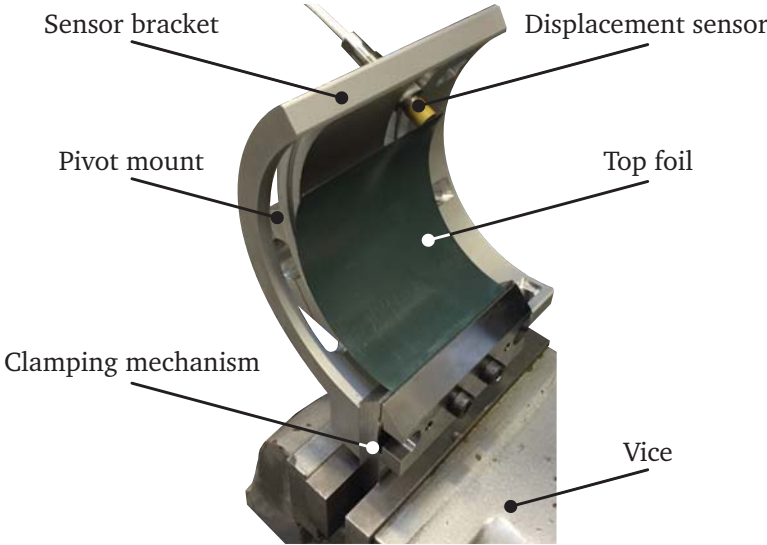
Figure 2.15: The testing bracket placed in a vice. This configuration enables the experimental investigation of the structural and dynamic properties of the top foil.

simply supported journal rotating at constant speed. Results show that it is possible to change the resonance frequencies of the PTF by applying a constant EPD to the IDEs, e.g., the third resonance frequency of the PTF is found to vary within the range from 126 to 166 Hz. The changes in the resonance frequencies is attributed to a change in the stiffness of the air film. Furthermore, it was also found that the damping was affected by the applied EPD. The experimental results were presented in the master thesis by Nielsen (2016).

Chapter 3

Multi-physical modelling of an air bearing – from rigid to controllable compliant surface

In this chapter the mathematical model for the piezoelectric air foil bearing (PAFB) is developed, implemented numerically and partially validated. The final model is derived in three steps as indicated by the three sketches of air bearings seen in figure 3.1. The starting point is a rigid air bearing (RAB), i.e., it has a rigid bearing surface. In the second step the rigid bearing surface is substituted by a flexible top foil supported by a bump foil, i.e., the RAB is turned into an air foil bearing (AFB). Finally, a piezoelectric patch of the macro fibre composite (MFC) type is added to the back side of the top foil creating an PAFB. Different electric circuits can be connected to the interdigitated electrodes (IDE) on the MFC patch depending on the operational objective for the PAFB. The final mathematical model incorporates three physical domains - fluid, electrical and mechanical - making it a fluid-electro-mechanical model.

The numerical implementation of the mathematical model utilizes the finite element method (FEM) for discretising the continuous piezoelectric top foil (PTF) and air film. The bump foil is modelled by the bilinear simple elastic foundation model (SEFM) and is included as a support pressure acting on the top foil elements. The journal and electrical circuit connected to the IDEs are defined as a discrete sub-system in the mathematical model and therefore directly numerically implementable. This is followed by a description of the numerical implementation of the mathematical model.

The validation of the developed mathematical model is twofold. The linear electro-mechanical model of the PTF is validated by experiments performed with an PTF mounted in the testing bracket and excited by the MFC placed on the back side of the PTF. The non-linear fluid-mechanical model of an AFB is validated by numerical results obtained from an experimentally-validated model known from the literature, e.g. Larsen and Santos (2015).

(a) Rigid air bearing (RAB).   (b) Air foil bearing (AFB).   (c) Piezoelectric air foil bearing (PAFB).
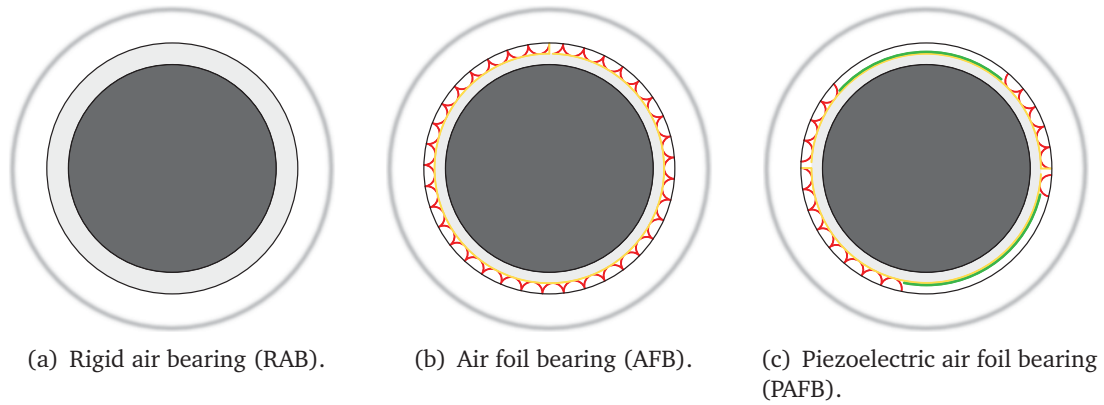
Figure 3.1: Cross-section view of three air bearings. The AFB has one top foil (yellow) clamped at the leading edge with a bump foil (red) for radial support. The PAFB has two piezoelectric top foils (PTFs), which are clamped at their leading edge. Each of the PTFs has a macro fibre composite (MFC) patch (green) mounted on their backside in an area where the bump foil has been removed.
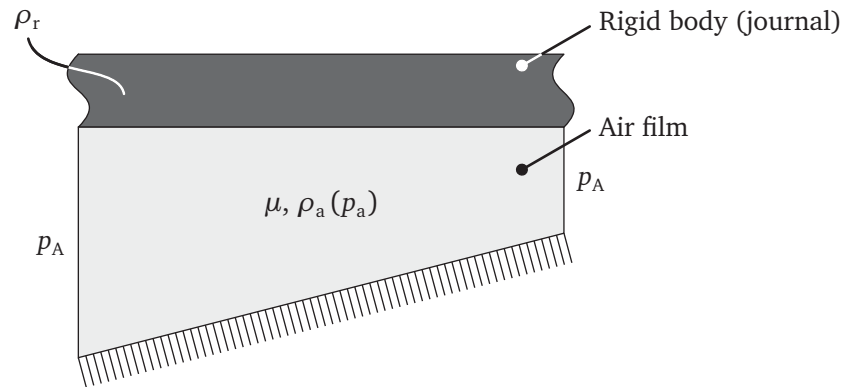
Figure 3.2: The projection of the RAB into a fluid-mechanical system. The system consists of a continuous air film and a discrete rigid journal.

3.1   Rigid air bearing – rigid bearing surface

The RAB seen in figure 3.1(a) can be projected in a fluid-mechanical system like the one shown in figure 3.2. The system consists of two domains, namely an air film and a rigid body. The air film is situated in between the rigid body and a lower rigid surface. The rigid body has a sliding velocity along the air film and is supported by the aerodynamic pressure formed in the air film. The boundary conditions for the air film is ambient pressure. In the projection from the physical RAB to fluid-mechanical system the following assumptions have been made: 1) the surface of the journal is rigid; 2) the air film is continuous along the bearing segment; and 3) the bearing segment is rigid and cannot move or deflect.

The mathematical model for the RAB is based on the following assumptions: 1) the journal rotates at a constant speed and acts like a lumped mass; 2) the air is an ideal gas and independent of temperature, which is valid according to, e.g., Paulsen et al. (2011); 3) the airflow in the air film is laminar and unaffected by body forces
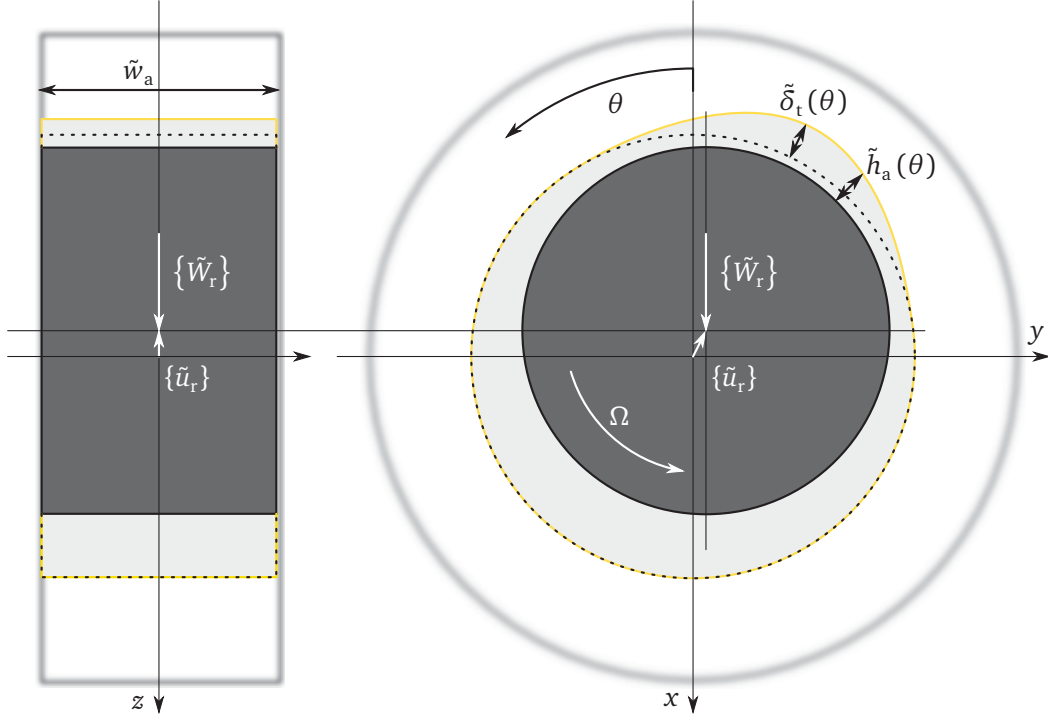
Figure 3.3: A sketch describing the notations used in the stepwise derivation of the PAFB. The sketch is valid for both an AFB and an PAFB, but for an RAB $\tilde{\delta}_t(\theta) = 0$ since the bearing surface is rigid, hence it follow the dashed line.

and 4) there are no pressure gradients perpendicular to the air film. The motion of the rigid journal is governed by Newton's second law (3.1). The air film follows Reynolds equation for compressible fluids (3.2), which is derived by combining Navier-Stokes equations, the equation of continuity and the ideal gas law. The equation was initially presented by Harrison (1913), although without the transient term.

$$\left[\tilde{M}_r\right]\{\ddot{\tilde{u}}_r\} = -\{\tilde{F}_r\} + \{\tilde{F}_{ub}\} + \{\tilde{W}_r\} \tag{3.1}$$

$$\nabla\left(\tilde{p}_a\tilde{h}_a^3\nabla\tilde{p}_a\right) = \nabla\left(\tilde{p}_a\tilde{h}_a\right)\{\Lambda\} + 2\Lambda\frac{\partial}{\partial\tilde{t}}\left(\tilde{p}_a\tilde{h}_a\right) \tag{3.2}$$

The dimensionless, indicated by the $(\tilde{\ })$, forces acting on the journal are the aerodynamic forces from the air film $\{\tilde{F}_r\}$, unbalance forces $\{\tilde{F}_{ub}\}$ due to journal mass unbalance and the static load $\{\tilde{W}_r\}$, e.g., due to gravity. The aerodynamic forces are calculated by integrating the aerodynamic pressure acting on the journal, as given in equation (3.3), where $\tilde{w}_a$ is the width of the air film and $\tilde{\theta}_a$ is the angular extension. The static load are shown in figure 3.3 along various spatial variables and constants.

$$\{\tilde{F}_r\} = \int_{-\frac{\tilde{w}_a}{2}}^{\frac{\tilde{w}_a}{2}}\int_0^{\theta_a}(\tilde{p}_a(\theta,\tilde{z})-1)\begin{Bmatrix}\cos\theta\\\sin\theta\end{Bmatrix}d\theta d\tilde{z} \tag{3.3}$$

The aerodynamic pressure $\tilde{p}_a$, which depends on the axial and circumferential position $(\tilde{z},\theta)$, is affected by the thickness of the air film $\tilde{h}_a$ and bearing number Λ. The bearing number depends on the absolute viscosity of the air μ, the angular speed
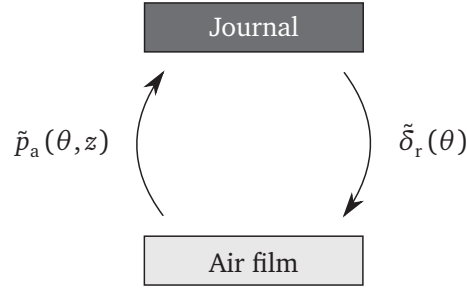
Figure 3.4: Domain interactions in an RAB. The aerodynamic pressure acts as a load on the journal, while the movement of the journal changes the thickness of the air film.

of the journal Ω, the ambient pressure p_A, the bearing radius r and the radial clearance c, as given below.

$$\Lambda = \frac{6\mu\Omega}{p_A}\left(\frac{r}{c}\right)^2$$

The air film thickness is given by the geometry of the bearing surface and journal as well as by the location of the journal within the air bearing $\{\tilde{u}_r\}$. Assuming the journal and bearing are both cylindrical, the equation for the thickness of the air film is given below. $\delta_r(\theta)$ is the journal displacement projected into radial direction at the angle θ.

$$\tilde{h}_a(\theta) = 1 - \begin{Bmatrix}\cos\theta\\\sin\theta\end{Bmatrix}^{\mathrm{T}}\{\tilde{u}_r\} = 1 - \tilde{\delta}_r(\theta)$$

The interactions between the two domains found in an RAB are highlighted in figure 3.4. A movement of the journal changes the thickness of the air film affecting the aerodynamic pressure. This will in turn change the aerodynamic forces acting on the journal, resulting in a movement of the journal within the RAB.

3.2   Air foil bearing – compliant bearing surface

An air foil bearing (AFB), such as the one shown in figure 3.1(b), is an attempt to improve the RAB according to Heshmat et al. (1983b). The engineer can modify the flexibility of the bearing segment by adjusting the bump foil based on the operational conditions for the AFB. The compliance of the bearing surface in an AFB results in a thicker air film relative to one in an RAB at corresponding rotor eccentricities. This results in a lower torque, but also a lower load-carrying capacity for the AFB. However, for identical minimum air film thicknesses the load-carrying capacity is higher for an AFB.

The fluid-mechanical system for an AFB is shown in figure 3.5. The additional components used in an AFB compared to an RAB highlighted in the figure, i.e., the top foil and bump foil, which are placed on top of each other. The change from a rigid bearing surface to a compliant top foil supported by bump foil affects the thickness of the air film. Depending on the aerodynamic pressure on the top foil relative to the ambient pressure, the top foil will either be pushed into, or pulled away from the bump foil, i.e., the two components separate. The additional assumptions for an AFB are: 1) the top foil is a thin flexible curved shell; and 2) there are no interactions between
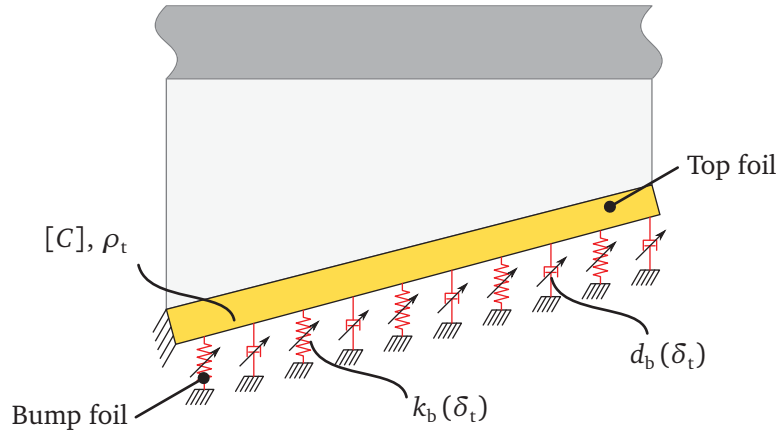
Figure 3.5: The fluid-mechanical projection of an AFB. The projection consists of a continuous flexible top foil supported by a discrete bump foil in addition to the continuous air film and discrete rigid journal seen in the air bearing with a rigid bearing surface.

bumps in the bump foil, i.e., the bump foil can be represented by a pattern of individual bilinear springs and dampers, allowing for a partially separation of top and bump foil. This representation is based on the SEFM presented by Heshmat et al. (1983a).

Shells are known to exhibit non-linear behaviour due to their geometry when the vibration amplitudes exceed the thickness of the shell, e.g., Selmane and Lakis (1997). However, the vibration magnitude in an AFB is comparable with the radial clearance c, and since the ratio between the radial clearance and top foil thickness commonly is bigger than three-to-one the non-linear behaviour will not come into effect. The mathematical model of the top foil is therefore assumed to be linear, both for geometry as well as for the material, e.g., the material does not yield. The constitutive equation used is Hooke's law, which is given below, with $[C]$ describing the compliance of the shell.

$$\{\varepsilon\} = [C]\{\sigma\}$$

The stiffness k_b and damping d_b coefficients used in the SEFM are bilinear and seen below as a function of the top foil radial deflection δ_t.

$$k_b = \begin{cases} \frac{1}{\alpha_b} & , \delta_t \geq 0, \\ 0 & , \delta_t < 0 \end{cases} \tag{3.4}$$

$$d_b = \begin{cases} \frac{k_b \beta_b}{\Omega} & , \delta_t \geq 0, \\ 0 & , \delta_t < 0 \end{cases} \tag{3.5}$$

When the top foil deflects radially outwards into the supporting bump foil the coefficients are equivalent to classical SEFM, i.e., given by Heshmat et al. (1983b). For radially inwards deflection the top foil separates from the bump foil, hence the bump foil does not provide any support to the top foil and therefore the stiffness and damping coefficients are zero. The bump foil support pressure acting on the top foil is given by
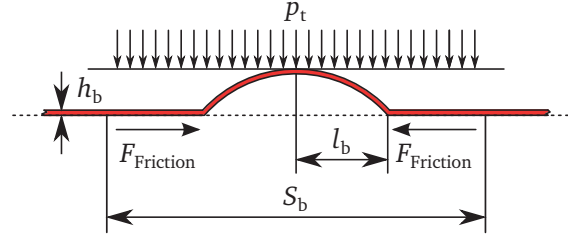
Figure 3.6: Sketch of a single bump from the bump foil. h_b is the thickness of the bump foil, l_b is the half bump length and S_b is the pitch of the bump, i.e., the distance between two adjacent bumps.

equation (3.6) and is a function of the top foil deflection and velocity.

$$p_b = \begin{cases} d_b \dot{\delta}_t + k_b \delta_t & , \delta_t \geq 0, \\ 0 & , \delta_t < 0 \end{cases} \tag{3.6}$$

The support stiffness and damping are a result of the structural compliance of the bump foil and the friction forces acting in each of the contact points between the bump foil, the top foil and the bearing housing. Walowit and Anno (1975) proposed equation (3.7) for the cross-sectional compliance α_b of the bump foil based solely on the geometry of the bump as shown in figure 3.6.

$$\alpha_b \approx \frac{2S_b}{E_b} \left(\frac{l_b}{h_b} \right)^3 \left(1 - v_b^2 \right) \tag{3.7}$$

In figure 3.7 the domain interactions are shown for an AFB. The figure shows the air film being dependent on both the journal and the top foil deflections, i.e., the thickness of the air film can be described by equation (3.8). The aerodynamic pressure in an AFB affects both the journal and the top foil. However, the top foil is also affected by the bump foil when they are in contact.

$$\tilde{h}_a(\theta, z) = 1 - \tilde{\delta}_r(\theta) + \tilde{\delta}_t(\theta, z) \tag{3.8}$$

The fluid-mechanical model of an AFB, including inertia and flexibility of the top foil, was presented in detail by Nielsen and Santos (2017) (publication P2).

3.3 Piezoelectric air foil bearing – controllable compliant bearing surface

The piezoelectric air foil bearing (PAFB) is a next-step development of the AFB. The inclusion of piezoelectric material in the top foil offers the opportunity to either affect or monitor the performance of the PAFB during operation, since piezoelectric material provides a coupling between the mechanical and electrical domains. With an PAFB the engineer has the option to modify the bearing performance during the design phase, which is associated with AFB, and in addition gains the option of additional modification during operation, allowing for an adjustment of the bearing performance to the specific operational conditions.
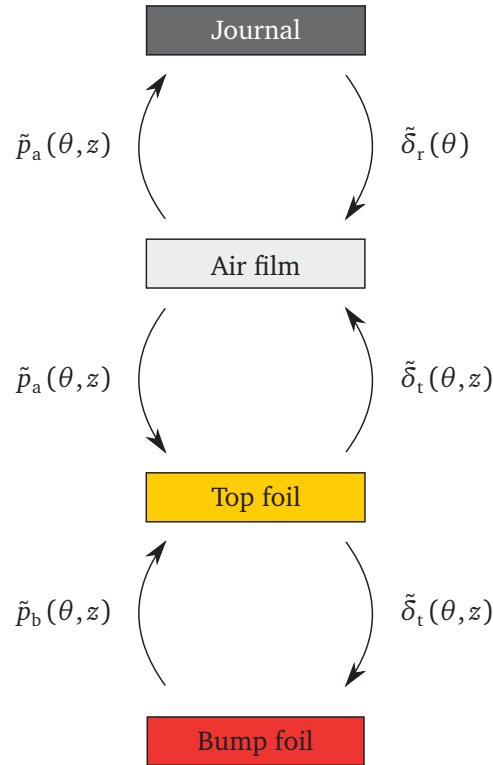
Figure 3.7: Domain interactions for an AFB. The top foil is affected by the support pressure from the bump foil and the aerodynamic pressure in the air film. The aerodynamic pressure also affects the journal. The bump foil is affected by the radial deflections of the top foil, which also affects the thickness of the air film together with the movement of the journal.

Figure 3.8 displays the projection of the PAFB into fluid-electro-mechanical system. The additional component in the PAFB, in comparison to the AFB, is the patch of piezoelectric material located on the backside of the top foil, as highlighted in the figure. The assumptions used for the AFB also apply to the PAFB. In addition, it is assumed that the piezoelectric patch is included as a layer in the top foil, and the wires connected to the electrodes do not have any mechanical properties.

The inclusion of the piezoelectric material in the top foil requires a constitutive equation, which describe both the mechanical and the electrical relationships as well as the couplings between the two physical domains. A description of the constitutive equation is given by Damjanovic (1998), including the thermal couplings, as well as material non-linearities. However, assuming isothermal conditions and that the load is kept within the linear range, the PTF is governed by the constitutive equation (3.9) given by, amongst others, Tiersten (1969).

$$\{\varepsilon\} = [C]\{\sigma\} + [d]^{\mathrm{T}}\{E\} \tag{3.9a}$$

$$\{D\} = [d]\{\sigma\} + [\epsilon]\{E\} \tag{3.9b}$$

The piezoelectric patch included in the PAFB is a macro fibre composite (MFC) patch, one of many commercially available piezoelectric patches. The advantages of using an MFC patch are the configuration of its electrodes and the arrangement of the piezoelectric material, which is shown in figure 3.9(a). The MFC patch consists
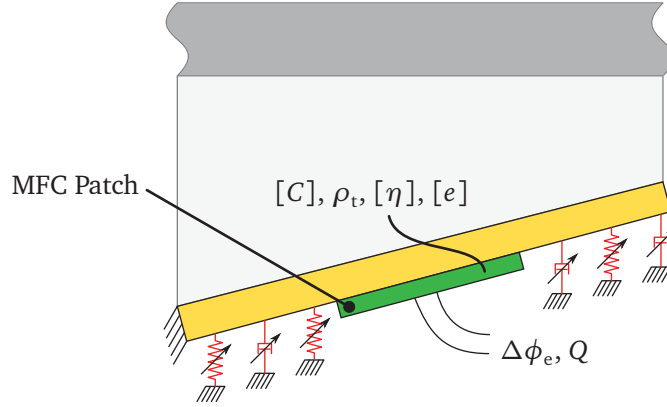
Figure 3.8: Fluid-electro-mechanical system for an PAFB with MFC patch mounted on the back side of the top foil. The piezoelectric material and electrodes are included in the model of the continuous top foil as an additional layer.

of several parallel piezoelectric fibres, isolated from each other, and with two pairs of interdigitated electrodes (IDEs) placed perpendicular to the fibre direction on the top and bottom of the patch. Each pair of IDEs are equipotential, which ensure the electrical field $\{E\}$ created is aligned with the direction of the fibres and is applied uniformly to the MFC patch. It also implies the electrical potential difference (EPD) $\Delta\phi_e$ measured between the IDEs is an average of the electrical field within the MFC patch. This gives the possibility of tailoring the impact of piezoelectric material on the performance of an PAFB by, for example, changing the direction of fibres.

The electrical field is defined as the derivative of the electrical potential as stated in equation (3.10). In general when an EPD is applied between a pair of electrodes placed on each side of a piezoelectric material a uniform electrical field is created with the material, hence $\kappa_e = 1$. The size and direction of the electrical field depends on the EPD and the distance between the electrodes. However, the electrical field created via the IDEs on an MFC patch is non-uniform. A sketch of the field lines is shown in figure 3.9(b) where areas with a low field intensity, called dead zones, are marked in red. Nasser et al. (2008) proposed the correction factor κ_e compensating for the dead zones, i.e., making it possible to treat the non-uniform electrical field in the same manner as a traditional uniform field. The correction factor is a function of the geometry of the IDEs and is given in equation (3.11). Figure 3.10 shows the distance between the electrode fingers Δx_e and width w_e, while h_e is the thickness of the piezoelectric fibres.

$$\{E\} = -\nabla\phi_e \approx -\kappa_e \frac{\Delta\phi_e}{\Delta x_e} \tag{3.10}$$

$$\kappa_e = \left[1 - \frac{h_e}{\Delta x_e}\left(\frac{1}{2} + \frac{2}{\pi^2}\right)\right]\left[\frac{\Delta x_e - w_e}{\Delta x_e - h_e}\right] \tag{3.11}$$

Including an MFC patch in the flexible top foil structure adds an electrical domain to the mathematical model when compared to the AFB as indicated in figure 3.11. The IDEs on the MFC patch can be connected to an electrical circuit, which can either impose an EPD on the IDEs or use the electrical charge generated by a deformation of the PTF.

(a) A sketch of an MFC patch.

(b) The electrical field and dead zones due to the use of IDEs.
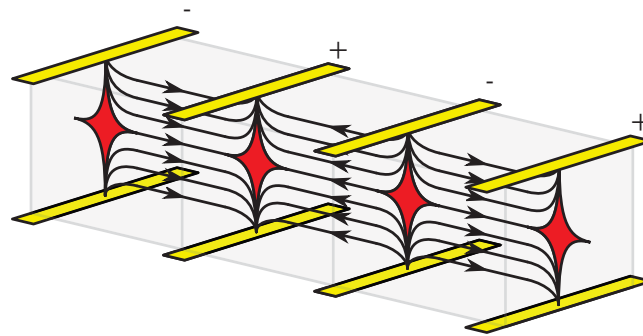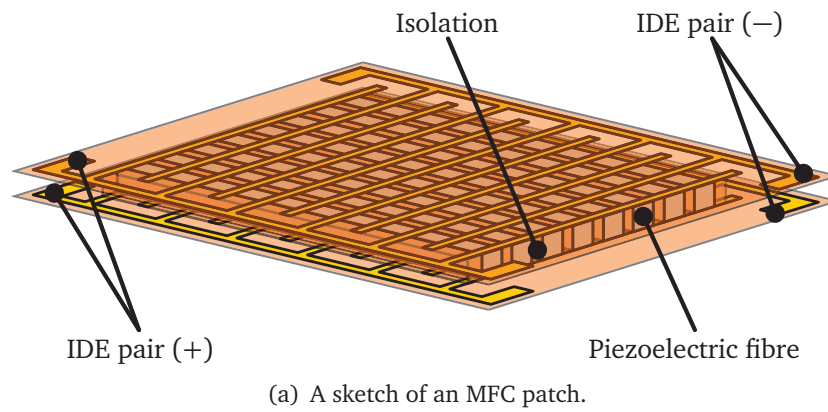
Figure 3.9: An MFC patch consists of aligned isolated piezoelectric fibres placed in a plane with four IDEs placed on top and bottom, perpendicular to the fibre direction. Each IDE on the top are aligned with an IDE on the bottom, and each aligned pair of IDEs are equipotential. The electric field in the fibre direction can be monitored or changed by the IDEs.
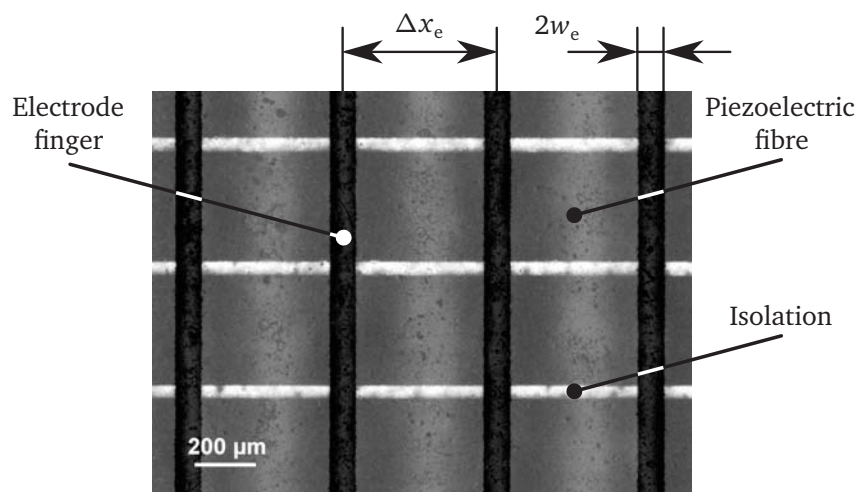
Figure 3.10: A photo of a MFC patch taken by an Olympus GX41 microscope with a Leica DFC450 C camera. Δx_e is the distance between two electrode fingers and w_e is the width of an electrode finger.
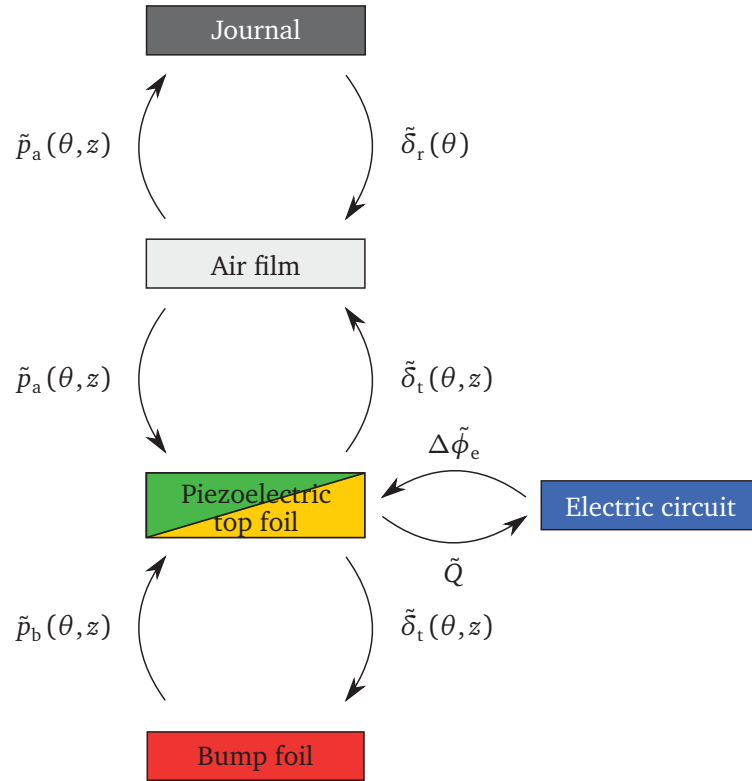
Figure 3.11: Domain interaction in an PAFB. The addition of a MFC patch to the top foil enables the PTF to interact with an electrical circuit. The circuit can either imposes an EPD between the IDEs or receives an electrical charge due to a deformation of the PTF. The remaining domain interactions are the same as for the AFB, seen in figure 3.7.

The electro-mechanical model of an PTF was presented in detail by Nielsen et al. (2016) (publication P1).

Electrical circuit

Generally speaking, a piezoelectric patch is connected to a structure to fulfil one of two purposes: 1) putting energy into the system, i.e., excite the structure, or 2) extracting energy from the system, i.e., as a sensor or for energy harvesting. However, for a vibrating structure it is possible to combine the two, i.e., use the harvested energy to reduce the vibrations of the structure. Figure 3.12 shows three simple electrical circuits, each of which are designed to fulfil one of the aforementioned purposes, i.e., an actuator circuit for actuation in figure 3.12(a), a sensor circuit for monitoring in figure 3.12(b) and a shunt circuit for energy dissipation in figure 3.12(c).

A common configuration for piezoelectric patches used in conjunction with electrical circuits is the collocated actuator/sensor set-up described by, e.g., Tzou and Tseng (1990). Two piezoelectric patches are placed, one on either side, of, e.g., a beam structure, with one patch connected to an actuator circuit and the other to a sensor circuit. The motion of the beam measured by the sensor circuit is, via a feedback control, used to, e.g., dampen the beam vibration. However, this is not possible for an PAFB due to the requirement of a smooth bearing surface in order to make the PAFB function.

Mechanical vibration energy converted to electrical energy via the indirect piezo-

(a) Actuator circuit.   (b) Sensor circuit.   (c) Shunt circuit.
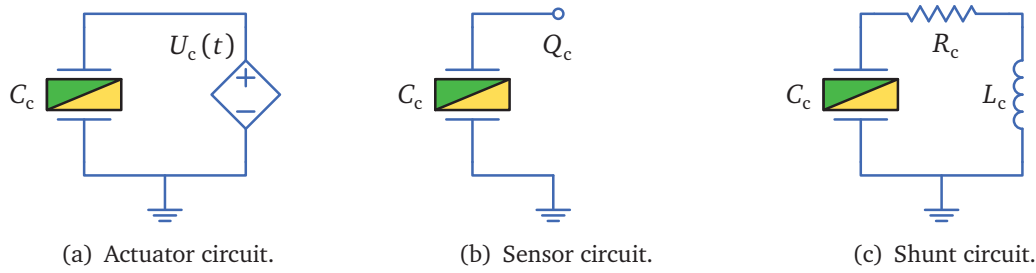
Figure 3.12: Three types of electrical circuits that can be connected to the IDEs. (a) The actuator circuit is used to put energy into the system, (b) the sensor circuit is used for monitoring the system, while (c) the shunt circuit is used to dissipate energy from the system, i.e., increase the damping of the mechanical vibrations.

electric effect can be dissipated passively in a shunt circuit. This was introduced by Hagood and Flotow (1991), who showed an increase in the damping properties for a beam structure with piezoelectric patches connected to a shunted electric circuit. More advanced shunt circuits have been developed over the past couple of decades (e.g., Behrens et al. (2003), Clark (2000), Corr and Clark (2002), Edberg et al. (1992), Hollkamp (1994) and Wu (1998)), but they all serve the purpose of dissipating the electrical energy converted by the piezoelectric material from the mechanical vibrations.

In the numerical results presented in the next chapter, the only electrical circuit used is the actuator circuit. The sensor circuit is only used in figure 3.21(d) in order to show one of the optional outputs of the mathematical model.

Actuator Circuit

When using an actuator circuit, the intention is to affect the movement of the PTF, either through a feed-forward or a feedback control loop. Figure 3.12(a) shows a simple actuator circuit capable of putting energy into the system. A voltage supply generates an EPD, which is directly applied to the IDEs on the MFC patch, causing the PTF to deflect. Assuming the electrical energy generated by the voltage supply is much larger than the energy converted from the mechanical vibrations, Kirchhoff's voltage law yields the governing equation for the electrical circuit as stated below.

$$\Delta\phi_e - U_c(t) = 0 \tag{3.12}$$

Sensor Circuit

In the sensor circuit the electrical charge created by a deformation of the piezoelectric material can be recorded by a data acquisition system. Figure 3.12(b) shows a simple sensor circuit, where the electrical charge generated by a deformation of the piezoelectric patch is measured. Assuming that: the signal is without noise; the generated charge is large enough to measure; and that no EPD arises between the electrodes, the equation for the measurement point is given by Kirchhoff's current law.

$$Q_e = Q_c \tag{3.13}$$

3.4 Finite element discretisation

An PAFB consists of five domains, as seen in figure 3.11, and two of these are continuous, the air film and PTF. Both of these domains have been discretised using the finite element method (FEM) before they are coupled with the other domains. First, the discretisation of the domains is presented, followed by a description of the elements, and closing with the coupling of the domains and the coupled governing equations in time.

Air film

The compressible Reynolds equation (3.2) governing the air film is discretised using a Bubnov-Galerkin finite element procedure as presented by Larsen et al. (2015b). In the discretisation a combined state variable $\tilde{\psi}_a = \tilde{p}_a \tilde{h}_a$ is included. This has been reintroduced by Pham and Bonello (2013), to enable a simultaneous solution of all state variables in time. The FEM formulation of the compressible Reynolds equation is given below as a system of first order differential equations. The state matrix $\left[A_{a,e}\right]$ and residual vector $\{R_{a,e}\}$ are presented on the element level.

$$[A_a]\left\{\dot{\tilde{\psi}}_a\right\} = \{R_a\} \tag{3.14}$$

$$\left[A_{a,e}\right] = 2\Lambda \int [N_a]^\mathrm{T}[N_a]\,dA$$

$$\{R_{a,e}\} = -\int [B_a]^\mathrm{T}\left(\tilde{p}_a\tilde{h}_a^3\right)^*[B_a]\{\tilde{p}_{a,e}\}\,dA + \int [B_a]^\mathrm{T}\tilde{h}_a^*\{\Lambda\}[N_a]\{\tilde{p}_{a,e}\}\,dA$$

In order to solve the above equation in time spatial boundary conditions for the time derivative of the combined state variable is required. These boundary conditions depend on the boundary conditions for the aerodynamic pressure and thickness of the air film.

$$\dot{\tilde{\psi}}_a = \dot{\tilde{p}}_a\tilde{h}_a + \tilde{p}_a\dot{\tilde{h}}_a$$

At the boundaries of the air film the aerodynamic pressure is constant and is given as the ambient pressure p_A, while the thickness of the air film follows equation (3.8), i.e., the boundary conditions for the time derivative of the combined state variable are equal to the velocity of the air film thickness at the boundaries, as stated below.

$$\dot{\tilde{\psi}}_a(\theta_i, z) = \dot{\tilde{h}}_a(z)\Big|_{\theta_i}$$

$$\dot{\tilde{\psi}}_a(\theta, z_i) = \dot{\tilde{h}}_a(\theta)\Big|_{z_i}$$

Piezoelectric top foil

The derivation of the electro-mechanical finite element used for discretising of the PTF is given in publication P1. It is obtained from: the Lagrange equation; the constitutive equations (3.9) for piezoelectric material; a Legendre transformation; and

a separation of the variables. After a variable transformation from the strain ε and the electrical field E to displacement u and electrical potential ϕ the derivation results in the governing equation for the piezoelectric material that is given below.

$$\int \left[\rho \left[N_{\mathrm{t,\,u}} \right]^{\mathrm{T}} \left[N_{\mathrm{t,\,u}} \right] \{\ddot{u}_{\mathrm{t},e}\} + \left[B_{\mathrm{t,\,u}} \right]^{\mathrm{T}} \left[C \right] \left[B_{\mathrm{t,\,u}} \right] \{u_{\mathrm{t},e}\} + 2 \left(\left[B_{\mathrm{t,\,\phi}} \right]^{\mathrm{T}} \left[e \right] \left[B_{\mathrm{t,\,u}} \right] \right)^{\mathrm{T}} \{\phi_e\} \right.$$
$$\left. + 2 \left[B_{\mathrm{t,\,\phi}} \right]^{\mathrm{T}} \left[e \right] \left[B_{\mathrm{t,\,u}} \right] \{u_{\mathrm{t},e}\} - \left[B_{\mathrm{t,\,\phi}} \right]^{\mathrm{T}} \left[\eta \right] \left[B_{\mathrm{t,\,\phi}} \right] \{\phi_e\} \right] dV = \{F_{\mathrm{t}}\}$$

The electrical potential is split into an internal electrical potential, within the piezoelectric material and an EPD between the IDEs, as described by equation (3.10). This is followed by a Guyan reduction of the internal electrical potentials thereby lowering the number of degrees of freedom (DoFs) in the PTF. This is possible since the internal electrical potentials are quasi-static and it is only their effect on the system that is important, rather than their actual values. The FEM discretisation of the PTF is given below with displacements and EPD as independent variables. Rayleigh damping may be included for the mechanical part of the PTF.

$$\begin{bmatrix} \left[\tilde{M}_{\mathrm{t,\,uu}} \right] & \left[0 \right] \\ \left[0 \right]^{\mathrm{T}} & \left[0 \right] \end{bmatrix} \begin{Bmatrix} \{\ddot{\tilde{u}}_{\mathrm{t}}\} \\ \{\Delta \ddot{\tilde{\phi}}_{\mathrm{e}}\} \end{Bmatrix} + \begin{bmatrix} \left[\hat{\tilde{K}}_{\mathrm{t,\,uu}} \right] & \left[\hat{\tilde{K}}_{\mathrm{t,\,eu}} \right] \\ \left[\hat{\tilde{K}}_{\mathrm{t,\,eu}} \right]^{T} & -\left[\hat{\tilde{K}}_{\mathrm{t,\,ee}} \right] \end{bmatrix} \begin{Bmatrix} \{\tilde{u}_{\mathrm{t}}\} \\ \{\Delta \tilde{\phi}_{\mathrm{e}}\} \end{Bmatrix} = \begin{Bmatrix} \{\hat{\tilde{F}}_{\mathrm{t}}\} \\ \{\hat{\tilde{Q}}_{\mathrm{e}}\} \end{Bmatrix} \quad (3.15)$$

The EPD in the equation above is given as a relative value, i.e., the difference between two absolute electrical potentials, one on each the IDEs. This corresponds to one of the IDEs being grounded, while an electrical potential is imposed on the other, i.e., creating the EPD. For this reason the electrical DoFs are bounded and the equations are liner independent from EPDs of the other IDE pairs.

The mechanical displacement requires boundary conditions, since the deflection values are absolute, thereby allowing rigid body motion. The boundary conditions for an PTF with the bearing axis aligned with the z-direction and either the leading or trailing edge being clamped, is given below.

$$\{\tilde{u}_{\mathrm{t},\,i}\} (x_i, y_i, z) = \{0\} \Big|_{x_i, y_i}$$

The number of DoFs in equation (3.15) can be reduced further by a modal reduction. This limits the deflection pattern of the PTF to a given number of selected mode shapes. The equation of motion for the PTF must be given on state-space form $\left(\{v_{\mathrm{t}}\} = \{\{u_{\mathrm{t}}\}, \{\dot{u}_{\mathrm{t}}\}\}^{\mathrm{T}} \right)$, which then can be reduced as stated below.

$$\left[\hat{\tilde{A}}_{\mathrm{t}} \right] \{\dot{\tilde{v}}_{\mathrm{t}}\} + \left[\hat{\tilde{B}}_{\mathrm{t}} \right] \{\tilde{v}_{\mathrm{t}}\} = \left\{ \hat{\tilde{F}}_{\mathrm{t}} \right\} \quad (3.16)$$

The relationship between the reduced and non-reduced state space system for the PTF is given below.

(a) Element with local coordinate systems in each node.

(b) Local and global coordinate system and nodal kinematic variables.
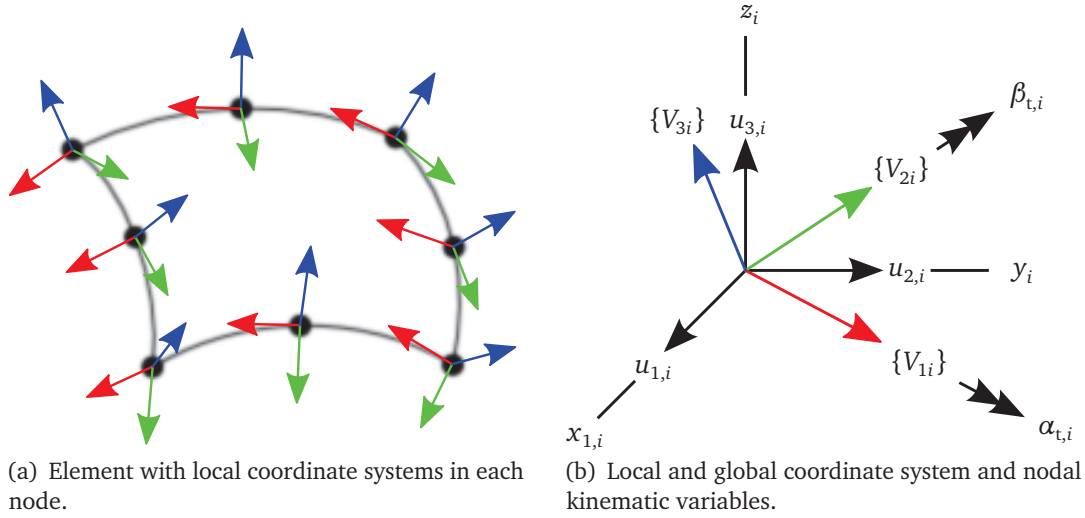
Figure 3.13: 8-node double curved shell element with local coordinates given in each node. The first local coordinate axis (red) and the second (green) are tangential to the element surface, while the third (blue) is normal to the element.

$$\{\tilde{v}_{\mathrm{t}}\} = \left[V_{\mathrm{t,\,r}}\right]\{\hat{\tilde{v}}_{\mathrm{t}}\}$$

$$\left[\hat{\tilde{A}}_{\mathrm{t}}\right] = \left[V_{\mathrm{t,\,l}}\right]\left[\tilde{A}_{\mathrm{t}}\right]\left[V_{\mathrm{t,\,r}}\right]$$

$$\left[\hat{\tilde{B}}_{\mathrm{t}}\right] = \left[V_{\mathrm{t,\,l}}\right]\left[\tilde{B}_{\mathrm{t}}\right]\left[V_{\mathrm{t,\,r}}\right]$$

$$\left\{\hat{\tilde{F}}_{\mathrm{t}}\right\} = \left[V_{\mathrm{t,\,l}}\right]\{\tilde{F}_{\mathrm{t}}\}$$

A detailed derivation of the FEM formulation for the PTF is found in Nielsen et al. (2016) (publication P1). However, since the notation used in publication P1 and the thesis differs from one another, the mathematical model presented in publication P1 is reprinted in appendix using the notation of the thesis.

Elements for piezoelectric top foil and air film

Two types of element are used in the discretisation of the PTF and the air film, namely an 8-node double-curved layered isoparametric serendipity element and the flat equivalent, i.e., an 8-node flat isoparametric serendipity element. The double-curved element shown in figure 3.13(a) was presented in a static mechanical version by Panda and Natarajan (1981). The nodes making up the double curved element follow the geometrical mid-plane of the physical shell; the geometry of the physical shell in relationship to the nodes is given below.

$$\{x_{\mathrm{t,\,u}}\} = \sum_{i=1}^{8} N_{\mathrm{t},i}\left(\{x_{\mathrm{t},i}\} + \zeta\frac{h_{\mathrm{t},i}}{2}\{V_{3i}\}\right)$$

Each node has a local coordinate system with two in-plane coordinate axes $\{V_{1i}\}$, $\{V_{2i}\}$ and one out-of-plane axis $\{V_{3i}\}$, i.e., normal to the shell surface. Two rotational

DoFs are aligned with the in-plane axes, as seen in figure 3.13(b), while the three linear deflections are aligned with the global coordinate axes. The kinematic relationship between the double curved element and the physical shell is given in equation (3.17), with in-plane coordinate axes being represented by $[\mu_i] = [-\{V_{2i}\}, \{V_{1i}\}]$. The kinematic relationship implies the usage of first order shear deformation theory.

$$\{u_\mathrm{t}\} = \sum_{i=1}^{8} N_{\mathrm{t},i} \left(\{u_{\mathrm{t},i}\} + \zeta \frac{h_{\mathrm{t},i}}{2} [\mu_i] \left\{ \begin{matrix} \alpha_{\mathrm{t},i} \\ \beta_{\mathrm{t},i} \end{matrix} \right\} \right) \tag{3.17}$$

In order to align the nodes in the two domains, the locations of the nodes in the flat elements used for the air film are dictated by the elements used for the PTF. This nodal alignment simplifies the transfer of information between the meshes. The location, pressure and air film thickness relationships are given below, when the curvature axis of the PTF is aligned with the z-direction.

$$\theta = \sum_{i=1}^{8} N_{\mathrm{a},i} \theta_i$$

$$z = \sum_{i=1}^{8} N_{\mathrm{a},i} z_i$$

$$p_\mathrm{a} = \sum_{i=1}^{8} N_{\mathrm{a},i} p_{\mathrm{a},i}$$

$$h_\mathrm{a} = \sum_{i=1}^{8} N_{\mathrm{a},i} h_{\mathrm{a},i}$$

Coupling of the elements and fluid-mechanical domains

The couplings between the different domains in an AFB have been shown in figure 3.7. The left hand side shows the aerodynamic pressure affecting the journal and top foil, which is also affected by the support pressure from the bump foil. Both types of pressures must be integrated into forces before they can be applied. However, both the aerodynamic pressure and the support pressure acts perpendicular to the bearing surface, while the external forces acting on both the journal and top foil are given in global coordinates. Therefore a coordinate transformation is required together with the integration. It is assumed that the aerodynamic pressure only affects the top foil by a radial load, i.e., traction loading is neglected. A pressure-to-force matrix relating the radial pressure to nodal loads on the top foil is given below, and is based on Cook et al. (2002). The aerodynamic forces acting on the journal $\{F_\mathrm{r}\}$ are equal to the resulting aerodynamic forces acting on the nodes of the top foil.

$$\left[T_{\mathrm{a},e} \right] = \int_{-1}^{1} \int_{-1}^{1} \left[N_{\mathrm{t,\,u}} \right]^\mathrm{T} \{J_3\}^* [N_\mathrm{a}] \, d\xi d\eta \tag{3.18}$$

On the right hand side of figure 3.7, describing the domain couplings, the radial top foil deflection affects the bump foil, and together with the journal movement, the thickness of the air film. Both the journal motion and top foil deflection are given

in global coordinates, hence a coordinate transformation is required in both cases before the thickness of the air film and the support pressure from the bump foil can be calculated by equation (3.8) and equation (3.6), respectively. The top foil deflections and journal movement in radial coordinates are given below at nodal level.

$$\tilde{\delta}_{\text{t},i} = \{V_{3i}\}^{\text{T}} [N_{\text{t, u}}]_i \{\tilde{u}_{\text{t},i}\}$$

$$\tilde{\delta}_{\text{r},i} = \{V_{3i}\}^{\text{T}} \{\tilde{u}_{\text{r}}\}$$

$$(3.19)$$

It is possible to reformulate the support forces acting on the top foil as a function of the top foil deflection, since the bump foil is without inertia. This will eliminate the calculation of the bump foil support pressure. Combining the pressure-to-force matrix in equation (3.18) with the coordinate transformation vector in equation (3.19) results in the support stiffness and damping matrices given below.

$$[K_{\text{b}}] = \int_{-1}^{1} \int_{-1}^{1} [N_{\text{t},u}]^{\text{T}} \left(\{J_3\} k_{\text{b}} \{V_3\}^{\text{T}} \right)^* [N_{\text{t},u}] \, d\xi d\eta$$

$$[D_{\text{b}}] = \int_{-1}^{1} \int_{-1}^{1} [N_{\text{t},u}]^{\text{T}} \left(\{J_3\} d_{\text{b}} \{V_3\}^{\text{T}} \right)^* [N_{\text{t},u}] \, d\xi d\eta$$

The external forces acting on the top foil due to aerodynamic pressure from the air film and the bump foil support are given below.

$$\{F_{\text{t}}\} = [T_{\text{a}}] \{p_{\text{a}}\} + [D_{\text{b}}] \{\dot{u}_{\text{t}}\} + [K_{\text{b}}] \{u_{\text{t}}\}$$

$$(3.20)$$

Coupling the fluid-mechanical and the electrical equations in the time domain

The combined fluid-mechanical governing equation for an PAFB is presented below in state-space form: the linear equation (3.1) of the journal; the non-linear Reynolds equation (3.14) for the air film and the linear modal reduced equation (3.16) for the PTF. All coupling between the fluid-mechanical domains are included on the right hand side of the equation, i.e., the aerodynamic forces on the journal, the air film residual vector and the aerodynamic forces and support forces on the top foil. The coupling from the electrical domain to the PTF is included as an external force depended on the EPD between the IDEs.

$$\begin{bmatrix} [I] & 0 & 0 & 0 \\ 0 & [\tilde{M}_{\text{r}}] & 0 & 0 \\ 0 & 0 & [\tilde{A}_{\text{a}}] & 0 \\ 0 & 0 & 0 & [\hat{\tilde{A}}_{\text{t}}] \end{bmatrix} \begin{Bmatrix} \{\dot{\tilde{x}}_{\text{r}}\} \\ \{\ddot{\tilde{x}}_{\text{r}}\} \\ \{\dot{\tilde{\psi}}_{\text{a}}\} \\ \{\dot{\hat{\tilde{v}}}_{\text{t}}\} \end{Bmatrix} = - \begin{bmatrix} 0 & -[I] & 0 & 0 \\ 0 & 0 & 0 & 0 \\ 0 & 0 & 0 & 0 \\ 0 & 0 & 0 & [\hat{\tilde{B}}_{\text{t}}] \end{bmatrix} \begin{Bmatrix} \{\tilde{x}_{\text{r}}\} \\ \{\dot{\tilde{x}}_{\text{r}}\} \\ \{\tilde{\psi}_{\text{a}}\} \\ \{\hat{\tilde{v}}_{\text{t}}\} \end{Bmatrix}$$

$$+ \begin{Bmatrix} 0 \\ \{\tilde{W}_{\text{r}}\} - \{\tilde{F}_{\text{r}}\left(\tilde{x}_r, \dot{\tilde{x}}_r, \tilde{\psi}_{\text{a}}, \hat{\tilde{v}}_{\text{t}}\right)\} + \{\tilde{F}_{ub}(\tilde{t})\} \\ \{\tilde{R}_{\text{a}}\left(\tilde{x}_r, \dot{\tilde{x}}_r, \tilde{\psi}_{\text{a}}, \hat{\tilde{v}}_{\text{t}}\right)\} \\ \{\hat{\tilde{F}}_{\text{t}}\left(\tilde{x}_r, \dot{\tilde{x}}_r, \tilde{\psi}_{\text{a}}, \hat{\tilde{v}}_{\text{t}}\right)\} + \{\hat{\tilde{F}}_{\text{b}}\left(\hat{\tilde{v}}_{\text{t}}\right)\} + \{\hat{\tilde{F}}_{\text{e}}\left(\Delta\tilde{\phi}_{\text{e}}\right)\} \end{Bmatrix}$$

$$(3.21)$$

Figure 3.14: The overall flow chart of the numerical implementation.

In the combined governing equation above, the explicit coupling between the mechanical and electrical domain within the PTF has been broken into an implicit coupling. The reasoning behind these efforts is threefold: 1) the electrical DoF depends on the chosen electrical circuit, i.e., it is not consistent; 2) the couplings within the combined governing equation are already implicit due to the non-linearities from the air film and bump foil; and 3) the combined governing equation for the fluid-mechanical domains is independent of the electrical circuit, since the coupling is on the right hand side. The procedure for solving the fluid-mechanical part of the PAFB remains the same and is independent of the electrical circuit.

The coupling from the PTF to the electrical domain is given in equation (3.15). The specific governing equation for the electrical domain depends on the electric circuit connected to the IDEs. The actuator and sensor circuits described by equations (3.12) and (3.13) are only coupled one-way either into, or out of, the PAFB, and is given below.

$$\{\tilde{F}_e\} = \left[\hat{\tilde{K}}_{t,\,eu}\right] \Delta \tilde{\phi}_e(\tilde{t})$$

$$\tilde{Q}_c = \left[\hat{\tilde{K}}_{t,\,eu}\right]^T \{\tilde{u}_t(\tilde{t})\}$$

3.5   Numerical implementation

The numerical implementation follows the classical layout of commercial finite element programs as highlighted in figure 3.14: the preprocess initialises the system; the solver-process simulates the response of the system; and the postprocess displays the simulated results in a convenient way. Each of the three steps are described in the following sections.

Preprocess

The preprocess is divided into two main steps: 1) generate a bearing segment with an air film; and 2) set up a bearing using the previously generated bearing segments and include a journal. The flow chart for generating a bearing segment is shown in figure 3.15. To begin with the geometry of the top foil is defined, including the number and types of layers it consists of and which areas the bump foil will support. Based on the geometry, a mesh is created and the matrices for the mathematical model are calculated. It is possible to generate a rigid with an air film or a flexible bearing segment with or without an air film. These different set-ups correspond to the different subsystems that the PAFB can be divided into experimentally, as highlighted in figure 2.3 explaining the stepwise validation.

The geometry of the PTF defined in cylindrical coordinates (θ, r, z) is transformed into Cartesian coordinates (x, y, z), as required by the FEM formulation (see figure 3.16).
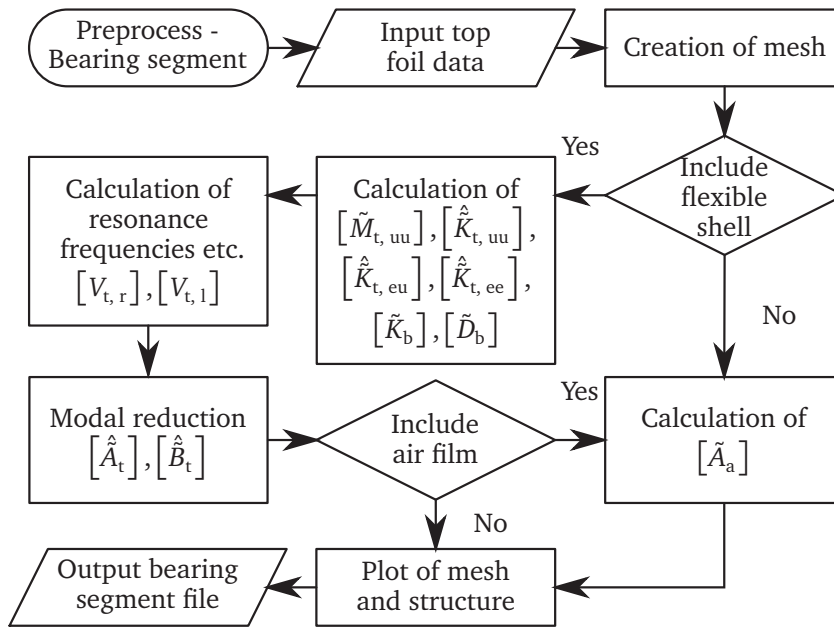
Figure 3.15: The preprocess flow chart of the bearing segment generation. Three set-ups are possible: 1) a rigid bearing segment with an air film; 2) a flexible (piezoelectric) top foil with an air film; or 3) a flexible (piezoelectric) top foil without an air film. The preprocess generates a datafile that may be used for setting up an air bearing with a journal.

The defined geometry of the PTF is the bearing surface and therefore the innermost layer. Additional layers such as an MFC patch are added to the outside. Based on the bearing surface geometry the mesh is created with the required number of elements and nodes evenly distributed. One exception is the alignment of element boundaries with additional layers or bump foil, which only partly covers the bearing surface. The flat elements used for the air film follows the geometry of the PTF elements, i.e., the z coordinates remains the same, while the x and y coordinates are transformed into angular coordinates (θ).

Figure 3.17 shows the preprocess of setting up the air bearing with the generated bearing segment(s). The matrices from each of the bearing segments are joined into a mathematical model of the air bearing, and if one or more of the bearing segments include a piezoelectric layer, an electrical circuit may be connected to each layer, i.e., a mathematical model of the circuit.

To illustrate the graphical output from the preprocess an PAFB has been generated, consisting of one bearing segment with an MFC patch in the middle of an larger unsupported area. The result is shown in figure 3.18. Figure 3.18(a) shows the nodes in the top foil and their local coordinate systems. The outer edges of the top foil are marked with a yellow line. The straight yellow line at the top of the bearing, aligned with the z-direction, indicates the location of the leading and trailing edges. In this case they are located next to each other, hence only one yellow line is visible. The green lines located to the right of the yellow straight line marks the edges of the MFC patch. Figure 3.18(b) shows the unfolded top foil. The blue dots are the nodes, while the yellow, red and green dots mark the areas within the elements (appearing as coloured areas). Yellow elements are top foil supported by bump foil, red elements are unsupported top
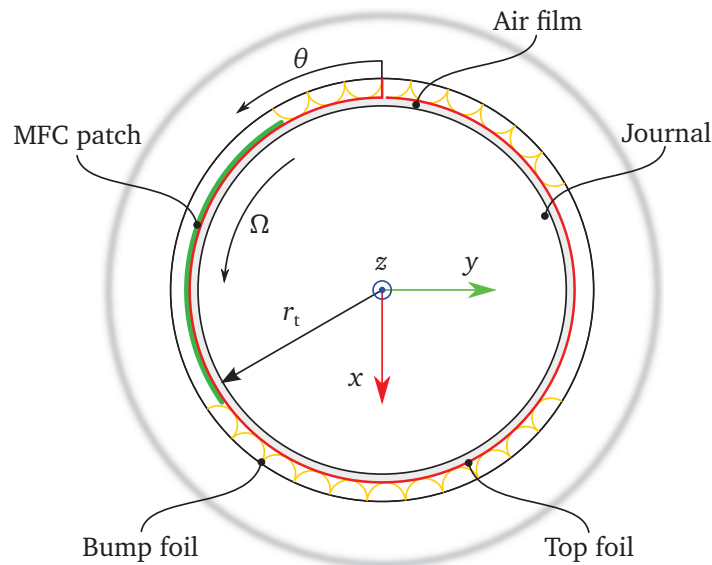
Figure 3.16: Schematics of an PAFB with one partially supported PTF, i.e., the bump foil does not support the entire PTF.
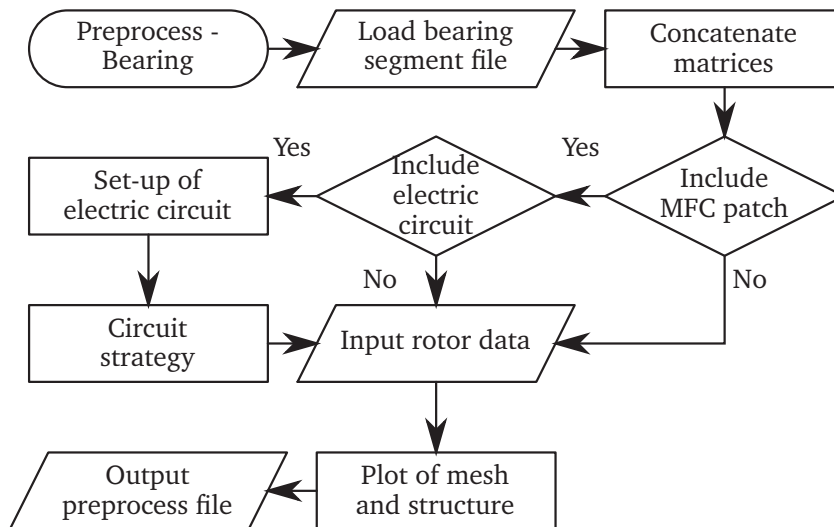
Figure 3.17: The preprocess flow chart for setting up an air bearing. The bearing segment(s) required for the specific air bearing is(are) loaded, and if any MFC patches are placed on the top foil(s), the electrical circuit(s) connected to the patch(es) is(are) included.
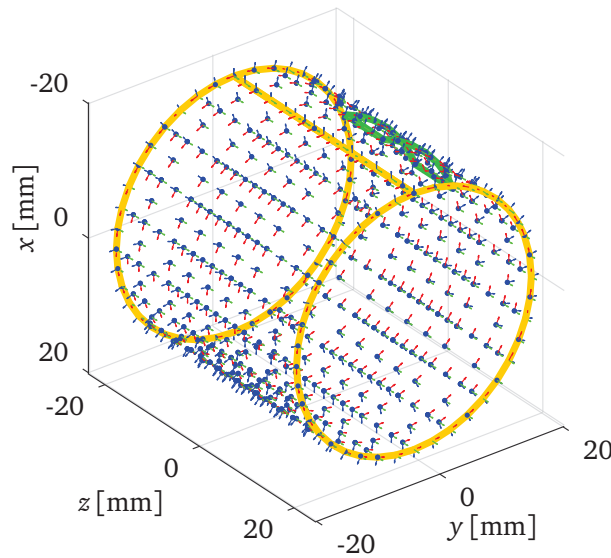
(a) An PAFB with local coordiante systems at each node and lines marking the edges of its layers.
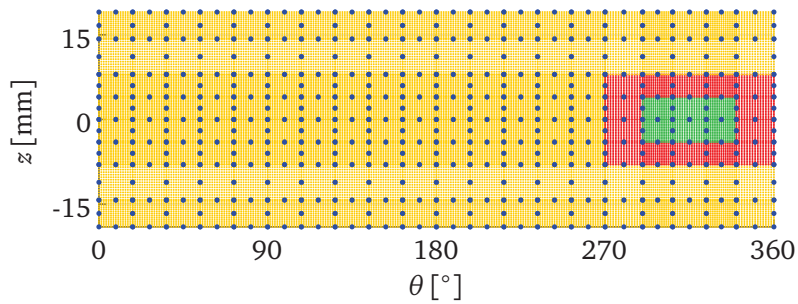
(b) An unfolded PTF. The yellow aera represents top foil supported by bump foil, red marks the unsupported top foil and the green shows the unsupported top foil with a MFC patch.

Figure 3.18: Examples of graphical output from the preprocess. The mesh consists of 20×8 elements corresponding to 537 nodes, and the PTF model utilizes the first 20 mode shapes in the modal reduction.

foil and green elements are unsupported top foil with an MFC patch mounted on the outside of the top foil.

Solver-process

Figure 3.19 shows the solver-process. The process is divided into three parts: 1) loading the file from the preprocess and preparing the simulation; 2) running the simulation; and 3) saving the simulated data. Parts two and three are interconnected, since the solver-process can divide the simulation into smaller portions which are saved during the simulation. This enables a preliminary postprocessing while the simulation is running.

A bearing set-up generated in the preprocess is loaded into the solver-process and the initial conditions (ICs) are set for all the state variables $\left(\{\tilde{z}_r\}, \{\tilde{\psi}_a\}, \{\tilde{z}_t\} \right)$. The ICs
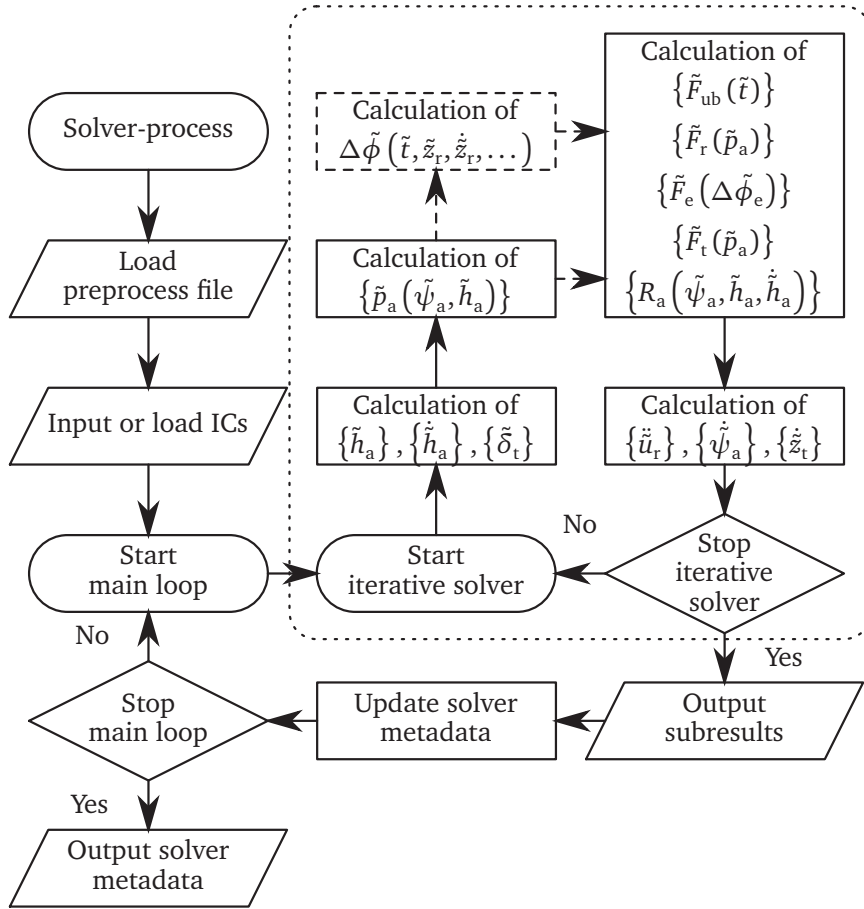
Figure 3.19: The flow chart of the solver-process. An air bearing set-up is loaded and the initial conditions (ICs) are set for all solver variables. The iterative solver simulates the response and the results are saved. It is possible to sub-divide the simulation enabling a preliminary postprocessing of the simulation.

are either entered or loaded from a previous simulation. The main loop subdivides the simulation and saves the partial results as they are simulated by the iterative solver. The iterative solver, marked by the dotted box in figure 3.19, solves the combined governing equation (3.21). An electrical circuit is only included in the simulations if the circuit imposes an EPD between the IDEs in the PTF, hence the dashed box. The performance of an electrical circuit, only affected by the deformations of the PTF, is calculated in the postprocess. By the time the simulation is completed the solver-process has created two files: 1) a file for each subdivision of the simulation, containing the time and state space variables at each time step and; 2) a file containing metadata regarding the solver process, e.g., wall-clock time for solving each sub-simulation.

Postprocess

The result of the postprocess can be divided into three groups: 1) three dimensional plots at a given time step; 2) transient and steady state responses of a few chosen DoFs; and 3) video files of transient and steady state responses for all nodes, i.e., three dimensional plots in time. In order to illustrate the first two groups, the system response

of the PAFB, shown in figure 3.18, has been simulated with a large rotor unbalance and a sensor circuit connected to the MFC patch.

In figure 3.20 the pressure profile, air film thickness and top foil deflection are seen as functions of the axial position z and circumferential location θ in a three dimensional representation, i.e., the first group of plots. The color coding is the same as for the preprocess graphical output, i.e., blue dots are the nodal values, yellow dots indicate the values in the area where top foil is supported by bump foil. Red marked elements shows the values where the top foil is unsupported, and the green dots indicates the values in area corresponding to unsupported top foil with an MFC patch mounted on the backside. The values of the yellow, red and green dots are interpolated using the shape functions of the elements.

Examples of the second plot group, i.e., system response in time, are shown in figure 3.21. The figure only contains the steady state part of the simulated response. Figure 3.21(a) shows the rotor orbit (blue line) and the top foil along the centre of the bearing: the initial non-deformed geometry (red); and the deflection at the final time step (yellow). The starting point of the orbit is marked with a star, the end point with a big dot and two decreasingly smaller dots close to the end point. These smaller dots indicate the previous rotor positions, thereby showing the direction of the rotor along the orbit. Four of the top foil nodes are marked with coloured squares indicating the points where the radial steady state responses of the top foil are obtained. These responses are shown in figure 3.21(c).

The transient responses of the rotor, top foil nodes, electrical charge and EPD between the IDEs are shown in figure 3.21(b), (c) and (d), respectively. In each figure the two plots in the top are given in time domain and show either: the movement and velocity; or the electrical charge and EPD. The two lower plots in each figure show the steady state responses in the frequency domain, i.e., FFTs of the movements and electrical charge.

3.6 Validation

The validation of the mathematical model is divided into two parts: 1) an experimental validation of the PTF model and 2) a numerical validation of the AFB model. The experimental validation of the PTF was presented in publication P1, while the numerical validation of the AFB was presented in publication P2. For this reason, only the highlights from the validation will be presented, while further details are found in the papers.

Piezoelectric top foil - experimental validation

An PTF with the dimensions and properties given in table 3.1 has been mounted in the testing bracket, see figure 2.15 and has been meshed with 12×10 elements. The layout of the PTF is shown in figure 3.22(a) while the orientation of the PTF in the testing bracket is as shown in figure 3.22(b). In the following experiments, the MFC patch has been used as an actuator, i.e., a random EPD has been applied to the IDEs causing the PTF to vibrate. The average amplitude of the EPD was 300 volts.

The experimental and numerical frequency response functions (FRFs) are shown in figure 3.23. A close resemblance is seen between the obtained numerical and experimental amplitudes up to 450 Hz, i.e., the first five resonance frequencies. The

(a) Pressure profile.

(b) Air film thickness.

(c) Top foil deflection. A positive downward value corresponds to a deflection into the bump foils, while an upward negative value is a deflection towards the journal.
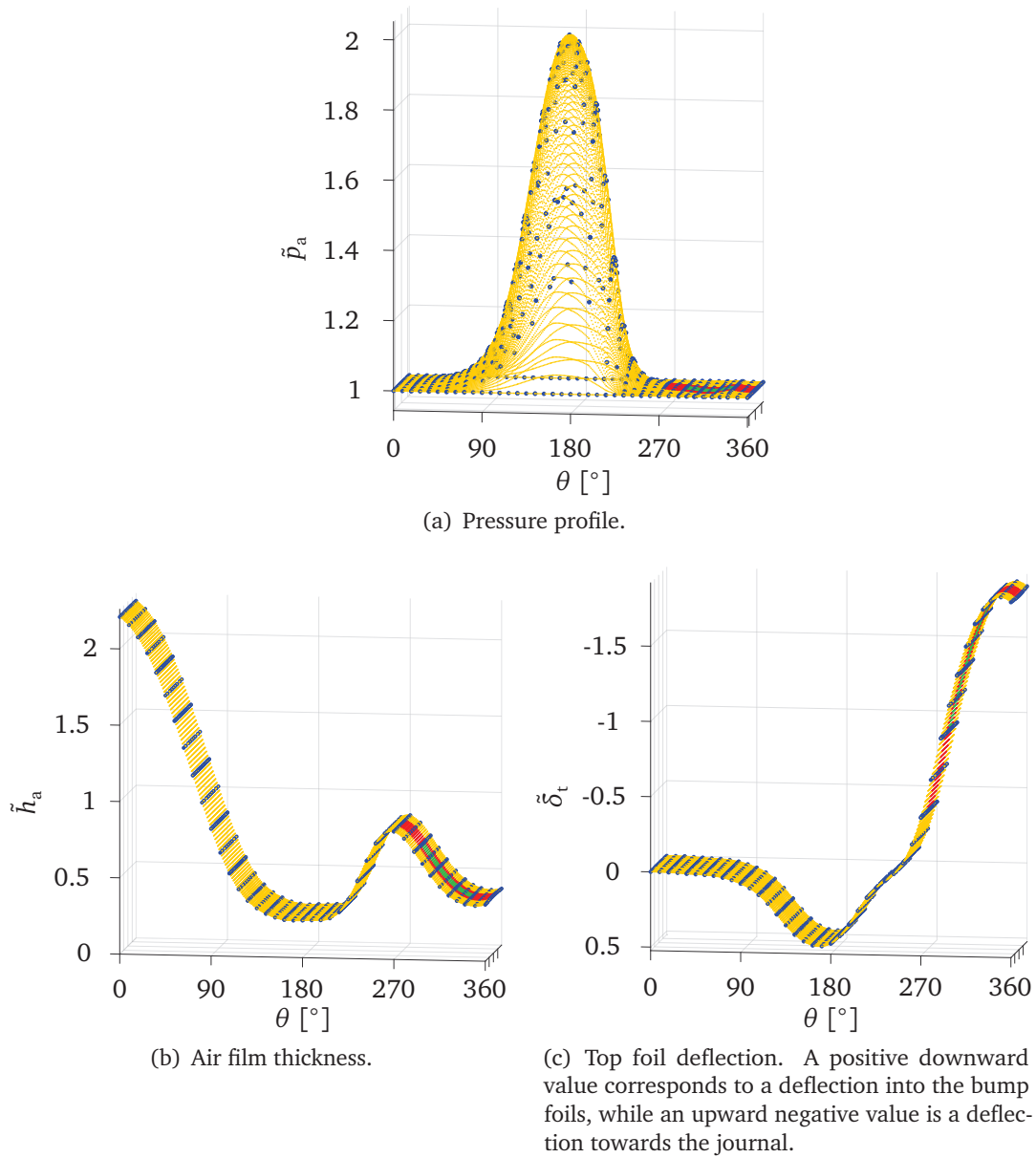
Figure 3.20: Three dimensional output: pressure profile, air film thickness and top foil deflection as functions of axial position z and circumferential location θ. The blue dots are the nodal values, while the yellow, red and green are interpolated using the shape functions. The yellow marks the area where top foil is supported by bump foil, the red marks unsupported top foil and the green marks unsupported top foil with a MFC layer.

(a) Rotor orbit with the top foil deflection at the last time step. The four coloured squares mark the top foil nodes which have their transient responses displayed in subfigure (c).

(b) Transient response of the rotor in time and frequency domain. The x-movement is coloured with blue, while the y-movement is red.

(c) Transient response of the top foil nodes marked in subfigure (a) in time and frequency domain.

(d) Electrical charge and EPD in time. The electrical charge is also shown in frequency domain.

Figure 3.21: Transient responses from the simulated PAFB after steady state has been reached. The sizes of the plots are for illustrative purposes only.

Table 3.1: The adopted dimensions and material properties of the PTF.

Metal Shell		
Top foil radius (with MFC patch)	43.0	[mm]
Angular length (θ_t)	119	[°]
Width (w_t)	68	[mm]
Thickness (h_t)	0.254	[mm]
Young's modulus	207	[GPa]
Poisson's ratio	0.30	[-]
Density (ρ_t)	8.100	$\left[\frac{\mathrm{g}}{\mathrm{cm}^3}\right]$
MFC Patch		
Leading edge ($\theta_{\mathrm{MFC},s}$)	25.6	[°]
Angular length (θ_MFC)	76.8	[°]
Width (w_MFC)	28	[mm]
Thickness (h_MFC)	0.15	[mm]
Electrode centreline distance (Δx_e)	0.5	[mm]
Electrode width (w_e)	50	[μm]
Young's modulus (E_1)	30.336	[GPa]
Young's modulus (E_2)	15.857	[GPa]
Shear modulus (G_{12})	5.512	[GPa]
Shear modulus (G_{23})	0	[GPa]
Shear modulus (G_{31})	0	[GPa]
Poisson's ratio (ν_{12})	0.31	[-]
Poisson's ratio (ν_{21})	0.16	[-]
Density	5.440	$\left[\frac{\mathrm{g}}{\mathrm{cm}^3}\right]$
Direct piezoelectric constant (d_{33})	800	$\left[\frac{\mathrm{pC}}{\mathrm{N}}\right]$
Direct piezoelectric constant (d_{31}), (d_{32})	-340	$\left[\frac{\mathrm{pC}}{\mathrm{N}}\right]$
Direct piezoelectric constant (d_{24}), (d_{15})	0	$\left[\frac{\mathrm{pC}}{\mathrm{N}}\right]$
Permittivity (ϵ_{33})	0.42	$\left[\frac{\mathrm{nF}}{\mathrm{cm}^2}\right]$
Permittivity (ϵ_{11}), (ϵ_{22})	0	$\left[\frac{\mathrm{nF}}{\mathrm{cm}^2}\right]$

(a) Layout of the PTF.
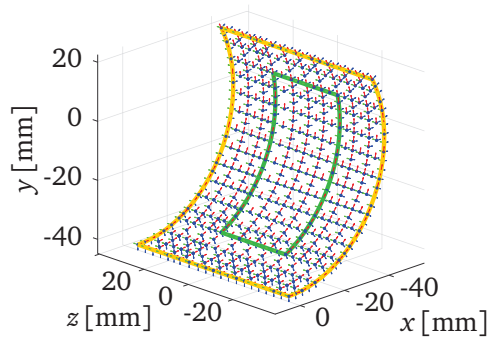
(b) The orientation of the PTF in the testing bracket.

Figure 3.22: The PTF used in the experimental validation of the mathematical model.
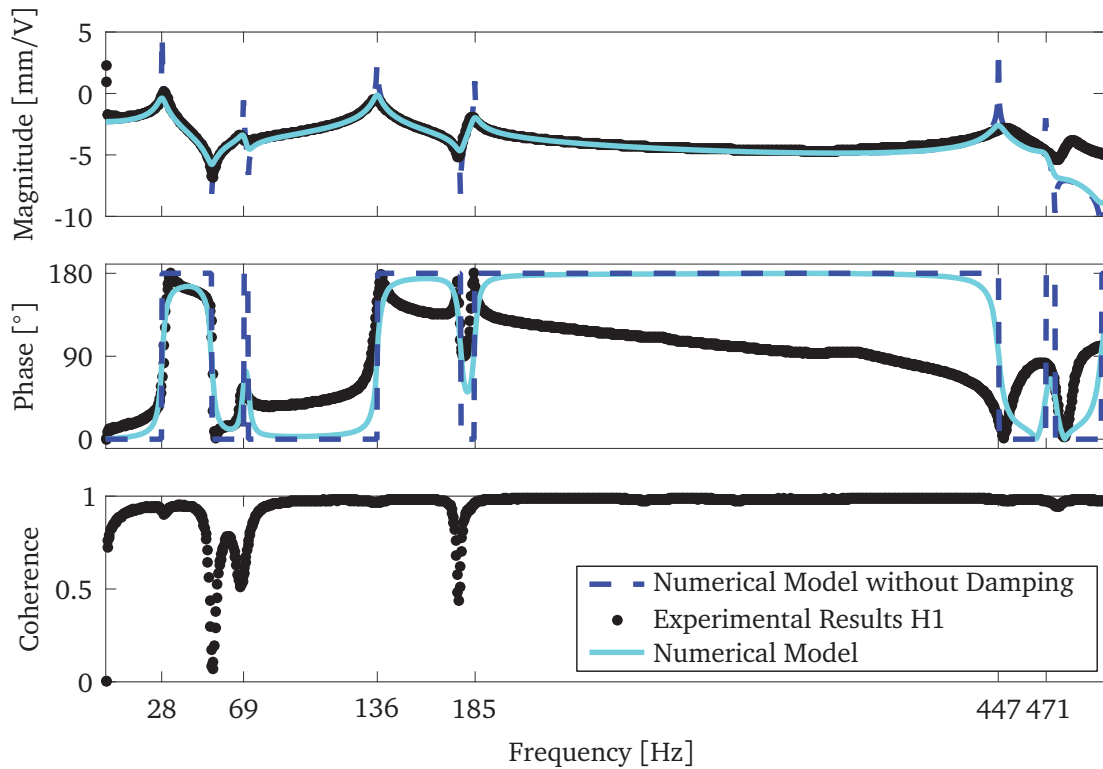
Figure 3.23: Experimental FRF obtained by applying a random EPD with an average amplitude of 300 volt to the IDEs on the MFC patch. The displacement sensor is located 90° from the clamped edge, and along the outer edge, i.e., at y = 0 and z = 30 and the sensor is aligned with the x-direction (see figure 3.22(b)).

models ability to predict the experimentally obtained phase is overall acceptable and better close to the resonance frequencies. However, discrepancies are detected between the third and fifth resonance frequencies. This has contributed to the use of Rayleigh structural damping, incapable of describing the energy dissipation behaviour in the entire frequency range.

The first six experimental and numerical mode shapes are shown in figure 3.24. Close resemblance is seen between the first and the third to sixth experimental and numerical mode shapes. The nodal line in the second mode is straight in the numerical calculation, though it bends in the experimental one. The detected discrepancy is due to a poor excitation of the second mode during the experiment. This is a result of the placement of the MFC patch, i.e., a pure twisting mode is difficult to excite with the symmetrically placed MFC patch.

Air foil bearing - numerical validation

The AFB used in the validation is well known from the literature, and is sometimes referred to as the NASA air/gas foil bearing. The AFB used in the numerical validation is shown in figure 3.25(a) while the data used in the simulation of the journal-bearing system is listed in table 3.2. The mesh of the top foil contains 20×6 elements and utilizes the first 20 model shapes in the modal reduction. These choices are based on a

(a) 1$^{\text{st}}$ experimental mode shape   (b) 2$^{\text{nd}}$ experimental mode shape   (c) 3$^{\text{rd}}$ experimental mode shape

(d) 1$^{\text{st}}$ numerical mode shape   (e) 2$^{\text{nd}}$ numerical mode shape   (f) 3$^{\text{rd}}$ numerical mode shape

(g) 4$^{\text{th}}$ experimental mode shape   (h) 5$^{\text{th}}$ experimental mode shape   (i) 6$^{\text{th}}$ experimental mode shape

(j) 4$^{\text{th}}$ numerical mode shape   (k) 5$^{\text{th}}$ numerical mode shape   (l) 6$^{\text{th}}$ numerical mode shape
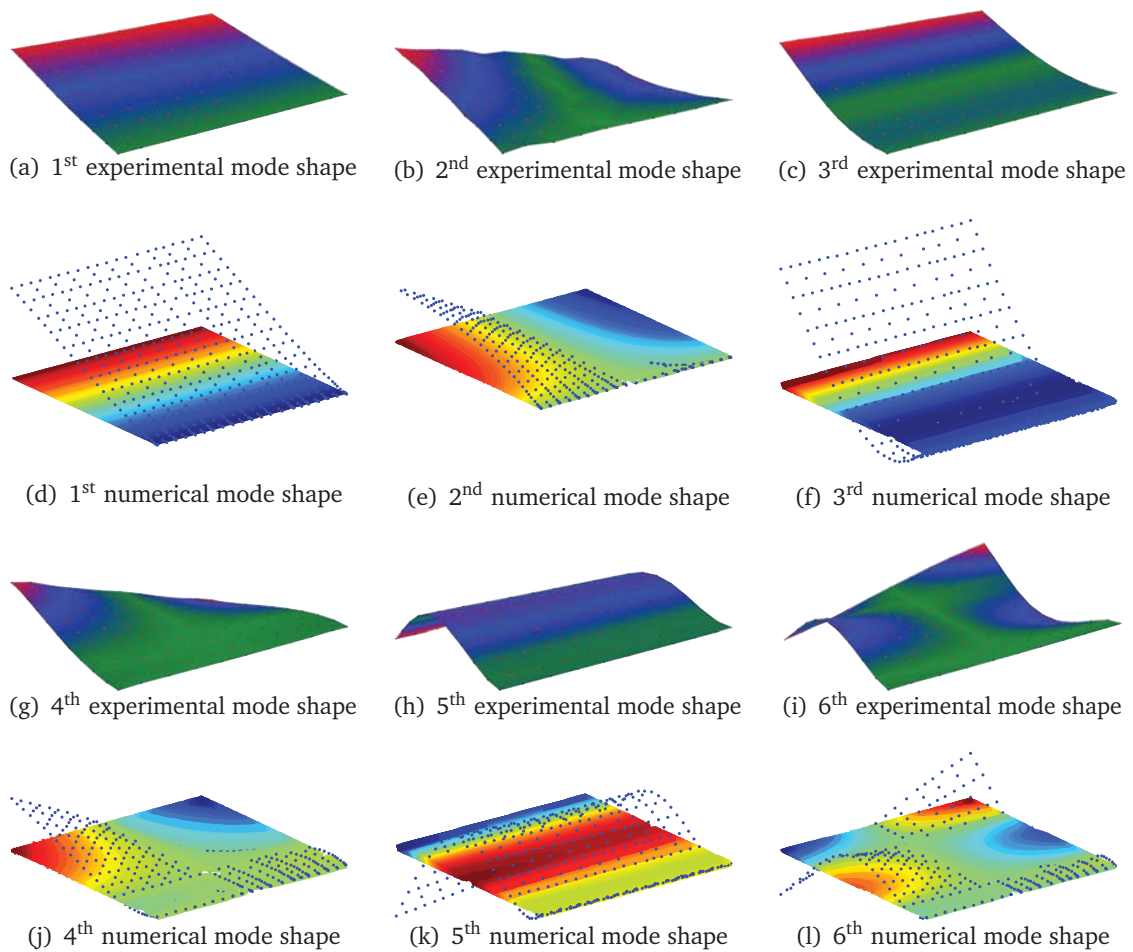
Figure 3.24: The first six experimental and numerical mode shapes projected onto a vertical plane parallel to the clamped edge, i.e, the y-z plane in figure 3.22(b). The green color in the experimental mode shapes corresponds to no movement, hence nodal lines are green. The red color corresponds to maximum movement amplitude, which can either point inward or outward.

convergence study presented in publication P2.

The mathematical model of an AFB has been validated with the transient response obtained from an experimentally validated AFB model known from the literature, e.g., Larsen and Santos (2015). Both models are FEM-based, i.e., the presented model uses eight-node second order elements, while the validation model uses four-node first order elements. The validation model utilizes; classical SEFM; includes no structural model of the top foil; and uses the Gümbel condition to eliminate sub-ambient pressure in the force integration. The validation model does not take into account whether the edges are clamped or free, since the classical SEFM implies no deflection of the bearing surface at the air film boundaries. The presented model does, however, distinguish between clamped and free edges. For this reason the leading edge has been clamped, since pressure profiles obtained with this configuration resembles the profile obtained with the validation model when the Gümbel condition is applied.

The rotor orbits from the two simulations are shown in figure 3.26. Only a small discrepancy is seen between the orbits, which is largest just before the lowest turning point. The discrepancy is contributed to the differences between the two models, e.g.,

(a) The AFB with the clamped leading edges located at the top of the bearing.

(b) The mesh of the AFB used in the numerical validation. The top foil is clamped at the leading edge, i.e., $\theta_t = 0$.
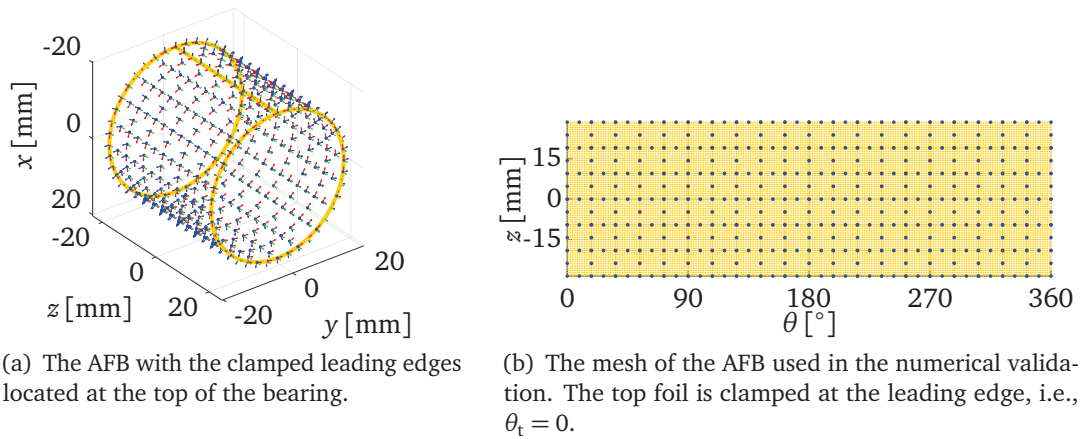
Figure 3.25: The AFB used in the numerical validation.

Table 3.2: Bearing system data used in the numerical validation of the mathematical model. The bearing data are similar to that of the well-known NASA bump foil bearing frequently studied in the literature.

Journal Data		
Mass	m_r	3.055 [kg]
Unbalance	m_{ub}	0 [kg · m]
Load	W	$\{30, 0\}^T$ [N]
Rotational speed	Ω	12,000 [rpm]
Gas Film Data		
Absolute viscosity	μ_a	$19.5 \cdot 10^{-6}$ [Pa · s]
Ambient pressure	p_A	$1.01325 \cdot 10^5$ [Pa]
Radial clearance	c	31.8 [μm]
Top Foil Data		
Number of top foils		1 [-]
Diameter	$2r_t$	38.1 [mm]
Width	w_t	38.1 [mm]
Thickness	h_t	0.2032 [mm]
Leading (clamped) edge	$\theta_{t,s}$	0 [°]
Arc length	θ_t	360 [°]
Young's modulus	E_t	207 [GPa]
Poisson's ratio	ρ_t	0.3 [-]
Damping factor	d_t	0.005 [-]
Bump Foil Data		
Bump pitch	S_b	4.572 [mm]
Half bump length	l_b	1.778 [mm]
Thickness	h_b	0.1016 [mm]
Young's modulus	E_b	207 [GPa]
Poisson's ratio	ρ_b	0.3 [-]
Loss Factor	β_b	0.25 [-]
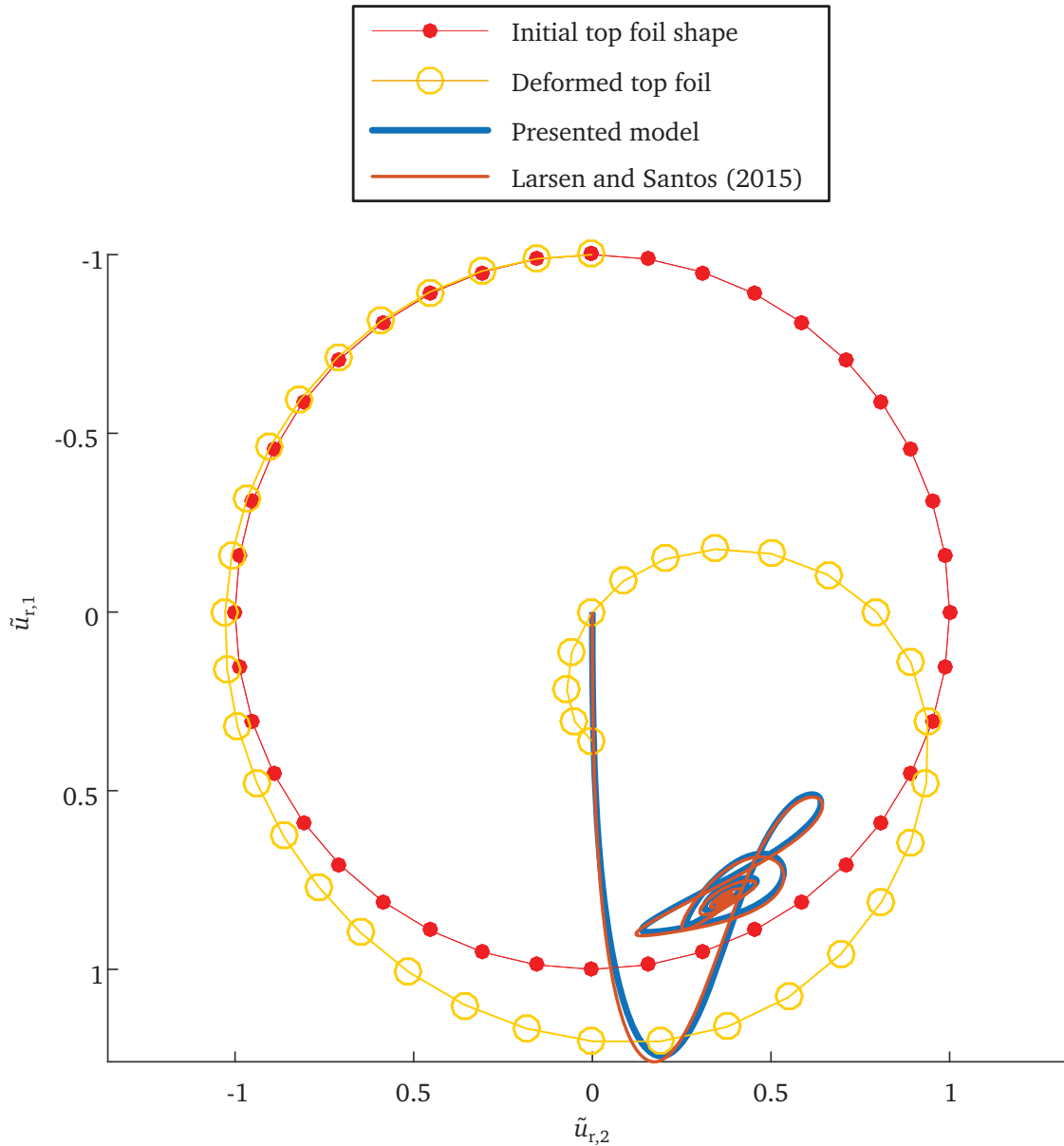
Figure 3.26: Plot of the transient response for the same AFB simulated using two different AFB models. The presented model utilizing the first 20 mode shapes in the modal reduction and a mesh of 20×6 elements.

the structure model for the top foil, which the validation model does not include.

3.7 Conclusion

The mathematical multi-physical model of the PAFB has been developed and validated in two steps. It shows good compliance with experimental results and numerical simulations produced with a model presented in literature.

In the numerical implementation, a great effort has been dedicated to optimise the computational execution in order to reduce wall-clock time for each simulation. This is one of the primary reasons for dividing the numerical implementation into

two preprocess, one solver and multiple postprocess scripts. This allows for multiple simulations being solved in parallel with the same solver script, but with different input files, while at the same time additional input files can be generated with the preprocess scripts and the simulated data can be evaluated with the postprocess scripts. This enables an efficient work process when multiple simulations are required, e.g., for the waterfall diagrams seen in publication P2.

Chapter 4

Numerical results

This chapter presents the numerical simulations performed with the mathematical model of the PAFB. The presented results can be divided into two categories: 1) investigations of a passive PAFB, i.e., an AFB; and 2) simulation of an active PAFB. The chapter begins with an investigation of the top foil clamping in an AFB, i.e., clamping the leading and/or trailing edge. A comparison is made with results from the literature. This is followed by a parameter study looking into the effects on the bearing performance caused by a partly supported top foil when the AFB supports a journal with a large unbalance. In the study, the size of the unsupported area is varied and the transient response is simulated until the steady state response is achieved. The final study of the first type is two investigations of the onset speed of instability for an AFB: 1) with a single top foil and; 2) with three preloaded top foils. In both investigations the journal supported by the AFBs is balanced. Results are discussed and compared with results in literature.

The chapter ends with a parameter study of the aerodynamic forces arising between a PTF and a fixed rotor, i.e., the simulation focus on the coupling between the EPD applied to the IDEs and aerodynamic pressure. The size and location of the MFC patch placed on the backside of the top foil is varied, as well as the EPD applied to the IDEs. The study is followed by a convergence analysis of both the number of elements and mode shapes.

4.1   Air foil bearing performance due to clamping of top foil edge

In the previously presented numerical validation of the AFB model, the leading edge of the top foil was clamped. The clamping of the leading edge ensured conditions similar to those found in simulations using the classical SEFM and the Gümbel condition. However, most AFBs found in the literature and in used in the industry are designed with a clamped trailing edge. A single-pad AFB with a clamped leading edge will not function in an application, since the top foil will be torn off due to capstan/Eytelwein forces according to Larsen (2015). For this reason an investigation of the top foil clamping location is performed.

Three cases of top foil clamping are investigated: 1) clamped leading edge; 2) clamped trailing edge; and 3) clamped leading and trailing edges. In all cases the parameters for the simulated journal-bearing system are given in table 3.2, i.e., case 1 is identical to the simulation from the numerical validation. Besides the difference in the clamping of the top foil, case 2 deviates from cases 1 and 3 by including the first 50
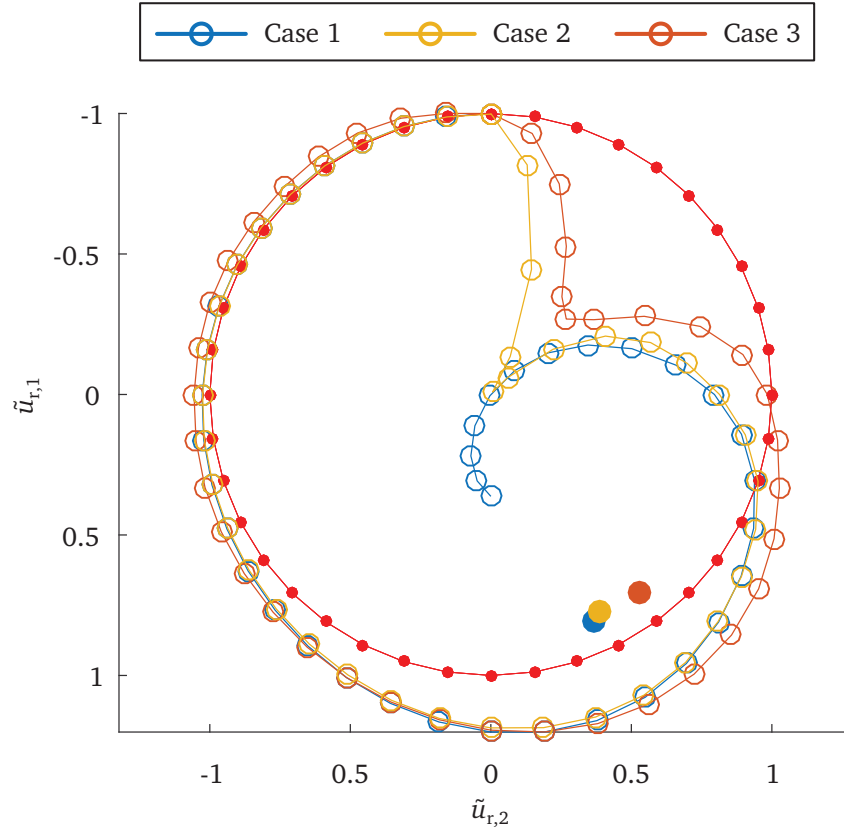
Figure 4.1: Equilibrium points and top foil deflections at steady state for the three different cases of top foil clamping.

mode shapes in the modal reduction instead of the first 20 mode shapes. The increased number of mode shapes included in case 2 is to ensure numerical convergence of the simulation.

The equilibrium points shown in figure 4.1 reveal that cases 1 and 2 have steady state points located close to each other, while case 3 differs somewhat. This difference is also observed in the top foil deflections displayed in the same figure. The deflected top foil for cases 1 and 2 are very similar when compared from the leading edge until the point where the top foil deflects inwards. For the remaining part of the top foil the difference is clearly visible. The top foil for case 1 follows the curvature of the journal, i.e., bending inward in the bearing, while for case 2 the initial inward deflection is restricted and bent outward towards the clamped trailing edge. The top foil deflection for case 3 differs from cases 1 and 2. This is due to the clamping of both ends of the top foil, which restricts the circumferential movement of the top foil.

The pressure profiles at the steady state points are shown in figure 4.2. In case 1 the pressure close to the trailing edge, i.e., from 270° to 360°, equals ambient pressure, since any sub-ambient pressure sucks the top foil inward. This results in the contribution from this region to the aerodynamic forces being approximately zero, i.e., the same result as when using classical SEFM combined with the Gümbel condition and in accordance with the assumption of Heshmat et al. (1983b). In case 2 the effect of the clamped trailing edge is seen on the pressure profile by a small pressure peak followed by a drop below ambient pressure, i.e. a pressure valley, after the main pressure peak. The pressure
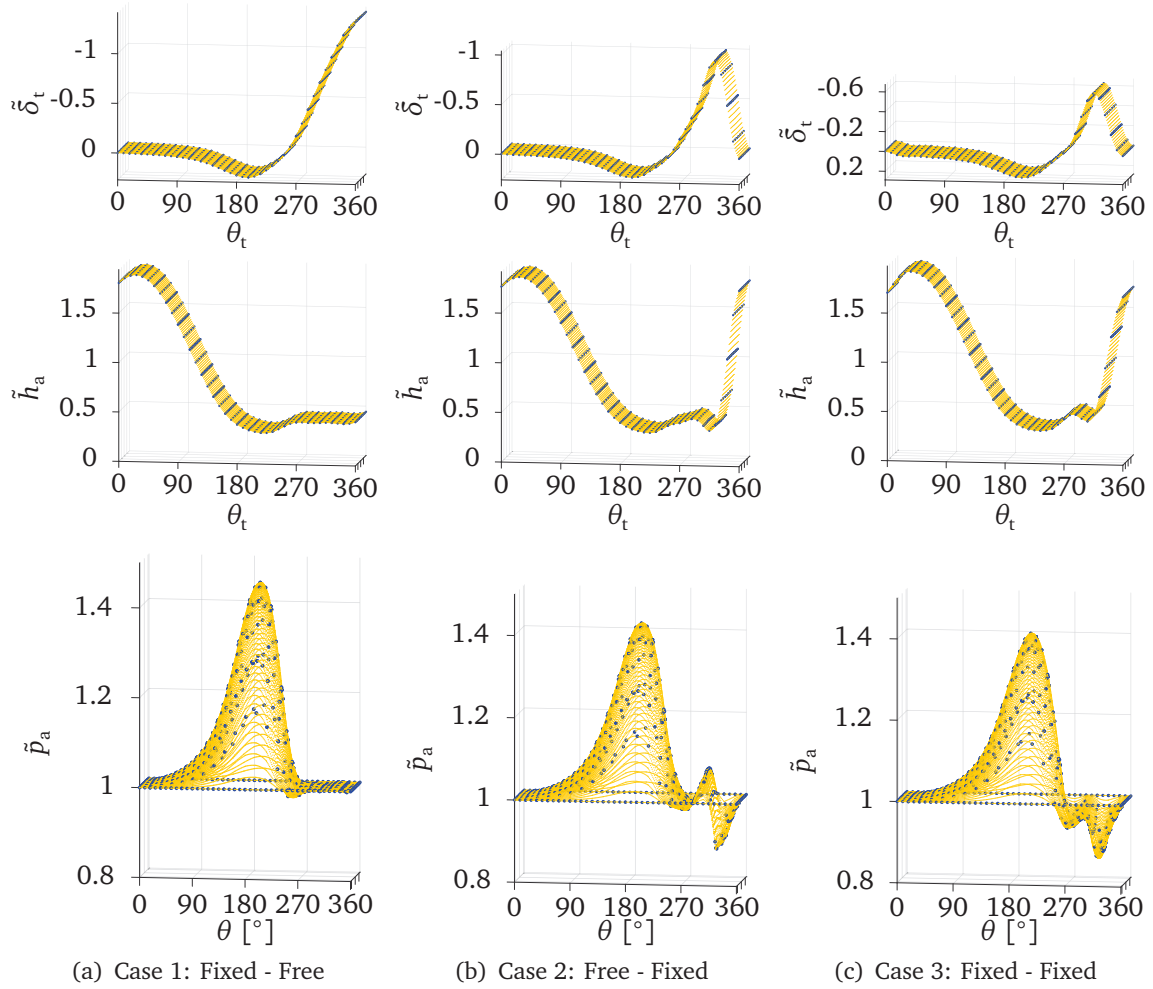
Figure 4.2: The pressure profiles for cases 1 to 3. The pressure in the region from 270° to 360° corresponds to the area of the top foil, which deflects inwards. The classical SEFM is commonly combined with the Gümbel condition to eliminate the sub-ambient pressure from the calculation of the aerodynamic forces acting on the journal. However, this is only valid for case 1, where the pressure in the aforementioned region equals ambient pressure.

peak is smaller than the pressure valley, resulting in a small non-zero contribution to the aerodynamic forces pointing in the upward direction. This results in a slightly different equilibrium position when compared with case 1. A similar pattern for the pressure profile next to the trailing edge is seen for case 3. However, the overall pressure in the trailing edge region is lower, meaning that instead of the minor pressure peak seen for case 2 an additional pressure valley is seen in case 3. This results in a larger upward contribution to the aerodynamic forces, partially explaining the location of the equilibrium point for case 3 being located higher than in cases 1 and 2.

The location of the top foil fixation also has an effect on the main pressure peak covering the region from 0° to 270°. The peak seen for case 1 is the highest, but also the most narrow. Case 2 is a bit lower but wider, followed by case 3. Despite the differences, all three pressure peaks have a similar magnitude.

The journal orbits, from the centre of the bearing to the three equilibrium points, are seen in figure 4.3. They differ for all three cases. The effects of the top foil clamping
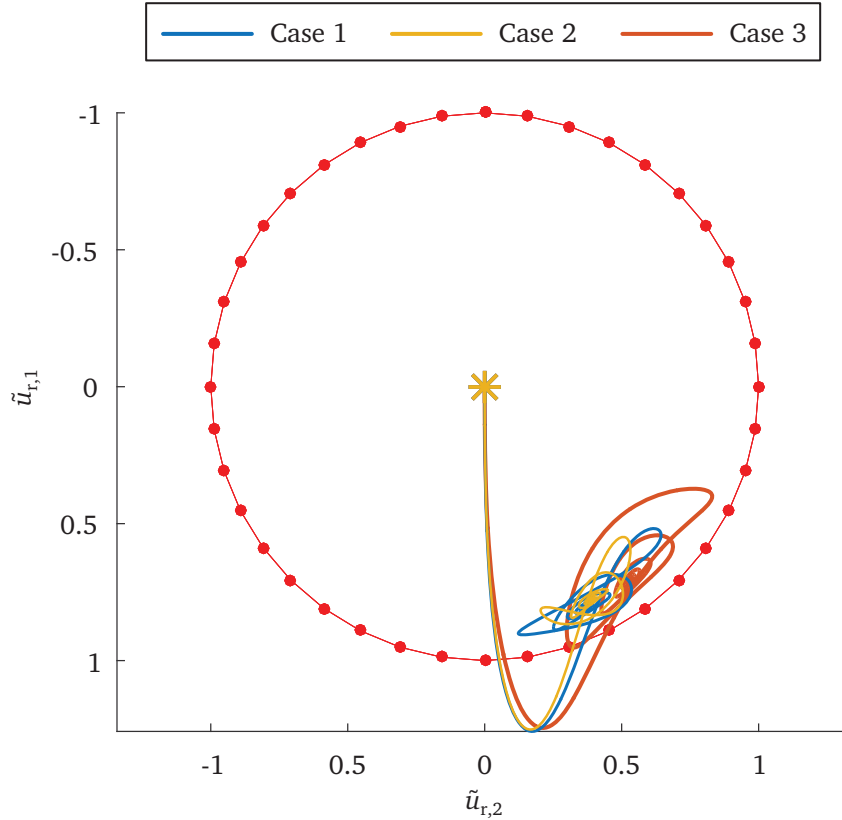
Figure 4.3: The transient responses of the three cases of top foil clamping in an AFB.

on the pressure profile changes the orbit of the journal on its way to equilibrium. For case 1 the ambient pressure zone located in the vicinity of the trailing edge expands and contracts as the journal moves around within the bearing, i.e., a larger or smaller part of the top foil is sucked towards the journal in order to eliminate the subambient pressure seen for the other cases in the divergent zone of the top foil. In the two remaining cases the subambient pressure provides extra aerodynamic forces of a magnitude depending on the location of the journal within the AFB.

The difference in the journal orbits for cases 1 and 2 shows the influences of the top foil mounting on the system response. Mathematical models of an AFB utilizing classical SEFM and the Gümbel condition will not be able to simulate the orbits for case 2, due to the Gümbel condition. In fact, the classical SEFM presented by Heshmat et al. (1983b) was introduced to an AFB with a clamped leading edge, i.e., case 1 and not case 2.

Figure 4.4 shows equilibrium points; top foil deflections; and journal orbits presented in the literature (see Larsen et al. 2015b; Pham and Bonello 2013) and calculated for case 3. The models from the literature do not utilize the Gümbel condition in the sub-ambient pressure zones, hence allowing an inward deflection of the top foil in the sub-ambient pressure zones. Case 3 is the case resembles the the most, since neither the leading nor the trailing edge is allow to move, just as the sub-ambient pressure is allow to affect the top foil and journal.

The equilibrium points from the literature are located further up in the AFB when compared to case 3. This is due to the inward deflection of the top foil being larger for
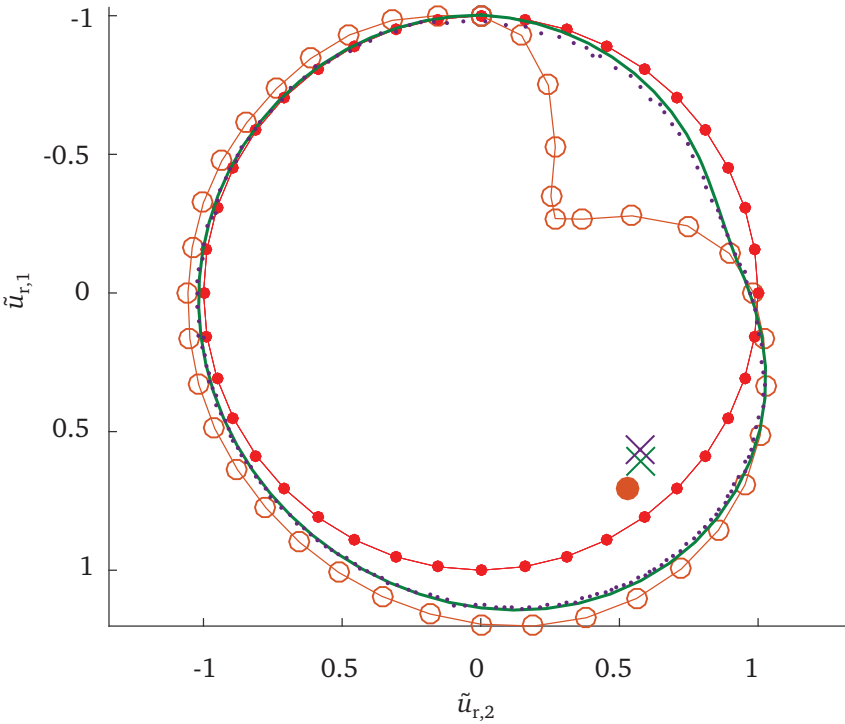
(a) Equilibrium points and top foil deflection.
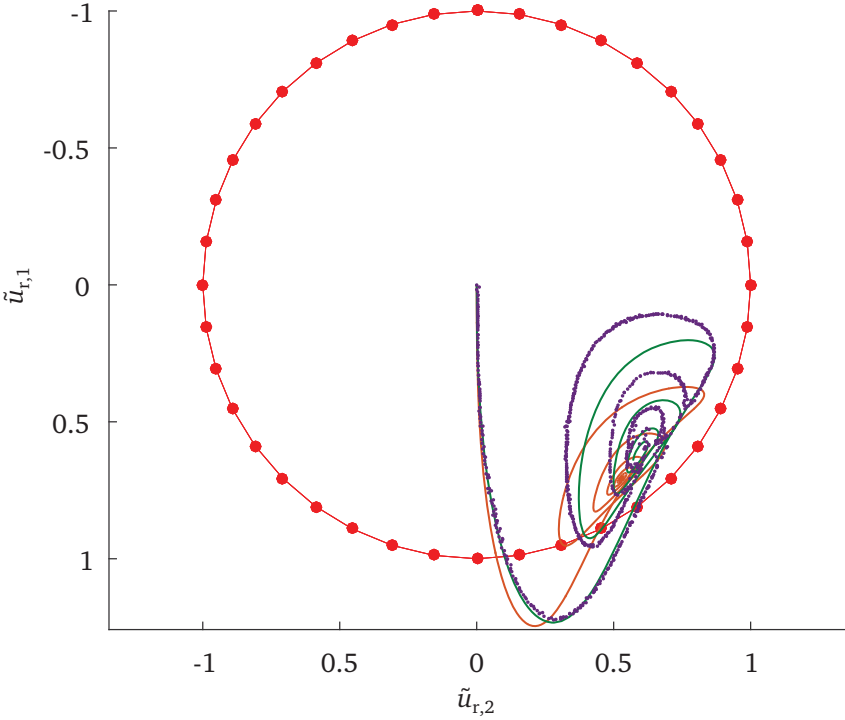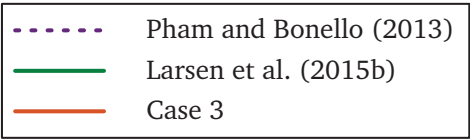
(b) Journal orbits.

Figure 4.4: Comparison of rotor orbits for an AFB with a top foil clamped at both leading and trailing edges.

case 3, which results in the sub-ambient pressure for case 3 being closer to ambient pressure. The smaller inward deflections in the simulations from Larsen et al. (2015b) and Pham and Bonello (2013) also affect the journal orbits seen by, e.g., the journal being lifted further up in the AFB after the initial drop. The difference between the simulations from the literature and case 3 are expected. The models from the literature use the same bump foil stiffness for both radial outward and inward deflections, i.e., not taking into account the much lower bending stiffness of the top foil, thereby limiting the inward deflection after the separation of the top foil and bump foil too much. This is the main reason for using the Gümbel condition in connection with the classical SEFM. A remedy for this discrepancy may be to change the linear stiffness used in the classical SEFM to a bilinear stiffness, where the stiffness for inward radial deflection is based on the top foil stiffness, as shown below. This remedy is not investigated in this thesis.

$$
\tilde{\delta}_{\mathrm{t}} = \begin{cases} (\tilde{p}-1)\,\tilde{\alpha}_{\mathbf{b}} & \tilde{p} \geq 1 \\ (\tilde{p}-1)\,\tilde{k}_{\mathbf{t}}^{-1} & \tilde{p} < 1 \end{cases}
$$

4.2   Improved dynamic performance of an air foil bearing by only partly supporting top foil thereby introducing a shallow pocket

The MFC patch used in the proposed PAFB is placed on the backside of the top foil. This limits the area where the bump foil can support the top foil, since the localised support forces from the bump foil will damage the MFC, i.e., IDEs and piezoelectric material. In order to examine the effects of a partly supported top foil on the bearing performance, a numerical study was performed on an AFB. The dimensions of the AFB is the same as used in the numerical validation (see table 3.2). The results were presented in publication P2. In the study four cases were investigated: 1) an ordinary AFB, i.e., no bump foil removed; 2) bump foil removed close to the leading edge; 3) bump foil removed at the high pressure zone and 4) bump foil removed at the trailing edge. The area of bumps removed in cases 2, 3 and 4 measured 90°×16 mm , which corresponds to the size of a commercially available MFC patch. The steady state responses were obtained for all cases at two different journal unbalances (5 g·mm and 20 g·mm) and a rotational speed range from 6,000 to 20,000 rpm. The steady state responses for case 1 supporting a journal with the small unbalance are trivial in the entire speed range, i.e., only a harmonic vibration is seen. A similar performance was seen for cases 2, 3 and 4. For the large unbalance, the steady state response for case 1 contained subharmonic vibrations in parts of the speed range. Similar subharmonic vibrations were seen for cases 2 and 4, while no subharmonic vibrations were found for case 3. In case 3 only the harmonic vibration was present.

A Parameter study

The parameter study is centred around case 3, and investigates the relationship between the size of the unsupported area and the elimination of the subharmonic vibrations, hence the journal unbalance is 20 g·mm. The rotational speed used in the parameter study is 13,000 rpm. The speed is chosen as the midpoint in the speed range containing multiple subharmonic vibrations for a fully supported AFB, i.e., case 1
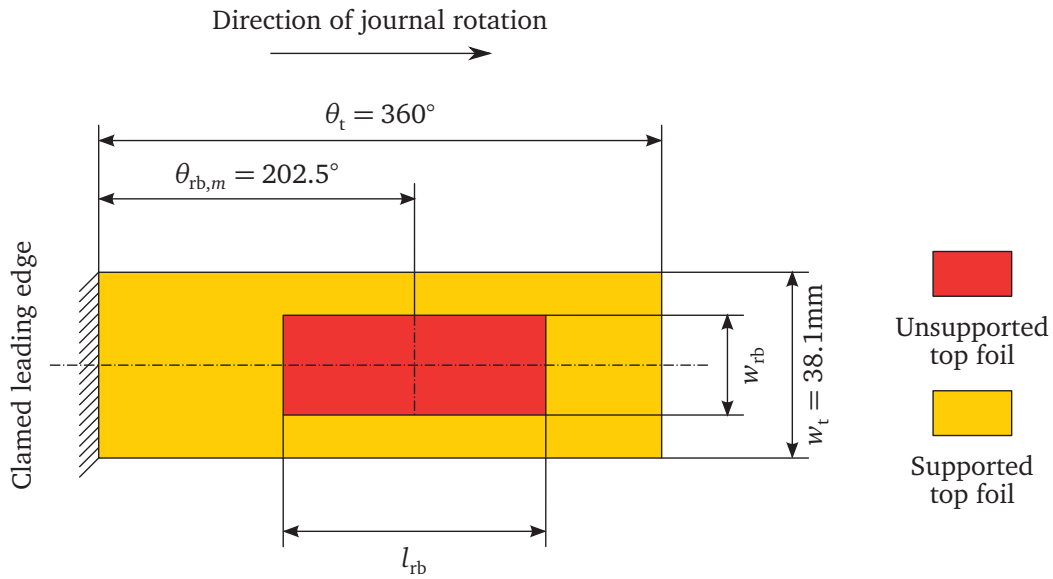
Direction of journal rotation

$\theta_t = 360°$

$\theta_{rb,m} = 202.5°$

Clamed leading edge

w_{rb}

$w_t = 38.1mm$

Unsupported top foil

Supported top foil

l_{rb}

Figure 4.5: Sketch of the design variables used in the parameter study of the partly supported top foil. The unsupported area is symmetrically placed along the axial center line and along a line placed 202.5° from the clamped leading edge. This is similar to case 3.

presented in publication P2. A sketch of the top foil with the unsupported area is shown in figure 4.5. The variables in the parameter study are: the circumferential length l_{rb}; and the axial width w_{rb}. The location of the midpoint in the unsupported area remains the same as for case 3, i.e., the angular position of the centre is located $\theta_{rb,m} = 202.5°$ from the clamped leading edge, just as the area is placed symmetrically in an axial direction.

Table 4.1 presents the results from all the simulations performed in the parameter study. For each design the simulation is run until the steady state response is reached. A ✓ indicates that the subharmonic vibrations are eliminated, while an ✗ shows that the subharmonic vibration is still present, although the frequencies may have shifted and the magnitudes changed. The (✗) indicates that only one subharmonic vibration is present in the steady state response, i.e., the whirl frequency. Finally, a journal-bearing failure is marked with ✗✗.

The parameter study reveals that the subharmonic vibrations will be eliminated if the softening of the support is large enough, i.e., enough bumps have been removed. The most important design variable is the arc length θ_{rb} of the unsupported area. For lengths above 108° the subharmonic vibrations will be removed independently of the axial width w_{rb} of the unsupported area. There are two exceptions: 1) a too narrow area does not lower the stiffness enough, and 2) an unsupported top foil, axially, causes a journal-bearing failure, i.e., the rigidity of the top foil is too weak to support the journal by itself. At a arc length of 90° the more narrow unsupported area becomes inadequate to eliminate the subharmonic vibrations, and when the length goes below 72° it is not possible to eliminate the subharmonic vibrations.

Figure 4.6 shows the journal orbits and FEM meshes for an AFB supported by four different cases of bump foil support. Results are presented as follows: figure 4.6(a) shows design (a), a fully supported AFB; figure 4.6(b) is design (b) where a long, thin strip of bump foil is removed (180°×8 mm); figure 4.6(c) is design (c) which has a

Table 4.1: The results from the parameter study of the partly supported top foil. The table shows the effect of removing a given area of bump foil on the steady state response of a rotor-bearing system affected by an unbalance of 20 g·mm. ✓: subharmonic vibrations have been eliminated; ✗: multiple subharmonic vibrations are present; (✗): only one subharmonic vibration is present, which is the whirl frequency; and ✗✗: journal-bearing failure, i.e., negative thickness of the air film. The three letters refer to the journal orbits shown in figure 4.6

	Arc length θ_{rb} [°]								
	36	54	72	90	108	126	144	162	180
4.0				✗	✗	✗	✗	✗	✗
8.0			✗	✗	✓	✓	✓	✓	✓ (b)
12.0			✗	✓	✓	✓	✓	✓	✓
16.0			✗ (c)	✓					
20.0			✗	✓					
24.0		✗	✗	✓					
28.0		✗	✓	✓	✓				
32.0		✗	(✗)	(✗)	✓	✓	✓	✓	
36.0	✗	(✗) (d)	✓	✓	✗✗	✓	✗✗	✓	✓
38.1	(✗)	n/a	✓	✗✗	✗✗	✗✗	✗✗	✗✗	✗✗

Axial width w_{rb} [mm]

shorter but wider section of bump foil removed (72°×12 mm) and figure 4.6(d) is design (d) and has a short but much wider area of unsupported top foil (56°×36 mm). For cases (b), (c) and (d), i.e., partly supported AFB, the magnitude of the journal orbits are reduced compared to the fully supported AFB. This can also be seen in the FFTs of the steady state responses shown in figure 4.7. The fully supported AFB and design (c) have the same dominating subharmonic frequencies in the steady state response, although of different magnitudes. The two main subharmonic peaks are symmetrically placed around the whirl frequency. This was also reported in publication P2. Design (d) only has one subharmonic frequency, i.e., the whirl frequency, while no subharmonic frequencies are present in the steady state response for design (b).

Of the four journal orbits shown in figure 4.6 design (d) reaches the largest eccentricity ($\tilde{\delta}_r = 2.1$). This remains within the geometrically linear deflection range of the top foil, and it is assumed that this is within the linear range of the bump foil. Larsen et al. (2014) showed by experiment that the linear range of the bump foil stiffness is more than 200 μm for a bump foil with a 7 mm pitch, hence the linear range of the bump foil used in these particular AFBs is assumed to be 130 μm since the bump foil pitch is 4.572 mm, see table 3.2.

The top foil deflection for design (a) and (b) are similar. They have the largest top foil deflection located at the minimum air film thickness, their pressure profiles has one peak and the region next to the trailing edge deflects inwards. This is in line with expectations. For design (c) a slight modification of the pressure peak is caused by the additional deformation of the unsupported top foil when compared to design (a). This feature is mostly pronounced for design (d). Figure 4.8 shows the top foil deflection, thickness of the air film and the pressure profile at the last time step of the simulation, i.e., the point marked with the largest blue dot in figure 4.6(d). The minimum thickness of the air film is located around 160° from the clamped leading edge as seen in figure 4.8(b). However, the largest deflection of the top foil in radial direction is located at

(a) Design (a): $\theta_{br} = 0°$, $w_{br} = 0$ mm

(b) Design (b): $\theta_{br} = 180°$, $w_{br} = 8$ mm

(c) Design (c): $\theta_{br} = 72°$, $w_{br} = 16$ mm
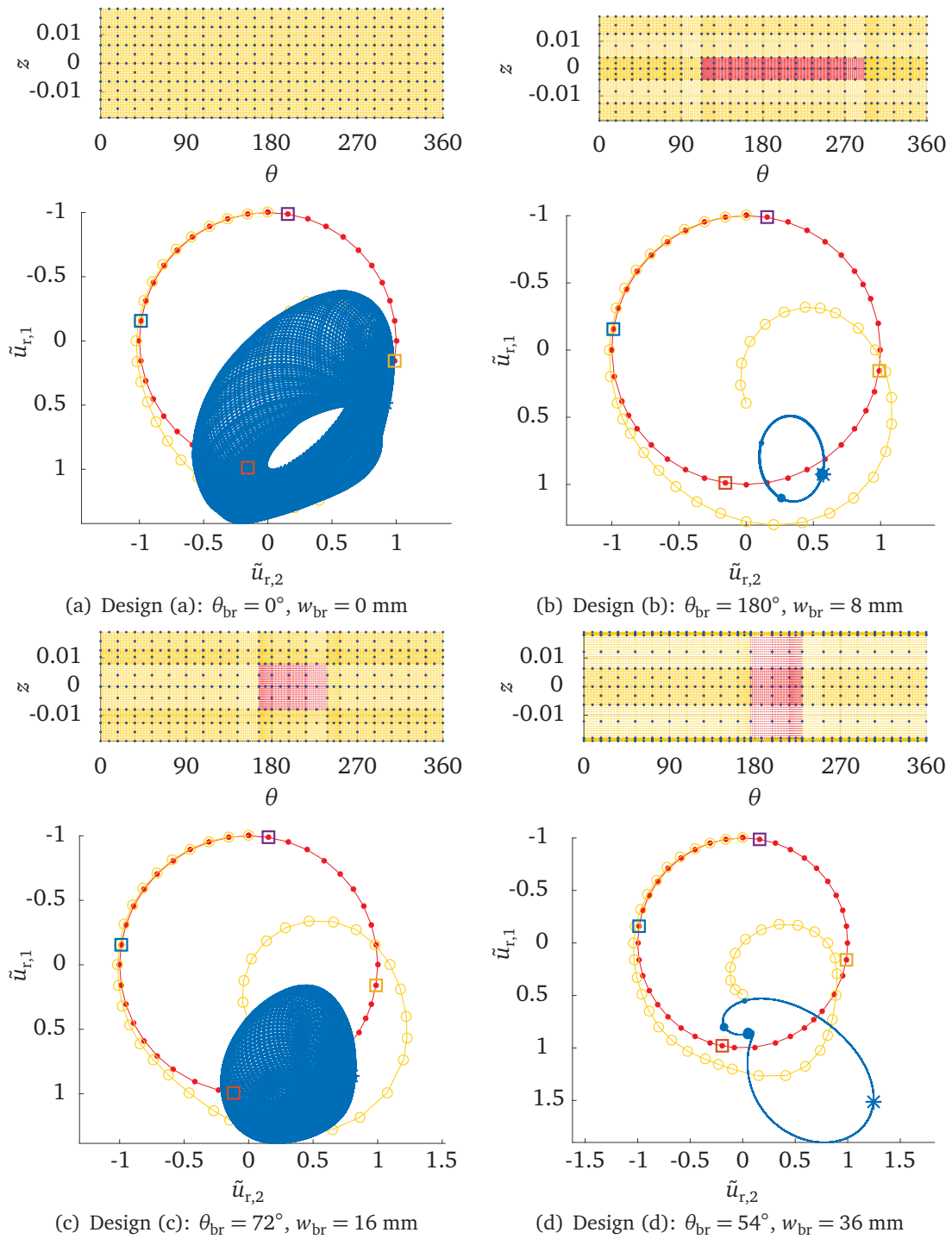
(d) Design (d): $\theta_{br} = 54°$, $w_{br} = 36$ mm

Figure 4.6: The FEM meshes employed in the simulations and steady state journal orbits for the selected AFBs from the parameter study.

(a) Design a: $\theta_{\mathrm{br}} = 0°$, $w_{\mathrm{br}} = 0$ mm

(b) Design b: $\theta_{\mathrm{br}} = 180°$, $w_{\mathrm{br}} = 8$ mm

(c) Design c: $\theta_{\mathrm{br}} = 72°$, $w_{\mathrm{br}} = 16$ mm

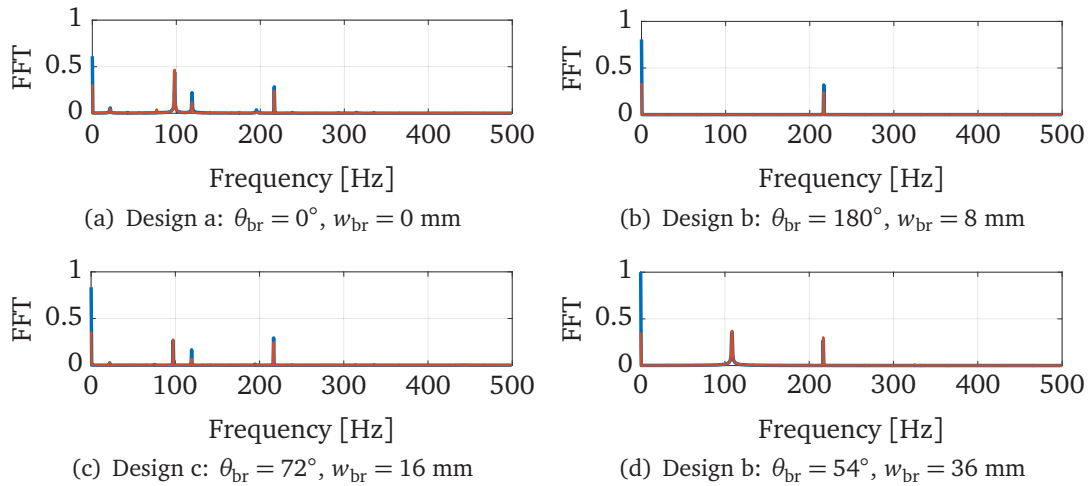(d) Design b: $\theta_{\mathrm{br}} = 54°$, $w_{\mathrm{br}} = 36$ mm

Figure 4.7: FFTs of the steady state response for the fully supported AFB and the three selected designs, i.e., the three configurations of AFBs with partly supported top foils. The blue lines are the FFTs of the x-direction and the red are the FFTs of the y-direction. The rotational speed is 13,000 rpm and the journal unbalance is 20 g·mm. The selected configurations are marked in table 4.1 by letters corresponding to the figures shown.

approximately 200°, as seen in figure 4.8(c), i.e., at the center of the unsupported area. This affects the thickness of the air film seen by the plateauing just after the minimum thickness of the air film. This results in double pressure peaks, as seen in figure 4.8(a). The large peak is associated with the minimum thickness of the air film and the smaller peak is due to the unsupported area of the top foil.

4.3   Increasing the rotational speed limit of an air foil bearing

One of the reasons for using PAFBs in a rotor-bearing system is to increase the rotational speed of the rotor. Hence to create a baseline, the upper limit of the rotational speed is found for two types of AFBs. In figure 4.9 journal orbits are shown for four different rotational speeds. The initial condition for the orbits in the left hand column is the centre of the bearing $\left(\tilde{u}_{\mathrm{r},1} = 0 ,\; \tilde{u}_{\mathrm{r},2} = 0\right)$, while the initial condition for the right hand column is the equilibrium point for the journal-bearing system running at 19,000 rpm $\left(\tilde{u}_{\mathrm{r},1} = 0.68 ,\; \tilde{u}_{\mathrm{r},2} = 0.37\right)$. The orbits reveal that the attraction of the equilibrium point decreases as the rotational speed increases. A journal rotating with 19,000 rpm dropped from the center of the bearing is attracted to the stable equilibrium point, while equilibrium position is not reached for a rotational speed of 19,500 rpm. The onset speed of instability has not, however, been passed, since the journal will reach the equilibrium position if the initial condition is closer to this point. In the right hand column the initial condition is a drop from the equilibrium position at a rotation speed of 19,000 rpm. The onset speed of instability is passed between 21,500 and 22,000 rpm, as seen by the journal orbit being attracted to a point of equilibrium at 21,500 rpm $\left(\tilde{u}_{\mathrm{r},1} = 0.65 ,\; \tilde{u}_{\mathrm{r},2} = 0.37\right)$, while being repelled at 22,000 rpm.

A common strategy employed in the effort to increase the onset speed of instability is to use an AFB with multiple preloaded top foil segments. An AFB with three preloaded top foils is used in the simulations. The bearing parameters remain the same as for the

(a) Pressure profile

(b) Thickness of air film

(c) Top foil deflection
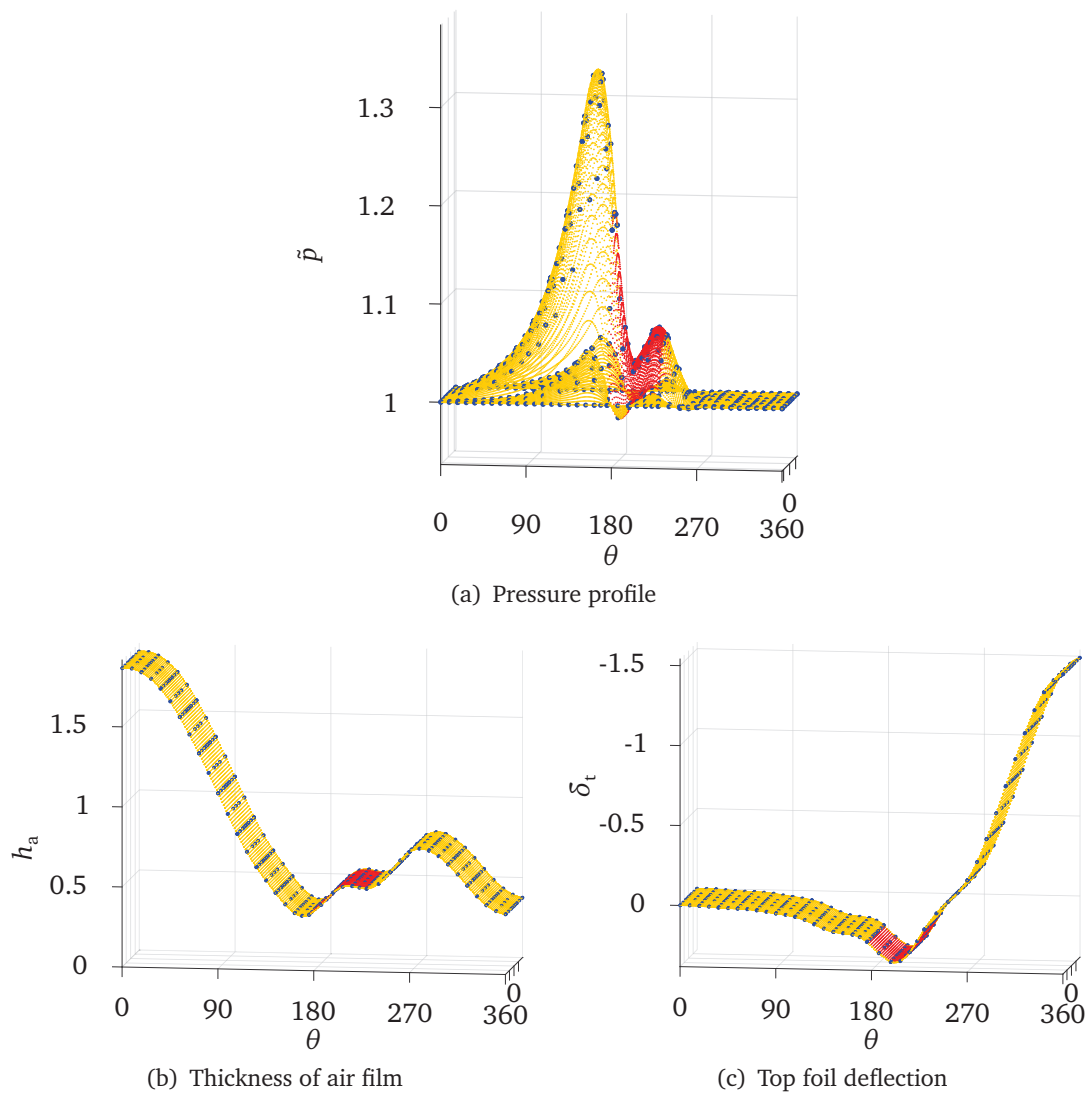
Figure 4.8: Pressure profile, air film thickness and top foil deflection for the AFB with an unsupported top foil area measuring 54°×36 mm. The profiles correspond to the position of the journal marked with the largest dot in figure 4.6(d).

AFB with one top foil (data given in table 3.2), with the exception of the parameters given in table 4.2. The AFB is shown in figure 4.10. The results of the simulations are seen in figure 4.11. When a journal running at 39,500 rpm is dropped from the bearing centre, it is attracted to the stable equilibrium point, while at 40,000 rpm the attraction of the equilibrium point is too low, i.e., the journal escapes, resulting in a bearing failure. Similar to the previous AFB, the journal will reach the point of equilibrium, while running at 40,000 rpm, if its initial condition is closer to the equilibrium point, i.e., if it is dropped from the equilibrium point associated with the rotational speed of 39,500 rpm. The onset speed of instability for this AFB is between 44,500 and 45,000 rpm, i.e., 44,500 rpm is the highest rotational speed where the journal will reach a stable equilibrium point. From 45,000 rpm the journal orbit follows a limit cycle, i.e., a Hopf bifurcation has occurred. Between 46,000 and 46,500 rpm the limit cycle becomes unstable and the journal orbit spins outward until bearing failure.

Ω	Initial conditions	
[rpm]	$\tilde{u}_{r,1} = 0, \tilde{u}_{r,2} = 0$	$\tilde{u}_{r,1} = 0.68, \tilde{u}_{r,2} = 0.37$
19,000		
19,500		
21,500		
22,000		
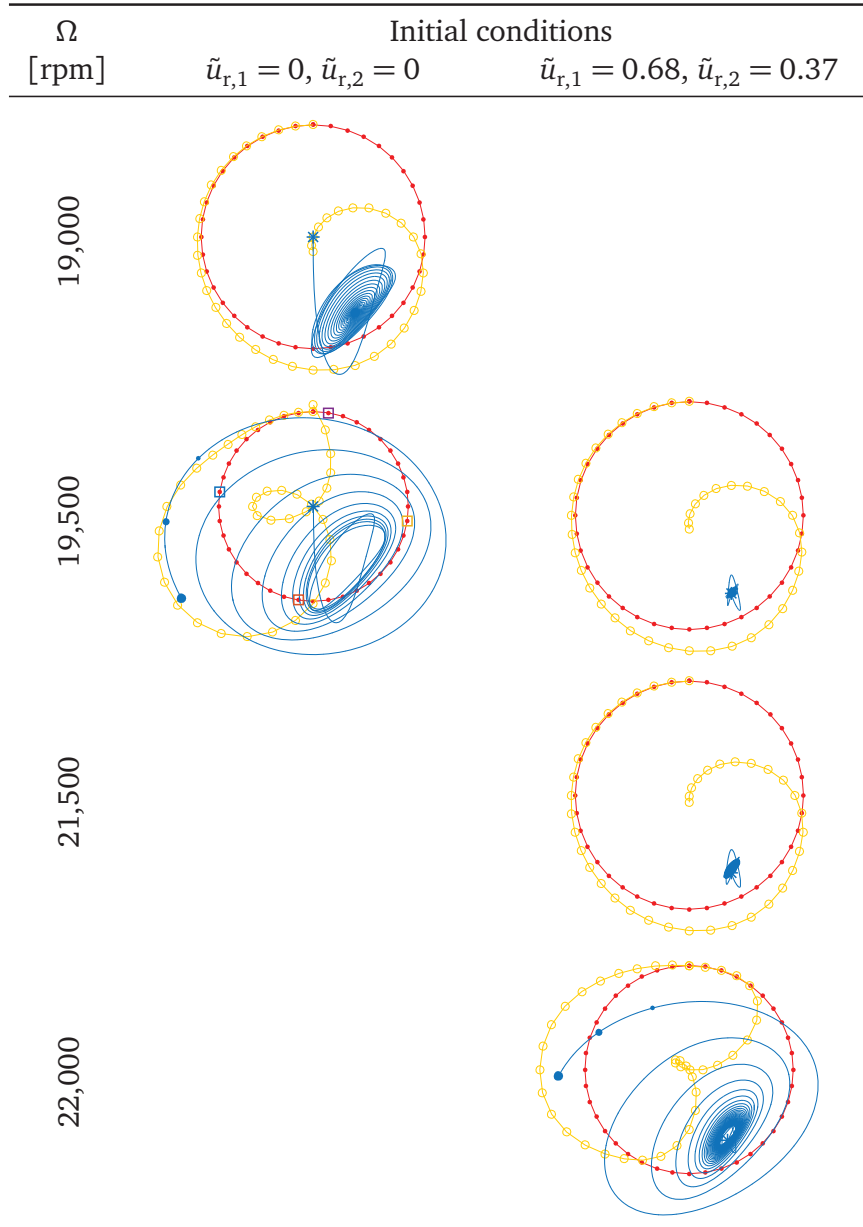
Figure 4.9: Orbits from a journal supported by an AFB with a single top foil at various rotational speeds. The stability limit of the equilibrium point is between 21,500 and 22,000 rpm. However, since the journal-bearing system is non-linear, the transient response depends on the initial conditions, i.e., the equilibrium point is only stable for a small disturbance.

Table 4.2: Additional or altered bearing data for the AFB with three preloaded top foils.

Gas Film Data		
Radial clearance	c	64 $[\mu\mathrm{m}]$
Preload		$0.5c$ [-]
Top Foil Data		
Number of top foils		3 [-]
Leading (clamped) edge	$\theta_{t,s}$	0, 120, 240 [°]
Arc length	θ_t	120 [°]

(a) The AFB with three preloaded top foils. The top foils are clamped at the leading edges.

(b) Mesh of the AFB used in the numerical validation. The top foils are clamped at the leading edges, i.e., $\theta_t = \{0, 120, 240\}$.

Figure 4.10: The AFB used in the numerical simulations of the onset speeds of instability.

Stability limits for two similar AFBs have been presented in the literature. Kim (2007) performed orbits simulations and found the onset speed of instability for the AFB with a single top foil being clamped at the trailing edge to be 24,000 rpm, while the AFB with three preloaded top foils also being clamped at their trailing edges had an onset speed of instability at 47,000 rpm. In both cases these onset speeds are slightly higher than the ones found above, i.e., 2,000 rpm (9.1%) and 2,50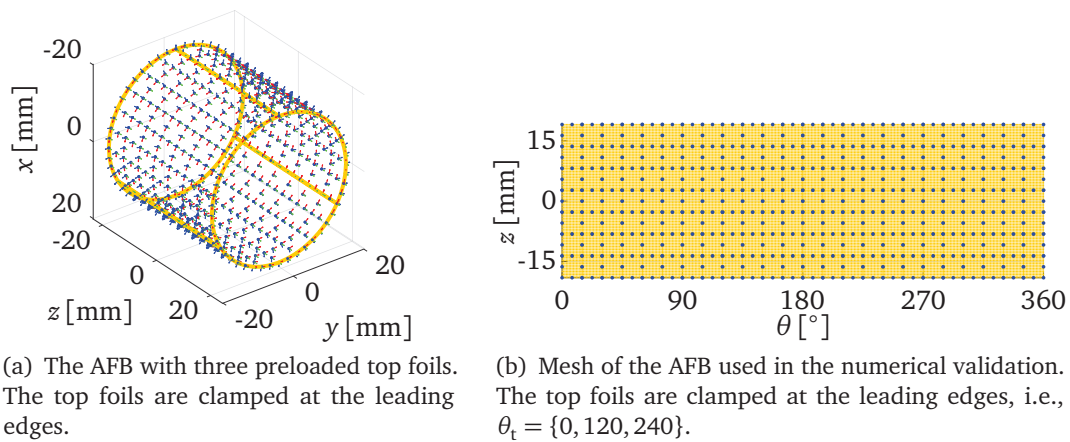0 rpm (5.6%), respectively. As illustrated in the numerical validation of the AFB model, calculations performed with classical SEFM and the Gümbel condition bear a closer resemblance to the simulation performed with a clamped leading edge than simulations with a clamped trailing edge, i.e., the discrepancies is not caused by the variation in mounting of the top foils.

An explanation for the discrepancy can be deduced from the onset speed of instability presented by Larsen et al. (2016). The results show a decrease in onset speed with an increase in SEFM stiffness, and since the contribution from the top foil to the SEFM stiffness is neglected in the simulations presented by Kim (2007), slightly higher onset speeds of instability are to be expected. This is also confirmed by Hoffmann et al. (2015a), who find the onset speed for the AFB with a single top foil to be 22,400 rpm when using the same parameters for the bump foil, but also including a top foil of 0.1016 mm, which is around half the thickness of the top foils employed in the simulations presented.

Whip frequency at the onset speeds are identified by performing an FFT on the transient response of the journal. The FFT for both AFBs are shown in figure 4.12. The whip frequency for the AFB with a single top foil is 101.2 Hz, which corresponds well with the results from the literature, i.e., 100 Hz is found by Kim (2007), while Hoffmann et al. (2015a) obtained 100.8 Hz. The whip frequency for the AFB with three preloaded top foils is 80.0 Hz, thereby also corresponding to the frequency (78.3 Hz) obtained by Kim (2007).

In classical terms, the onset speed of instability equals the stability limit of the equilibrium point, but for non-linear systems the stability limit only states the stability of the equilibrium point for a sufficiently small disturbance, i.e., the system may not be stable for larger disturbances. This is the case for the AFB as seen in figure 4.9 and 4.11, due to the AFB being governed by the compressible Reynolds equation (3.2) and the bilinear SEFM presented in equation (3.6). It is possible to reach the onset speed of
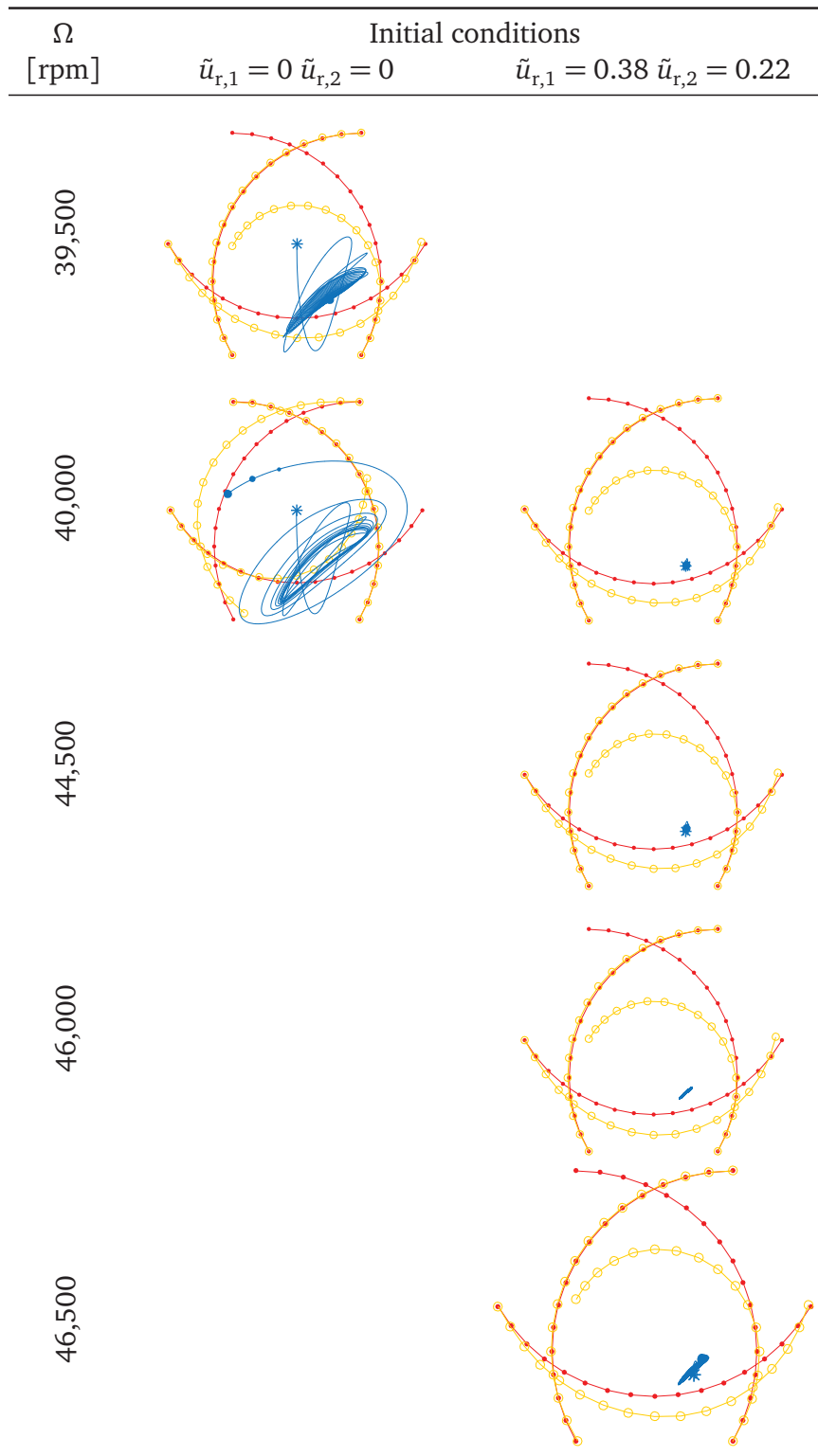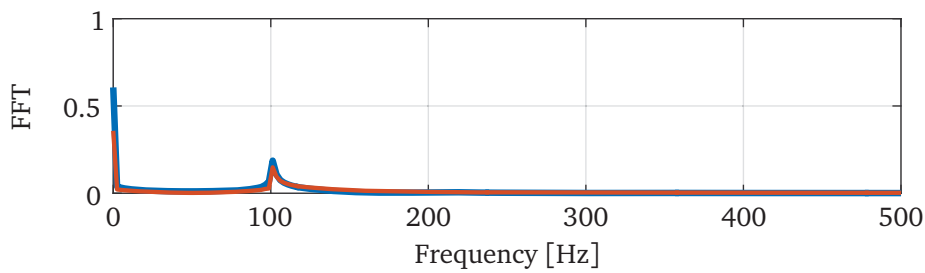
Figure 4.11: Orbits from a journal supported by an AFB with three preloaded top foils (the clearance is 64 μm and the preload is 0.5c) at various rotational speeds. The stability limit of the equilibrium point is between 44,500 and 45,000 rpm. At 46,000 rpm the journal orbit is bound by a stable limit cycle.

(a) AFB with a single top foil and a journal rotating at 22,000 rpm, i.e., the simulation of the journal spinning outwards.
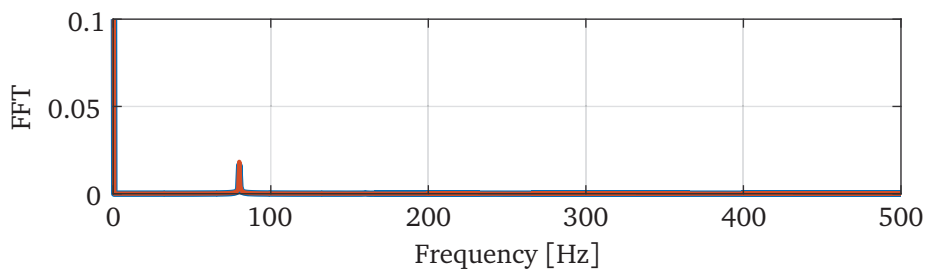
(b) AFB with three top foils and a journal rotation at 45,000 rpm, i.e., the steady state response of the limit cycle.

Figure 4.12: FFT of the transient response for rotational speeds just after the onset speed of instability has been passed.

instability since the journal reaches the point of equilibrium at a lower speed, i.e., below 39,500 rpm, which means the journal centre is very close to the point of equilibrium as the rotational speed approaches 44,500 rpm. However, in reality the journal will never be perfectly unbalanced; the drive will most likely affect the journal with a force besides the driving torque; and an external excitation will most likely affect the system at some point during its operational lifespan, etc. All of these may induce a large disturbance and therefore the onset speed of instability will "in practice" be lower than the stability limit.

4.4 Piezoelectric air foil bearing

The mounting of a MFC patch on the backside of a top foil segment enables a controllable deformation of the top foil. The deformation and its effect on the aerodynamic pressure depends on the size and the placement of the MFC patch, the direction of the piezoelectric fibers within the MFC patch and the EPD applied to the IDEs.

Figure 4.13 shows a sketch of the piezoelectric top foil. Within the top foil area three regions are seen: MFC patch, bump foil support and adjusted bump foil support. In the area where the MFC patch is mounted the bump foil structure is removed and therefore the remaining bump foil in axial direction has been adjusted in order to maintain the overall axial line support stiffness. The correction factor κ_b is given in equation (4.1), and it is multiplied with the stiffness calculated with equation (3.4), i.e., the bump foil stiffness in the regions located before and after the MFC patch in the circumferential
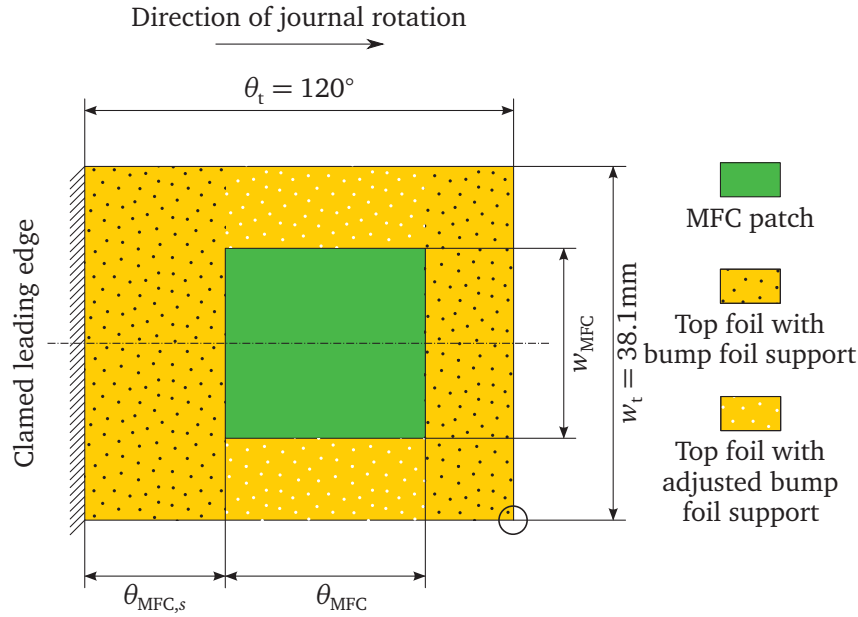
Figure 4.13: Sketch of the design variables for a piezoelectric top foil. The ◯ marks the node for which a selected transient response is shown in figure 4.15(a).

direction.

$$\kappa_{\mathrm{b}} = \frac{w_{\mathrm{t}}}{w_{\mathrm{MFC}}} \tag{4.1}$$

A Parameter study

A numerical parameter study has been performed to clarify the effects on the aerodynamic forces $\{F_{\mathrm{a}}\}$ affecting the journal due to the layout of the PTF, hence the placement of the MFC patch. The investigation is conducted with a flexible top foil segment, with a single MFC patch, supported by bump foil, and with a journal simply supported in its centre and rotating at 20,000 rpm. The piezoelectric fibres in the MFC patch were aligned with the circumferential direction. The PAFB system is seen in figure 4.14 and the constant parameters are given in table 3.2, with the exception of the parameters given in table 4.3. The eccentricity of the journal centre is fixed at 0.75 $\left(\{\tilde{u}_{\mathrm{r}}\} = \{0, 0.75\}^{\mathrm{T}}\right)$ corresponding to a 0.75 preloaded bearing. The design variables investigated in the parameter study are width, foil arc length and circumferential position of the MFC patch, which are shown in figure 4.13. Table 4.4 lists the combinations of design variables used in the study. Not all combinations of length and position are possible due to the fixed overall length of the top foil.

In order to obtain the steady state condition for the non-linear bearing system the transient response is simulated as indicated in figure 4.15. The initial condition for the air film is ambient pressure, while the top foil is undeformed and no EPD $\Delta\phi_{\mathrm{e}} = 0$ is applied to the IDEs, i.e, the bearing system is passive. Once the steady state has been achieved for the passive system, an EPD is gradually imposed on the IDEs. The response is simulated beyond the point in time where the full EPD has been applied in order to obtain the steady state for the active system. Figure 4.15(a) shows the transient radial
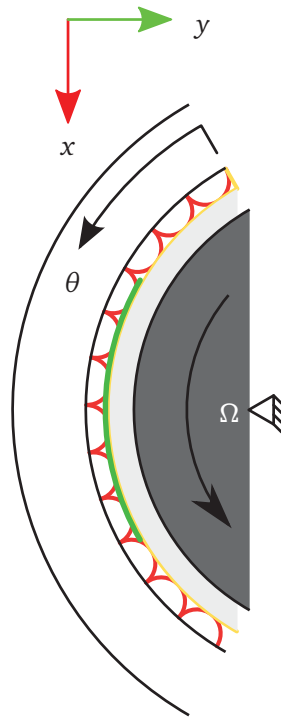
Figure 4.14: A sketch of the PAFB design used in the parameter study. The journal is simply supported with an eccentricity of 0.75 $\{\tilde{u}_\mathrm{r}\} = \{0, 0.75\}^\mathrm{T}$.

Journal Data		
Rotational speed	Ω	$20,000$ [rpm]
Top foil		
Number		1 [-]
Clamped (leading) edges	$\theta_{t,s}$	30 [°]
Arc length	θ_t	120 [°]
MFC patch		
Fibre direction		0 [°]
Thickness	h_{MFC}	0.3 [mm]

Table 4.3: The parameters used for the PAFB are given in table 3.2, with the exception of parameters given in this table and in conjunction with a specific simulation.

| | | θ_{MFC} | | | |
		30°	60°	90°	120°
w_{MFC}	8 mm	x	x	x	x
	16 mm	x	x	x	x
	24 mm	x	x	x	x
$\theta_{\mathrm{MFC},\,s}$	0°	——	——	——	——
	30°	– – –	– – –	– – –	
	60°	··········	··········		
	90°	– ·– ·–			

Table 4.4: Design variables used in the parameter study of the MFC patch. The effect of the added MFC patch is quantified by the change in the aerodynamic forces on the fixed journal as a result of varying EPD applied to the IDEs. Three variables are varied: 1) the arc length of the MFC patch θ_{MFC} in circumferential direction; 2) the width of the MFC patch w_{MFC} in axial direction; and 3) the angular placement of the MFC patch in circumferential direction measured from the clamped leading edge $\theta_{\mathrm{MFC,\,Start}}$.
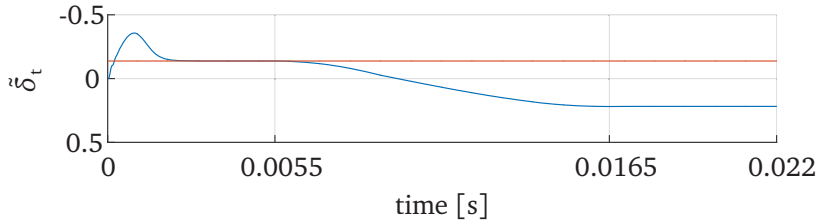
(a) Transient response in radial direction of top foil corner node marked with ◯ in figure 4.13. The red line marks the steady state where there is no EPD between the IDEs.
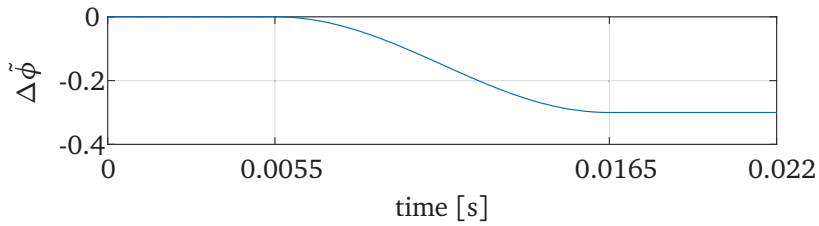
(b) EPD applied to the IDEs on the MFC patch.

Figure 4.15: The simulated transient response from a top foil with a 16 mm × 90° MFC patch placed 30° from the clamped edge. In the simulation a mesh of 12 × 11 elements was used with a modal reduction including the first 40 mode shapes.

deflection of a corner node at the free trailing edge of the top foil marked in figure 4.13. Figure 4.15(b) shows the corresponding EPD applied to the IDEs during the simulation.

Results of the parameter study

The aerodynamic forces acting on the journal are shown in figure 4.16 as a function of the EPD applied to the IDEs. The graphs are divided into six coordinate systems corresponding to the two forces direction and the three widths. The aerodynamic forces for an AFB are included in all six coordinate systems in order to highlight the impact of including a MFC patch in the top foil design.

The computational effort used to obtain the results should be noted. For each design layout at least seven, and up to 12, simulations have been performed in order to obtain either the steady state aerodynamic forces, or to find a negative air film thickness, thereby setting the limit for that particular design. A grand total of 193 simulations have been performed, with time spend simulating the response ranging from minutes to several days. The very long solver times occurred for simulations where very small air film thickness was encountered in certain areas, i.e., where the non-linear effects of the air film were pronounced, while in other areas the top foil and bump foil barely touched each other, i.e., the bilinear effect of the SEFM was pronounced.

The first thing to notice is that the size and placement of the MFC patch have little impact on the aerodynamic forces when no EPD is imposed between the IDEs. The limited effect is seen in figure 4.16 by all lines almost passing through the same point at zero EPD and on top of the reference lines for the AFB. In all 30 design layouts the aerodynamic forces vary within the range $F_{a,x} = 2.24^{+0.15}_{-0.17}$ and $F_{a,y} = 14.49^{+0.0}_{-0.6}$. These differences are less than $\pm7.6\%$ and $\pm4.2\%$, respectively. The design with the largest deviation is the 24 mm $\times$ 120° MFC patch covering the entire circumferential length of the top foil. Figure 4.17 shows the top foil deformations and pressure profiles for the aforementioned design and the AFB at steady state. As seen in the figure, the maximum pressure is higher for the AFB ($\tilde{p} = 1.263$ vs. $\tilde{p} = 1.237$) while the pressure profile is somewhat wider for the top foil with a MFC patch.

The second thing to notice is the range of EPD applied to IDEs for each design layout. For all design layouts the positive amplitude of EPD is limited by the occurrence of negative air film thickness. This is observable in the graphs in that none of the design layouts have aerodynamic forces at the highest EPD. The design allowing for the highest EPD $\left(\Delta\tilde{\phi}_e = 0.8\right)$ has an 8 mm $\times$ 30° MFC patch located 60° from the leading edge, i.e., one of the smallest patches in the parameter study. A commercial supplier states the linear operation range for the EPD to be from -500 V to +1500 V $\left(\Delta\tilde{\phi}_e = \left[-\frac{1}{3}, 1\right]\right)$. For most design layouts no negative air film thickness is encountered within the liner operation range. The larger EPD range for the smaller patches is due to the relatively smaller piezoelectric forces $\{F_{MFC}\}$ they generate, when compared to the larger patches, i.e., a larger patch creates a larger deformations of the PTF than a smaller patch affected by the same EPD. This is indirectly seen by the larger EPD range for the smaller patches, e.g., by comparing the dotted purple line for all three widths, the largest EPD ranges are found for the narrowest patch.

The third thing to notice is the correlation between the size of the MFC patch and the aerodynamic forces. A larger patch increases the change in the y-component of the aerodynamic forces $\left(F_{a,y}\right)$, i.e., perpendicular to the top foil center (see figure 4.14). This is exemplified by the three dashed lines in figure 4.16(e) for the length l_{MFC}, where the orange line (90°) is steeper than the yellow line (60°), which is steeper than the purple line (30°). For the width w_{MFC} the effect is visible by comparing, for instance, the orange dashed lines for 8 mm and 16 mm. However, only a minor additional gain
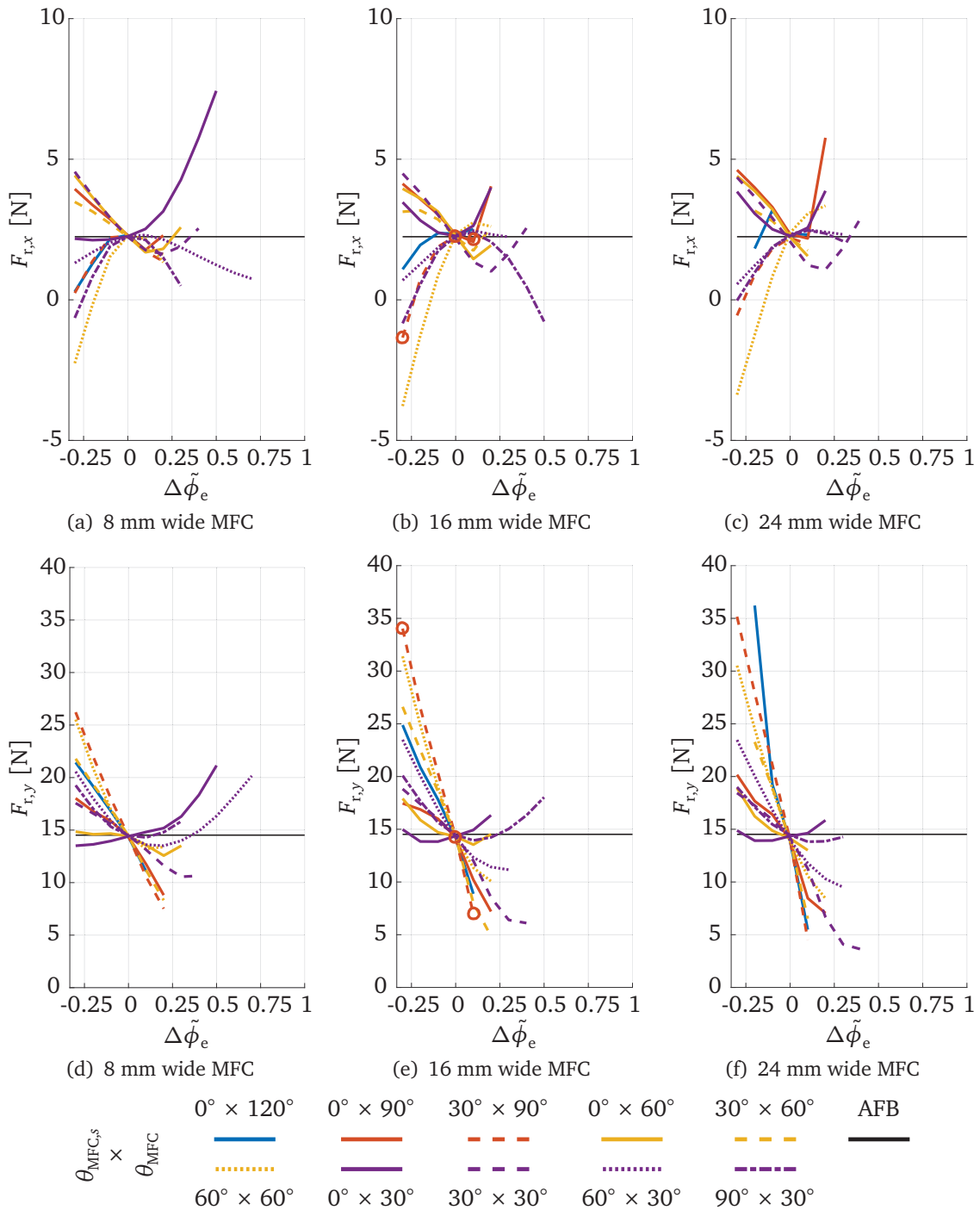
Figure 4.16: The resulting aerodynamic forces $\{F_a\}$ on the journal at different levels of EPD. The values used for the design variables investigated are listed in table 4.4. The mesh used in the parameter study is 12×11 with the first 40 mode shapes included in the modal reduction. The x-axis shows the entire EPD range for a commercial available MFC patch according to the data sheet.

(a) Top foil deflection - 24 mm × 120° MFC patch placed 0° from the clamped leading edge.

(b) Top foil deflection - No MCF patch, i.e., AFB.

(c) Pressure profile - 24 mm × 120° MFC patch placed 0° from the clamped leading edge.

(d) Pressure profile - No MCF patch, i.e., AFB.

Figure 4.17: Top foil deflection and pressure profile simulated with a 12 × 11 mesh and with the first 40 modes in the modal reduction. The blue dots are the nodal values from the simulation, while the interpolated green area shows where the MFC patch is mounted, i.e., the yellow area is passive top foil, which is supported by the bump foil.

is obtained by increasing the width from 16 mm and 24 mm. The relationship between EPD and the aerodynamic force in the x-direction $\left(\{F_{a,x}\}\right)$, i.e., tangential to the top foil center (see figure 4.14), is not as clear as for the y-direction. However, the magnitude of the aerodynamic forces in the x-direction is small when compared to those of the y-direction, and for most design layouts, the forces do not change significantly with neither length nor width when compared to the amplitude of the aerodynamic force in the y-direction.

The fourth thing to notice is the effect on the aerodynamic forces originating from the placement of the MFC patch, i.e., the leading edge of the MFC $\theta_{\mathrm{MFC},s}$. The closer towards the free trailing edge the MFC patch is placed the larger the aerodynamic force in the y-direction. This is seen, for example, in the three yellow lines in figure 4.16(e). The dotted line (60°) is s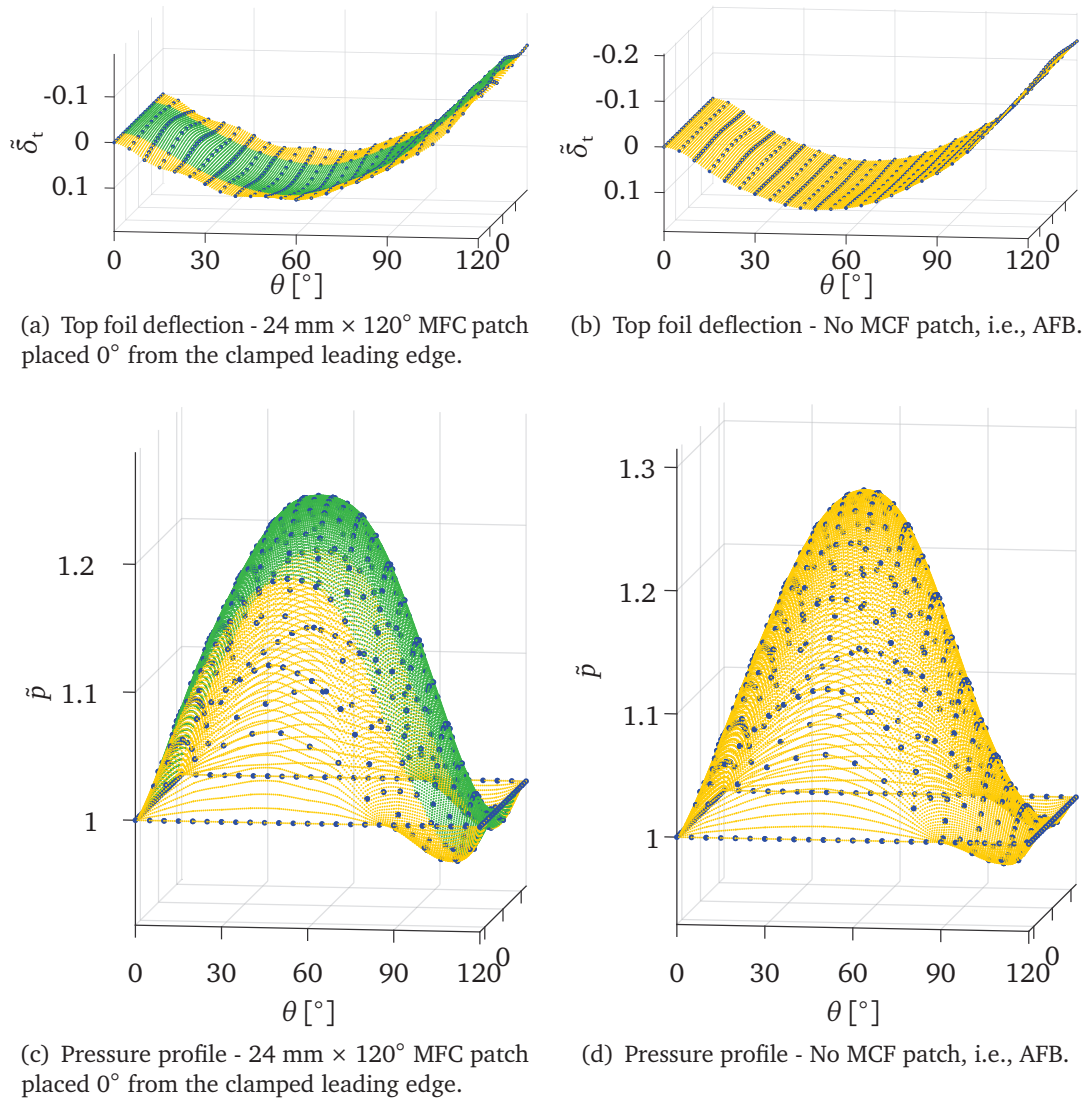teeper than the dashed line (30°), which is steeper than the full line (0°). A different trend is seen for the aerodynamic force in the x-direction: looking at the same three design layouts in figure 4.16(b). First and foremost, the magnitude is smaller. Secondly, the dotted line remains the steepest, however, its inclination is opposite of the dash and full lines. The dashed line is the flattest. This suggests an intermediate position for the MFC patch where change in EPD has a minimal effect on the aerodynamic force in the x-direction.

The final thing to notice is the linear relationship between the EPD and the resulting aerodynamic force in the y-direction, especially for the longer MFC patch.

Based on the parameter study the best design layout has the 16 mm × 90° MFC patch located 30° from the leading edge. The resulting aerodynamic force on the journal in the x-direction is close to zero $\left(F_{a,x} = [-1.3, 2.2]\,\mathrm{N}\right)$. In the y-direction the force is in the vicinity of the largest one obtained $\left(F_{a,y} = [34, 7]\,\mathrm{N}\right)$, and it displays a linear relation with respect to the EPD in the entire range used $\left(\Delta\tilde{\phi}_e = [-0.3, 0.1]\right)$. The additional force obtained with the larger MFC patches does not justify the removal of extra bumps, which a larger patch requires. A reduction of the bump foil area reduces the contact surfaces and thereby the friction forces, which provides hysteresis damping to the bearing system.

In figure 4.18 top foil deflections and pressure profiles at steady state are shown for the PTF with the best design layout. The three different EPD shown are the most positive EPD case $\Delta\tilde{\phi}_e = 0.1$, the passive case $\Delta\tilde{\phi}_e = 0.0$ and the most negative EPD case $\Delta\tilde{\phi}_e = -0.3$. These cases correspond to the aerodynamic forces marked with orange circles in figure 4.16(b) and (e).

The top foil deflection pattern for the passive case, figure 4.18(b), has an outward deflection into the supporting bump foil for the first 90° from the fixed leading edge. The last 30° deflects inward towards the journal, hence this section has no contact with the bump foil. In the area with the largest outward deflection located 30° to 90° from the leading edge, the top foil has an additional outward deflection at the axial center when compared to the edges, essentially creating a shallow pocket in the top foil. This is due to the unsupported area where the MFC patch is located. The area of the MFC patch is marked in green in the figures. The forming of a shallow pocket affects the entire top foil deflection, e.g., at the free trailing edge the center has an additional inward deflection when compared to the corners of the top foil. The corresponding pressure profile seen in figure 4.18(e) has a single pressure peak located a 60° and two sub-ambient pressure zones close to the corners of the free trailing edge.

In figures 4.18(a) and (d) the pressure profile and top foil deformation are shown

(a) Top foil deflection - most positive EDP case ($\Delta\phi_e = 0.1$)

(b) Top foil deflection - passive case ($\Delta\phi_e = 0$)

(c) Top foil deflection - most negative EDP case ($\Delta\phi_e = -0.3$)

(d) Pressure profile - most positive EDP case ($\Delta\phi_e = 0.1$)

(e) Pressure profile - passive case ($\Delta\phi_e = 0$)

(f) Pressure profile - most negative EDP case ($\Delta\phi_e = -0.3$)
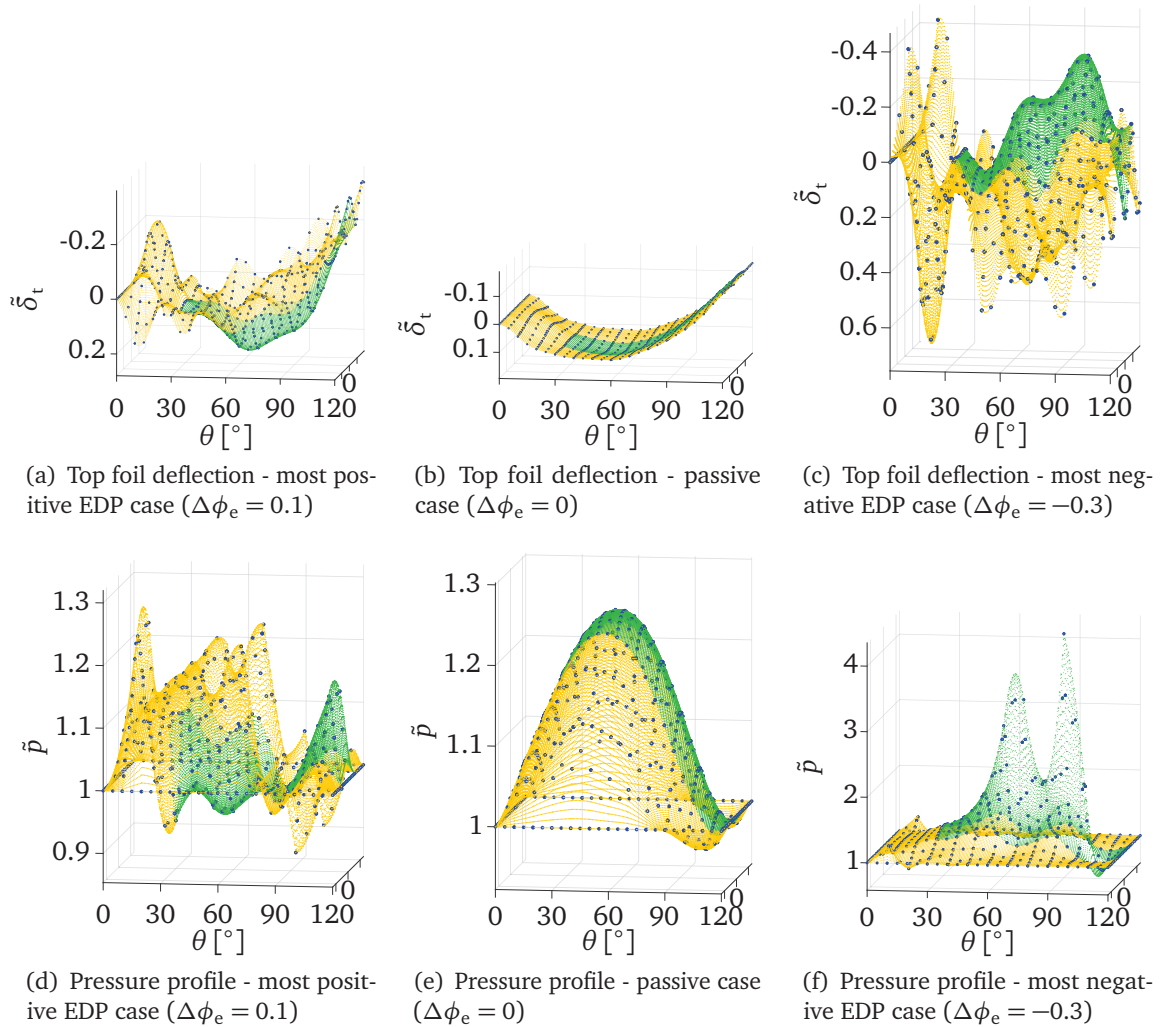
Figure 4.18: Pressure profile and top foil deflection at steady state for a PTF with a 16 mm × 90° MFC patch placed 30° from the clamped edge at three different cases of EPD. The cases correspond to the aerodynamic forces marked with orange circles in figure 4.16(b) and (e). A mesh of 12 × 11 elements including the first 40 mode shapes in the modal reduction was used in the simulations. The blue dots are the nodal values from the simulation, while the interpolated green area shows where the MFC patch is mounted, i.e., the yellow area indicates where the PTF is supported by bump foil.

for the case with the most positive EPD $\left(\Delta\tilde{\phi}_e = 0.1\right)$. The top foil deflection in the area of the MFC patch forms a large valley in circumferential direction, which at the ends is changed to a peak in axial direction. This is consistent with expectations, since a positive EPD applied to the IDEs will elongate the MFC patch in the fibre direction but contract it in the perpendicular direction. This effect increases the outside circumference and thereby the effective curvature while also reducing the outside axial length, introducing an outward arcing curvature. The remaining top foil area, i.e., outside the MFC patch area, deflects with many peaks and valleys. The most noticeable feature is the peak in front of the MFC patch $\theta = [0°, 30°]$. The peak is created by the increased curvature in circumferential direction due to the MFC patch and t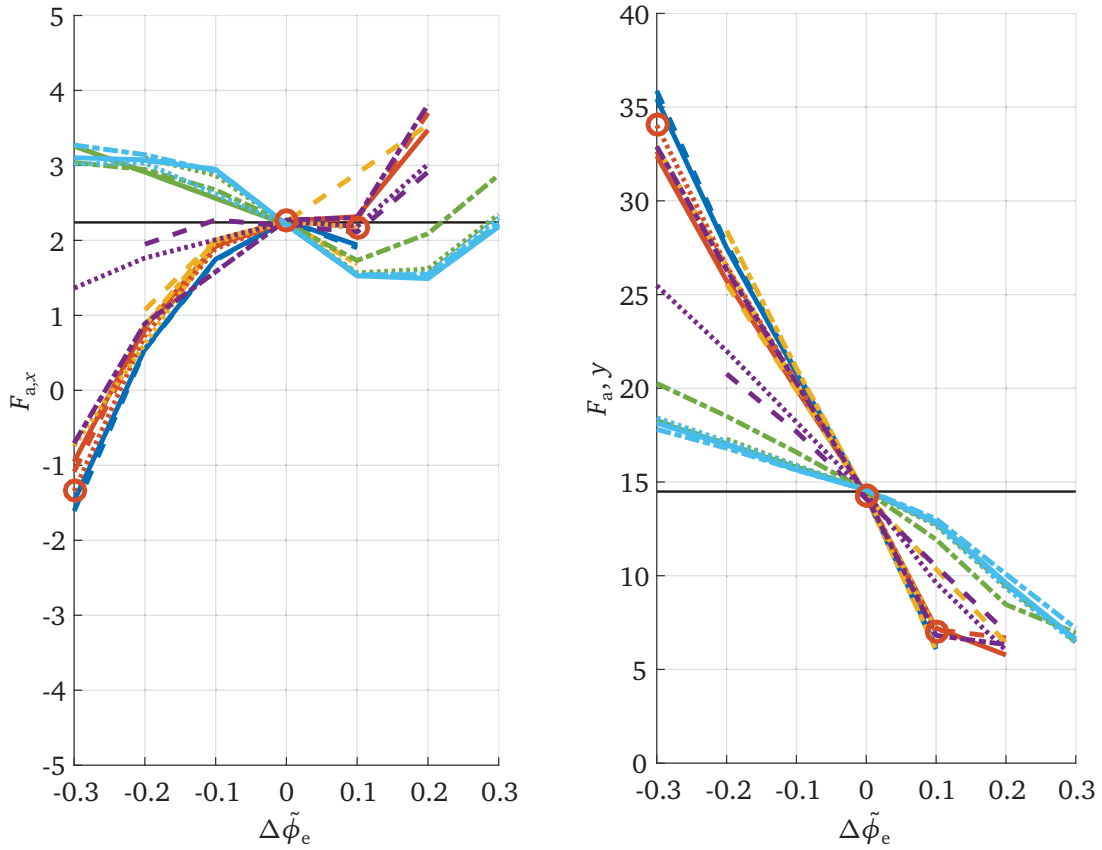he leading edge, which is fixed. The top foil deformation is clearly visible on the pressure profile. The pressure in the initial two thirds of the area where the MFC patch is located ($\theta = [30°, 90°]$) is close to ambient pressure and therefore not contributing to aerodynamic forces on the fixed journal. This leaves the area next to the top foil edges to form the pressure zone, and due to the effectively reduced pressure area the aerodynamic forces are reduced.

The top foil deflection and pressure profile in figures 4.18(c) and (f) show the most negative EPD case $\left(\Delta\tilde{\phi}_e = -0.3\right)$. The top foil deflection in the area of the MFC patch is similar to the previous case, although with opposite direction of deflection. A peak is formed in the circumferential direction with a top at 90° and an initial bump located in front at 60°. The deflection in the axial direction flattens out towards the circumferential ends of the MFC patch, changing the peak to a valley. The deflection in the remaining area consists of many peaks and valleys with the most significant feature located between the fixed leading edge and the MFC patch, i.e., from 0° to 30°. This also resembles the deflection pattern from the most positive EPD case, but with an opposite direction of deflection. The pressure profile for the most negative EPD case differs from the most positive EPD case. The location of the two high pressure peaks corresponds to the location of the initial bump and peak top in the plot of the top foil deflection. The pressure peaks are approximately 9 times higher for the most negative EPD case in comparison to the two other case. This results in a 139 % increase in the aerodynamic force (34.0 N) as compared to the passive case (14.2 N).

Convergence analysis of the result

Figure 4.19 shows the convergence of the aerodynamic forces as a result of mesh refinement and the number of the lowest mode shapes included in the modal reduction. The graphs representing the same number of mode shapes clump together, indicating that the number of mode shapes included in the modal reduction is of greater importance than the number of elements in the mesh. The clusters of graphs for 35 and more mode shapes are located close to each other, with a trend of increasing aerodynamic forces for higher numbers of mode shapes. The effect of including more elements in the mesh reduces the aerodynamic forces, hence the lack of including more mode shapes will compensate by a coarser mesh.

The effect on the top foil deflection and aerodynamic pressure of including more elements in the mesh is seen by comparing figure 4.18(c) with 4.20(a) and figure 4.18(f) with 4.20(c), i.e., 12 × 11 mesh and 17 × 17 mesh. The only clear difference, as the number of elements is increased, is seen in the pressure profiles, where the highest pressure peak shifts from the second peak (at 90°) to the first (at 60°), just as the magnitude of the peak falls from 4.3 to 3.6.

Figure 4.19: Convergence analysis for the PAFB with a 16 mm × 90° wide MFC patch place 30° from the fixed leading edge. In the convergence analysis both mesh size and number of modes included in the modal reduction are varied. The results are shown as resulting aerodynamic forces on the fixed journal.
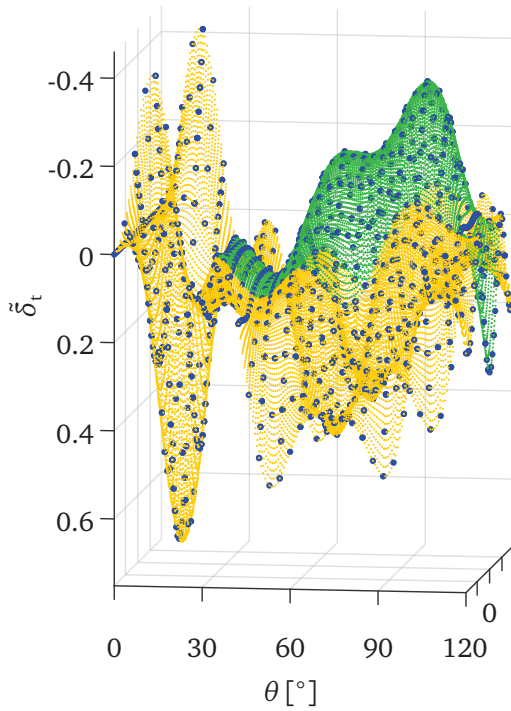
(a) Top foil deflection - 17 × 17 mesh with the first 40 mode shapes.
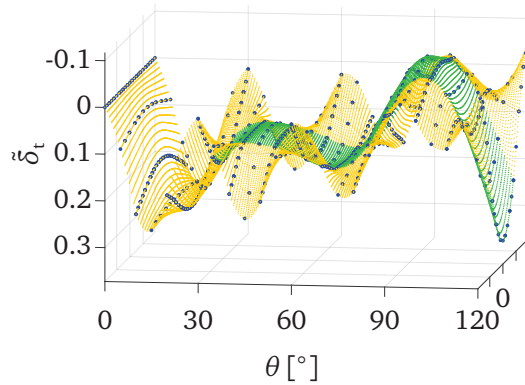
(b) Top foil deflection - 12 × 11 mesh with the first 20 mode shapes.
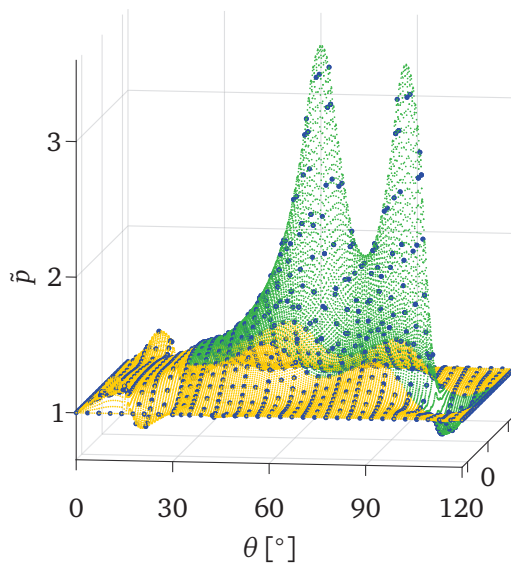
(c) Pressure profile - 17 × 17 mesh with the first 40 mode shapes.
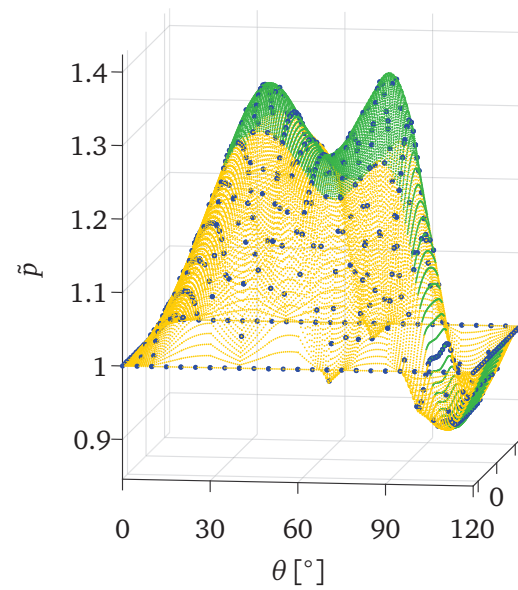
(d) Pressure profile - 12 × 11 mesh with the first 20 mode shapes.

Figure 4.20: The pressure profile and top foil deflection simulated with either the first 40 mode shape in the modal reduction and a mesh of 17 × 17 elements or the first 20 mode shapes and a mesh of 12 × 10 elements. The top foil has a 16 mm × 90° MFC patch placed 30° from the clamped leading edge. The blue dots are the nodal values from the simulation, while the interpolated green area shows where the MFC patch is mounted, i.e., the yellow area is passive top foil, which is supported by the bump foil.

The effects of the number of mode shapes included in the simulations are visible by comparing the top foil deflections (figures 4.18(c) with 4.20(b)) and the pressure profiles (4.18(f) with 4.20(d)). The first clear difference is the magnitude of the top foil deflection, which increases from $[-0.1, 0.3]$ to $[-0.4, 0.6]$ when the number of mode shapes is increased. A second difference is the number of peaks and valleys in the deflection figures, which indicates the influence of the higher order modes on the deflection pattern. When too few mode shapes are included in the modal reduction an artificial stiffening of the top foil is introduced. This is due to the deflection pattern being limited to the lower order modes, which are insufficient for describing the top foil deflection.

The results simulated with a 12×11 mesh and with the 40 first mode shapes in the modal reduction are valid based on the convergence analysis.

4.5 Conclusion

Results presented for a fully supported AFB shows the influence of top foil clamping on the: i) equilibrium point of the journal; ii) journal orbit; and iii) deflection of the top foil. Although the equilibrium point of the journal for a clamped leading edge and clamped trailing edge are close, the journal orbits differ just as the top foil deflections (see figure 4.1 and 4.3). This is important, since most AFBs found in literature have a clamped trailing edge. The traditional simulations of AFB, utilizing classical SEFM automatic implies clamped leading and trailing edges. However, due to the Gümbel condition applied in the subambient pressure zone at the clamping of the trailing edge has no effect, i.e., the traditional simulations mostly resembles an AFB with a clamped leading edge, c.f., figure 3.26.

Additional investigations into the elimination of subharmonic vibrations reported in publication P2 was conducted. The parameter study focused on the successful case, removal of bump foil in the high pressure area. Results show the arc length (θ_{br}) being the most important parameter of the variables varied. Essentially the removal of bump foil creates a shallow pocket, when the journal approaches the softer supported area. This allows the top foil to deflect further than for the fully supported case, thereby achieving a thicker air film, hence the non-linearities are less predominant.

A parameter study was conducted to investigate the effects of the PTF on the aerodynamic forces. In order to isolated the effect the journal was simply supported and the EPD was applied slowly to limit dynamic effects, i.e., a slow feed forward control strategy was applied. The study showed that the aerodynamic forces was not affect when a passive MFC patch was added to the top foil, no matter size or location of the patch. However, when a EPD was applied the aerodynamic forces was affected. Depending on the size and location it was possible to obtain an increase in the aerodynamic forces upto 139 %.

Chapter 5

Conclusion and future aspects

Important steps towards the development of a PAFB have been done in the PhD project. The objectives of the project have been to: 1) develop a multi-physic mathematical model of an AFB combined with a model of smart material; 2) design a versatile test facility; 3) validation the mathematical model and evaluate the performance of the PAFB. The research has resulted in two publications, which together with the thesis document the achievements of these objectives. In overall terms all of the objectives been achieved.

The development and validation of the mathematical model of the PAFB was done stepwise, i.e., PTF (publication P1) and AFB (publication P2). In publication P1 the resonance frequencies and mode shapes of a PTF measured experimentally where captured by the mathematical model in a frequency range upto 500 Hz. The experiments revealed non-linear geometric effects, i.e., a shift in the location of the resonance peaks in the experimental FRF. These effects were visible for vibration amplitudes of a magnitude similar to the thickness of the PTF. This a well known non-linear phenomenon for curved shells, which been reported in literature. But, since the vibration amplitudes in an AFB are much smaller, the non-linear effects have been neglected from the mathematical model.

The structural model of the top foil used in the AFB model is a passive version of the PTF, i.e., without a MFC patch. It incorporates a bi-linear modelling of the bump foil, thus allowing the top foil and bump foil to separate. An investigation into the clamping of the top foil revealed that AFB models known from literature produces journal orbits similar to the presented model, when the leading edge of the top foil is clamping. This is in contrast to AFBs found in industry, which in almost all cases have clamped trailing edges.

Similarly results are seen for the onset speed of instability. Two different AFBs have been simulated, both with clamped leading edges: 1) one top foil and; 2) three preloaded top foils. The calculated onset speeds of instability are similar, although the presented model found slightly lower speeds, than results reported in literature for AFBs with clamped trailing edges. These lower speeds are contributed to the modelling of the non-linear transient response, which have been reported in literature.

Another option when including a structural model of the top foil is to simulated an AFB with a partially support top foil. Such a bearing has been investigated in both publication P2 and in the thesis. It has been found than the removal of bump foil in

the high pressure area can eliminate the subharmonic vibrations affecting the fully supported equivalent, when supporting at highly unbalanced journal. The investigation revealed the most important design parameter to be the circumferential length of the unsupported area. A sharp transition zone is found between areas spans 90° and 72°, i.e., to eliminate the subharmonic vibration the unsupported area must span 90° or more.

The result of functioning AFBs with partially supported top foils is a stepping stone towards the PAFB. The removal of bump foil creates an area for the MFC patch, where it will not be damaged due to radial loading. Results from such a set-up have been reported in the thesis. An PTF, spanning 120° × 38.1 mm, clamped at the leading edge and partially supported by a bump foil, has been loaded by the aerodynamic forces arising between PTF and a simply supported journal running a constant speed. The EPD applied to the MFC patch affect the deflection of the PTF, thereby changing the aerodynamic forces, which directly relates to the load carrying capacity of the PAFB. A parameter study shows that a very significant impact is achieved with a 90° × 16 mm MFC patch, placed at the trailing edge of the PTF. This can increased the load carrying capacity by 139 %.

5.1   Future aspects

In light of the numerical findings presented in this PhD thesis the possibilities of successfully creating an PAFB with better performance than the AFB is still very likely, but further investigations, both numerically and experimentally, are required. First and foremost an experimental validation of the presented PAFB model, i.e., beyond the validations of the individual submodels. This is achievable with the presented test facility.

Objectives for future investigations can be divided into two main categories: 1) used the mathematical model to investigate the structural effects of the top foil in an AFB and; 2) investigate the static and dynamic behaviour of the PAFB. Of the first type the focus may be, e.g., mechanical stresses at the clamping point; the influence of the top foil structural stiffness on the static and dynamic properties of the AFB or; the influence of top foil inlet inclinations. For the other type objectives may be, e.g., active control of the rotor-bearing response based on rotational speed or rotor vibrations; connecting the MFC patches to shunt circuits thereby increasing the energy dissipation from the system or; use a small MFC patch to monitor the structural integrity of the system.

The current mathematical model can address the suggested objectives of the first category, i.e., for the AFB. Although minor work is required in order to calculate the mechanical stresses in the top foil. However, for the second category some additional physical phenomena have to been included. The electrical circuit use, i.e., the actuator circuit, is very simple, and further computational code has to be written before numerical simulations of, e.g., shunt circuits connected to the PAFB, are possible.

Furthermore, piezoelectric material will creep when a constant EPD is applied to the electrodes for a long time. Hence, if a rotational speed based control strategy is implemented, and the goal is to study the static and dynamic behaviour of the PAFB at a constant rotational speed, the current version of the mathematical model will produce incorrect results.

For both cases the mathematical model requires further refinement. The wall-clock

time spend to complete a simulation of the transient response are in some cases more than six hours and some times days. This is within an acceptable time frame if only a limited number of simulation are required. But for larger parameter studies examining the influence of several design variables the wall-clock time for the simulation is too long. A further optimisation of the computational code is required.

The numerical results produced with the mathematical model can be validated via experiments preformed with the versatile test facility presented in the thesis. However, modifications may be required before an experiment can be performed. The design of the test facility allows for this without irreversibly changing the test facility. Hence, any future modifications should be viewed as add ons, which can be mounted and dismounted depending on the experimental requirements.

References

Agrawal, G. L. (1997). 'Foil Air/Gas Bearing Technology — An Overview'. *International Gas Turbine and Aeroengine Congress and Exhibition*. Orlando, Florida, USA: ASME, ASME–97–GT–347. DOI: `10.1115/97-GT-347`.

Allik, H. and T. J. R. Hughes (1970). 'Finite element method for piezoelectric vibration'. *International Journal for Numerical Methods in Engineering* **2**(2), pp. 151–157. DOI: `10.1002/nme.1620020202`.

Arghir, M., S. Le Lez and J. Frene (2006). 'Finite-volume solution of the compressible Reynolds equation: linear and non-linear analysis of gas bearings'. *Proceedings of the Institution of Mechanical Engineers, Part J: Journal of Engineering Tribology* **220**(7), pp. 617–627. DOI: `10.1243/13506501JET161`.

Balamurugan, V. and S. Narayanan (2001). 'Shell finite element for smart piezoelectric composite plate/shell structures and its application to the study of active vibration control'. *Finite Elements in Analysis and Design* **37**(9), pp. 713–738. DOI: `10.1016/S0168-874X(00)00070-6`.

Balamurugan, V. and S. Narayanan (2009). 'Multilayer Higher Order Piezolaminated Smart Composite Shell Finite Element and its Application to Active Vibration Control'. *Journal of Intelligent Material Systems and Structures* **20**(4), pp. 425–441. DOI: `10.1177/1045389X08095269`.

Balducchi, F., M. Arghir and S. Gaudillere (2014). 'Experimental Analysis of the Unbalance Response of Rigid Rotors Supported on Aerodynamic Foil Bearings'. *Proceedings of ASME Turbo Expo 2014: Turbine Technical Conference and Exposition*. Düsseldorf, Germany: ASME, GT2014–25552. DOI: `10.1115/GT2014-25552`.

Behrens, S., A. J. Fleming and S. O. R. Moheimani (2003). 'A broadband controller for shunt piezoelectric damping of structural vibration'. *Smart Materials and Structures* **12**(1), pp. 18–28. DOI: `10.1088/0964-1726/12/1/303`.

Belforte, G., T. Raparelli, V. Viktorov, A. Trivella and F. Colombo (2006). 'An Experimental Study of High-Speed Rotor Supported by Air Bearings: Test RIG and First Experimental Results'. *Tribology International* **39**, pp. 839–845. DOI: `10.1016/j.triboint.2005.07.013`.

Bellabarba, E., R. Ruiz, S. Díaz and V. Rastelli (2005). 'A Test Rig for Air Bearings Dynamic Characterization'. *World Tribology Congress III*, pp. 1–2.

Benjeddou, A., M. A. Trindade and R. Ohayon (1997). 'A Unified Beam Finite Element Model for Extension and Shear Piezoelectric Actuation Mechanisms'. *Journal of Intelligent Material Systems and Structures* **8**(12), pp. 1012–1025. DOI: `10.1177/1045389X9700801202`.

Benjeddou, A., M. A. Trindade and R. Ohayon (1999). 'New shear actuated smart structure beam finite element'. *AIAA Journal* **37**(July 2015), pp. 378–383. DOI: 10.2514/3.14176.

Bent, A. A. and N. W. Hagood (1997). 'Piezoelectric Fiber Composites with Interdigitated Electrodes'. *Journal of Intelligent Material Systems and Structures* **8**(11), pp. 903–919.

Bilgen, O., A. Erturk and D. J. Inman (2010). 'Analytical and Experimental Characterization of Macro-Fiber Composite Actuated Thin Clamped-Free Unimorph Benders'. *Journal of Vibration and Acoustics* **132**(5), p. 051005. DOI: 10.1115/1.4001504.

Biscani, F., H. Nasser, S. Belouettar and E. Carrera (2011). 'Equivalent electro-elastic properties of Macro Fiber Composite (MFC) transducers using asymptotic expansion approach'. *Composites Part B: Engineering* **42**(3), pp. 444–455. DOI: 10.1016/j.compositesb.2010.12.009.

Bonello, P. and H. M. Pham (2014). 'The efficient computation of the nonlinear dynamic response of a foil air bearing rotor system'. *Journal of Sound and Vibration* **333**(15), pp. 3459–3478. DOI: 10.1016/j.jsv.2014.03.001.

Braun, M. J., F. K. Choy, M. Dzodzo, J. Hsu, R. Veillette and D. Deckler (1995). 'A Theoretical and Numerical Development of the Concept of the Active Control Foil Bearing (ACFB)'. *International Gas Turbine & Aeroengine Congress & Exhibition*. Houston, Texas, USA, pp. 1–8.

Brockmann, T. H. and R. Lammering (2006). 'Beam Finite Elements for Rotating Piezoelectric Fiber Composite Structures'. *Journal of Intelligent Material Systems and Structures* **17**(5), pp. 431–448. DOI: 10.1177/1045389X06058632.

Bryant, R. G. (2007). 'Overview of NASA Langley's Piezoelectric Ceramic Packaging Technology and Applications'. *10th Japan International SAMPE Symposium Exhibition: JISSE-10*. Tokyo, Japan, pp. 1–8.

Carpino, M. and G. Talmage (2003). 'A Fully Coupled Finite Element Formulation for Elastically Supported Foil Journal Bearings'. *Tribology Transactions* **46**(4), pp. 560–565. DOI: 10.1080/10402000308982664.

Chen, S., Y. Hou, L. Niu, S. Yang and T. Lai (2015). 'Study on double-layer protuberant gas foil journal bearings with different foil layers arrangement'. *Journal of Advanced Mechanical Design, Systems, and Manufacturing* **9**(2), pp. 1–12. DOI: 10.1299/jamdsm.2015jamdsm0014.

Clark, W. W. (2000). 'Vibration Control with State-Switched Piezoelectric Materials'. *Journal of Intelligent Material Systems and Structures* **11**(4), pp. 263–271. DOI: 10.1106/18CE-77K4-DYMG-RKBB.

Cook, R. D., D. S. Malkus, M. E. Plesha and R. J. Witt (2002). *Concepts and Applications of Finite Element Analysis*. 4th. Hoboken, New Jersey: John Wiley & Sons. Inc.

Corr, L. R. and W. W. Clark (2002). 'Comparison of low-frequency piezoelectric switching shunt techniques for structural damping'. *Smart Materials and Structures* **11**(3), p. 307. DOI: 10.1088/0964-1726/11/3/307.

Damjanovic, D. (1998). 'Ferroelectric, dielectric and piezoelectric properties of ferroelectric thin films and ceramics'. *Reports on Progress in Physics* **61**(9), pp. 1267–1324. DOI: 10.1088/0034-4885/61/9/002.

Deckler, D. C., R. J. Veillette, M. J. Braun and F. K. Choy (2004). 'Simulation and Control of an Active Tilting-Pad Journal Bearing'. *Tribology Transactions* **47**(3), pp. 440–458. DOI: 10.1080/05698190490463277.

Dellacorte, C. (1998). 'A New Foil Air Bearing Test Rig for Use to 700C and 70,000 rpm'. *Tribology Transactions* **41**(3), pp. 335–340. DOI: 10.1080/10402009808983756.

Deraemaeker, A., H. Nasser, A. Benjeddou and A. Preumont (2009). 'Mixing Rules for the Piezoelectric Properties of Macro Fiber Composites'. *Journal of Intelligent Material Systems and Structures* **20**(12), pp. 1475–1482. DOI: 10.1177/1045389X09335615.

Edberg, D., A. Bicos, C. Fuller, J. Tracy and J. Fechter (1992). 'Theoretical and Experimental Studies of a Truss Incorporating Active Members'. *Journal of Intelligent Material Systems and Structures* **3**(2), pp. 333–347. DOI: 10.1177/1045389X9200300209.

Ertas, B., M. Drexel, J. Van Dam and D. Hallman (2009a). 'A General Purpose Test Facility for Evaluating Gas Lubricated Journal Bearings'. *Journal of Engineering for Gas Turbines and Power* **131**(2), p. 022502. DOI: 10.1115/1.2979004.

Ertas, B., H. Luo and D. Hallman (2009b). 'Dynamic Characteristics of Shape Memory Alloy Metal Mesh Dampers'. *50th AIAA/ASME/ASCE/AHS/ASC Structures, Structural Dynamics, and Materials Conference*. May. Reston, Virigina: American Institute of Aeronautics and Astronautics, pp. 1–8. DOI: 10.2514/6.2009-2521.

Ertas, B. H. (2009). 'Compliant Hybrid Journal Bearings Using Integral Wire Mesh Dampers'. *Journal of Engineering for Gas Turbines and Power* **131**(2), p. 022503. DOI: 10.1115/1.2967476.

Ertas, B. H., M. Camatti and G. Mariotti (2010). 'Synchronous Response to Rotor Imbalance Using a Damped Gas Bearing'. *Journal of Engineering for Gas Turbines and Power* **132**(3), p. 032501. DOI: 10.1115/1.3157097.

Glienicke, J. (1966). 'Experimental Investigation of the Stiffness and Damping Coefficients of Turbine Bearings and Their Application to Instability Prediction'. *Proceedings of the Institution of Mechanical Engineers, Conference Proceedings* **181**(2), pp. 116–129. DOI: 10.1243/PIME_CONF_1966_181_038_02.

Grathwol, N. (2015). 'Load Capacity and Stability Limit for a Circular Gas Bearing - Theory and Experiment'. Master Thesis. Technical University of Denmark, p. 56.

Guennam, A. E. and B. M. Luccioni (2006). 'FE modeling of a closed box beam with piezoelectric fiber composite patches'. *Smart Materials and Structures* **15**(6), pp. 1605–1615. DOI: 10.1088/0964-1726/15/6/012.

Guennam, A. E. and B. M. Luccioni (2009). 'Piezoelectric shell FE for the static and dynamic analysis of piezoelectric fibre composite laminates'. *Smart Materials and Structures* **18**(9), p. 095044. DOI: 10.1088/0964-1726/18/9/095044.

Guyan, R. J. (1965). 'Reduction of stiffness and mass matrices'. *AIAA Journal* **3**(2), pp. 380–380. DOI: 10.2514/3.2874.

Hagood, N. W. and A. A. Bent (1993). 'Development of Piezoelectric Fiber Composites for Structural Actuation'. *34th AIAA/ASME/ASCE/AHS/ASC Structures, Structural Dynamics, and Materials Conference*. AIAA, pp. 3625–3638.

Hagood, N. W., R. Kindel, K. Ghandi and P. Gaudenzi (1993). 'Improving Transverse Actuation of Piezoceramics Using Interdigitated Surface Electrodes'. *SPIE Smart Structures and Intelligent Systems*. Vol. 1917, pp. 341–352. DOI: 10.1117/12.152766.

Hagood, N. and A. von Flotow (1991). 'Damping of structural vibrations with piezoelectric materials and passive electrical networks'. *Journal of Sound and Vibration* **146**(2), pp. 243–268. DOI: 10.1016/0022-460X(91)90762-9.

Harrison, W. J. (1913). 'The Hydrodynamical Theory of Lubrication With Special Reference to Air as a Lubricant'. *Transactions Cambridge Philosophical Society* **22**, pp. 37–54.

Haugaard, A. M. (2010). *On Controllable Elastohydrodynamic Fluid Film Bearings*. Kgs. Lyngby, Denmark: Technical University of Denmark, p. 178.

Heshmat, H. (1994). 'Advancements in the performance of aerodynamic foil journal bearings: high speed and load capability'. *ASME Journal of Tribology* **116**(April), pp. 287–294.

Heshmat, H. and C.-P. R. Ku (1994). 'Structural Damping of Self-Acting Compliant Foil Journal Bearings'. *Journal of Tribology* **116**(January), pp. 76–82.

Heshmat, H., W. Shapiro and S. Gray (1982). 'Development of Foil Journal Bearings for High Load Capacity and High Speed Whirl Stability'. *Journal of Lubrication Technology* **104**(2), pp. 149–156. DOI: 10.1115/1.3253173.

Heshmat, H., J. A. Walowit and O. Pinkus (1983a). 'Analysis of Gas Lubricated Compliant Thrust Bearings'. *Journal of Lubrication Technology* **105**(4), p. 638. DOI: 10.1115/1.3254696.

Heshmat, H., J. A. Walowit and O. Pinkus (1983b). 'Analysis of Gas-Lubricated Foil Journal Bearings'. *Journal of Lubrication Technology* **105**(4), p. 647. DOI: 10.1115/1.3254697.

Hoffmann, R., T. Pronobis and R. Liebich (2015a). 'Non-linear Stability Analysis of a Modified Gas Foil Bearing Structure'. *Mechanisms and Machine Science* **21**, pp. 1259–1276. DOI: 10.1007/978-3-319-06590-8_103.

Hoffmann, R., T. Pronobis and R. Liebich (2015b). 'Non-linear Stability Analysis of a Modified Gas Foil Bearing Structure'. *SIRM 2015 – 11th International Conference on Vibrations in Rotating Machines*. Magdeburg, Deutschland.

Hollkamp, J. J. (1994). 'Multimodal Passive Vibration Suppression with Piezoelectric Materials and Resonant Shunts'. *Journal of Intelligent Material Systems and Structures* **5**(1), pp. 49–57. DOI: 10.1177/1045389X9400500106.

Horikawa, O., K. Sato and A. Shimokohbe (1992). 'An active air journal bearing'. *Nanotechnology* **3**(2), pp. 84–90. DOI: 10.1088/0957-4484/3/2/006.

Horikawa, O., K. Yasuhara, H. Osada and A. Shimokohbe (1989). 'Dynamic stiffness control of active air bearing'. *Journal of the Japan Society for Precision Engineering* **55**(3), pp. 569–574. DOI: 10.2493/jjspe.55.569.

Howard, S. A. (2009). 'Misalignment in Gas Foil Journal Bearings: An Experimental Study'. *Journal of Engineering for Gas Turbines and Power* **131**(2), p. 022501. DOI: 10.1115/1.2966392.

Kapuria, S. and P. Hagedorn (2007). 'Unified efficient layerwise theory for smart beams with segmented extension/shear mode, piezoelectric actuators and sensors'. *Journal of Mechanics of Materials and Structures* **2**(7), pp. 1267–1298. DOI: 10.2140/jomms.2007.2.1267.

Kim, D. (2007). 'Parametric Studies on Static and Dynamic Performance of Air Foil Bearings with Different Top Foil Geometries and Bump Stiffness Distributions'. *ASME Journal of Tribology* **129**(2), pp. 354–364. DOI: 10.1115/1.2540065.

Kim, T. H. and L. San Andrés (2008). 'Heavily Loaded Gas Foil Bearings: A Model Anchored to Test Data'. *ASME Journal of Engineering for Gas Turbines and Power* **130**(1), pp. 012504–1–8. DOI: 10.1115/1.2770494.

Kim, T. H. and L. San Andrés (2009). 'Effect of Side Feed Pressurization on the Dynamic Performance of Gas Foil Bearings: A Model Anchored to Test Data'. *ASME Journal of Engineering for Gas Turbines and Power* **131**(1), p. 012501. DOI: 10.1115/1.2966421.

Ku, C.-P. R. (1994). 'Dynamic Structural Properties of Compliant Foil Thrust Bearings—Comparison Between Experimental and Theoretical Results'. *Journal of Tribology* **116**(1), p. 70. DOI: 10.1115/1.2927049.

Larsen, J. S. (2015). 'Nonlinear Analysis of Rotors Supported by Air Foil Journal Bearings – Theory & Experiments'. PhD thesis. Kgs. Lyngby, Denmark: Technical University of Denmark, p. 105.

Larsen, J. S., A. J. T. Hansen and I. F. Santos (2015a). 'Experimental and theoretical analysis of a rigid rotor supported by air foil bearings'. *Mechanics & Industry* **16**(1), pp. 106–118. DOI: 10.1051/meca/2014066.

Larsen, J. S., B. B. Nielsen and I. F. Santos (2015b). 'On the Numerical Simulation of Nonlinear Transient Behavior of Compliant Air Foil Bearings'. *SIRM 2015 – 11th International Conference on Vibrations in Rotating Machines*. February. Magdeburg, Germany, Paper–ID 39.

Larsen, J. S. and I. F. Santos (2014). 'Efficient solution of the non-linear Reynolds equation for compressible fluid using the finite element method'. *Journal of the Brazilian Society of Mechanical Sciences and Engineering* **37**. DOI: 10.1007/s40430-014-0220-5.

Larsen, J. S. and I. F. Santos (2015). 'On the nonlinear steady-state response of rigid rotors supported by air foil bearings - Theory and experiments'. *Journal of Sound and Vibration* **346**, pp. 284–297. DOI: 10.1016/j.jsv.2015.02.017.

Larsen, J. S., I. F. Santos and S. von Osmanski (2016). 'Stability of rigid rotors supported by air foil bearings: Comparison of two fundamental approaches'. *Journal of Sound and Vibration*. DOI: 10.1016/j.jsv.2016.06.022.

Larsen, J. S., A. C. Varela and I. F. Santos (2014). 'Numerical and experimental investigation of bump foil mechanical behaviour'. *Tribology International* **74**, pp. 46–56. DOI: 10.1016/j.triboint.2014.02.004.

Larsen, J. S. and I. F. Santos (2013). 'Compliant Foil Journal Bearings - Investigation of Dynamic Properties'. *SIRM 2013 – 10th International Conference on Vibrations in Rotating Machines*. February. Berlin, Deutschland, pp. 1–12.

Le Lez, S., M. Arghir and J. Frêne (2009). 'Nonlinear Numerical Prediction of Gas Foil Bearing Stability and Unbalanced Response'. *Journal of Engineering for Gas Turbines and Power* **131**(1), p. 012503. DOI: 10.1115/1.2967481.

Lee, D.-H., Y.-C. Kim and K.-W. Kim (2009). 'The Dynamic Performance Analysis of Foil Journal Bearings Considering Coulomb Friction: Rotating Unbalance Response'. *Tribology Transactions* **52**(2), pp. 146–156. DOI: 10.1080/10402000802192685.

Lee, Y. B., C. H. Kim, N. S. Lee and T. H. Kim (2003). 'Smart Foil Journal Bearing with Piezoelectric Actuators'. US Patent No US 6,582,125 B1.

Lee, Y.-B., D.-J. Park, C.-H. Kim and S.-J. Kim (2008). 'Operating characteristics of the bump foil journal bearings with top foil bending phenomenon and correlation among bump foils'. *Tribology International* **41**(4), pp. 221–233. DOI: 10.1016/j.triboint.2007.07.003.

Lund, J. W. (1968). 'Calculation of Stiffness and Damping Properties of Gas Bearings'. *Journal of Lubrication Technology* **90**(4), pp. 793–803. DOI: 10.1115/1.3601723.

Lund, J. (1964). 'Spring and damping coefficients for the tilting-pad journal bearing'. *ASLE transactions* **7**, pp. 342–352.

Ma, Y., Q. Zhang, D. Zhang, F. Scarpa, B. Liu and J. Hong (2015). 'Tuning the vibration of a rotor with shape memory alloy metal rubber supports'. *Journal of Sound and Vibration* **351**, pp. 1–16. DOI: 10.1016/j.jsv.2015.04.005.

Matta, P. and M. Arghir (2012). 'Identification method for rotordynamic coefficients of cylindrical air bearing using an impact hammer'. *Proceedings of the Institution of Mechanical Engineers, Part J: Journal of Engineering Tribology* **226**(3), pp. 199–212. DOI: 10.1177/1350650111427508.

Matta, P, M. Arghir and O. Bonneau (2010). 'Experimental Analysis of Cylindrical Air-Bearing Dynamic Coefficients'. *Tribology Transactions* **53**(3), pp. 329–339. DOI: 10.1080/10402000903283318.

Mizumoto, H., S. Arii, Y. Kami, K. Goto, T. Yamamoto and M. Kawamoto (1996). 'Active inherent restrictor for air-bearing spindles'. *Precision Engineering* **19**(2-3), pp. 141–147.

Mizumoto, H., S. Arii, Y. Yabuta, Y. Tazoe and S. Yoshito (2010). 'Vibration control of a high-speed air-bearing spindle using an active aerodynamic bearing'. *International Conference on Control, Automation and Systems*. Vol. 2. Gyeonggi-do, Korea, pp. 2261–2264.

Morosi, S. (2011). 'From Hybrid to Actively-Controlled Gas Lubricated Bearings – Theory and Experiment'. Ph.D. Thesis. Technical University of Denmark, p. 249.

Morosi, S. and I. F. Santos (2012). 'Experimental Investigations of Active Air Bearings'. *ASME Turbo Expo 2012*. Copenhagen, Denmark, pp. 1–10.

Nasser, H., F. Biscani and S. Belouettar (2011). 'Effect of Matrix Properties on the Overall Piezoelectric Constants of Piezocomposite Transducers'. *Mechanics of Advanced Materials and Structures* **18**(7), pp. 531–539. DOI: 10.1080/15376494.2011.605011.

Nasser, H., A. Deraemaeker and S. Belouettar (2008). 'Electric Field Distribution in Macro Fiber Composite Using Interdigitated Electrodes'. *Advanced Materials Research* **47-50**, pp. 1173–1177. DOI: 10.4028/www.scientific.net/AMR.47-50.1173.

Nguyen, C.-H. and X. Kornmann (2006). 'A Comparison of Dynamic Piezoactuation of Fiber-based Actuators and Conventional PZT Patches'. *Journal of Intelligent Material Systems and Structures* **17**(1), pp. 45–55. DOI: 10.1177/1045389X06056065.

Nielsen, M. S. (2016). 'Smart Materials Applied to Control Gas Bearing Dynamics'. Master thesis. Technical University of Denmark, p. 236.

Panda, S. and R. Natarajan (1981). 'Analysis of laminated composite shell structures by finite element method'. *Computers & Structures* **14**(3-4), pp. 225–230. DOI: 10.1016/0045-7949(81)90008-0.

Park, J.-S. and J.-H. Kim (2005). 'Analytical development of single crystal Macro Fiber Composite actuators for active twist rotor blades'. *Smart Materials and Structures* **14**(4), pp. 745–753. DOI: 10.1088/0964-1726/14/4/033.

Paulsen, B. T., S. Morosi and I. F. Santos (2011). 'Static, Dynamic, and Thermal Properties of Compressible Fluid Film Journal Bearings'. *Tribology Transactions* **54**(2), pp. 282–299. DOI: 10.1080/10402004.2010.538490.

Peng, J. P. and M. Carpino (1993). 'Calculation of Stiffness and Damping Coefficients for Elastically Supported Gas Foil Bearings'. *ASME Journal of Tribology* **115**(January), pp. 21–27.

Pham, H. M. and P. Bonello (2013). 'Efficient Techniques for the Computation of the Nonlinear Dynamics of a Foil-Air Bearing Rotor System'. *Proceedings of ASME Turbo Expo 2013: Turbine Technical Conference and Exposition*. San Antonio, Texas, USA: ASME, GT2013–94389. DOI: 10.1115/GT2013-94389.

Pierart, F. G. (2016). 'Model-Based Control Design for Flexible Rotors Supported by Active Gas Bearings - Theory & Experiment'. PhD Thesis. Technical University of Denmark.

Pierart, F. G. and I. F. Santos (2015). 'Steady state characteristics of an adjustable hybrid gas bearing - Computational fluid dynamics, modified Reynolds equation and experimental validation'. *Proceedings of the Institution of Mechanical Engineers, Part J: Journal of Engineering Tribology* **229**(7), pp. 807–822. DOI: 10.1177/1350650115570404.

Pipeleers, G., B. Demeulenaere, F. Al-Bender, J. De Schutter and J. Swevers (2009). 'Optimal Performance Tradeoffs in Repetitive Control: Experimental Validation on an Active Air Bearing Setup'. *IEEE Transactions on Control Systems Technology* **17**(4), pp. 970–979. DOI: 10.1109/TCST.2009.2014358.

Qiu, J., J. Tani and T. Kwon (2003). 'Control of Self-Excited Vibration of a Rotor System With Active Gas Bearings'. *Journal of Vibration and Acoustics* **125**(3), p. 328. DOI: 10.1115/1.1576423.

Reynolds, O. (1886). 'On the Theory of Lubrication and its Application to Mr. Beauchamp Tower's Experments, including an Experimental Determination of the Viscosity of Olive Oil'. *Philosophical Transactions of the Royal Society of London* **177**, pp. 157–234.

Rudloff, L., M. Arghir, O. Bonneau, S. Guingo, G. Chemla and E. Renard (2012). 'Experimental Analysis of the Dynamic Characteristics of a Hybrid Aerostatic Bearing'. *ASME Journal of Engineering for Gas Turbines and Power* **134**(8), p. 082503. DOI: 10.1115/1.4006060.

Ruscitto, D., J. Mc Cormick and S. Gray (1978). *Hydrodynamic Air Lubricated Compliant Surface Bearing for an Automotive Gas Turbine Engine I - Journal Bearing Performance*. Tech. rep. Cleveland, Ohio 44135: National Aeronautics and Space Administration, Lewis Research Center, p. 136. DOI: 10.2172/6793795.

Rylander, H. G., M. J. T. Carlson and C. R. Lin (1995). 'Actively Controlled Bearing Surface Profiles Theory and Experiments'. *Tribology Symposium ASME* **72**. Ed. by H. Masudi, pp. 11–14.

Salazar, J. G. and I. F. Santos (2015). 'Feedback-controlled lubrication for reducing the lateral vibration of flexible rotors supported by tilting-pad journal bearings'. *Proceedings of the Institution of Mechanical Engineers, Part J: Journal of Engineering Tribology* **229**(10), pp. 1264–1275. DOI: 10.1177/1350650115577027.

Samanta, B., M. C. Ray and R. Bhattacharyya (1996). 'Finite element model for active control of intelligent structures'. *AIAA Journal* **34**(9), pp. 1885–1893. DOI: 10.2514/3.13322.

San Andrés, L. and T. A. Chirathadam (2013). 'Performance Characteristics of Metal Mesh Foil Bearings: Predictions Versus Measurements'. *Journal of Engineering for Gas Turbines and Power* **135**(12), pp. 122503–1–8. DOI: 10.1115/1.4025146.

San Andrés, L., T. A. Chirathadam and T.-H. Kim (2010a). 'Measurement of Structural Stiffness and Damping Coefficients in a Metal Mesh Foil Bearing'. *Journal of Engineering for Gas Turbines and Power* **132**(3), p. 032503. DOI: 10.1115/1.3159379.

San Andrés, L. and T. H. Kim (2007). 'Improvements To The Analysis of Gas Foil Bearings: Intergration of Top Foil 1D and 2D Structural Models'. *ASME Turbo Expo 2007: Power for Land, Sea and Air*. Montreal, Canada, pp. 779–789. DOI: 10.1115/GT2007-27249.

San Andrés, L. and T. H. Kim (2009). 'Analysis of gas foil bearings integrating FE top foil models'. *Tribology International* **42**(1), pp. 111–120. DOI: 10.1016/j.triboint.2008.05.003.

San Andrés, L. and J. Norsworthy (2015). 'Structural and Rotordynamic Force Coefficients of a Shimmed Bump Foil Bearing: An Assessment of a Simple Engineering Practice'. *Journal of Engineering for Gas Turbines and Power* **138**(1), pp. 012505–1–8. DOI: 10.1115/1.4031238.

San Andrés, L., M. Rohmer and S. Park (2015). 'Failure of a Test Rig Operating With Pressurized Gas Bearings: A Lesson on Humility'. *Proceedings of ASME Turbo Expo 2015: Turbine Technical Conference and Exposition*. Montréal, Canada: ASME, GT–2015–42556. DOI: DOI:.

San Andrés, L., D. Rubio and T. H. Kim (2007). 'Rotordynamic Performance of a Rotor Supported on Bump Type Foil Gas Bearings: Experiments and Predictions'. *Journal of Engineering for Gas Turbines and Power* **129**(3), pp. 850–857. DOI: 10.1115/1.2718233.

San Andrés, L. and T. A. Chirathadam (2011). 'Metal Mesh Foil Bearing: Effect of Motion Amplitude, Rotor Speed, Static Load, and Excitation Frequency on Force Coefficients'. *Journal of Engineering for Gas Turbines and Power* **133**(12), p. 122503. DOI: 10.1115/1.4004112.

San Andrés, L., T. A. Chirathadam, K. Ryu and T. H. Kim (2010b). 'Measurements of Drag Torque, Lift-Off Journal Speed, and Temperature in a Metal Mesh Foil Bearing'. *Journal of Engineering for Gas Turbines and Power* **132**(11), p. 112503. DOI: 10.1115/1.4000863.

San Andrés, L. and K. Ryu (2008). 'Hybrid Gas Bearings With Controlled Supply Pressure to Eliminate Rotor Vibrations While Crossing System Critical Speeds'. *Journal of Engineering for Gas Turbines and Power* **130**(6), p. 062505. DOI: 10.1115/1.2966391.

Santos, I. F. (1995). 'On the adjusting of the dynamic coefficients of tilting-pad journal bearings'. *Tribology transactions* **38**(3), pp. 700–706.

Santos, I. F. (2010). 'Mechatronics Applied to Machine Elements with Focus on Active Control of Bearing, Shaft and Blade Dynamics'. Doctor thesis. Technical University of Denmark, pp. 1–95.

Santos, I. F. and F. H. Russo (1998). 'Tilting-pad journal bearings with electronic radial oil injection'. *ASME Journal of Tribology* **120**(July), pp. 583–594.

Selmane, A. and A. A. Lakis (1997). 'Influence of Geometric Non-Linearities on the Free Vibrations of Orthotropic Open Cylindrical Shells'. *International Journal for Numerical Methods in Engineering* **40**(6), pp. 1115–1137. DOI: 10.1002/(SICI)1097-0207(19970330)40:6<1115::AID-NME105>3.0.CO;2-H.

Shimokohbe, A., O. Horikawa, K. Sato and H. Sato (1991). 'An Active Air Journal Bearing with Ultraprecision, Infinite Static Stiffness, High Damping Capability and New Functions'. *CIRP Annals - Manufacturing Technology* **40**(1), pp. 563–566. DOI: 10.1016/S0007-8506(07)62054-X.

Song, J.-H. and D. Kim (2007). 'Foil Gas Bearing With Compression Springs: Analyses and Experiments'. *ASME Journal of Tribology* **129**(3), pp. 628–639. DOI: 10.1115/1.2736455.

Suleman, A. and V. B. Venkayya (1995). 'A Simple Finite Element Formulation for a Laminated Composite Plate with Piezoelectric Layers'. *Journal of Intelligent Material Systems and Structures* **6**(November), pp. 776–782.

Sun, L. and J. M. Krodkiewski (2000). 'Experimental Investigation of Dynamic Properties of an Active Journal Bearing'. *Journal of Sound and Vibration* **230**(5), pp. 1103–1117. DOI: `10.1006/jsvi.1999.2671`.

Talukder, H. and T. Stowell (2003). 'Pneumatic hammer in an externally pressurized orifice-compensated air journal bearing'. *Tribology International* **36**(8), pp. 585–591. DOI: `10.1016/S0301-679X(02)00247-5`.

Temis, Y. M., M. Y. Temis and A. B. Meshcheryakov (2011). 'Gas-dynamic foil bearing model'. *Journal of Friction and Wear* **32**(3), pp. 212–220. DOI: `10.3103/S1068366611030111`.

Theisen, L. R. S., H. H. Niemann, I. F. Santos, R. Galeazzi and M. Blanke (2016). 'Modelling and identification for control of gas bearings'. *Mechanical Systems and Signal Processing* **70-71**, pp. 1150–1170. DOI: `10.1016/j.ymssp.2015.09.016`.

Thurston, E. G. (1953). 'The Theoretical Sensitivity of Three Types of Rectangular Bimorph Transducers'. *The Journal of the Acoustical Society of America* **25**(4), p. 828. DOI: `10.1121/1.1917696`.

Tiersten, H. F. (1969). *Linear Piezoelectric Plate Vibrations*. New York: Plenum Press, p. 212.

Trindade, M. A., A. Benjeddou and R. Ohayon (2001). 'Finite element modelling of hybrid active-passive vibration damping of multilayer piezoelectric sandwich beams - part I : Formulation'. *International Journal for Numerical Methods in Engineering* **51**, pp. 835–854.

Tzou, H. S. and M. Gadre (1989). 'Theoretical analysis of a multi-layered thin shell coupled with piezoelectric shell actuators for distributed vibration controls'. *Journal of Sound and Vibration* **132**(3), pp. 433–450. DOI: `10.1016/0022-460X(89)90637-8`.

Tzou, H. S. and C. I. Tseng (1991). 'Distributed Modal Identification and Vibration Control of Continua: Piezoelectric Finite Element Formulation and Analysis'. *Journal of Dynamic Systems, Measurement, and Control* **113**(3), p. 500. DOI: `10.1115/1.2896438`.

Tzou, H. S. and R. Ye (1996). 'Analysis of piezoelastic structures with laminated piezoelectric triangle shell elements'. *AIAA Journal* **34**(1), pp. 110–115. DOI: `10.2514/3.12907`.

Tzou, H. and C. Tseng (1990). 'Distributed piezoelectric sensor/actuator design for dynamic measurement/control of distributed parameter systems: A piezoelectric finite element approach'. *Journal of Sound and Vibration* **138**(1), pp. 17–34. DOI: `10.1016/0022-460X(90)90701-Z`.

Varela, A. C. (2013). 'Mechatronics Applied to Fluid Film Bearings: Towards More Efficient Machinery'. Ph.D. Thesis. Technical University of Denmark, p. 186.

Walowit, J. A. and J. N. Anno (1975). *Modern Developments in Lubrication Mechanics*. London, England: Applied Science Publishers.

Walton II, J. F., H. Heshmat and M. J. Tomaszewski (2007). 'Design and Test Program in the Development of a 100 HP Oil-Free, High-Speed Blower'. *ASME Turbo Expo 2007*. Montreal, Canada, pp. 1–7.

Wu, A., Z. Cai and M. S. de Queiroz (2007). 'Model-Based Control of Active Tilting-Pad Bearings'. *IEEE/ASME Transactions on Mechatronics* **12**(6), pp. 689–695. DOI: `10.1109/TMECH.2007.911636`.

Wu, S.-Y. (1998). 'Method for Multiple Mode Piezoelectric Shunting with Single PZT Transducer for Vibration Control'. *Journal of Intelligent Material Systems and Structures* **9**(12), pp. 991–998. DOI: 10.1177/1045389X9800901204.

Xu, F., Z. Liu, G. Zhang and Z. Cao (2013). 'Effects of shear stiffness in top foil structure on gas foil bearing performance based on thick plate theory'. *Proceedings of the Institution of Mechanical Engineers, Part J: Journal of Engineering Tribology* **227**(7), pp. 761–776. DOI: 10.1177/1350650112468071.

Xu, F., Z. Liu, G. Zhang and L. Xie (2011). 'Hydrodynamic Analysis of Compliant Foil Bearings with Modified Top Foil Model'. *Proceedings of ASME Turbo Expo 2011*. Vancouver, British Columbia, Canada, GT2011–46018. DOI: 10.1115/GT2011-46018.

Yasin, M. Y. and S. Kapuria (2013). 'An efficient finite element with layerwise mechanics for smart piezoelectric composite and sandwich shallow shells'. *Computational Mechanics* **53**(1), pp. 101–124. DOI: 10.1007/s00466-013-0896-x.

Yu, H., C. Shuangtao, C. Rugang, Z. Qiaoyu and Z. Hongli (2011). 'Numerical study on foil journal bearings with protuberant foil structure'. *Tribology International* **44**(9), pp. 1061–1070. DOI: 10.1016/j.triboint.2011.04.015.

Appendix A

Theory from publication P1 with the nomenclature used in the thesis

The nomenclature used in the thesis and in publication P1 is the same. The change was done in order to streamline nomenclature used for the different domains of the PAFB. This makes comparison between the thesis and publication P1 difficault, hence the mathematical model presented in publication P1 have been reprinted below utilizing the nomenclature used in the thesis.

The appendices referred to in the reprinted text, is those of publication P1

A.1   Mathematical Model

A layered shell containing one or more layers of piezoelectric fiber patches must be regarded as a electro-mechanical system in order to take the piezoelectric coupling effects into account. In the derivation of a mathematical model, Lagrange equation (A.1) is used.

$$\frac{\partial}{\partial t}\left(\frac{\partial L}{\partial \dot{q}_i}\right) - \frac{\partial L}{\partial q_i} = F_i \tag{A.1}$$

This requires the Lagrangian to be discrestized, which is done by shape functions and the nodal degrees of freedom used in the FEM formulation. The Lagrangian for a electro-mechanical system is given by the kinetic energy minus the potential energy.

$$L = T - H$$

The Continuous System

The potential energy is calculated based on the constitutive equation. The potential energy used in the Lagrangian depends on which variables are dependent and independent. In the constitutive equation (3.9) for the electro-mechanical system, mechanical strain $\{\varepsilon\}$ and electric displacement $\{D\}$ are the extensive properties, while

the mechanical stress $\{\sigma\}$ and the electrical field $\{E\}$ are the intensive properties. The infinitesimal change of the internal energy of a system is given by a infinitesimal change in the extensive properties, hence mechanical strain and electrical displacement as seen in equation (A.2a), but since the independent variables required for the FEM model is mechanical strain and electrical field a Legendre transformation of the internal energy is done leading to infinitesimal change of the enthalpy, which depends on the required variables as shown in equation (A.2b).

$$\delta U = \{\sigma\}^{\mathrm{T}} \delta \{\varepsilon\} + \{E\}^{\mathrm{T}} \delta \{D\} \tag{A.2a}$$

$$\delta H = \{\sigma\}^{\mathrm{T}} \delta \{\varepsilon\} - \{D\}^{\mathrm{T}} \delta \{E\} \tag{A.2b}$$

The Legendre transformation from the internal energy to the enthalpy is

$$H = U - \{E\}^{\mathrm{T}} \{D\} \tag{A.3}$$

The constitutive equation required by the enthalpy is given in equation (A.4), in which the mechanical stress and electrical displacement are the dependent variables and the mechanical strain and electrical field are the independent variables.

$$\{\sigma\} = [C]\{\varepsilon\} - [e]^{\mathrm{T}}\{E\} \tag{A.4a}$$

$$\{D\} = [e]\{\varepsilon\} + [\eta]\{E\} \tag{A.4b}$$

The structural stiffness $[C]$, inverse piezoelectric constant $[e]$ and electric permittivity $[\eta]$ matrices are given in the appendix.

The energies required to calculate the Lagrangian are

$$T = \frac{1}{2}\int \rho\,\{\dot{u}_{\mathrm{t}}\}^{\mathrm{T}}\{\dot{u}_{\mathrm{t}}\}\,dV \tag{A.5a}$$

$$H = \frac{1}{2}\int \Big[\,\{\varepsilon\}^{\mathrm{T}}[C]\{\varepsilon\} - 4\{E\}^{\mathrm{T}}[e]\{\varepsilon\} - \{E\}^{\mathrm{T}}[\eta]\{E\}\,\Big]dV \tag{A.5b}$$

The electromechanical system is assumed to be electrostatic. For details in the derivation of the enthalpy see appendix. In FEM models it is custom to use displacement u and electrical potential ϕ as the independent variables rather than mechanical strain and electrical field. Equation (A.6) shows the relationship between mechanical strain and displacement as well as the relationship between electric field and electric potential.

$$\{\varepsilon\} = [\partial]\{u_{\mathrm{t}}\} \tag{A.6a}$$

$$\{E\} = -\{\nabla\}\phi_{\mathrm{t}} \tag{A.6b}$$

The differential operators are given in appendix.

The Lagrangian for the continuous system given in equation (A.7) is a function of the displacement, time derivative of the deflection (velocity) and electrical potential.

$$L = \frac{1}{2}\int \Big[\rho\,\{\dot{u}_{\mathrm{t}}\}^{\mathrm{T}}\{\dot{u}_{\mathrm{t}}\} - ([\partial]\{u_{\mathrm{t}}\})^{\mathrm{T}}[C][\partial]\{u_{\mathrm{t}}\}$$
$$-4(\{\nabla\}\phi_{\mathrm{t}})^{\mathrm{T}}[e][\partial]\{u_{\mathrm{t}}\} + (\{\nabla\}\phi_{\mathrm{t}})^{\mathrm{T}}[\eta]\{\nabla\}\phi_{\mathrm{t}}\Big]dV \tag{A.7}$$

The Discretized System

The Lagrangian for the continuous system (A.7) must be given by generalised coordinates before it can be used in the Lagrange Equation (A.1). The continuous degrees of freedom are discretized by separation of variables and given in equation (A.8). The separated variables are the nodal variables $\{u_{t,\,e}\}$ and $\{\phi_e\}$ and known shape functions $\left[N_{t,\,u}\right]$ and $\left[N_{t,\,\phi}\right]$.

$$\{u_t(t,x,y,z)\} = \left[N_{t,\,u}(x,y,z)\right]\{u_{t,e}(t)\} \tag{A.8a}$$

$$\phi(t,x,y) = \{N_{t,\,\phi}(x,y)\}\{\phi_{t,\,e}(t)\} \tag{A.8b}$$

The differential operators used in the calculation of the mechanical strain and electrical field in equation (A.6) are spacial derivatives, hence only the shape functions are affected. Derivative matrices are set up for differentiated shape functions as given by

$$\left[B_{t,\,u}\right] = [\partial]\left[N_{t,\,u}\right] \tag{A.9a}$$

$$\left[B_{t,\,\phi}\right] = \{\nabla\}\left[N_{t,\,\phi}\right] \tag{A.9b}$$

When the nodal degrees of freedom equation (A.8) and derivative matrices equation (A.9) are introduced in the continuous Lagrangian (A.7) ones obtains

$$
\begin{aligned}
L = \frac{1}{2}\int\Big[& \overbrace{\rho\left(\left[N_{t,\,u}\right]\{\dot{u}_{t,\,e}\}\right)^{\mathrm{T}}\left[N_{t,\,u}\right]\{\dot{u}_{t,\,e}\}}^{\text{Term: I}} \\
& -\overbrace{\left(\left[B_{t,\,u}\right]\{u_{t,\,e}\}\right)^{\mathrm{T}}[C]\left[B_{t,\,u}\right]\{u_{t,\,e}\}}^{\text{Term: II}} \\
& -4\underbrace{\left(\left[B_{t,\,\phi}\right]\{\phi_{t,\,e}\}\right)^{\mathrm{T}}[e]\left[B_{t,\,u}\right]\{u_{t,\,e}\}}_{\text{Term: III}} \\
& +\underbrace{\left(\left[B_{t,\,\phi}\right]\{\phi_{t,\,e}\}\right)^{\mathrm{T}}[\eta]\left[B_{t,\,\phi}\right]\{\phi_{t,\,e}\}}_{\text{Term: IV}}\Big]dV
\end{aligned}
\tag{A.10}
$$

the discrete version of the Lagrangian given in generalized coordinates.

The Governing Equation for the Electro-Mechanical System

Calculating the weak form of the governing equation (A.11) via Lagrange equation (A.1) and the descretized Lagrangian (A.10) requires differentiation with respect to the two generalized coordinate types, i.e. the deflection and electrical potential, and the time derivatives of these. These calculation is given in appendix. The governing equation is
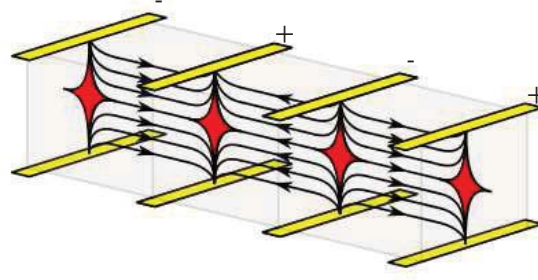
Figure A.1: Sketch of the IDE (yellow bars) electric field (black lines with arrows) and the dead zone in between to equipotential electrode fingers (red areas). A set of electrode fingers above and below each other are equipotential, and a dead zone exists along these fingers.

$$\int_V \Big[\overbrace{\rho \, [N_{\mathrm{t},\,e}]^{\mathrm{T}} [N_{\mathrm{t},\,e}]}^{\text{Part: I}} \{\ddot{u}_{\mathrm{t},\,e}\}$$
$$+ \overbrace{[B_{\mathrm{t},\,\mathrm{u}}]^{\mathrm{T}} [C] [B_{\mathrm{t},\,\mathrm{u}}]}^{\text{Part: II}} \{u_{\mathrm{t},\,e}\} + \overbrace{2 \left([B_{\mathrm{t},\,\phi}]^{\mathrm{T}} [e] [B_{\mathrm{t},\,\mathrm{u}}] \right)_{\mathrm{T}}}^{\text{Part: III}} \{\phi_{\mathrm{t},\,e}\} \tag{A.11}$$
$$+ \underbrace{2 [B_{\mathrm{t},\,\phi}]^{\mathrm{T}} [e] [B_{\mathrm{t},\,\mathrm{u}}]}_{\text{Part: IV}} \{u_{\mathrm{t},\,e}\} - \underbrace{[B_{\mathrm{t},\,\phi}]^{\mathrm{T}} [\eta] [B_{\mathrm{t},\,\phi}]}_{\text{Part: V}} \{\phi_{\mathrm{t},\,e}\} \Big] dV = \{F\}$$

The Electrical Field Created by the Interdigitated Electrodes

So far, the derivation has been kept general, hence no restrictions have been introduced for the shape or geometry of the electro-mechanical system. In order to include the external electric field in the piezoelectric fiber due to the electrodes (see figure 2a in publication P1) the electric field variable $\{E\}$ must be expanded and rewritten. The electrical field created by an electrical potential difference between the electrodes is added via superposition to the existing electrical field within the fibers, hence the total electrical field is given by

$$\{E\} = -(\{\nabla\} \, \phi_{\mathrm{t}} + \{E_{\mathrm{e}}\}) \tag{A.12}$$

IDEs have dead zones between two equipotential electrode fingers in the thickness direction marked with red in figure A.1. These dead zones introduce a challenge for selecting the correct distance between two electrode pairs in the in-plane direction needed for calculating the electric field due to the direction of the electrical field as seen in the same figure (figure A.1). Nasser et al. (2008) gives an analytical expression for the effective electrical field produced by the electric potential difference between the interdigitated electrodes taking the dead zones into account. The correction factor is

$$\kappa_{\mathrm{e}} = \left[1 - \frac{h_{\mathrm{e}}}{\Delta x_{\mathrm{e}}} \left(\frac{1}{2} + \frac{2}{\pi^2} \right) \right] \left[\frac{\Delta x_{\mathrm{e}} - w_{\mathrm{e}}}{\Delta x_{\mathrm{e}} - h_{\mathrm{e}}} \right] \tag{A.13}$$
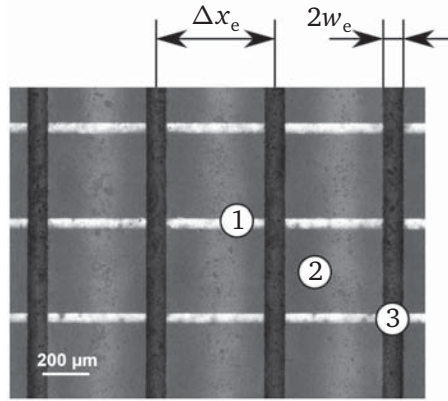
Figure A.2: A photo of the interior of a MFC patch. **1** - isolation (white lines), **2** - piezoelectric fibers (gray areas), **3** - interdigitated electrodes (black lines). The picture is taken with a Olympus GX41 microscope and a Leica DFC450 C camera.

The figure distance between the centreline of two adjacent electrode fingers Δx_e and half the width of an electrode finger w_e are shown in figure A.2.

Each of the two electrodes in a IDE pair has the same electrical potential in the entire electrode and the electrical field created by an IDE is only non-zeros perpendicular to the electrode fingers in accordance with Nasser et al. (2008). In equation (A.14) the electrical field is given via separation of the variables into the derivative matrix $\{B_{t,\,\phi}\}$ depending on spatial coordinates and the electrical potential difference $\Delta\phi_e$ depending on time.

$$\{E_e\} = \{B_{t,\,\phi}\}\,\Delta\phi_e = [T_e] \begin{Bmatrix} 0 \\ 0 \\ \frac{\kappa_e}{\Delta x_e} \end{Bmatrix} \Delta\phi_e \qquad (A.14)$$

There are two important things to note regarding the electrical field of the IDEs. First note; the electrical field created by the IDEs has different direction on each side of an electrode finger as illustrated by the arrows on the electrical field lines seen in figure A.1, but since the manufacture uses the IDEs for polarisation of the piezoelectric fibers the polarisation also has different direction on each side of an electrode finger, hence the electrical field is always aligned with the polarisation. Second note; the third spatial direction of a piezoelectric material is conventionally aligned with the direction of polarisation, which for piezoelectric fibers differs from the convention for plates and shells, where the third spacial direction is the surface normal, hence a coordinate transformation $[T_e]$ is needed to make them compatible as seen in equation (A.14).

The governing equation for the electric-mechanical system (A.11) must include the DoF related to the IDE. Of the equation's five parts, part I and II are kept unchanged, while part III, IV and V are expanded to accommodate the effect IDE. The governing equation, which includes the IDE is

$$
\int_V \Big[\rho \left[N_{t,\,u} \right]^T \left[N_{t,\,u} \right] \{\ddot{u}_e\} + \Big(\left[B_{t,\,u} \right]^T [C] \left[B_{t,\,u} \right]
$$

$$
+ 2 \left[B_{t,\,\phi} \right]^T [e] \left[B_{t,\,u} \right] + 2 \left[B_{t,\,e} \right]^T [e] \left[B_{t,\,u} \right] \Big) \{u_e\}
$$

$$
+ \Big(2 \big(\left[B_{t,\,\phi} \right]^T [e] \left[B_{t,\,u} \right] \big)^T - \left[B_{t,\,\phi} \right]^T [\eta] \left[B_{t,\,\phi} \right] \tag{A.15}
$$

$$
- \left[B_{t,\,e} \right]^T [\eta] \left[B_{t,\,\phi} \right] \Big) \{\phi_t\} + \Big(2 \big(\left[B_{t,\,e} \right]^T [e] \left[B_{t,\,u} \right] \big)^T
$$

$$
- \big(\left[B_{t,\,e} \right]^T [\eta] \left[B_{t,\,\phi} \right] \big)^T - \left[B_{t,\,e} \right]^T [\eta] \left[B_{t,\,e} \right] \Big) \{\Delta \phi_e\} \Big] dV = \{F_{t,\,e}\}
$$

The matrix form of equation (A.15), where the volume integrals are included in the matrix elements, is

$$
\begin{bmatrix} \left[M_{t,\,uu} \right] & [0] & [0] \\ [0]^T & [0] & [0] \\ [0]^T & [0]^T & [0] \end{bmatrix} \begin{Bmatrix} \{\ddot{u}_e\} \\ \{\ddot{\phi}_e\} \\ \{\Delta\ddot{\phi}_e\} \end{Bmatrix}
$$

$$
+ \begin{bmatrix} \left[K_{t,\,uu} \right] & \left[K_{t,\,\phi u} \right] & \left[K_{t,\,eu} \right] \\ \left[K_{t,\,\phi u} \right]^T & \left[K_{t,\,\phi\phi} \right] & \left[K_{t,\,e\phi} \right] \\ \left[K_{t,\,eu} \right]^T & \left[K_{t,\,e\phi} \right]^T & \left[K_{t,\,ee} \right] \end{bmatrix} \begin{Bmatrix} \{u_e\} \\ \{\phi_e\} \\ \{\Delta\phi_e\} \end{Bmatrix} = \begin{Bmatrix} \{F_{t,\,e}\} \\ \{Q_{\phi,\,e}\} \\ \{Q_e\} \end{Bmatrix} \tag{A.16}
$$

The Eight Node Double Curved Isoparametric Element

As base for the new dynamic electro-mechanical element the static eight node double curved layered isoparametric serendipity element presented by Panda and Natarajan (1981) is chosen. A schematic can be seen in the centre of figure A.3(a). The physical double curved layered shell is prescribed by a 2D four sided shell with nodes in each corner and on each side. This eight node shell element follows the geometrical mid plane of the physical shell, with the spacial location of the physical shell given by

$$
\{x_{t,\,u}\} = \sum_{i=1}^{8} N_{t,i} \left(\{x_{t,i}\} + \zeta \frac{h_{t,i}}{2} \{V_{3i}\} \right) \tag{A.17}
$$

The nodal placement is given in global coordinate system, while the thickness is given by the third coordinate direction of the local nodal coordinate system (see figure A.3(a)). The transformation matrices from global to local coordinates are given in appendix.

In the derivation of the governing equation via Lagrange equation the discretization via separation of variables is done with unspecified shape functions and nodal degrees of freedom, see equation (A.8). For the eight node element the shape functions are given in isoparametric coordinates and listed in appendix along with the derivative matrices in appendix. The nodal displacement $\{u_{t,\,e}\}$ has a kinematic relation based on first order shear deformation and is

$$
\{u_{t,\,e}\} = \{u_{t,\,i}\} + \zeta \frac{h_{t,\,i}}{2} [\mu_i] \begin{Bmatrix} \alpha_i \\ \beta_i \end{Bmatrix} \tag{A.18}
$$

(a) Element with local coordinate systems in each node

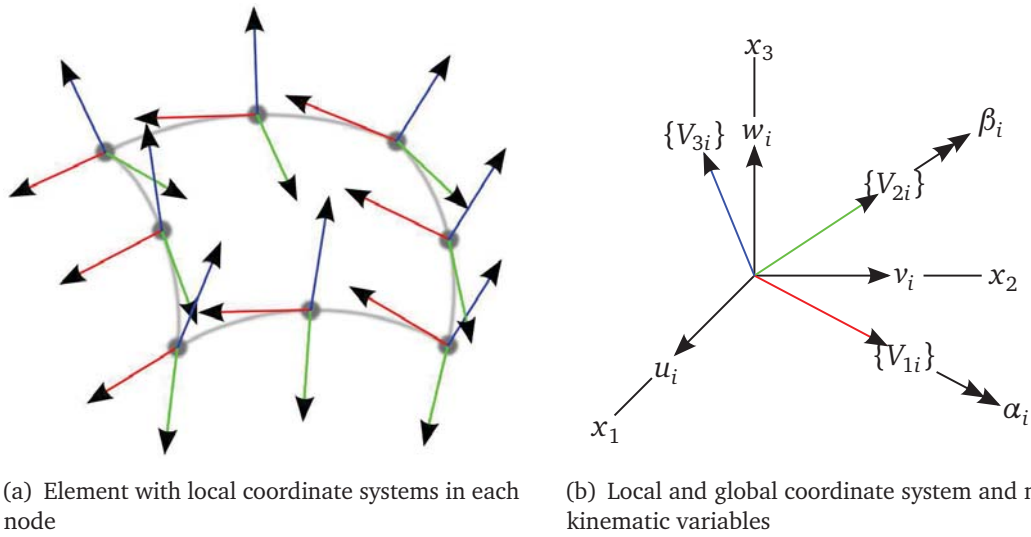(b) Local and global coordinate system and nodal kinematic variables

Figure A.3: 8-node double curved shell element with local coordinates given in each node and the relationship between the local and global coordinates and the kinematic nodal variables.
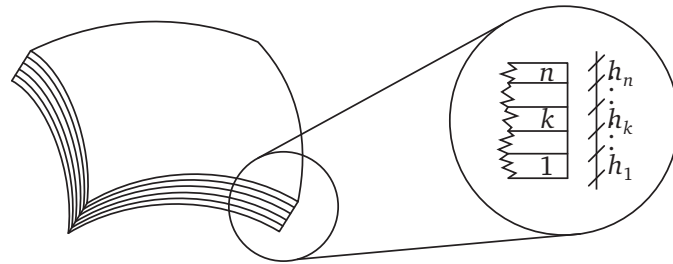

Figure A.4: Layers in the shell with numbering and thicknesses.

The nodal electrical potential, which is the new addition, is divided into an internal nodal electric potential $\{\phi_{t,i}\}$ for each layer, and an external electrical potential difference $\{\Delta\phi_e\}$ for each of the IDE pairs.

For Multi-Layers

For a shell structure with multiple layers the volume integration in the thickness direction must be done individually for each layer as proposed by Panda and Natarajan (1981). This procedure utilizes that the material properties are well known at layer level, hence making the procedure straight forward. The infinitesimal relationship between the isoparametric thickness coordinate ζ of the shell and the layer isoparametric thickness coordinate ζ_k is

$$d\zeta = \frac{h_k}{h_t} d\zeta_k \tag{A.19}$$

where h_k is the thickness of the layer and h_t is the thickness of the shell as shown in figure A.4).

Using this infinitesimal relationship for the Gaussian integration, the mass and stiffness matrices in equation (A.16) are given in equation (A.20) on element level. The matrices for the piezoelectric coupling and electrical relation are given on layer level, i.e. they are not added together. This is due to the assumption of each piezoelectric layer being electrically isolated from the others and having their own electrodes. Therefore their also have own degree of freedom with respect to electrical potential difference. The assumption is valid for MFC due to the isolation on top and bottom (see figure 1.3(b)).

$$\left[M_{\mathrm{t,\,uu},\,e}\right] = \int_{-1}^{1}\int_{-1}^{1}\sum_{k=1}^{n}\int_{-1}^{1}\rho_k\left[N_{\mathrm{t,\,u}}\right]^{\mathrm{T}}\left[N_{\mathrm{t,\,u}}\right]\det\left[J\right]\frac{h_k}{h_{\mathrm{t}}}d\zeta_k d\xi d\eta \qquad (\mathrm{A.20a})$$

$$\left[K_{\mathrm{t,\,uu},\,e}\right] = \int_{-1}^{1}\int_{-1}^{1}\sum_{k=1}^{n}\int_{-1}^{1}\left[B_{\mathrm{t,\,u}}\right]^{\mathrm{T}}\left[C\right]_k\left[B_{\mathrm{t,\,u}}\right]\det\left[J\right]\frac{h_k}{h_{\mathrm{t}}}d\zeta_k d\xi d\eta \qquad (\mathrm{A.20b})$$

$$\left[K_{\mathrm{t,\,\phi u},\,e}\right]_k = 2\int_{-1}^{1}\int_{-1}^{1}\int_{-1}^{1}\left[B_{\mathrm{t,\,\phi}}\right]^{\mathrm{T}}\left[e\right]_k\left[B_{\mathrm{t,\,u}}\right]\det\left[J\right]\frac{h_k}{h_{\mathrm{t}}}d\zeta_k d\xi d\eta \qquad (\mathrm{A.20c})$$

$$\left[K_{\mathrm{t,\,\phi\phi},\,e}\right]_k = -\int_{-1}^{1}\int_{-1}^{1}\int_{-1}^{1}\left[B_{\mathrm{t,\,\phi}}\right]^{\mathrm{T}}\left[\eta\right]_k\left[B_{\mathrm{t,\,\phi}}\right]\det\left[J\right]\frac{h_k}{h_{\mathrm{t}}}d\zeta_k d\xi d\eta \qquad (\mathrm{A.20d})$$

$$\left[K_{\mathrm{t,\,eu},\,e}\right]_k = 2\int_{-1}^{1}\int_{-1}^{1}\int_{-1}^{1}\left[B_{\mathrm{t,\,e}}\right]^{\mathrm{T}}\left[e\right]_k\left[B_{\mathrm{t,\,u}}\right]\det\left[J\right]\frac{h_k}{h_{\mathrm{t}}}d\zeta_k d\xi d\eta \qquad (\mathrm{A.20e})$$

$$\left[K_{\mathrm{t,\,e\phi},\,e}\right]_k = -\int_{-1}^{1}\int_{-1}^{1}\int_{-1}^{1}\left[B_{\mathrm{t,\,e}}\right]^{\mathrm{T}}\left[\eta\right]_k\left[B_{\mathrm{t,\,\phi}}\right]\det\left[J\right]\frac{h_k}{h_{\mathrm{t}}}d\zeta_k d\xi d\eta \qquad (\mathrm{A.20f})$$

$$\left[K_{\mathrm{t,\,ee},\,e}\right]_k = -\int_{-1}^{1}\int_{-1}^{1}\int_{-1}^{1}\left[B_{\mathrm{t,\,e}}\right]^{\mathrm{T}}\left[\eta\right]_k\left[B_{\mathrm{t,\,e}}\right]\det\left[J\right]\frac{h_k}{h_{\mathrm{t}}}d\zeta_k d\xi d\eta \qquad (\mathrm{A.20g})$$

Guyan Reduction of Internal Electrical Potential Degrees of Freedom

The internal electrical field can be generated by a deflection of the shell or an electrical potential difference over the IDE, and since the actual magnitude of this field is of no interest the degrees of freedom associated with this can be eliminated via a Guyan reduction presented by Guyan (1965) and originally in a piezoelectric context by Allik and Hughes (1970). This will result in a lowering of the total number of variables leading to a reduction of the computational effort needed, but still maintain the effects of the internal electrical field due to the modification of the remaining stiffness matrices and their corresponding external force vectors. From equation (A.16) electrical potential related to the internal electrical field can be isolated. For simplicity equation (A.21) shows the reduction for one element in a layer

$$\left\{\phi_{\mathrm{e},\,e}\right\}_k = -\left[K_{\mathrm{t,\,\phi\phi},\,e}\right]_k^{-1}\left(\left[K_{\mathrm{t,\,\phi u},\,e}\right]_k^{\mathrm{T}}\left\{u_{\mathrm{t,\,e}}\right\} + \left[K_{\mathrm{t,\,e\phi},\,e}\right]_k\left\{\Delta\phi_{\mathrm{e}}\right\}_k - \left\{Q_{\phi,\,e}\right\}_k\right) \quad (\mathrm{A.21})$$

When the expression for the internal electrical potential is inserted into equation

(A.16) it yields

$$
\begin{bmatrix} [M_{t,\,uu}] & [0] \\ [0]^{T} & [0] \end{bmatrix} \begin{Bmatrix} \{\ddot{u}_{t,\,e}\} \\ \{\Delta\ddot{\phi}_{e}\} \end{Bmatrix}
$$
$$
+ \begin{bmatrix} [\hat{K}_{t,\,uu}] & [\hat{K}_{t,\,eu}] \\ [\hat{K}_{t,\,eu}]^{T} & -[\hat{K}_{t,\,ee}] \end{bmatrix} \begin{Bmatrix} \{u_{t,\,e}\} \\ \{\Delta\phi_{e}\} \end{Bmatrix} \tag{A.22}
$$
$$
= \begin{Bmatrix} \{\hat{F}_{t,\,e}\} \\ \{\hat{Q}_{e}\} \end{Bmatrix}
$$

The DoFs are reduced to deflection and electric potential difference from the electrode pairs.

The modified stiffness matrices and force vectors are given in equation (A.23).

$$
[\hat{K}_{t,\,uu}] = [K_{t,\,uu}] - \sum_{k=1}^{n} [K_{t,\,\phi u}]_{k} [K_{t,\,\phi\phi}]_{k}^{-1} [K_{t,\,\phi u}]^{T} \tag{A.23a}
$$

$$
[\hat{K}_{t,\,eu}]_{k} = [K_{t,\,eu}]_{k} - [K_{t,\,\phi u}]_{k} [K_{t,\,\phi\phi}]_{k}^{-1} [K_{t,\,e\phi}] \tag{A.23b}
$$

$$
[\hat{K}_{t,\,ee}]_{k} = [K_{t,\,ee}]_{k} - [K_{t,\,e\phi}]_{k}^{T} [K_{t,\,\phi\phi}]_{k}^{-1} \{K_{t,\,e\phi}\}_{k} \tag{A.23c}
$$

$$
\{\hat{F}_{t}\} = \{F_{t}\} - \sum_{k=1}^{n} [K_{t,\,\phi\phi}]_{k}^{-1} \{Q_{\phi}\}_{k} \tag{A.23d}
$$

$$
\{\hat{Q}_{e}\}_{k} = \{Q_{e}\}_{k} - [K_{t,\,\phi\phi}]_{k}^{-1} \{Q_{\phi}\}_{k} \tag{A.23e}
$$

Boundary Conditions

The developed element has two types of degrees of freedom i.e. displacement $\{u_{t,\,e}\}$ and electrical potential difference $\{\Delta\phi_{e}\}$. The variable related to the electrical system is taken as the difference between the two electrodes. This is a relative degree of freedom corresponding to one of the electrodes is grounded, hence no boundary condition is needed.

The mechanical displacement requires boundary conditions, since rigid body motion is possible. Fixation of a mechanical degree of freedom can be done by setting the corresponding diagonal value in the mass $[\hat{M}_{t,\,uu}]$ and stiffness matrices $[\hat{K}_{t,\,uu}]$ to one and the associated column and row values as well as the force vector $\{\hat{F}_{t}\}$ row to zero. For additional explanation see e.g. Cook et al. (2002).

A layered shell containing patches of piezoelectric fibers and interdigitated electrodes: Finite element modeling and experimental validation

This paper was published on-line in Journal of Intelligent Material Systems and Structures in May 2016. The paper presents the finite element used for modelling the piezoelectric top foil (PTF).

Original Article

A layered shell containing patches of piezoelectric fibers and interdigitated electrodes: Finite element modeling and experimental validation

Bo B Nielsen, Martin S Nielsen and Ilmar F Santos

Abstract

The work gives a theoretical and experimental contribution to the problem of smart materials connected to double curved flexible shells. In the theoretical part the finite element modeling of a double curved flexible shell with a piezoelectric fiber patch with interdigitated electrodes (IDEs) is presented. The developed element is based on a purely mechanical eight-node isoparametric layered element for a double curved shell, utilizing first-order shear deformation theory. The electromechanical coupling of piezoelectric material is added to all elements, but can also be excluded by setting the piezoelectric material properties to zero. The electrical field applied via the IDEs is aligned with the piezoelectric fibers, and hence the direct d_{33} piezoelectric constant is utilized for the electromechanical coupling. The dynamic performance of a shell with a microfiber composite (MFC) patch is investigated using frequency response functions (FRFs) obtained via external impact test as well as internal random signal excitation using the MCF patch as an actuator. The experiments are used to validate the numerical results. Good agreement between theory and experiments is obtained in a large frequency range. Discrepancies and insights into optimal modeling frequency range and non-linear behavior are discussed.

Introduction

The past few decades have seen an intense development and integration of smart materials into a variety of flexible structures, with the goal of sensing, monitoring and controlling the static and dynamic behavior of such flexible structures. Piezoelectric material adds a new dimension into the design of smart structures, since it allows for adaptation and optimization of their static and dynamic properties via electronics and software, and with the development of piezoelectric patches these properties are easily added to a flexible structure.

Sensing and actuating via piezoelectric structures have been a topic of research for many years, dating back to at least the 1950s; see for example Thurston (1953). Over the years different types of sensors and actuators have been developed, but the focus of this article is on piezoelectric patches. Many of these patches have been developed by NASA, and Bryant (2007) gives a timeline for the development of different

types of piezoelectric patches, from the thin layer unimorph driver (THUNDER) in the beginning of the 1990s to the microfiber composite (MFC) in 1996, and so on. These two types of piezoelectric patches are shown in Figure 1. As seen in the figure the THUNDER patch consists of a thin piezoelectric sheet covered by electrodes on top and bottom, while the MFC consists of rectangular piezoelectric fibers isolated from each other and covered by interdigitated electrodes (IDEs). The idea for the piezoelectric fiber and IDEs originates from the active fiber composite (AFC) presented by Hagood et al. (1993) and Hagood and Bent (1993). An overview of the MFC technology and applications has been given

DTU Mechanical Engineering, Kongens Lyngby, Denmark

Corresponding author:
Ilmar F Santos, Technical University of Denmark, Department of Mechanical Engineering, Niels Koppels Alle 404, 2900, Kongens Lyngby, Denmark.
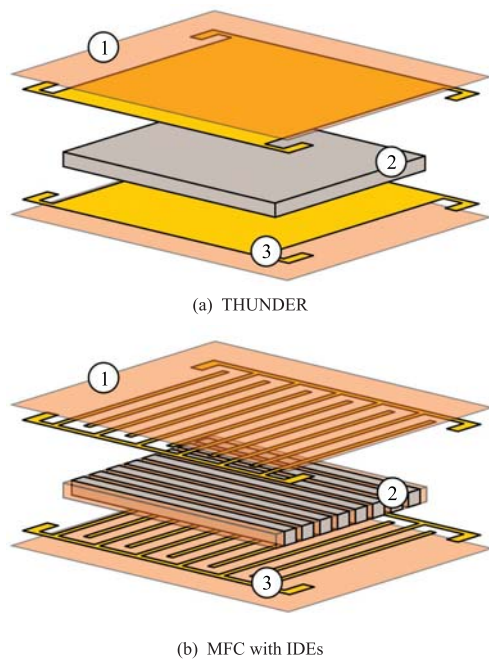Email: ifs@mek.dtu.dk

(a) THUNDER

(b) MFC with IDEs

Figure 1. Two types of piezoelectric patches. The THUNDER and the MFC P1. (1) Isolation layer, (2) piezoelectric sheet and (3) electrodes.

by Williams et al. (2002) and Schönecker et al. (2006). MFC patches with the top and bottom electrode configuration exist, although this version cannot match the THUNDER patch for actuation as shown by Bent et al. (1995). For this reason all subsequent references to MFC or piezoelectric fiber patches assumes IDEs are used.

The literature within the topic of modeling piezoelectric patches can be divided into three categories: (1) analytical and finite element method (FEM) models of beams, plates and shells of or with the THUNDER patch, (2) analytical material models validated by full three-dimensional (3D) FEM models of a so-called unit cell or representative volume, and (3) analytical and FEM models of beam-like structures utilizing MFC patches in the design.

Among the first models of piezoelectric patches are the dynamic equations presented by Tzou and Gadre (1989) and the solid FEM model by Tzou and Tseng (1991), which include the piezoelectric material in the layers of a shell. These models utilize the extension mode or d_{31} piezoelectric constant, where the electrical field is applied to the shell normal direction, the same direction as the polarization, but with the mechanical reaction acting in the plane of the shell. The subsequent FEM models presented in the literature are layered-beam-, plate- or shell-based, utilizing different shear

deformation theory. Suleman and Venkayya (1995) presented a four-node Mindlin element for plates with the possibility of including multiple piezoelectric patches in the same layer, while Samanta et al. (1996) presented a FEM model based on high-order deformation theory. Tzou and Ye (1996) utilized zigzag theory with individual shear and electrical potential in each layer for a FEM model with six-by-two-node triangular elements. A mixed formulation FEM model was presented by Saravanos (1997) combining first-order shear deformation theory through the entire shell thickness with a piecewise linear electrical potential in the layers. Piefort and Henrioulle (2000) present a FEM model based on Kirchhoff plate theory. A nine-node shell element was presented by Balamurugan and Narayanan (2001) based on first-order shear deformation theory. Gabbert et al. (2002) described three different ways of including the piezoelectric effect in an eight-node semi-loof shell element ranging from an external force to the inclusion of the electrical potential at each node. Varelis and Saravanos (2006) introduced a double curved layered shell finite element, which can handle large deformations and is capable of modeling large curved shells. A five-layer shallow shell finite element was presented by Boudaoud et al. (2008), based on a classical three-node flat triangular element, while Balamurugan and Narayanan (2009) utilize respectively higher-order shear deformation theory on an eight-node shell element. Vidal et al. (2011) presented an eight-node shell element based on the Reissner–Mindlin plate model with an additional quadratic thickness stretching displacement term. The four-node shallow element presented by Yasin and Kapuria (2013) utilizes zigzag theory to describe the shear deformation.

In the same period FEM models have been published for the THUNDER patch taking into account the thermal effects on the piezoelectric material. Chattopadhyay et al. (1998) presented an analytical plate model including the thermal coupling to the electromechanical system. A FEM model of this was presented by Bansal and Ramaswamy (2002) in a four-node plate element and in a nine-node shell element version by Narayanan and Balamurugan (2003).

The piezoelectric layers in all the models presented above are of the THUNDER type and utilize the extension mode, as opposed to the shear mode or d_{15} piezoelectric constant, where the electrical field is applied in the shell normal direction, but the polarization is in-plane with the shell. The mechanical reaction acting on the electrical field is in-plane shear. Benjeddou et al. (1997, 1999) and Trindade et al. (2001) presented a FEM model capable of including both extension and shear mode for a sandwich beam. This was later expanded by Kapuria and Hagedorn (2007) to include multiple layers, and the internal electric mechanical effects.

In the second category of topics the main focus is homogenization of the material properties of an extension mode piezoelectric fiber patch with IDEs due to the complex structure and electrical field from the electrodes. The first model presented by Bent and Hagood (1997) is known as the uniform field method. The method is developed for the AFC with IDEs, but due to the close resemblance between the MFC and the AFC, the method may also be used for homogenization of the MFC material properties. Park and Kim (2005) presented an alternative method to calculate the homogenized material properties. Results were presented for single crystal MFC, standard MFC and AFC, showing a better performance for the MFC. This can be attributed to the better contact between the MFC and IDEs due to the squared fiber as opposed to the round fiber used in AFC. Deraemaeker et al. (2009) used the mixing rule for calculating the average material properties, and validated the results via a 3D finite element model of the unit cell. Biscani et al. (2011) presented the asymptotic expansion homogenization for calculating the material properties of the MFC with top and bottom surface electrodes. The characterization of the material properties in a shear mode MFC with top and bottom electrodes has been presented by Trindade and Benjeddou (2011), which shows the packaging lowers the effective stiffness and inverse piezoelectric coupling effect of the shear mode MFC.

The temperature dependency for the homogenized material properties of the extension mode MFC is presented by Prasath and Arockiarajan (2015) as a function of the bonding layer thickness between the piezoelectric fiber and the IDEs, since the bonding layer obstructs the electrical field produced by the IDEs. Nasser et al. (2008, 2011) focus on the electrical field between two electrodes, making it possible to create a correction for the dead zones in the electrical field. This gives an insight into the distribution of the electrical field associated with the IDEs used for piezoelectric fiber patches.

Within the third topic Nguyen and Kornmann (2006) used a 3D FEM model of a beam to investigate the dynamic performance of the three collocated pairs of piezoelectric patches, that is, THUNDER, AFC and MFC, and compared results with experimental data. An analytical investigation of a MFC patch mounted on a beam was performed by Bilgen et al. (2010), which agrees with experimentally obtained results. Brockmann and Lammering (2006) developed a hollow beam FEM model for modeling a helicopter rotor blade. An air foil with 18 MFC patches has been modeled by Guennam and Luccioni (2006, 2009) using two different approaches. In the first one, the box beam of the air foil is modeled by FEM in a piece of commercial software, while in the second approach the box beam is modeled by a four-node piezoelectric shell element. The two models show very similar results. The latter model,

which is the model most comparable to the one presented in this article, has been expanded by Guennam and Luccioni (2015) to take the non-linearity of the piezoelectric coupling into account.

In this framework the main original contribution of this work relies on the development and experimental validation of a linear electromechanical finite element for double curved layered shells with the capability of including one or more piezoelectric fiber patches by adding one single additional degree of freedom (DoF) per electrode pair, that is, the electrical potential difference over the IDEs while taking the dead zones due to the IDEs into account. The dynamic shell element model is based on a static eight-node serendipity isoparametric layered double curved finite element developed by Panda and Natarajan (1981). Capabilities and limitations of the new electromechanical finite element are shown by comparison to experiment results performed with a single curved shell with one MFC patch. The neutral bending axis in the electromechanical shell is not located at the mid-plane of the shell due to the asymmetric layup. It is important to highlight that, in most of the contributions found in the literature, patches are symmetrically distributed on both sides of the shell, leading to no extension–bending coupling. In this work such a symmetric stacking of layers is not imposed due the practical application in mind.

Electromechanical model

A piezoelectric MFC patch consists of aligned rectangular piezoelectric fibers isolated from each other and with IDEs on the top and bottom surfaces. The IDEs creates an electrical field due to the electrical potential difference between the electrode fingers in the plane of the patch and perpendicular to the electrodes, that is, in the same direction as the fibers and the wanted action. This results in an extension mode and utilizes the direct piezoelectric constant d_{33}, which has a larger magnitude than the d_{31} utilized in the THUNDER piezoelectric patches, and hence a bigger effect is gained in the fiber direction (Bent et al., 1995). In Figure 2(a) a sketch of the MFC is seen, while in Figure 2(b) a single piezoelectric fiber (2) is shown with its isolation on its sides (1) and one pair of IDEs (3) on its top and bottom. The enclosed square marked with black lines is the unit cell in a MFC patch.

The unit cell is assumed to be governed by two physical domains, one mechanical and one electrical, which are coupled by the piezoelectric effect. Figure 3 shows the MFC unit cell (a) and the two domains (b): on the left-hand side the mechanical domain is described by three direct and three shear strain variables, and on the right-hand side the electrical domain is represented by three direct electrical field directions.

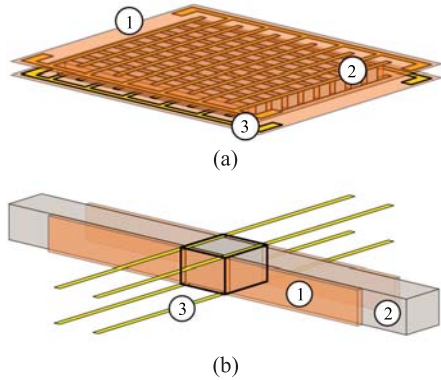The piezoelectric constitutive equation (1) is given in for example Tiersten (1969), where $[S]$ is the structural

Figure 2. The origin of the MFC unit cell consists of a piezoelectric fiber with isolation and one pair of the electrode fingers. (a) MFC patch. (b) Unit cell marked with bold black lines.
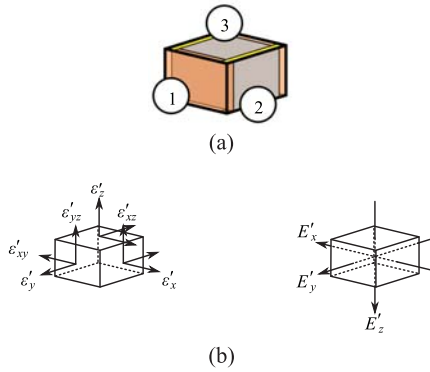

Figure 3. The unit cell of the MFC and the two physical domains with their variables. The mechanical domain is on the left-hand side and the electrical domain is on the right-hand side. In the mechanical domain only the strains on the outward pointing surfaces are displayed. (a) MFC unit cell. (b) Strains and electric field.

compliance, $[d]$ is direct piezoelectric constant and $[\epsilon]$ is the electric permittivity. The specific configuration of the piezoelectric fiber patch, for example fiber fraction ratio and so on, affects the material properties in the constitutive equations, which may be calculated by for example the uniform field model mentioned in the introduction. The constitutive equation may also be used for non-piezoelectric materials, since a non-piezoelectric material will have zero piezoelectric constant and dielectric permittivity, and hence equation (1a) reduces to Hook's law.

$$\{\varepsilon\} = [S]\{\sigma\} + [d]^{\mathrm{T}}\{E\} \qquad (1a)$$

$$\{D\} = [d]\{\sigma\} + [\epsilon]\{E\} \qquad (1b)$$

The physics behind the constitutive equations can be explained by the crystal structure of a piezoelectric
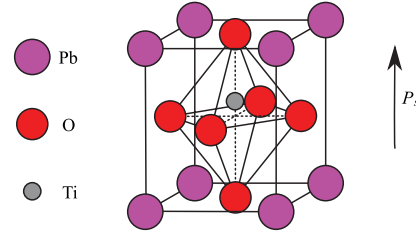

Figure 4. The crystal lattice of LZT (PbTiO$_3$). The non-symmetric placement of the ions in the lattice results in a dipole moment. The direction of the dipole moment may point in any of the three spatial directions depending on the displacement of the ions.

material. The crystal lattice of a typical piezoelectric material like lead zirconate titanate (LZT) is tetragonal (non-cubic), which below the Curie temperature results in a spontaneous polarization of the ions within the material due to their internal position in the lattice. The non-symmetric lattice in a dipole moment; see Figure 4. The dipole moments within the material structure, or even within a material crystal, are not necessarily aligned upon initial manufacturing. An alignment of the dipoles is ensured by poling the material with a strong electric field, which ensures alignment of the piezoelectric properties. A thorough explanation is given by Damjanovic (1998).

Mathematical model

A layered shell containing one or more layers of piezoelectric fiber patches must be regarded as an electromechanical system in order to take the piezoelectric coupling effects into account. In the derivation of a mathematical model, the Lagrange equation (2) is used.

$$\frac{\partial}{\partial t}\left(\frac{\partial L}{\partial \dot{q}_i}\right) - \frac{\partial L}{\partial q_i} = F_i \qquad (2)$$

This requires the Lagrangian to be discretized, which is done by shape functions and the nodal DoFs used in the FEM formulation. The Lagrangian for an electromechanical system is given by the kinetic energy minus the potential energy.

$$L = T - H$$

The continuous system

The potential energy is calculated based on the constitutive equation. The potential energy used in the Lagrangian depends on which variables are dependent and independent. In the constitutive equation (1) for the electromechanical system, mechanical strain $\{\varepsilon\}$ and electric displacement $\{D\}$ are the extensive

properties, while the mechanical stress $\{\sigma\}$ and the electrical field $\{E\}$ are the intensive properties. The infinitesimal change in the internal energy of a system is given by an infinitesimal change in the extensive properties, hence mechanical strain and electrical displacement as seen in equation (3a), but since the independent variables required for the FEM model are mechanical strain and electrical field a Legendre transformation of the internal energy is performed, leading to infinitesimal change in the enthalpy, which depends on the required variables as shown in equation (3b).

$$\delta U = \{\sigma\}^{\mathrm{T}}\delta\{\varepsilon\} + \{E\}^{\mathrm{T}}\delta\{D\} \qquad (3a)$$

$$\delta H = \{\sigma\}^{\mathrm{T}}\delta\{\varepsilon\} - \{D\}^{\mathrm{T}}\delta\{E\} \qquad (3b)$$

The Legendre transformation from the internal energy to the enthalpy is

$$H = U - \{E\}^{\mathrm{T}}\{D\} \qquad (4)$$

The constitutive equation required by the enthalpy is given in equation (5), in which the mechanical stress and electrical displacement are the dependent variables, and the mechanical strain and electrical field are the independent variables.

$$\{\sigma\} = [C]\{\varepsilon\} - [e]^{\mathrm{T}}\{E\} \qquad (5a)$$

$$\{D\} = [e]\{\varepsilon\} + [\eta]\{E\} \qquad (5b)$$

The structural stiffness $[C]$, inverse piezoelectric constant $[e]$ and electric permittivity $[\eta]$ matrices are given in the appendix.

The energies required to calculate the Lagrangian are

$$T = \frac{1}{2}\int \rho\{\dot{u}\}^{\mathrm{T}}\{\dot{u}\}dV \qquad (6a)$$

$$\begin{aligned} H = \frac{1}{2}\int & \{\varepsilon\}^{\mathrm{T}}[C]\{\varepsilon\} \\ & -4\{E\}^{\mathrm{T}}[e]\{\varepsilon\} \\ & -\{E\}^{\mathrm{T}}[\eta]\{E\}]dV \end{aligned} \qquad (6b)$$

The electromechanical system is assumed to be electrostatic. For details on the derivation of the enthalpy see the appendix. In FEM models it is customary to use displacement u and electrical potential ϕ as the independent variables rather than the mechanical strain and electrical field. Equation (7) shows the relationship between mechanical strain and displacement as well as the relationship between electric field and electric potential.

$$\{\varepsilon\} = [\partial]\{u\} \qquad (7a)$$

$$\{E\} = -\{\nabla\}\phi \qquad (7b)$$

The differential operators are given in the appendix.

The Lagrangian for the continuous system given in equation (8) is a function of the displacement, time derivative of the deflection (velocity) and electrical potential.

$$\begin{aligned} L = \frac{1}{2}\int & \rho\{\dot{u}\}^{\mathrm{T}}\{\dot{u}\} \\ & -([\partial]\{u\})^{\mathrm{T}}[C][\partial]\{u\} \\ & -4(\{\nabla\}\phi)^{\mathrm{T}}[e][\partial]\{u\} \\ & +(\{\nabla\}\phi)^{\mathrm{T}}[\eta]\{\nabla\}\phi]dV \end{aligned} \qquad (8)$$

The discretized system

The Lagrangian for the continuous system (8) must be given by generalized coordinates before it can be used in Lagrange equation (2). The continuous DoFs are discretized by separation of variables and given in equation (9). The separated variables are the nodal variables $\{u\}$ and $\{\phi\}$ and known shape functions $[N]$.

$$\{u(t,x,y,z)\} = [_uN(x,y,z)]\{u_e(t)\} \qquad (9a)$$

$$\phi(t,x,y) = \{_\phi N(x,y)\}\{\phi_e(t)\} \qquad (9b)$$

The differential operators used in the calculation of the mechanical strain and electrical field in equation (7) are spatial derivatives, and hence only the shape functions are affected. Derivative matrices are set up for differentiated shape functions as given by

$$[_uB] = [\partial][_uN] \qquad (10a)$$

$$[_\phi B] = \{\nabla\}[_\phi N] \qquad (10b)$$

When the nodal DoFs equation (9) and derivative matrices equation (10) are introduced in the continuous Lagrangian (8) one obtains

$$\begin{aligned} L = \frac{1}{2}\int & \overbrace{[\rho([_uN]\{\dot{u}_e\})^{\mathrm{T}}[_uN]\{\dot{u}_e\}}^{\text{Term:I}} \\ & -\underbrace{([_uB]\{u_e\})^{\mathrm{T}}[C][_uB]\{u_e\}}_{\text{Term:II}} \\ & -4\underbrace{([_\phi B]\{\phi_e\})^{\mathrm{T}}[e][_uB]\{u_e\}}_{\text{Term:III}} \\ & +\underbrace{([_\phi B]\{\phi_e\})^{\mathrm{T}}[\eta][_\phi B]\{\phi_e\}}_{\text{Term:IV}}]dV \end{aligned} \qquad (11)$$

the discrete version of the Lagrangian given in generalized coordinates.

The governing equation for the electromechanical system

Calculating the weak form of the governing equation (12) via Lagrange equation (2) and the discretized

Lagrangian (11) requires differentiation with respect to the two generalized coordinate types, that is, the deflection and the electrical potential, and the time derivatives of these. These calculations are given in the appendix. The governing equation is

$$
\begin{aligned}
\int_V [& \overbrace{\rho [_eN]^{\mathrm{T}} [_eN]}^{\text{Part:I}} \{_e\ddot{u}\} \\
& + \underbrace{[_uB]^{\mathrm{T}} [C] [_uB]}_{\text{Part:II}} \{_eu\} \\
& + \underbrace{2 \left([_\phi B]^{\mathrm{T}} [e] [_uB] \right)^{\mathrm{T}}}_{\text{Part:III}} \{_e\phi\} \\
& + \underbrace{2 [_\phi B]^{\mathrm{T}} [e] [_uB]}_{\text{Part:IV}} \{_eu\} \\
& - \underbrace{[_\phi B]^{\mathrm{T}} [\eta] [_\phi B]}_{\text{Part:V}} \{_e\phi\}] dV = \{F\}
\end{aligned}
\tag{12}
$$

The electrical field created by the interdigitated electrodes

So far, the derivation has been kept general, and hence no restrictions have been introduced for the shape or geometry of the electromechanical system. In order to include the external electric field in the piezoelectric fiber due to the electrodes (see Figure 2(a)) the electric field variable $\{E\}$ must be expanded and rewritten. The electrical field created by an electrical potential difference between the electrodes is added via superposition to the existing electrical field within the fibers; hence the total electrical field is given by

$$
\{E\} = -(\{\nabla\}\phi + \{_eE\})
\tag{13}
$$

IDEs have dead zones between two equipotential electrode fingers in the thickness direction marked with red in Figure 5. These dead zones introduce a challenge for selecting the correct distance between two electrode pairs in the in-plane direction needed for calculating the electric field due to the direction of the electrical field as seen in the same figure (Figure 5). Nasser et al. (2008) give an analytical expression for the effective electrical field produced by the electric potential difference between the IDEs taking the dead zones into account. The correction factor is

$$
\alpha_{\mathrm{corr}} = \left[1 - \frac{h_f}{p_f} \left(\frac{1}{2} + \frac{2}{\pi^2} \right) \right] \left[\frac{p_f - w_f}{p_f - h_f} \right]
\tag{14}
$$

The figure distance between the centerline of two adjacent electrode fingers p_f and half the width of an electrode finger w_f is shown in Figure 6.

Each of the two electrodes in an IDE pair has the same electrical potential in the entire electrode and the electrical field created by IDEs is only non-zero perpendicular to the electrode fingers in accordance with Nasser et al. (2008). In equation (15) the electrical field
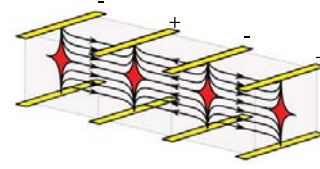

Figure 5. Sketch of the IDEs (yellow bars), electric field (black lines with arrows) and the dead zones in-between equipotential electrode fingers (red areas). A set of electrode fingers above and below each other is equipotential, and dead zones exist along these fingers.
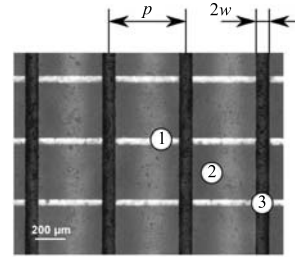

Figure 6. A photo of the interior of a MFC patch. (1) Isolation (white lines), (2) piezoelectric fibers (gray areas), (3) IDEs (black lines). The picture is taken with an Olympus GX41 microscope and a Leica DFC450 C camera.

is given via separation of the variables into the derivative matrix $\{_eB\}$ depending on spatial coordinates and the electrical potential difference $\Delta_e\phi$ depending on time.

$$
\{_eE\} = \{_eB\}\Delta_e\phi = [T_e] \begin{Bmatrix} 0 \\ 0 \\ \frac{\alpha_{\mathrm{corr}}}{p} \end{Bmatrix} \Delta_e\phi
\tag{15}
$$

There are two important things to note regarding the electrical field of the IDEs. First note: the electrical field created by the IDEs has a different direction on each side of an electrode finger as illustrated by the arrows on the electrical field lines seen in Figure 5, but since the manufacturer uses the IDEs for polarization of the piezoelectric fibers the polarization also has a different direction on each side of an electrode finger, and hence the electrical field is always aligned with the polarization. Second note: the third spatial direction of a piezoelectric material is conventionally aligned with the direction of polarization, which for piezoelectric fibers differs from the convention for plates and shells, where the third spatial direction is the surface normal, and hence a coordinate transformation $[T_e]$ is needed to make them compatible as seen in equation (15).

The governing equation for the electromechanical system (12) must include the DoFs related to the IDEs.

Of the equation's five parts, parts I and II are kept unchanged, while parts III, IV and V are expanded to accommodate the effect IDEs. The governing equation, which includes the IDEs, is

$$
\begin{aligned}
\int_V & [\rho[_eN]^{\mathrm{T}}[_eN]\,\{\ddot{u}_e\} \\
& + ([_uB]^{\mathrm{T}}[C]\,[_uB] + 2[_\phi B]^{\mathrm{T}}[e]\,[_uB] \\
& + 2[_eB]^{\mathrm{T}}[e]\,[_uB])\,\{u_e\} \\
& + \left(2([_\phi B]^{\mathrm{T}}[e]\,[_uB])^{\mathrm{T}}\right. \\
& - [_\phi B]^{\mathrm{T}}[\eta]\,[_\phi B] - [_eB]^{\mathrm{T}}[\eta]\,[_\phi B])\,\{\phi_e\} \\
& + (2\left([_eB]^{\mathrm{T}}[e]\,[_uB]\right)^{\mathrm{T}} - \left([_eB]^{\mathrm{T}}[\eta]\,[_\phi B]\right)^{\mathrm{T}} \\
& - [_eB]^{\mathrm{T}}[\eta]\,[_eB])\,\{\Delta_e\phi\}]dV = \{F\}
\end{aligned}
\tag{16}
$$

The matrix form of equation (16), where the volume integrals are included in the matrix elements, is

$$
\begin{aligned}
& \begin{bmatrix} [_{u-u}M] & [0] & [0] \\ [0]^{\mathrm{T}} & [0] & [0] \\ [0]^{\mathrm{T}} & [0]^{\mathrm{T}} & [0] \end{bmatrix} \begin{Bmatrix} \{\ddot{u}_e\} \\ \{\ddot{\phi}_e\} \\ \{\ddot{\Delta}_e\phi\} \end{Bmatrix} \\
& + \begin{bmatrix} [_{u-u}K] & [_{\phi-u}K] & [_{e-u}K] \\ [_{\phi-u}K]^{\mathrm{T}} & [_{\phi-\phi}K] & [_{e-\phi}K] \\ [_{e-u}K]^{\mathrm{T}} & [_{e-\phi}K]^{\mathrm{T}} & [_{e-e}K] \end{bmatrix} \begin{Bmatrix} \{u_e\} \\ \{\phi_e\} \\ \{\Delta_e\phi\} \end{Bmatrix} \\
& = \begin{Bmatrix} \{_uF_e\} \\ \{_\phi Q_e\} \\ \{_eQ\} \end{Bmatrix}
\end{aligned}
\tag{7}
$$

The eight-node double curved isoparametric element

As the base for the new dynamic electromechanical element the static eight-node double curved layered isoparametric serendipity element presented by Panda and Natarajan (1981) is chosen. A schematic can be seen in the center of Figure 7(a). The physical double curved layered shell is prescribed by a 2D four-sided shell with nodes in each corner and on each side. This eight-node shell element follows the geometrical mid-plane of the physical shell, with the spatial location of the physical shell given by

$$
\{x\} = \sum N_i\left(\{x_i\} + \zeta\frac{t_i}{2}\{V_{3i}\}\right)
\tag{18}
$$

The nodal placement is given in the global coordinate system, while the thickness is given using the third coordinate direction of the local nodal coordinate system (see Figure 7(a)). The transformation matrices from global to local coordinates are given in the appendix.

In the derivation of the governing equation via the Lagrange equation the discretization via separation of variables is done with unspecified shape functions and
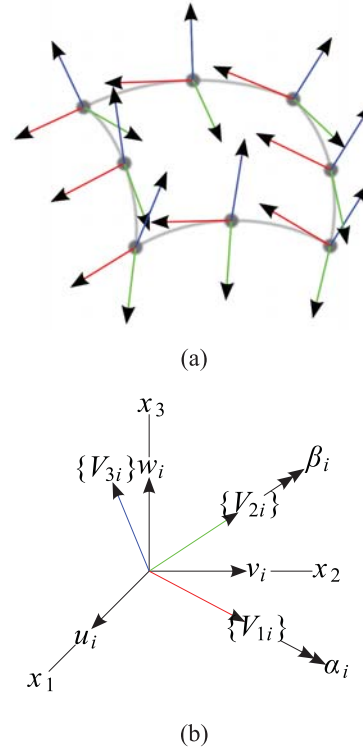

Figure 7. Eight-node double curved shell element with local coordinates given at each node and the relationship between the local and global coordinates and the kinematic nodal variables. (a) Element with local coordinate systems at each node. (b) Local and global coordinate systems and nodal kinematic variables.

nodal DoFs; see equation (9). For the eight-node element the shape functions are given in isoparametric coordinates and listed in the appendix along with the derivative matrices in the appendix. The nodal displacement $\{u_e\}$ has a kinematic relation based on first-order shear deformation and is

$$
\{u_e\} = \{u_i\} + \zeta\frac{t_i}{2}[\mu_i]\alpha_i\beta_i
\tag{19}
$$

The nodal electrical potential, which is the new addition, is divided into an internal nodal electric potential $\{\phi_i\}$ for each layer, and an external electrical potential difference $\{\Delta_e\phi\}$ for each of the IDE pairs.

For multi-layers

For a shell structure with multiple layers the volume integration in the thickness direction must be done individually for each layer as proposed by Panda and Natarajan (1981). This procedure utilizes that the material properties are well known at layer level, making the procedure straightforward. The infinitesimal
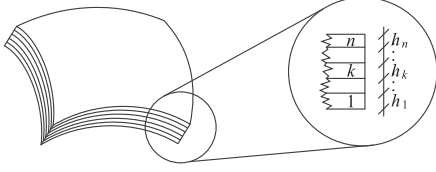
Figure 8. Layers in the shell with numbering and thicknesses.

relationship between the isoparametric thickness coordinate ζ of the shell and the layer isoparametric thickness coordinate ζ_k is

$$d\zeta = \frac{h_k}{t} d\zeta_k \tag{20}$$

where h_k is the thickness of the layer and t is the thickness of the shell as shown in Figure 8.

Using this infinitesimal relationship for the Gaussian integration, the mass and stiffness matrices in equation (17) are given in equation (21) at element level. The matrices for the piezoelectric coupling and electrical relation are given at layer level, in other words, they are not added together. This is due to the assumption that each piezoelectric layer is electrically isolated from the others and that they have their own electrodes. Therefore they also have their own DoF with respect to the electrical potential difference. The assumption is valid for a MFC patch due to the isolation on the top and bottom (see Figure 1(b)).

$$[_{u-u}M_e] = \int_{-1}^{1}\int_{-1}^{1}\sum_{k=1}^{n}\int_{-1}^{1}\rho_k[_uN]^{\mathrm{T}}[_uN] \\ \det[J]\frac{h_k}{t}d\zeta_k d\xi d\eta \tag{21a}$$

$$[_{u-u}K_e] = \int_{-1}^{1}\int_{-1}^{1}\sum_{k=1}^{n}\int_{-1}^{1}[_uB]^{\mathrm{T}}[C]_k[_uB] \\ \det[J]\frac{h_k}{t}d\zeta_k d\xi d\eta \tag{21b}$$

$$[_{\phi-u}K_e]_k = 2\int_{-1}^{1}\int_{-1}^{1}\int_{-1}^{1}[_uB]^{\mathrm{T}}[e]_k^{\mathrm{T}}[_\phi B] \\ \det[J]\frac{h_k}{t}d\zeta_k d\xi d\eta \tag{21c}$$

$$[_{\phi-\phi}K_e]_k = -\int_{-1}^{1}\int_{-1}^{1}\int_{-1}^{1}[_\phi B]^{\mathrm{T}}[\eta]_k[_\phi B] \\ \det[J]\frac{h_k}{t}d\zeta_k d\xi d\eta \tag{21d}$$

$$[_{e-u}K_e]_k = 2\int_{-1}^{1}\int_{-1}^{1}\int_{-1}^{1}[_uB]^{\mathrm{T}}[e]_k^{\mathrm{T}}[_eB] \\ \det[J]\frac{h_k}{t}d\zeta_k d\xi d\eta \tag{21e}$$

$$[_{e-\phi}K_e]_k = -\int_{-1}^{1}\int_{-1}^{1}\int_{-1}^{1}[_\phi B]^{\mathrm{T}}[\eta]_k^{\mathrm{T}}[_eB] \\ \det[J]\frac{h_k}{t}d\zeta_k d\xi d\eta \tag{21f}$$

$$[_{e-e}K_e]_k = -\int_{-1}^{1}\int_{-1}^{1}\int_{-1}^{1}[_eB]^{\mathrm{T}}[\eta]_k[_eB] \\ \det[J]\frac{h_k}{t}d\zeta_k d\xi d\eta \tag{21g}$$

Guyan reduction of internal electrical potential degrees of freedom

The internal electrical field can be generated by a deflection of the shell or an electrical potential difference over the IDEs, and since the actual magnitude of this field is of no interest the DoFs associated with this can be eliminated via a Guyan reduction presented by Guyan (1965) and originally in a piezoelectric context by Allik and Hughes (1970). This will result in a lowering of the total number of variables leading to a reduction of the computational effort needed, but still maintain the effects of the internal electrical field due to the modification of the remaining stiffness matrices and their corresponding external force vectors. From equation (17) electrical potential related to the internal electrical field can be isolated. For simplicity the following equation shows the reduction for one element in a layer

$$\{\phi_e\}_k = -[_{\phi-\phi}K_e]_k^{-1}([_{\phi-u}K_e]_k^{\mathrm{T}}\{u_e\} \\ + [_{e-\phi}K_e]_k\{\Delta_e\phi\}_k - \{_\phi Q_e\}_k) \tag{22}$$

When the expression for the internal electrical potential is inserted into equation (17) it yields

$$\begin{bmatrix}[_{u-u}M] & [0] \\ [0]^{\mathrm{T}} & [0]\end{bmatrix}\begin{Bmatrix}\{\ddot{u}_e\} \\ \{\ddot{\Delta}_e\phi\}\end{Bmatrix} \\ + \begin{bmatrix}[_{u-u}\hat{K}] & [_{e-u}\hat{K}] \\ [_{e-u}\hat{K}]^{\mathrm{T}} & [_{e-e}\hat{K}]\end{bmatrix}\begin{Bmatrix}\{u_e\} \\ \{\Delta_e\phi\}\end{Bmatrix} \\ = \begin{Bmatrix}\{_u\hat{F}\} \\ \{_e\hat{Q}\}\end{Bmatrix} \tag{23}$$

The DoFs are reduced to deflection and electric potential difference from the electrode pairs.

The modified stiffness matrices and force vectors are given in equation (24).

$$[_{u-u}\hat{K}] = [_{u-u}K] \\ - \sum_{k=1}^{n}[_{\phi-u}K]_k[_{\phi-\phi}K]_k^{-1}[_{\phi-u}K]_k^{\mathrm{T}} \tag{24a}$$

$$[_{e-u}\hat{K}]_k = [_{e-u}K]_k \\ - [_{\phi-u}K]_k[_{\phi-\phi}K]_k^{-1}[_{e-\phi}K]_k \tag{24b}$$

$$[_{e-e}\hat{K}]_k = [_{e-e}K]_k$$
$$- [_{e-\phi}K]_k^{\mathrm{T}} [_{\phi-\phi}K]_k^{-1} [_{e-\phi}K]_k \quad (24c)$$

$$\{_u\hat{F}\} = \{_uF\} - \sum_{k=1}^{n} [_{\phi-\phi}K]_k^{-1} \{_\phi Q\}_k \quad (24d)$$

$$\{_e\hat{Q}\}_k = \{_eQ\}_k - [_{\phi-\phi}K]_k^{-1} \{_\phi Q\}_k \quad (24e)$$

Boundary conditions

The developed element has two types of DoFs, that is, displacement $\{u_e\}$ and electrical potential difference $\{\Delta_e\phi\}$. The variable related to the electrical system is taken as the difference between the two electrodes. This is a relative DoF corresponding to one of the electrodes being grounded, and hence no boundary condition is needed.

The mechanical displacement requires boundary conditions, since rigid body motion is possible. Fixation of a mechanical DoF can be done by setting the corresponding diagonal value in the mass $[_{u-u}\hat{M}]$ and stiffness matrices $[_{u-u}\hat{K}]$ to one and the associated column and row values as well as the force vector $\{_{u-u}F\}$ row to zero. For additional explanation see for example Cook et al. (2002).

Experimental facility

The test facility shown in Figure 9(a) consists of the single curved shell mounted in a clamping mechanism. A sensor bracket gives the possibility of positioning an eddy current displacement sensor at different locations in the axial and circumferential directions to measure the normal deflections of the shell. The smart material MFC M5628-P1 patch is glued onto the outer curvature of the shell to avoid any relative movement between the two layers at the adjacent surfaces. The piezoelectric fibers in the MFC patch are aligned in the circumferential direction and the patch is placed symmetrically along the centerline in the axial direction and 25.6° from the clamped end, as illustrated in Figure 9(b). The remaining geometrical constants and material properties adopted for the electromechanical model are given in Table 1. Two radial dimensions are given for the shell, with and without the MFC patch. The originally flat MFC patch is bent to follow the shell curvature during montage. The residual forces from the MFC patch deformation affect the shell by straightening it, and hence the shell curvature after montage is 43.0 mm compared to the original 42.5 mm, as listed in Table 1. It is assumed the residual stress in the piezoelectric fibers will not affect the performance of the MFC patch, in other words, the MFC patch will still perform linearly. For all the following experiments a dSpace 1103 controller board has been used as the data acquisition unit, while Matlab has been used for the signal processing.
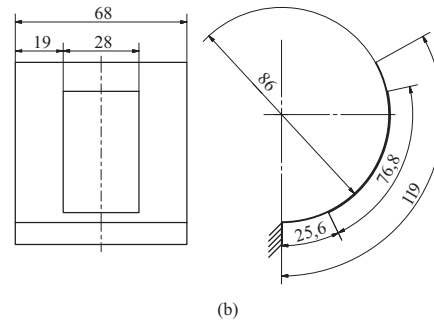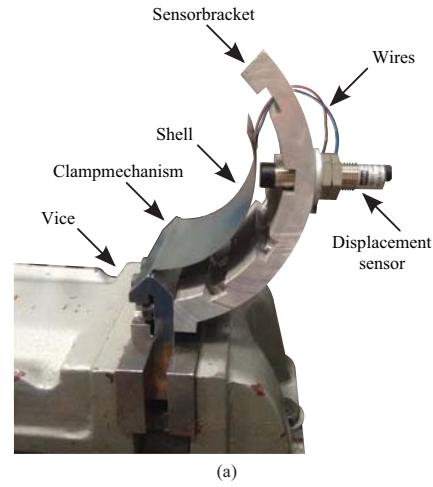

(a)

(b)

Figure 9. The piezoelectric layered shell used in the experiments and the test facility. (a) Piezoelectric layered shell mounted in the test facility. The clamping mechanism ensures equal possibility of the shell bending up or down. The sensor bracket provides the option for displacement measurements perpendicular to the shell surface at different locations circumferentially and axially. (b) The electromechanical model of the shell with selected dimensions. The remaining geometrical constants and material properties are given in Table 1.

Numerical and experimental results

Impact test

Experimental modal analysis is initially performed for three different cases via a hammer impact with a B & K 8200 force transducer and Pulsotronic KJ4-M12MN50-ANU eddy current displacement sensor. The sampling frequency is 2 kHz and the three cases are (1) the shell without the MFC patch; (2) the shell with the MFC patch and IDEs open circuit configuration; and (3) the shell with the MFC patch and IDEs short-circuited. Figure 10 illustrates a selected frequency response function (FRF) for the second case with amplitude unit mm/N. The impact force is applied close to the clamped extremity near the shell centerline to avoid loading

Table 1. The adopted dimensions and material properties of the physical shell.

Metal shell		
Curvature radius (without MFC patch)	42.5	[mm]
Curvature radius (with MFC patch)	43.0	[mm]
Angular extension	119	[°]
Width	68	[mm]
Thickness	0.254	[mm]
Young's modulus	207	[GPa]
Poisson's ratio	0.30	[−]
Density	8.100	$\left[\frac{g}{cm^3}\right]$
MFC patch		
Angular extension	76.8	[°]
Width	28	[mm]
Thickness	0.15	[mm]
Electrode centerline distance	0.5	[mm]
Electrode width	50	[μm]
Young's modulus (E_1)	30.336	[GPa]
Young's modulus (E_2)	15.857	[GPa]
Share modulus (G_{12})	5.512	[GPa]
Share modulus (G_{23})	0	[GPa]
Share modulus (G_{31})	0	[GPa]
Poisson's ratio (ν_{12})	0.31	[−]
Poisson's ratio (ν_{21})	0.16	[−]
Density	5.440	$\left[\frac{g}{cm^3}\right]$
Direct piezoelectric constant (d_{33})	800	$\left[\frac{pC}{N}\right]$
Direct piezoelectric constant (d_{31}), (d_{32})	−340	$\left[\frac{pC}{N}\right]$
Direct piezoelectric constant (d_{24}), (d_{15})	0	$\left[\frac{pC}{N}\right]$
Permittivity (ϵ_{33})	0.42	$\left[\frac{nF}{cm^2}\right]$
Permittivity (ϵ_{11}), (ϵ_{22})	0	$\left[\frac{nF}{cm^2}\right]$

Table 2. Theoretical and experimental natural frequencies for cases 1, 2 and 3. Deviations are calculated based on the experimental results.

	f[Hz]		
	First	Second	Third
Case 1: Shell without MFC			
Theory	27.71	60.95	116.4
Experiment	27.93	61.29	115.6
Deviation	−0.8 %	−0.6 %	0.7 %
Case 2: Shell with short-circuited MFC			
Theory	28.22	69.05	135.9
Experiment	27.76	68.25	136.5
Deviation	1.7 %	1.2 %	−0.4 %
Case 3: Shell with open-circuited MFC			
Theory	28.22	69.05	136.0
Experiment	27.95	68.55	136.3
Deviation	1.0 %	0.7 %	−0.2 %

Table 3. The Rayleigh damping coefficients obtained from the experimental modal analysis for all cases.

	$\alpha\left[\frac{1}{s}\right] - 1$	β[s]
Case 1	0.918	4.29×10^{-6}
Case 2	0.946	3.69×10^{-5}
Case 3	1.62	1.20×10^{-5}
Case 4	19.9	1.79×10^{-6}

problems such as overloading and double hit. The displacement sensor records the normal deflection of the shell and is placed as seen in Figure 9(a) at the edge of the shell in the axial direction. Similar FRFs have been obtained for cases 1 and 3 as well but are not shown here.

The large flexibility of the shell imposes a limitation on the magnitude of the impact force. This is to ensure the assumption of small vibration amplitudes is not violated and to keep the displacements within the range of the eddy current displacement sensor. The limitation for the impact force magnitude is reflected in a coherence around 0.9, as shown in Figure 10. This is the highest obtainable coherence under the given experimental conditions.

The three first resonance frequencies for the three cases are obtained experimentally as well as theoretically and given in Table 2. The agreement between the experimental and theoretical natural frequencies is good with discrepancies of less than 2%.

For all theoretical calculations with damping, Rayleigh damping $[_{u-u}D] = \alpha[_{u-u}M] + \beta[_{u-u}K]$ has been used as structural damping.

The parameters α and β given in Table 3 are calculated aided by the least squares method, using the experimental damping factors presented in Tables 4 and 5 with the corresponding experimental natural frequencies shown in Tables 2 and 6.

The natural frequencies depend more on geometry changes, that is, the curvature radius of the shell, due to the montage of the MFC patch than on the circuit configuration of the IDEs. The curvature radius significantly affects all natural frequencies, while the shell thickness has a more pronounced effect on the higher frequencies.

Excitation via MFC patch

In case 4 the MFC patch is used as an actuator and the shell is excited using either random signals (case 4a) or periodic signals (case 4b). The test setup remains the same as in the previous cases. Figure 11 shows the experimental and theoretical FRFs obtained for case 4a. The unit of the amplitude is mm/V. The theoretical
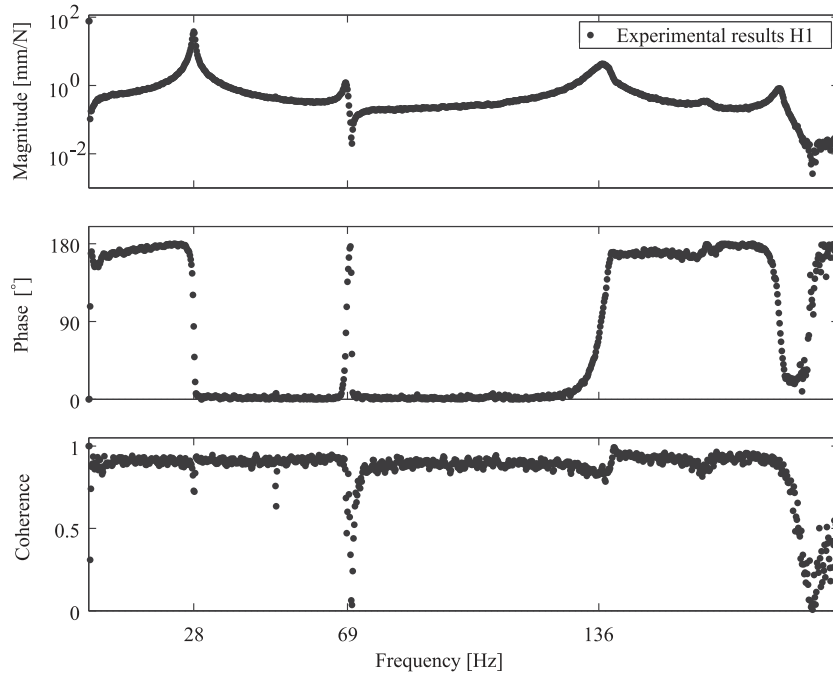
Figure 10. Experimental FRF, that is, amplitude, phase and coherence function, for the second case obtained via impact test with a B & K 8200 force transducer and Pulsotronic KJ4-M12MN50-ANU eddy current displacement sensor. The impact is close to the clamped edge near the centerline and the displacement sensor is located as seen in Figure 9(a) near the edge of the shell.

Table 4. Experimental damping factors for cases 1, 2 and 3.

	$\xi[-]$		
	First	Second	Third
Case 1: Shell without MFC	0.0030	0.0020	0.0022
Case 2: Shell with short-circuited MFC	0.0072	0.0050	0.0181
Case 3: Shell with open-circuited MFC	0.0048	0.0072	0.0049

FRF is calculated using the same excitation amplitude applied to the IDEs as that in the experiments.

Good agreement between theoretical and experimental FRF amplitudes is shown for the first five natural frequencies as seen in Table 6. Discrepancies are smaller than 4% for these natural frequencies and the amplitudes of the theoretical FRF results closely resemble the experimentally obtained ones up to approximately 450 Hz as seen in Figure 11. The phase of the theoretical FRF follows the behavior of the experimental one well, but some deviations are seen, especially between the third (69 Hz) and the sixth (471 Hz) natural frequencies. This is likely due to the simplifying assumption of Rayleigh structural damping and the α and β parameters used, which combined are not able to describe the more complex behavior of energy dissipation in the

Table 5. Damping factors corresponding to the six first natural frequencies obtained by actuation via the MFC patch. Case 4a shows the results obtained by the random signal FRF shown in Figure 11. Case 4b is a chip excitation via the MFC patch.

	$\xi[-] \times 10^{-2}$					
	First	Second	Third	Fourth	Fifth	Sixth
Case 4a						
Experiment	0.0101	0.00515	0.0126	0.00437	0.01430	0.00493
Case 4b: Chip signal						
Experiment	0.0552	0.0223	0.0208	0.00954	0.00332	0.00648

Table 6. The six first natural frequencies obtained by actuation via the MFC patch. Case 4a is the results obtained by the random signal FRF shown in Figure 11. Case 4b is a chip excitation via the MFC.

	f [Hz]					
	First	Second	Third	Fourth	Fifth	Sixth
Theory	28.17	69.03	135.9	184.7	447.1	470.8
Case 4a: Random signal						
Experiment	29.3	67.1	135	183	450	484
Deviation from theory	−3.8 %	2.9 %	0.7 %	0.9 %	−0.6 %	−2.7 %
Case 4b: Chip signal						
Experiment	28.14	69.51	134.7	183.2	443.4	468.3
Deviation from theory	0.1 %	−0.7 %	0.9 %	0.8 %	0.8 %	0.5 %
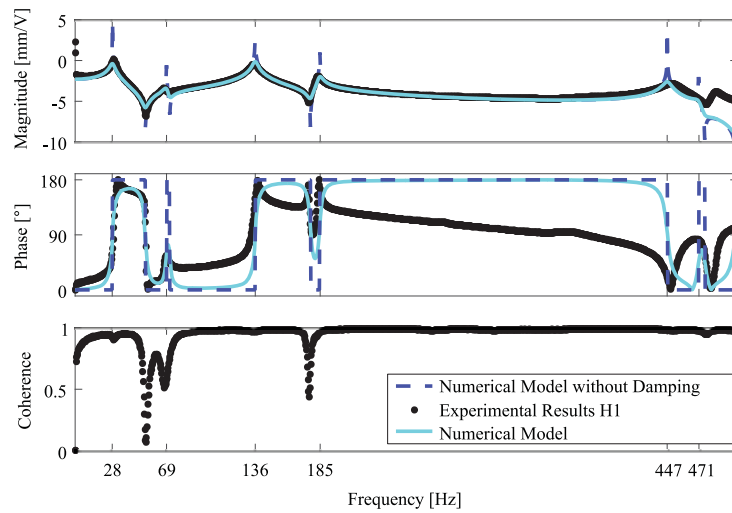
Figure 11. Experimental FRF obtained with a random 300 V amplitude excitation signal sent to the MFC patch and the displacement sensor located as seen in Figure 9(a) close to the edge (the same location as for cases 1, 2 and 3).

whole frequency range. The coherence function very close to 1 clearly shows the good quality of the measurement data.

The first six experimental and theoretical mode shapes are shown in Figure 12. The experimental modes are measured with a Polytec PSV-500 laser scanner. A laser beam is aimed in the horizontal direction at the shell measuring the vibration of the shell at the location. When the vibration is measured at several locations, the software ME'scope is used to calculate the mode shapes. The measured mode shapes are a projection of deflections onto a vertical plane parallel to the clamping surface; see Figure 9(b). The red color represents a large deflection, which can be either inward or outward. The green color represents no deflections, hence green lines seen in the mode shapes are nodal lines.

Comparing Figure 12(a) and (c), the reader can easily note the similarities between the theoretical and experimental first bending mode shapes. Theoretical as well as experimental mode shapes are symmetrical in relation to the middle plane in the axial direction.

Likewise, the same conclusion can be drawn for the third, fourth, fifth and sixth mode shapes, shown in Figure 12(e) to (l). The second bending mode shape can be clearly identified based on the first nodal line in the axial direction in Figure 12(e) and (g), while the third bending mode shape seen in Figure 12(i) and (k) has two nodal lines in the axial direction. The first and the second bending–twisting mode shapes are depicted in Figure 12(f) and (h) and Figure 12(j) and (l), respectively. One nodal line in the circumferential direction is seen in both cases. For the first bending–twisting mode shape only one single nodal line is detected in the axial direction while in the second two nodal lines are observed.

Poor results in terms of mode shapes can only be observed for the second one. A relatively large difference is detected when the theoretical (straight) and the experimental (bent) nodal lines in the circumferential direction are compared in Figure 12(b) and (d). The second mode is pure twisting, and since the MFC patch is mounted symmetrically on the shell with the piezo-electric fibers following the circumferential direction,
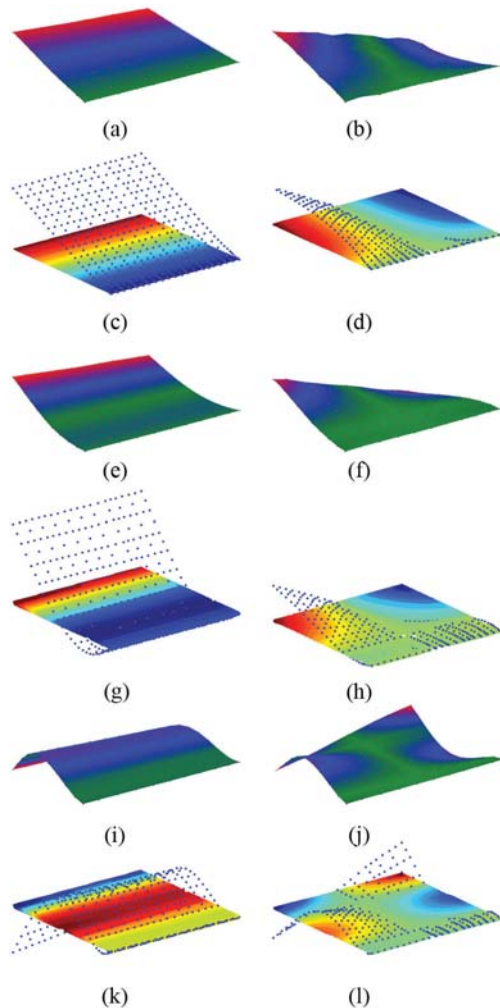
Figure 12. The six first experimental and numerical mode shapes projected onto a vertical plane parallel to the clamped edge. The green color in the experimental mode shapes corresponds to no movement, hence nodal lines are green. The red color corresponds to maximum movement, which can either be inward or outward. The vertical direction in the experimental mode shapes corresponds to the circumferential direction, and the horizontal direction corresponds to the axial direction. (a) First experimental mode shape. (b) Second experimental mode shape. (c) First numerical mode shape. (d) Second numerical mode shape. (e) Third experimental mode shape. (f) Fourth experimental mode shape. (g) Third numerical mode shape. (h) Fourth numerical mode shape. (i) Fifth experimental mode shape. (j) Sixth experimental mode shape. (k) Fifth numerical mode shape. (l) Sixth numerical mode shape.

an excitation of the second mode is hard to achieve. The vibration amplitude at the second resonance frequency is low due to this reason. This leads to insignificant participation of the second mode shape in the

total response of the shell, quantified by means of a low coherence value (around 0.5, seen in Figure 11, at the second resonance frequency at 69 Hz).

Limitations of the electromechanical model

The FEM model developed does not take into account any non-linearity, and despite the good agreement between the numerical and experimental results shown, the model has to be used with caution. An experimental example is given in Figure 13, where the amplitude of the input signal sent to the MCF actuator influences the maximum amplitudes of the resonances as well as the frequencies at which they occur. Generally speaking, the higher the MCF input voltage is, the higher the resonance peaks and the lower the resonance frequencies are. In Figure 13 the eight different FRFs are displayed based on voltage values ranging from 60 to 300 V, that is, from low voltage amplitudes in dark blue to high voltage amplitudes in light blue.

Piezoelectric materials are well known for their non-linear properties (see for example Peng and Chen, 2013, or Damjanovic, 1998), but with a voltage level of 300, well below the 1500 voltage specified by the supplier, the piezoelectric material is still in the linear range. In Figure 14 zoom views are seen of the first and third resonance peaks. This is a well-known geometric non-linearity for shells associated with large vibration amplitudes. Much literature exists on the subject, for example Selmane and Lakis (1997), who show a change in the resonance frequencies for a thin shell, at vibration amplitude levels equivalent to the thickness of the shell. The vibration amplitude at the first resonance frequency for the highest voltage level is approximately five times the thickness, in other words, the force generated by the MFC patch is large enough to excite the geometric non-linearities of the shell structure.

Conclusions

The electromechanical finite element model developed based on an eight-node double curved layered shell element takes the effects of piezoelectric fibers and IDEs mounted on the shell into account. The new electromechanical finite element only requires one extra DoF for each IDE pair when compared to the purely mechanical equivalent element, since the internal effects of the piezoelectric patch are included via Guyan reduction. Good agreement between experimental and theoretical FRFs are shown in a large frequency range from 0.5 to 450 Hz, that is, up to the fifth natural frequency. Natural frequencies are predicted with high accuracy and the deviations are smaller than 2% when using impact testing and 4% when using the MCF as an actuator. The six first mode shapes obtained experimentally agree very well with the theoretical ones, with the exception of the second mode shape, a pure twisting
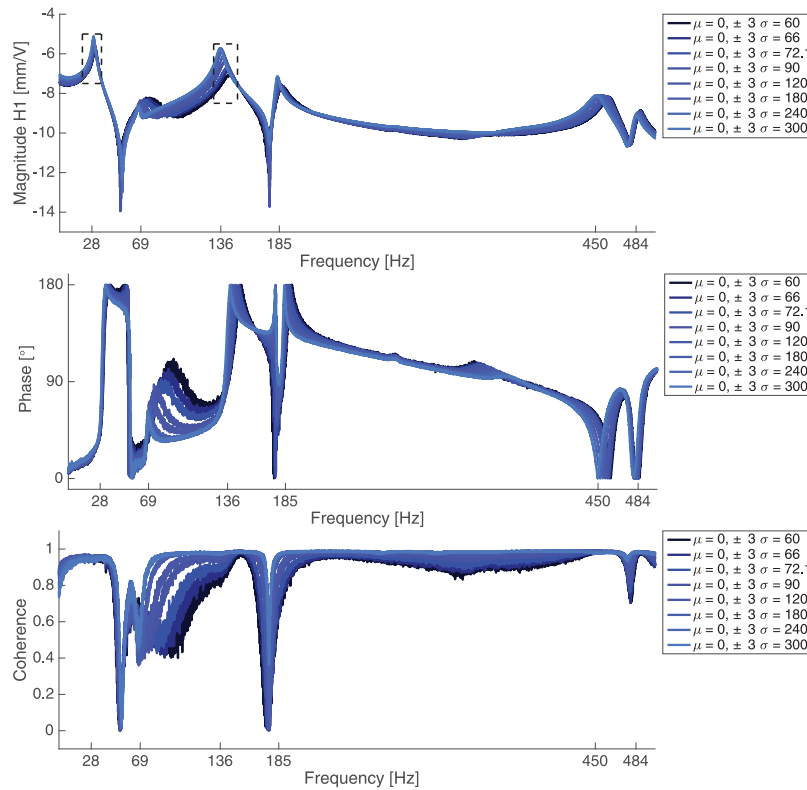
Figure 13. FRF with different excitation amplitudes. A non-linear effect dependent on the excitation amplitude is seen especially around the third resonance frequency.
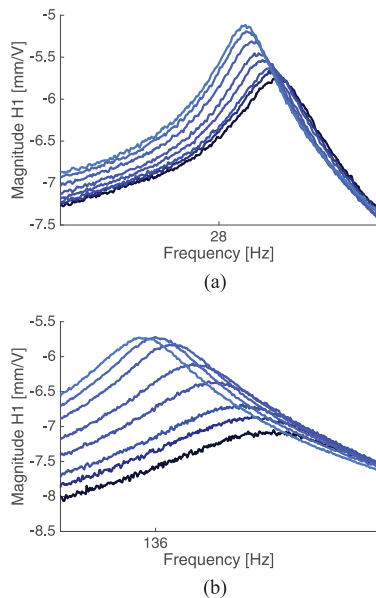

Figure 14. Zoom of the FRF at the first (a) and third (b) resonance frequencies.

mode, which hardly can be excited by the symmetrically mounted MFC patch on the shell. The electromechanical finite element model developed is able to resemble the linear dynamic behavior of the system very accurately. Further experimental evidence shown in the article leads to the conclusion that the behavior of the electromechanical system depends non-linearly on the amplitude of the input signal sent to the MCF actuator and the linear model must be used with caution. The higher the MCF input voltage is, the higher the resonance peaks and the lower the resonance frequencies are.

Declaration of Conflicting Interests

The author(s) declared no potential conflicts of interest with respect to the research, authorship, and/or publication of this article.

Funding

References

Allik H and Hughes TJR (1970) Finite element method for piezoelectric vibration. *International Journal for Numerical Methods in Engineering* 2(2): 151–157.

Balamurugan V and Narayanan S (2001) Shell finite element for smart piezoelectric composite plate/shell structures and its application to the study of active vibration control. *Finite Elements in Analysis and Design* 37(9): 713–738.

Balamurugan V and Narayanan S (2009) Multilayer higher order piezolaminated smart composite shell finite element and its application to active vibration control. *Journal of Intelligent Material Systems and Structures* 20(4): 425–441.

Bansal A and Ramaswamy A (2002) FE analysis of piezolaminate composites under thermal loads. *Journal of Intelligent Materials Systems and Structures* 13(5): 291–301.

Benjeddou A, Trindade MA and Ohayon R (1997) A unified beam finite element model for extension and shear piezoelectric actuation mechanisms. *Journal of Intelligent Material Systems and Structures* 8(12): 1012–1025.

Benjeddou A, Trindade MA and Ohayon R (1999) New shear actuated smart structure beam finite element. *AIAA Journal* 37: 378–383.

Bent AA and Hagood NW (1997) Piezoelectric fiber composites with interdigitated electrodes. *Journal of Intelligent Material Systems and Structures* 8(11): 903–919.

Bent AA, Hagood NW and Rodgers JP (1995) Anisotropic actuation with piezoelectric fiber composites. *Journal of Intelligent Material Systems and Structures* 6(3): 338–349.

Bilgen O, Erturk A and Inman DJ (2010) Analytical and experimental characterization of macro-fiber composite actuated thin clamped-free unimorph benders. *Journal of Vibration and Acoustics* 132(5): 051005.

Biscani F, Nasser H, Belouettar S, et al. (2011) Equivalent electro-elastic properties of macro fiber composite transducers using asymptotic expansion approach. *Composites Part B: Engineering* 42(3): 444–455.

Boudaoud H, Belouettar S, Daya EM, et al. (2008) A shell finite element for active-passive vibration control of composite structures with piezoelectric and viscoelastic layers. *Mechanics of Advanced Materials and Structures* 15(3–4): 208–219.

Brockmann TH and Lammering R (2006) Beam finite elements for rotating piezoelectric fiber composite structures. *Journal of Intelligent Material Systems and Structures* 17(5): 431–448.

Bryant RG (2007) Overview of NASA Langley's piezoelectric ceramic packaging technology and applications. In:*10th Japan international SAMPE symposium exhibition: JISSE-10*, Tokyo, Japan, pp. 1–8.

Chattopadhyay A, Li J and Gu H (1998) A coupled thermo-piezoelectric-mechanical model for smart composite laminates. In:*39th AIAA/ASME/ASCE/AHS/ASC structures, structural dynamics, and materials conference and exhibit*, Reston, VA, pp. 2902–2910.

Cook RD, Malkus DS, Plesha ME, et al. (2002) *Concepts and Applications of Finite Element Analysis*. 4th ed. New York, NY: John Wiley & Sons.

Damjanovic D (1998) Ferroelectric, dielectric and piezoelectric properties of ferroelectric thin films and ceramics. *Reports on Progress in Physics* 61: 1267–1324. DOI:10.1088/0034-4885/61/9/002.

Deraemaeker A, Nasser H, Benjeddou A, et al. (2009) Mixing rules for the piezoelectric properties of macro fiber composites. *Journal of Intelligent Material Systems and Structures* 20(12): 1475–1482.

Gabbert U, Köppe H, Seeger F, et al. (2002) Modeling of smart composite shell structures. *Journal of Theoretical and Applied Mechanics* 40(3): 575–593.

Guennam AE and Luccioni BM (2006) FE modeling of a closed box beam with piezoelectric fiber composite patches. *Smart Materials and Structures* 15(6): 1605–1615.

Guennam AE and Luccioni BM (2009) Piezoelectric shell FE for the static and dynamic analysis of piezoelectric fibre composite laminates. *Smart Materials and Structures* 18(9): 095044.

Guennam AE and Luccioni BM (2015) Model for piezoelectric/ferroelectric composites polarized with interdigitated electrodes. *Composite Structures* 131: 312–324.

Guyan RJ (1965) Reduction of stiffness and mass matrices. *AIAA Journal* 3(2): 380–380.

Hagood NW and Bent AA (1993) Development of piezoelectric fiber composites for structural actuation. In:*34th AIAA/ASME/ASCE/AHS/ASC structures, structural dynamics, and materials conference*, pp. 3625–3638.

Hagood NW, Kindel R, Ghandi K, et al. (1993) Improving transverse actuation of piezoceramics using interdigitated surface electrodes. In: *SPIE smart structures and intelligent systems*, pp. 341–352.

Kapuria S and Hagedorn P (2007) Unified efficient layerwise theory for smart beams with segmented extension/shear mode, piezoelectric actuators and sensors. *Journal of Mechanics of Materials and Structures* 2(7): 1267–1298.

Narayanan S and Balamurugan V (2003) Finite element modelling of piezolaminated smart structures for active vibration control with distributed sensors and actuators. *Journal of Sound and Vibration* 262(3): 529–562.

Nasser H, Biscani F and Belouettar S (2011) Effect of matrix properties on the overall piezoelectric constants of piezocomposite transducers. *Mechanics of Advanced Materials and Structures* 18(7): 531–539.

Nasser H, Deraemaeker A and Belouettar S (2008) Electric field distribution in macro fiber composite using interdigitated electrodes. *Advanced Materials Research* 47–50: 1173–1177.

Nguyen CH and Kornmann X (2006) A comparison of dynamic piezoactuation of fiber-based actuators and conventional PZT patches. *Journal of Intelligent Material Systems and Structures* 17(1): 45–55.

Panda S and Natarajan R (1981) Analysis of laminated composite shell structures by finite element method. *Computers & Structures* 14(3–4): 225–230.

Park JS and Kim JH (2005) Analytical development of single crystal macro fiber composite actuators for active twist rotor blades. *Smart Materials and Structures* 14(4): 745–753.

Peng J and Chen X (2013) A survey of modeling and control of piezoelectric actuators. *Modern Mechanical Engineering* 3(1): 1–20.

Piefort V and Henrioulle K (2000) Modelling of smart structures with colocated piezoelectric actuator/sensor pairs: Influence of the in-plane components. In: Roeck GD and Topping BHV (eds) *Identification, Control and Optimisation of Engineering Structures*. Edinburgh, UK: Civil-Comp Press, pp. 47–57.

Prasath SS and Arockiarajan A (2015) Effect of interphase and thermal environment on the effective properties of macro-fiber composites (MFC). *Composites Part B: Engineering* 75: 327–335.

Samanta B, Ray MC and Bhattacharyya R (1996) Finite element model for active control of intelligent structures. *AIAA Journal* 34(9): 1885–1893.

Saravanos DA (1997) Mixed laminate theory and finite element for smart piezoelectric composite shell structures. *AIAA Journal* 35: 1327–1333.

Schönecker AJ, Daue T, Brückner B, et al. (2006) Overview on macro fiber composite applications. In: *Proceedings of SPIE*, pp. 61701K 1-8.

Selmane A and Lakis AA (1997) Influence of geometric non-linearities on the free vibrations of orthotropic open cylindrical shells. *International Journal for Numerical Methods in Engineering* 40(6): 1115–1137.

Suleman A and Venkayya VB (1995) A simple finite element formulation for a laminated composite plate with piezoelectric layers. *Journal of Intelligent Material Systems and Structures* 6: 776–782.

Thurston EG (1953) The theoretical sensitivity of three types of rectangular bimorph transducers. *The Journal of the Acoustical Society of America* 25(4): 828.

Tiersten HF (1969) *Linear Piezoelectric Plate Vibrations*. New York, NY: Plenum Press.

Trindade MA and Benjeddou A (2011) Finite element homogenization technique for the characterization of d_{15} shear piezoelectric macro-fibre composites. *Smart Materials and Structures* 20(7): 075012.

Trindade MA, Benjeddou A and Ohayon R (2001) Finite element modelling of hybrid active-passive vibration damping of multilayer piezoelectric sandwich beams – Part I : Formulation. *International Journal for Numerical Methods in Engineering* 51: 835–854.

Tzou HS and Gadre M (1989) Theoretical analysis of a multi-layered thin shell coupled with piezoelectric shell actuators for distributed vibration controls. *Journal of Sound and Vibration* 132(3): 433–450.

Tzou HS and Tseng CI (1991) Distributed modal identification and vibration control of continua: Piezoelectric finite element formulation and analysis. *Journal of Dynamic Systems, Measurement, and Control* 113(3): 500.

Tzou HS and Ye R (1996) Analysis of piezoelastic structures with laminated piezoelectric triangle shell elements. *AIAA Journal* 34(1): 110–115.

Varelis D and Saravanos DA (2006) Coupled mechanics and finite element for non-linear laminated piezoelectric shallow shells undergoing large displacements and rotations. *International Journal for Numerical Methods in Engineering* 66(8): 1211–1233.

Vidal P, D'Ottavio M, Thaier MB, et al. (2011) An efficient finite shell element for the static response of piezoelectric laminates. *Journal of Intelligent Material Systems and Structures* 22(7): 671–690.

Williams RB, Park G, Inman DJ, et al. (2002) An overview of composite actuators with piezoceramic fibers. In: *20th IMAC conference on structural dynamics*, pp. 421–427.

Yasin MY and Kapuria S (2013) An efficient finite element with layerwise mechanics for smart piezoelectric composite and sandwich shallow shells. *Computational Mechanics* 53(1): 101–124.

Appendix

Constants and matrices in the constitutive equations

The constants in the constitutive equations are given by

$$[e] = [d][C] \quad [\eta] = [\epsilon] - [d][e]^{\mathrm{T}}$$

based on material parameters given by the manufacturer.

The material matrices are

$$[C] = \begin{bmatrix} c_{11} & \nu_{21}c_{11} & 0 & 0 & 0 & 0 \\ \nu_{12}c_{22} & c_{22} & 0 & 0 & 0 & 0 \\ 0 & 0 & 0 & 0 & 0 & 0 \\ 0 & 0 & 0 & G_{12} & 0 & 0 \\ 0 & 0 & 0 & 0 & G_{23} & 0 \\ 0 & 0 & 0 & 0 & 0 & G_{31} \end{bmatrix}$$

$$[d] = \begin{bmatrix} 0 & 0 & 0 & 0 & d_{15} & 0 \\ 0 & 0 & 0 & d_{24} & 0 & 0 \\ d_{31} & d_{32} & d_{33} & 0 & 0 & 0 \end{bmatrix}$$

$$[\epsilon] = \begin{bmatrix} \epsilon_{11} & 0 & 0 \\ 0 & \epsilon_{22} & 0 \\ 0 & 0 & \epsilon_{33} \end{bmatrix}$$

The elastic stiffness matrix $[C]$ is given for a plane stress, which is a valid assumption for the plates and shells. Both the direct piezoelectric constant $[d]$ and the dielectric permittivity $[\epsilon]$ have the direction of polarization in the third axis direction, while the elastic stiffness matrix has a surface normal in the third direction.

The constants for the elastic stiffness matrix are

$$c_{11} = \frac{E_1}{1 - \nu_{12}\nu_{21}} \quad c_{22} = \frac{E_2}{1 - \nu_{12}\nu_{21}}$$

Electric enthalpy

Combining the change in the enthalpy (3b) and the constitutive equations (1) we get

$$H = \int \left[\int \left([C]\{\varepsilon\} - [e]^{\mathrm{T}}\{E\} \right)^{\mathrm{T}} \{d\varepsilon\} \right.$$
$$\left. - \int \left([e]\{\varepsilon\} + [\eta]\{E\} \right)^{\mathrm{T}} \{dE\} \right] dV$$

Calculating the internal integrals and utilizing the diagonal symmetry of the elastic stiffness matrix $[C]$ and the electric permittivity matrix $[\eta]$ yields

$$H = \int \left[\frac{1}{2}\{\varepsilon\}^{\mathrm{T}}[C]\{\varepsilon\} - \{E\}^{\mathrm{T}}[e]\{\varepsilon\} \right.$$
$$\left. - \{\varepsilon\}^{\mathrm{T}}[e]^{\mathrm{T}}\{E\} - \frac{1}{2}\{E\}^{\mathrm{T}}[\eta]\{E\} \right] dV$$

The cross-coupling terms are the transposes of each other

$$\{\varepsilon\}^\mathrm{T}[e]^\mathrm{T}\{E\} = \left(\{E\}^\mathrm{T}[e]\{\varepsilon\}\right)^\mathrm{T}$$

When the transpose is ignored the equation for the total enthalpy given in equation (6b) is found. This is possible since the transposed result is a scalar.

Differential operators

The differential operators for the strain to displacement and for the electric field to electric potential are

$$[\partial] = \begin{bmatrix} \dfrac{\partial}{\partial x} & 0 & 0 \\ 0 & \dfrac{\partial}{\partial y} & 0 \\ 0 & 0 & \dfrac{\partial}{\partial z} \\ \dfrac{\partial}{\partial y} & \dfrac{\partial}{\partial x} & 0 \\ 0 & \dfrac{\partial}{\partial z} & \dfrac{\partial}{\partial y} \\ \dfrac{\partial}{\partial z} & 0 & \dfrac{\partial}{\partial x} \end{bmatrix} \quad \{\nabla\} = \begin{Bmatrix} \dfrac{\partial}{\partial x} \\ \dfrac{\partial}{\partial y} \\ \dfrac{\partial}{\partial z} \end{Bmatrix}$$

Lagrangian differentiated

The discretized Lagrangian is divided into four terms as shown in equation (11), where only the non-zero differentiated results are shown in the equations below. The "prime" terms in the five equations, for example $\{\dot{u}_e\}'$, are the DoFs differentiated with respect to one specific general coordinate.

Term I only depends on the velocities

$$\frac{\partial}{\partial t}\left(\frac{\partial}{\partial\{\dot{u}_i\}}\left[\rho\{\dot{u}_e\}^\mathrm{T}[_uN]^\mathrm{T}[_uN]\{\dot{u}_e\}\right]\right)$$
$$= 2\rho\frac{\partial}{\partial t}\left(\left(\{\dot{u}_e\}'\right)^\mathrm{T}[_uN]^\mathrm{T}[_uN]\{\dot{u}_e\}\right)$$
$$= 2\rho[_uN]^\mathrm{T}[_uN]\{\ddot{u}_e\}$$

Term II only depends on the deflections

$$\frac{\partial}{\partial u_i}\left[([_uB]\{u_e\})^\mathrm{T}[C][_uB]\{u_e\}\right]$$
$$= 2\left(\{u_e\}'\right)^\mathrm{T}[_uB]^\mathrm{T}[C][_uB]\{u_e\}$$
$$= 2[_uB]^\mathrm{T}[C][_uB]\{u_e\}$$

Term III depends both on the deflections and the electric potential

$$\frac{\partial}{\partial u_i}\left[([_\phi B]\{\phi_e\})^\mathrm{T}[e][_uB]\{u_e\}\right]$$
$$= \left(\{u_e\}'\right)^\mathrm{T}\left([_\phi B]^\mathrm{T}[e][_uB]\right)^\mathrm{T}\{\phi_e\}$$
$$= \left([_\phi B]^\mathrm{T}[e][_uB]\right)^\mathrm{T}\{\phi_e\}$$
$$\frac{\partial}{\partial\phi_i}\left[([_\phi B]\{\phi_e\})^\mathrm{T}[e][_uB]\{u_e\}\right]$$
$$= \left(\{\phi_e\}'\right)^\mathrm{T}[_\phi B]^\mathrm{T}[e][_uB]\{u_e\}$$
$$= [_\phi B]^\mathrm{T}[e][_uB]\{u_e\}$$

Term IV depends only on the electric potential

$$\frac{\partial}{\partial\phi_i}\left[([_\phi B]\{\phi_e\})^\mathrm{T}[\eta][_\phi B]\{\phi_e\}\right]$$
$$= 2\left(\{\phi_e\}'\right)^\mathrm{T}[_\phi B]^\mathrm{T}[\eta][_\phi B]\{\phi_e\}$$
$$= 2[_\phi B]^\mathrm{T}[\eta][_\phi B]\{\phi_e\}$$

Local coordinates

The local coordinate vectors are given as the cosine direction of the global coordinate system

$$\{V_{1i}\} = \begin{Bmatrix} l_{1i} \\ m_{1i} \\ n_{1i} \end{Bmatrix},\{V_{2i}\} = \begin{Bmatrix} l_{2i} \\ m_{2i} \\ n_{2i} \end{Bmatrix},\{V_{3i}\} = \begin{Bmatrix} l_{3i} \\ m_{3i} \\ n_{3i} \end{Bmatrix}$$

In order to relate the global coordinate system to the local coordinates the transformation matrix needed is restated from Cook et al. (2002) (transformation from global to local)

$$[T] = \begin{bmatrix} l_1 & m_1 & n_1 \\ l_2 & m_2 & n_2 \\ l_3 & m_3 & n_3 \end{bmatrix}$$

For the case of relating the strain or stress from the global to the local coordinate system the extended transformation matrix is

$$[T_\varepsilon] = \begin{bmatrix} l_1^2 & m_1^2 & n_1^2 & l_1 m_1 & \cdots \\ l_2^2 & m_2^2 & n_2^2 & l_2 m_2 & \cdots \\ l_3^2 & m_3^2 & n_3^2 & l_3 m_3 & \cdots \\ 2l_1 l_2 & 2m_1 m_2 & 2n_1 n_2 & l_1 m_2 + l_2 m_1 & \cdots \\ 2l_2 l_3 & 2m_2 m_3 & 2n_2 n_3 & l_2 m_3 + l_3 m_2 & \cdots \\ 2l_3 l_1 & 2m_3 m_1 & 2n_3 n_1 & l_3 m_1 + l_1 m_3 & \cdots \end{bmatrix}$$

$$\begin{bmatrix} \cdots & m_1 n_1 & n_1 l_1 \\ \cdots & m_2 n_2 & n_2 l_2 \\ \cdots & m_3 n_2 & n_3 l_3 \\ \cdots & m_1 n_2 + m_3 n_1 & n_1 l_2 + n_2 l_1 \\ \cdots & m_2 n_3 + m_2 n_2 & n_2 l_3 + n_3 l_2 \\ \cdots & m_3 n_1 + m_1 n_3 & n_3 l_1 + n_1 l_3 \end{bmatrix}$$

Shape functions

The shape function for an eight-node element given in isoparametric coordinates is

$$N_1 = \frac{1}{4}(1 - \xi)(1 - \eta) - \frac{1}{2}N_5 - \frac{1}{2}N_8$$

$$N_2 = \frac{1}{4}(1 + \xi)(1 - \eta) - \frac{1}{2}N_5 - \frac{1}{2}N_6$$

$$N_3 = \frac{1}{4}(1 + \xi)(1 + \eta) - \frac{1}{2}N_6 - \frac{1}{2}N_7$$

$$N_4 = \frac{1}{4}(1 - \xi)(1 + \eta) - \frac{1}{2}N_7 - \frac{1}{2}N_8$$

$$N_5 = \frac{1}{2}\left(1 - \xi^2\right)(1 - \eta)$$

$$N_6 = \frac{1}{2}(1 + \xi)\left(1 - \eta^2\right)$$

$$N_7 = \frac{1}{2}\left(1 - \xi^2\right)(1 + \eta)$$

$$N_8 = \frac{1}{2}(1 - \xi)\left(1 - \eta^2\right)$$

The shape function matrices used at the element level are

$$[_u N_i] = N_i \begin{bmatrix} 1 & 0 & 0 & -\zeta \frac{t}{2} l_{2i} & \zeta \frac{t}{2} l_{1i} \\ 0 & 1 & 0 & -\zeta \frac{t}{2} m_{2i} & \zeta \frac{t}{2} m_{1i} \\ 0 & 0 & 1 & -\zeta \frac{t}{2} n_{2i} & \zeta \frac{t}{2} n_{1i} \end{bmatrix}$$

$$[_\phi N_i] = N_i$$

Jacobian matrix

The volume integration of the double curved element required in governing equation (16) must be performed numerically in isoparametric coordinates due to the shape function. The transformation between the two types of coordinate systems is done via a Jacobian matrix, which is

$$[J] = \begin{bmatrix} x_{,\xi} & y_{,\xi} & z_{,\xi} \\ x_{,\eta} & y_{,\eta} & z_{,\eta} \\ x_{,\zeta} & y_{,\zeta} & z_{,\zeta} \end{bmatrix}$$

The in-plane derivatives for the Jacobian matrix are

$$x_{,\xi} = \sum N_{i,\xi}\left(x_i + \zeta \frac{t_i l_{3i}}{2}\right)$$

$$y_{,\xi} = \sum N_{i,\xi}\left(y_i + \zeta \frac{t_i m_{3i}}{2}\right)$$

$$z_{,\xi} = \sum N_{i,\xi}\left(z_i + \zeta \frac{t_i n_{3i}}{2}\right)$$

$$x_{,\eta} = \sum N_{i,\eta}\left(x_i + \zeta \frac{t_i l_{3i}}{2}\right)$$

$$y_{,\eta} = \sum N_{i,\eta}\left(y_i + \zeta \frac{t_i m_{3i}}{2}\right)$$

$$z_{,\eta} = \sum N_{i,\eta}\left(z_i + \zeta \frac{t_i n_{3i}}{2}\right)$$

The out-of-plane derivatives for the Jacobian matrix are

$$x_{,\zeta} = \sum N_i \frac{t_i l_{3i}}{2}$$

$$y_{,\zeta} = \sum N_i \frac{t_i m_{3i}}{2}$$

$$z_{,\zeta} = \sum N_i \frac{t_i n_{3i}}{2}$$

Derivative matrices

The derivative matrices needed for calculating the mass and stiffness matrices are

$$[B_u] = [_u H]\,[_u J]\,[_u N'] \tag{25a}$$

$$[B_\phi] = [J]^{-1}[_\phi N'] \tag{25b}$$

The derivative matrix for strain to displacement requires a relationship matrix $[_u H]$ to relate the displacement coordinates to strain coordinates. This is

$$[_u H] = \begin{bmatrix} 1 & 0 & 0 & 0 & 0 & 0 & 0 & 0 & 0 \\ 0 & 0 & 0 & 0 & 1 & 0 & 0 & 0 & 0 \\ 0 & 0 & 0 & 0 & 0 & 0 & 0 & 0 & 1 \\ 0 & 1 & 0 & 1 & 0 & 0 & 0 & 0 & 0 \\ 0 & 0 & 0 & 0 & 0 & 1 & 0 & 1 & 0 \\ 0 & 0 & 1 & 0 & 0 & 0 & 1 & 0 & 0 \end{bmatrix}$$

Jacobian matrix $[_u J]$ used in the derivative matrix for strain to displacement is expanded to accommodate shear terms in the transformation from isoparametric to physical coordinates

$$[_uJ] = \begin{bmatrix} [J]^{-1} & [0] & [0] \\ [0] & [J]^{-1} & [0] \\ [0] & [0] & [J]^{-1} \end{bmatrix}$$

The matrix containing the derivatives of the shape functions $[_uN']$ used for the strain-to-displacement derivative matrix is

$$[_uN_i]' = \begin{bmatrix} N_{i,\xi} & 0 & 0 & -\zeta t_i N_{i,\xi} l_{2i}/2 & \ldots \\ N_{i,\eta} & 0 & 0 & -\zeta t_i N_{i,\eta} l_{2i}/2 & \ldots \\ 0 & 0 & 0 & -t_i N_i l_{2i}/2 & \ldots \\ 0 & N_{i,\xi} & 0 & -\zeta t_i N_{i,\xi} m_{2i}/2 & \ldots \\ \vdots & \vdots & \vdots & \vdots \\ 0 & 0 & 0 & -t_i N_i n_{2i}/2 & \ldots \end{bmatrix}$$

$$\begin{aligned} \ldots & \quad \zeta t_i N_{i,\xi} l_{1i}/2 \\ \ldots & \quad \zeta t_i N_{i,\eta} l_{1i}/2 \\ \ldots & \quad \zeta t_i N_{i,\eta} l_{1i}/2 \\ \ldots & \quad \zeta t_i N_{i,\xi} m_{1i}/2 \\ & \quad \vdots \\ \ldots & \quad \zeta t_i N_{i,\eta} n_{1i}/2 \end{aligned}$$

This matrix results in strain from the nodal displacements in isoparametric coordinates.

The matrix containing the derivatives of the shape functions $[_\phi N']$ used for the electrical potential to electric field derivative matrix is

$$[_\phi N_i]' = \begin{bmatrix} N_{i,\xi} \\ N_{i,\eta} \\ 0 \end{bmatrix}$$

This matrix results in strain from the nodal displacements in isoparametric coordinates.

Publication P2

Transient and Steady-State Behaviour of Elasto-Aerodynamic Air Foil Bearings, Considering Bump Foil Compliance and Top Foil Inertia and Flexibility - Numerical Investigation

This paper was published on-line in Journal of Engineering Tribology (Proceedings of the Institution of Mechanical Engineers, Part J) in February 2017. The paper presents a non-linear mathematical model for an AFB including a structural model of the top foil and a bilinear version of the SEFM.

Transient and steady state behaviour of elasto–aerodynamic air foil bearings, considering bump foil compliance and top foil inertia and flexibility: A numerical investigation

Bo B. Nielsen[1] and Ilmar F. Santos[1]

Abstract

This work gives a theoretical contribution to the problem of modelling air foil bearings considering large sagging effects in the calculation of the non-linear transient and steady state response of a rigid rotor. This paper consists of two parts: the development of a miltiphysics model of the air foil bearing, and a numerical parameter study of a rigid journal supported in an air foil bearing with a partially supported top foil. The mathematical model of the air foil bearing is centred around the finite element models of both the air film and the top foil structure. These finite element models utilise two types of eight-node isoparametric elements. The rotor is modelled as a rigid body without rotational inertia, i.e. as a journal. The bump foil is included via a bilinear version of the simple elastic foundation model. This paper introduces the bilinear simple elastic foundation model, which combined with the top foil structure model, enables a separation of the top foil and the bump foil. A phenomenon associated within areas of the top foil is where the aerodynamic pressure is sub-ambient. The parameter study investigates the performance of three air foil bearings with partially supported top foils and one air foil bearing with a fully supported top foil. The steady state responses of a journal supported by these air foil bearings are investigated for varied rotational speeds and journal unbalances as well as the top foil sagging in the unsupported area. The study reveals that sub-harmonic vibrations associated with a large journal unbalance can be eliminated by a proper design layout of the bump foil, i.e. placement of the unsupported area. The positive effect is attributed to 'equivalent shallow pockets' formed by the sagging top foil.

Introduction

In many industrial sectors, air foil bearings (AFBs) are frequently used in the development of high speed rotor machinery, e.g. air cycle machines and auxiliary power units for aeroplanes, in cryogenic turbopumps and turbo compressors.[1–3] The advantages of AFBs are their mechanical simplicity, the possibility of using the process media as the lubricant, eliminating seals, their passive stability at high rotational speeds, i.e. without using a controller to stabilise them in contrast to active magnetic bearings, and their low energy losses due to the low viscosity of the gases. However, this last advantage does also restrict the load carrying capacity, especially at low rotational speeds. The AFB is an advanced machine element which requires high precision in the manufacturing

and assembly phases to work properly. Due to their non-linear nature, unwanted sub-harmonic vibrations may appear, imposing a limitation on the applicability of the AFB. Large sub-harmonic vibrations have in some cases been reported as the reason for a bearing failure due to the rotor bearing contact.[4]

Some of the first experimental and numerical results for AFBs known from the literature were

---
[1]Department of Mechanical Engineering, Technical University of Denmark, Denmark

Corresponding author:
Ilmar F Santos, Technical University of Denmark, Department of Mechanical Engineering, Niels Koppels Alle 404, 2800, Kgs. Lyngby, Denmark.
Email: ifs@mek.dtu.dk

presented in the late 1970s and early 1980s.[5–7] In the numerical model, a top foil without structural stiffness or mass was supported by individual linear springs and dampers representing the flexible bump foil. This way of modelling the bump foil is commonly called the simple elastic foundation model (SEFM). The bump foil only provides support to the top foil when the air film pressure is higher than the ambient pressure. Regions of the air film with sub-ambient pressures were neglected by the use of the Gümbel condition,[8] since sub-ambient pressures can cause the top foil and the bump foil to separate.

There are two main sources of non-linearities in AFBs: Aerodynamic forces from the air film and dry friction forces existing in the contact surfaces between bump foil, top foil and bearing housing. The dry friction was the first non-linear feature to be addressed, since a proper use of the SEFM requires knowledge about equivalent viscous damping factors due to the hysteresis and varying stiffness of each individual bump. Numerical and experimental investigations of the bump foil characteristics under stick–slip conditions were performed on flat bump foils,[9,10] and by using an AFB mounted on a non–rotating journal.[11] More recently, the non-linear characteristics of the bump foil have been experimentally examined.[12–15] More accurate bump foil models have also been developed that are better at predicting non-linear bump foil behaviour.[16]

Traditional dynamic analyses of rotors supported by AFBs are based on linearised aerodynamic and friction forces, i.e. linear stiffness and damping and SEFM. These analyses have shown good agreement with experimental results at low unbalance or with small perturbations from the equilibrium position.[3,17] However, predictions by a linear model are not sufficient for larger perturbations of the equilibrium position, since the non-linearities of the AFB will be more pronounced.[18] An efficient computational technique for solving the non-linear compressible Reynolds equation has therefore been introduced.[19,20] The technique was used to simulate the non-linear transient response of a rotor supported in an AFB.[21] Similar numerical simulations have shown good agreement with experimental results for both small and large levels of unbalance, i.e. capturing the most significant sub-harmonic vibrations.[22]

Many authors have presented AFB models with a structural model of the top foil.[23–29] These models have been used to investigate the influence of the top foil on the AFB performance. The most common studies are on the effects of top foil sagging, i.e. the equilibrium position, dynamic coefficients and top foil deformation amongst others.

In order to improve the performance of AFBs, two different approaches have been followed:

(a) change the support of the top foil by replacing the bump foil with another support structure,[30–33] e.g. a metal mesh;

(b) modify the properties of the bump foil along the circumferential and axial direction making a non–uniform stiffness support.[34,35]

Neither of the two approaches have yielded any significant improvement to the performance of the AFB, with the exception of placing shims between the bump foil and the bearing housing. This method introduces a mechanical preload in the AFB due to the elevation of the affected bumps. The sub-harmonic vibrations in an AFB supporting a rigid journal can be reduced or eliminated through the use of shims, at the cost of larger synchronous vibration amplitude.[36]

In this context, the main original contribution of this work relies on the development of a non-linear fluid–mechanical finite element (FE) model for an AFB with the capability of simulating the transient response of the journal, the air film and the top foil. The model consists of four parts:

(a) the journal is modelled as a particle, hence without rotational inertia and gyroscopic effects;
(b) the top foil with inertia and flexibility is modelled with dynamic eight-node double curved shell elements, which are based on the static equivalent;[37]
(c) the air film, which is governed by the compressible Reynolds equation, is modelled using a similar flat eight-node FE that follows the formulation presented for a four-node equivalent element;[38]
(d) the bump foil is modelled as a bilinear SEFM, only supporting compression caused by the outward movement of the top foil.

It is important to highlight that the support forces on the bump foil modelled by the bilinear SEFM depends on the deflection and velocity of the top foil. This differs from the classical SEFM, where the deflection of the bump foil defines the deflection of the top foil, and is based on the pressure difference between the aerodynamic pressure and the ambient pressure. The structure model of the top foil included in the AFB model enables the modelling of an AFB with a partially supported top foil, i.e. an area of the top foil is unsupported. This differs from models not incorporating the structure of the top foil, hence common models using a classical SEFM. The presented model is validated using an existing AFB model based on a classical SEFM known from the literature.[3]

A parameter study is performed showing the capabilities of the presented AFB model. In this study, a journal is supported by four variants of the same AFB, with the difference being the layouts of the bump foil supporting the top foil, i.e. a partially supported top foil.

Fluid mechanical model

In Figure 1(a) a schematic design of a journal in an AFB with one bearing segment is shown. The bearing

consists of four different elements: a rigid bearing sleeve and a bump foil supporting a flexible top foil and an air film. In the transformation from the physical system to the fluid–mechanical model, the four elements of the bearing and the journal have been reduced to: Two continuous domains, a rigid moving body and bilinear springs/viscous dampers (see Figure 1(b)). The main assumptions are listed below:

(a) the bearing sleeve is rigid;
(b) the journal rotates at a constant speed and moves linearly inside the bearing, parallel to the bearing housing;
(c) the gas is considered to be an ideal gas;
(d) the top foil is a flexible and linear elastic shell;
(e) the bump foil can be represented by a bilinear SEFM only supporting the top foil in a radial direction and only when the radial deflection of the top foil has passed the initial position going outwards.

In Figure 1(c) the interactions between the different domains are shown. The aerodynamic pressure affects the journal and the top foil, while the movement of the journal and the top foil defines the thickness of the air film. The interaction between the top foil and the bump foil depends on the movement of the top foil, i.e. if they are in contact or not. When the top foil and bump foil are in contact the bump foil provides a supporting pressure to the top foil based on the deflections and velocities of the top foil.

Mathematical model

The miltiphysics model describing the behaviour of an AFB is derived in accordance with the four domains shown in Figure 1(b) and (c). The governing equation for each domain is individually given and subsequently coupled to build the global mathematical model. The use of the FE method to discretise the continuous domains provides a structure for the transfer of information between different domains and coordinate systems. The spatial location of the nodes in each domain corresponds to the location of the nodes in the other domains; hence, nodal values are transferred directly from one domain to the next without any interpolation.

Rigid journal: Modelled as a particle

The equation for the motion of the rigid journal is obtained from Newton's second law, as given in equation (1) in the global coordinate system and on the state space form. $\mathbf{M}_r$ is the rotor mass matrix, W_r is the combined dead load and payload on the rotor, F_r is the bearing forces due to the aerodynamic pressure and F_{ub} is the unbalance force from
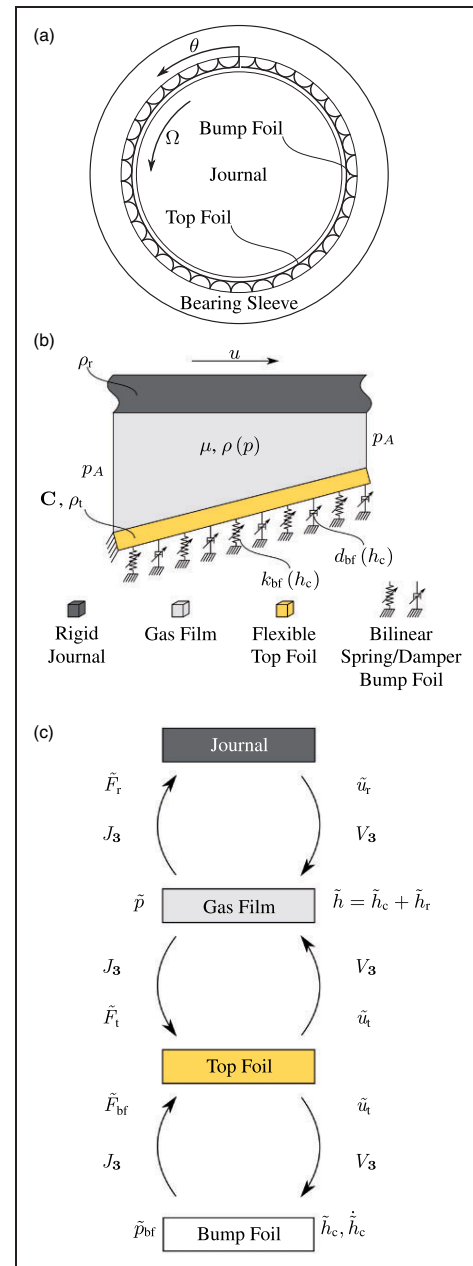

Figure 1. A sketch of the physical system, the corresponding fluid–mechanical model and the interactions between the domains of the fluid–mechanical system. (a) Schematics of an AFB with one bearing segment, i.e. one pair of top and bump foil. The sketches are not drawn to scale. (b) The fluid–mechanical model of a bearing segment consistent of four domains, i.e. two continous (air film and top foil) and two discrete (journal and bump foil). (c) Domain interactions. The top foil is affected by the support forces from the bump foil and the aerodynamic pressure, which also affects the journal. The bump foil is affected by the radial deflections and velocities of the top foil. The thickness of the air film is given by the movement of the top foil and the journal.

the rotor.

$$
\begin{bmatrix} \mathbf{I} & 0 \\ 0 & \tilde{\mathbf{M}}_r \end{bmatrix} \begin{Bmatrix} \dot{\tilde{x}}_r \\ \ddot{\tilde{x}}_r \end{Bmatrix} + \begin{bmatrix} 0 & -\mathbf{I} \\ 0 & 0 \end{bmatrix} \begin{Bmatrix} \tilde{x}_r \\ \dot{\tilde{x}}_r \end{Bmatrix}
$$
$$
= \begin{Bmatrix} 0 \\ \tilde{W}_r - \tilde{F}_r + \tilde{F}_{ub} \end{Bmatrix} \tag{1}
$$

Top foil: Modelled with finite elements

The top foil is assumed to be a flexible structure with inertia. The equation of motion for the top film can be derived, e.g. via Lagrange's equation (2), by taking the kinetic and internal energies of the top foil into account.

$$
\frac{\partial}{\partial t}\left(\frac{\partial L}{\partial \dot{q}_i}\right) - \frac{\partial L}{\partial q_i} = F_i \tag{2}
$$

The potential energy of the linear elastic top foil is governed by Hook's law given in equation (3), where **C** is the constitutive matrix.

$$
\sigma = \mathbf{C}\varepsilon \tag{3}
$$

The Lagrangian L is defined as the kinetic energy minus the internal energy for an elastic continuum with inertia and it is given by equation (4). A linear strain displacement relation has been used, $\varepsilon = {}_{\mathbf{u}}\partial u$, and via separation of the variables the deformation of the continuum is divided into a spatial dependent shape function ${}_{\mathbf{u}}\mathbf{N}$ and a time dependent discrete deflection variable.

$$
L = \frac{1}{2}\int\left[\overbrace{\rho({}_{\mathbf{u}}\mathbf{N}\dot{u}_{\mathbf{e}})^T{}_{\mathbf{u}}\mathbf{N}\dot{u}_{\mathbf{e}}}^{\text{Kinetic energy}} - \underbrace{({}_{\mathbf{u}}\partial_{\mathbf{u}}\mathbf{N}u_{\mathbf{e}})^T\mathbf{C}_{\mathbf{u}}\partial_{\mathbf{u}}\mathbf{N}u_{\mathbf{e}}}_{\text{Internal energy}}\right]\mathrm{d}V \tag{4}
$$

Using the Lagrangian in Lagrange's equation (2) yields the equation of motion stated in equation (5).

$$
\int_V\left(\rho_{\mathbf{u}}\mathbf{N}^T{}_{\mathbf{u}}\mathbf{N}\ddot{u}_{\mathbf{e}} + {}_{\mathbf{u}}\mathbf{B}^T\mathbf{C}_{\mathbf{u}}\mathbf{B}u_{\mathbf{e}}\right)\mathrm{d}V = F_t \tag{5}
$$

The same formulation is given in matrix form in equation (6), where the Rayleigh damping $\mathbf{C}_t = \alpha\mathbf{M}_t + \beta\mathbf{K}_t$ has been included as the structural damping for the top foil. F_t is the nodal force vector corresponding to the nodal deflection variables.

$$
\mathbf{M}_t\ddot{u}_t + \mathbf{C}_t\dot{u}_t + \mathbf{K}_tu_t = F_t \tag{6}
$$

The mass $\mathbf{M}_t$ and stiffness matrices $\mathbf{K}_t$ are given by equation (7).

$$
\mathbf{M}_e = \int_V {}_{\mathbf{u}}\mathbf{N}^T\rho_{\mathbf{u}}\mathbf{N}\mathrm{d}V \tag{7a}
$$

$$
\mathbf{K}_e = \int_V {}_{\mathbf{u}}\mathbf{B}^T\mathbf{C}_{\mathbf{u}}\mathbf{B}\mathrm{d}V \tag{7b}
$$

Neither the shape function nor the kinematic relationship for the nodal deflection variables used in the equation of motion have been specified yet.

The eight-node shell FE developed to analyse a layered double curved shell under static loading is used as the base element for the top foil,[37] hence, only a brief derivation of the dynamic version is presented in order to highlight the terms that are used in the coupling to the other domains. The shell element is based on first order shear deformation theory. The nodal degrees of freedom (DoFs) are linear displacement given in global coordinates and in–plane rotations, as seen in Figure 2(a). This results in 40 nodal DoFs per element. The location of each node in the double curved shell elements are given in the global
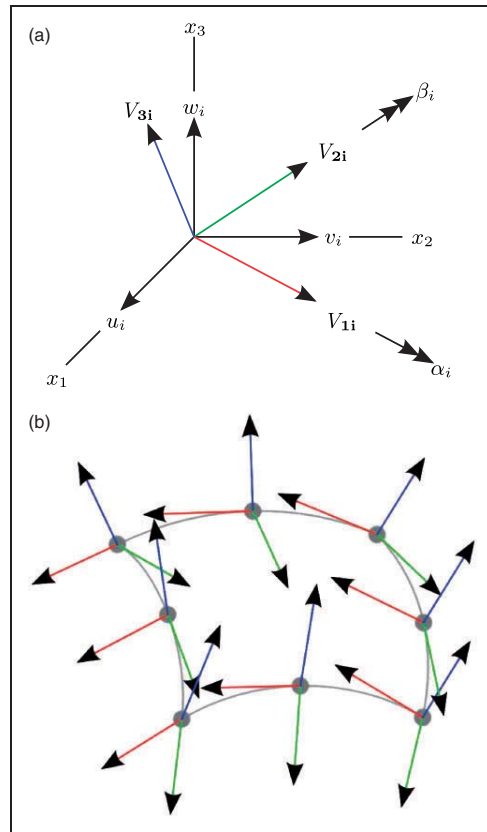

Figure 2. The eight-node double curved element used for discretising the top foil. The local colouring of the coordinate axis is as the following: The first axis is red; second axis is green and the third axis is blue. The first and second axes are tangent to the shell surface, while the third axis is the shell surface normal. (a) Local and global coordinate systems including nodal DoFs. (b) Eight–node double curved element with local coordinate systems.

coordinate system, while the cubic shape functions are given in in–plane isoparametric coordinates.[39] In equation (8), the spatial and kinematic relations of the nodes are given, with t_i being the thickness of the shell at the node. Each node has an associated local coordinate system, as shown in Figure 2(b). The first and second directions of the local coordinate system are tangential to the shell surface, i.e. in–plane, and define the two axes of rotation included in $\mu_\mathbf{i}$, which is used in the kinematic relationship. The third coordinate direction $V_{\mathbf{3i}}$ is the surface normal, hence it points away from the centre of the bearing.

$$x = \sum N_i\left(x_\mathbf{i} + \zeta \frac{t_i}{2} V_{\mathbf{3i}}\right) \tag{8a}$$

$$u_\mathrm{t} = \sum N_i\left(u_\mathbf{i} + \zeta \frac{t_i}{2}\mu_\mathbf{i}\left\{\begin{array}{c}\alpha_i\\\beta_i\end{array}\right\}\right) \tag{8b}$$

Boundary conditions for the top foil are required since the nodal displacements describe absolute displacements, thereby allowing rigid body motion. A fixed boundary, which is normally applied to one of the top foil edges, is obtained by setting the diagonal values in the stiffness matrix $\mathbf{K}_\mathrm{t}$ of the related DoF to a constant. The off diagonal values in the columns and rows associated with the DoF are set to zero, along with the corresponding position in the force vector F_t. This ensures that the deflections of the fixed boundary are equal to zero and no modal movement is possible.[39]

Air film: Modelled with finite elements

The air film is governed by the compressible Reynolds equation (9) and is derived via the Navier–Stokes equations, the equation of continuity and the equation of state for a perfect gas.[40] In the derivation of Reynolds equation (9), the pressure $\tilde{p}$ and the absolute viscosity μ are assumed to be constant throughout the thickness of the gas film. Furthermore, the no slip condition is assumed at the top and bottom of the gas film. Combining these assumptions, the integration of the flow velocities in the direction normal to the gas film can be performed analytically, hence the gradient and area integrals seen in Reynolds equation are functions of the in–plane coordinates. S denotes the bearing number.

$$\nabla\left(\tilde{p}\tilde{h}^3\nabla\tilde{p}\right) = \nabla\left(\tilde{p}\tilde{h}\right)S + 2S\frac{\partial}{\partial\tau}\left(\tilde{p}\tilde{h}\right) \tag{9}$$

The thickness of the air film $\tilde{h}$ in radial direction is given by equation (10) and depends on the radial movement of the journal $\tilde{h}_\mathrm{r}(\theta)$ and the top foil deflection $\tilde{h}_\mathrm{c}(\theta, z)$.

$$\tilde{h} = 1 - \tilde{h}_\mathrm{r}(\theta) + \tilde{h}_\mathrm{c}(\theta, z) \tag{10}$$

A Bubnov–Galerkin FE procedure is used to discretise the compressible Reynolds equation,[38] as seen in equation (11). A combined state variable, $\tilde{\psi} = \tilde{p}\tilde{h}$, is introduced allowing the state equations to be solved simultaneously in time.[19]

$$-\int {}_\mathbf{p}\mathbf{B}^\mathrm{T}\left(\tilde{p}\tilde{h}^3\right)^* {}_\mathbf{p}\mathbf{B}\tilde{p}_\mathbf{e}\mathrm{d}A + \int {}_\mathbf{p}\mathbf{B}^\mathrm{T}\tilde{h}^* S_\mathbf{p}\mathbf{N}\tilde{p}_\mathbf{e}\mathrm{d}A$$
$$- 2S\int {}_\mathbf{p}\mathbf{N}^\mathrm{T}{}_\mathbf{p}\mathbf{N}\dot{\tilde{\psi}}_\mathbf{e}\mathrm{d}A = 0 \tag{11}$$

Equation (11) can be written as a system of first order differential equations in time domain, as shown by equation (12).

$$\mathbf{A}_\mathrm{a}\dot{\tilde{\psi}}_\mathrm{a} = R_\mathrm{a} \tag{12}$$

The state matrix $\mathbf{A}_\mathrm{a}$ and residual vector R_a are shown by equation (13) at the element level. For calculations with a constant rotational speed of the journal, the state matrix is time independent, while the residual vector is time dependent.

$$\mathbf{A}_\mathbf{e} = 2S\int {}_\mathbf{p}\mathbf{N}^\mathrm{T}{}_\mathbf{p}\mathbf{N}\mathrm{d}A \tag{13a}$$

$$R_\mathrm{e} = -\int {}_\mathbf{p}\mathbf{B}^\mathrm{T}\left(\tilde{p}\tilde{h}^3\right)^* {}_\mathbf{p}\mathbf{B}\tilde{p}_\mathbf{e}\mathrm{d}A + \int {}_\mathbf{p}\mathbf{B}^\mathrm{T}\tilde{h}^* S_\mathbf{p}\mathbf{N}\tilde{p}_\mathbf{e}\mathrm{d}A \tag{13b}$$

Discretisation of the compressible Reynolds equation is made using a two dimensional isoparametric eight-node element. This element has the same in–plane shape functions as the eight-node element used for the top foil.

In the solution of the compressible Reynolds equation, initial conditions are required for the combined state variable. It is advisable to choose the initial condition in such a way that the air film is in equilibrium, hence the residual vector is zero. Besides the initial conditions, spatial boundary conditions are required for the time derivative of the combined state variable $\dot{\tilde{\psi}} = \tilde{p}\dot{\tilde{h}} + \dot{\tilde{p}}\tilde{h}$. The pressure at the spatial boundaries of the air film is equal to a constant ambient pressure $\tilde{p} = 1$, hence the time derivative of the pressure at these boundaries is zero, $\dot{\tilde{p}} = 0$. The boundary conditions for the combined state variable are given in equation (14).

$$\dot{\tilde{\psi}}(\theta_i, z) = \dot{\tilde{h}}(z)|_{\theta_i} \tag{14a}$$

$$\dot{\tilde{\psi}}(\theta, z_i) = \dot{\tilde{h}}(\theta)|_{z_i} \tag{14b}$$

It is possible to impose a symmetry condition in the axial direction by removing the above given boundary condition on the axial symmetry boundary. A symmetry condition would normally require the Neumann boundary condition at the symmetry line

to be zero to ensure continuity. However, this is automatically ensured due to the elliptic flow in the axial direction imposed by Reynolds equation.

Bump foil: Bilinear SEFM

The bump foil acts as a flexible support when it is in contact with the top foil. Due to the montage and configuration of both foils, a radially outward deflection of the top foil will result in a sliding deformation of the individual bumps. This deformation depends on: The geometry and material properties of the bump, the frictional conditions at the contact points between the bump foil, the top foil and bearing housing and the movement of adjacent bumps. This complex support system is commonly reduced to the so called SEFM, i.e. classical SEFM. The model represents the bump foil as a pattern of linear springs and viscous dampers, and the deflection of the bump foil depends on the aerodynamic pressure. Traditionally, a classical SEFM is not combined with a structural model of the top foil, and the deformation of the bump foil is therefore used directly in the calculation of the air film thickness. However, since the presented AFB model includes a structural model of the top foil, the air film thickness depends on the deformation of the top foil (see equation (10)). For this reason, the objective of the bilinear SEFM is to describe the support pressure on the top foil as a function of the deformation and velocity of the top foil.

The bump foil support is included as a distributed compliance in the classical SEFM and given by equation (15).[5,41] The bump foil distributed stiffness, which is required in the bilinear SEFM, is given as $k_{bf} = 1/Q_{bf}$.

$$Q_{bf} \approx \frac{2S_{bf}}{E_{bf}}\left(\frac{l_{bf}}{t_{bf}}\right)^3\left(1 - v_{bf}^2\right) \tag{15}$$

The equivalent viscous damping is a simplification of the friction losses due to the sticking/slipping state of the bump foil. The viscous damping, equivalent to an enclosed hysteresis loop for one cyclic deformation, is given by equation (16), where β is the loss factor, also known as the hysteresis damping constant and Ω is the excitation frequency.[42]

$$d_{bf} = \frac{k_{bf}\beta}{\Omega} \tag{16}$$

The support of the bump foil acts as a bilinear spring on the top foil, as mentioned above. The support pressures p_{bf} are given by equation (17), based on the distributed stiffness of the bump foil (see equation (15)) and the equivalent viscous damping (see equation (16)). The bump foil provides a support pressure, p_{bf}, when it is compressed, i.e. when the top foil deflects radially outwards past the initial position of the top foil, as indicated in Figure 1(b).

$$p_{bf} = \begin{cases} k_{bf}h_c + d_{bf}\dot{h}_c, & h_c \geqslant 0 \\ 0, & h_c < 0 \end{cases} \tag{17}$$

Coupling of the domains

The couplings between the four domains are shown in Figure 1(c), as previously mentioned. On the left hand side, the aerodynamic pressure and the support pressure from the bump foil are integrated and projected into forces given in the global coordinate system, acting on the top foil and the journal. On the right hand side, deflections of the top foil and the journal are transformed to the radial direction and then used to calculate the thickness of the air film and the deformation of the bump foil. The transformation from the global coordinate system to a given local radial direction is given by V_{3i}, i.e. $\tilde{h}_c = V_3^T u$.

The integration and projection of the pressure into forces can be performed simultaneously by utilising the Jacobian normal Jacobian vector J_3 and equation (18). The direction of the vector is normal to the initial top foil surface and its length corresponds to the scaling between the physical and the isoparametric area.[39]

$$\tilde{F} = \int_{-1}^1 \int_{-1}^1 {}_u\mathbf{N}^T \tilde{p}^* \underbrace{\begin{Bmatrix} J_{12}^* J_{23}^* - J_{13}^* J_{22}^* \\ J_{13}^* J_{21}^* - J_{11}^* J_{23}^* \\ J_{11}^* J_{22}^* - J_{12}^* J_{21}^* \end{Bmatrix}}_{J3*} d\eta d\xi \tag{18}$$

Both the Jacobian vector and the pressure $\tilde{p}^*$ are evaluated at the integration point based on the values at the nodes and the shape functions, e.g. $\tilde{p}^* = {}_p\mathbf{N}\tilde{p}_e$. Inserting this into the equation above yields the pressure–force relationship equation (19).

$$\tilde{F} = \mathbf{T}_p\tilde{p} \tag{19}$$

The pressure–force relationship matrix $\mathbf{T}_p$ is given by equation (20) at element level.

$$\mathbf{T}_e = \int_{-1}^1 \int_{-1}^1 {}_u\mathbf{N}^T J_3^* {}_p\mathbf{N} d\eta d\xi \tag{20}$$

The pressure–force relationship in equation (19) is used to calculate the aerodynamic forces on the nodes in the top foil, while the forces on the journal are the sum of all of the nodal forces in the x– and y–direction, respectively, i.e. $F_r = \sum F_t$. The support pressure from the bump foil acting on the backside of the top foil depends on the deflection and the velocity of the top foil in the radial direction (see equation (17)). Combining the pressure–force relation (equation (20)) and the transformation vector V_3 yields a stiffness $\mathbf{K}_{bf}$ and damping matrix $\mathbf{C}_{bf}$ for the bump foil as given

below. The matrices are given at element level by equation (21).

$$\tilde{\mathbf{K}}_{\mathbf{e}} = \int_{-1}^{1}\int_{-1}^{1} {}_{\mathbf{u}}\mathbf{N}^{\mathrm{T}}(J_3\tilde{k}_{\mathrm{bf}}V_3)^*{}_{\mathbf{p}}\mathbf{N}\mathrm{d}\eta\mathrm{d}\xi \tag{21a}$$

$$\tilde{\mathbf{C}}_{\mathbf{e}} = \int_{-1}^{1}\int_{-1}^{1} {}_{\mathbf{u}}\mathbf{N}^{\mathrm{T}}(J_3\tilde{d}_{\mathrm{bf}}V_3)^*{}_{\mathbf{p}}\mathbf{N}\mathrm{d}\eta\mathrm{d}\xi \tag{21b}$$

The support forces from the bump foil on the top foil are given as functions of the top foil deflections by equation (22).

$$\tilde{F}_{\mathrm{bf}} = \begin{cases} \tilde{\mathbf{K}}_{\mathrm{bf}}\tilde{u}_{\mathrm{t}} + \tilde{\mathbf{C}}_{\mathrm{bf}}\dot{\tilde{u}}_{\mathrm{t}}, & h_{\mathrm{c}} \geqslant 0 \\ 0, & h_{\mathrm{c}} < 0 \end{cases} \tag{22}$$

Reduction of the variables in the mathematical model

In order to keep the subsequent numerical calculation efficient and fast, the redundant variables can be neglected or reduced out. A gas foil bearing is typically cylindrical in shape and not loaded in the axial direction. This allows for the DoFs associated with the axial direction of the top foil to be removed when the bearing is axially aligned with the global coordinate system, i.e. aligning the AFB axis with the z–direction.

The remaining variables in the top foil equation (6) can be reduced further via a modal reduction resulting in the state space system given in equation (23).

$$\hat{\tilde{\mathbf{A}}}_{\mathrm{t}}\dot{\hat{\tilde{z}}}_{\mathrm{t}} + \hat{\tilde{\mathbf{B}}}_{\mathrm{t}}\hat{\tilde{z}}_{\mathrm{t}} = \hat{F} \tag{23}$$

The relationships between the state matrices and the force vector of the full and reduced systems are given in equation (24), together with the transformation between the top foil DoFs on the state space form $\tilde{z}_{\mathrm{t}}$ and the modal coordinate vector form $\hat{\tilde{z}}_{\mathrm{t}}$.

$$\begin{Bmatrix} \tilde{u}_{\mathrm{t}} \\ \dot{\tilde{u}}_{\mathrm{t}} \end{Bmatrix} = \tilde{\mathbf{V}}_{\mathbf{r}}\hat{\tilde{z}}_{\mathrm{t}} \tag{24a}$$

$$\hat{\tilde{\mathbf{A}}}_{\mathrm{t}} = \tilde{\mathbf{V}}_{\mathbf{l}}\begin{bmatrix} \mathbf{I} & 0 \\ 0 & \tilde{\mathbf{M}}_{\mathrm{t}} \end{bmatrix}\tilde{\mathbf{V}}_{\mathbf{r}} \tag{24b}$$

$$\hat{\tilde{\mathbf{B}}}_{\mathrm{t}} = \tilde{\mathbf{V}}_{\mathbf{l}}\begin{bmatrix} 0 & -\mathbf{I} \\ \tilde{\mathbf{K}}_{\mathrm{t}} & \tilde{\mathbf{C}}_{\mathrm{t}} \end{bmatrix}\tilde{\mathbf{V}}_{\mathbf{r}} \tag{24c}$$

$$\hat{\tilde{F}}_{\mathrm{t}} = \tilde{\mathbf{V}}_{\mathbf{l}}\begin{Bmatrix} 0 \\ \tilde{F}_t \end{Bmatrix} \tag{24d}$$

The mathematical miltiphysics model

The mathematical miltiphysics model of a journal supported in an AFB is presented in equation (25).

The two upper rows are the state space equation for the journal, i.e. equation (1). The third row is the Reynolds equation for the air film, i.e. equation (12), and the bottom row is the governing equation of the top foil after modal reduction, i.e. equation (23). The coupling of the four domains in the mathematical model is implicit, i.e. all coupling between the domains are included in the external loading terms.

$$\begin{bmatrix} \mathbf{I} & 0 & 0 & 0 \\ 0 & \tilde{\mathbf{M}}_{\mathrm{r}} & 0 & 0 \\ 0 & 0 & \tilde{\mathbf{A}}_{\mathrm{a}} & 0 \\ 0 & 0 & 0 & \hat{\tilde{\mathbf{A}}}_{\mathrm{t}} \end{bmatrix}\begin{Bmatrix} \dot{\tilde{x}}_{\mathrm{r}} \\ \ddot{\tilde{x}}_{\mathrm{r}} \\ \dot{\tilde{\psi}}_{\mathrm{a}} \\ \dot{\hat{\tilde{z}}}_{\mathrm{t}} \end{Bmatrix}$$
$$= -\begin{bmatrix} 0 & -\mathbf{I} & 0 & 0 \\ 0 & 0 & 0 & 0 \\ 0 & 0 & 0 & 0 \\ 0 & 0 & 0 & \hat{\tilde{\mathbf{B}}}_{\mathrm{t}} \end{bmatrix}\begin{Bmatrix} \tilde{x}_{\mathrm{r}} \\ \dot{\tilde{x}}_{\mathrm{r}} \\ \tilde{\psi}_{\mathrm{a}} \\ \hat{\tilde{z}}_{\mathrm{t}} \end{Bmatrix} \tag{25}$$
$$+\begin{Bmatrix} 0 \\ \tilde{W}_{\mathrm{r}} - \tilde{F}_{\mathrm{r}}\left(\tilde{\psi}_a, \hat{\tilde{z}}_{\mathrm{t}}, \tilde{x}_r, \dot{\tilde{x}}_r\right) + \tilde{F}_{ub}(\tilde{t}) \\ \tilde{R}_{\mathrm{a}}\left(\tilde{\psi}_{\mathrm{a}}, \hat{\tilde{z}}_{\mathrm{t}}, \tilde{x}_r, \dot{\tilde{x}}_r\right) \\ \tilde{F}_{\mathrm{t}}\left(\tilde{\psi}_{\mathrm{a}}, \hat{\tilde{z}}_{\mathrm{t}}, \tilde{x}_r, \dot{\tilde{x}}_r\right) + \hat{\tilde{F}}_{\mathrm{bf}}\left(\hat{\tilde{z}}_r\right) \end{Bmatrix}$$

Numerical validation

The numerical validation of the developed non-linear AFB model is divided into three different parts:

(a) the convergence study of the required number of mode shapes used in the modal reduction;
(b) the mesh refinement analysis;
(c) the comparison with results obtained from another non-linear AFB model known from the literature.[29]

Parts (a) and (b) are presented in Appendix 1 and 2, while a comparison of the journal orbits is treated below, i.e. part (c). In the following numerical simulation, a rigid journal is supported by an AFB with one bearing segment. The dimensions and material properties used in the validation and subsequent simulations are given in Table 1 and the rotational speed and journal unbalance used are 12,000 r/min and 0 g·mm, respectively.

Comparison with results from a validation air foil bearing model

The third part of the validation is a comparison of the journal orbits and the top foil deflections simulated

Table 1. Bearing data used in the numerical validation and investigation. The bearing data are those of the well known NASA bump foil bearing frequently studied in the literature.

Journal data	
Mass(m)	3.055 kg
Load(W)	$\{30, 0\}^T$ N
Gas film data	
Absolute viscosity(μ)	19.5×10^{-6} Pa·s
Ambient pressure(p_A)	1.01325×10^5 Pa
Radial clearance(C)	31.8 μm
Top Foil Data	
Diameter	38.1 mm
Length(l)	38.1 mm
Thickness(t)	0.2032 mm
Fixed edge	0°
Free edge	360°
Young's modulus	207 GPa
Poisson's ratio	0.3
Damping factor	0.005
Bump foil data	
Bump Pitch(S_{bf})	4.572 mm
Half bump length(l_{bf})	1.778 mm
Bump Foil Thickness(t_{bf})	0.1016 mm
Young's modulus(E_{bf})	207 GPa
Poisson's ratio(ν_{bf})	0.3
Loss Factor(β_{bf})	0.25

Figure 3. Plot of the transient response of the journal for the two FE models and the steady state deflection of the top foil. The blue colour is the presented model utilising the 20 first mode shapes in the modal reduction and a mesh of 20×6 elements. The red colour is the validation model known from the literature.

with the presented AFB model and a similar model is presented in the literature.[29] The differences between the two models are:

(a) the element type used for the air film, i.e. the eight-node element in the presented model and the four–node element in the validation model;

(b) the presented model includes a model of the top foil structure, which the validation model does not;

(c) the presented AFB model uses a bilinear SEFM, while the validation model uses a classic SEFM in combination with the Gümbel condition.

The results from the two simulations are shown in Figures 3 and 4, with the yellow colour being used for the presented model and the blue colour for the validation model. The nodes of the top foil located on the axial symmetry plane along the circumferential direction are shown in Figure 3. The red dots mark the initial location of the top foil, while the circles and crosses mark the radial deformation of the top foil at steady state for the two simulations.

The overall resemblance observed for the results are very good. The journal orbits follow each other closely, hence the difference between the two models does not affect the orbits. The top foil deflects outward in the region with pressures above the ambient

pressure for both simulations, while an inwards deflection is observed in the region where the sub-ambient pressures are seen for the validation model. The inward deflection for the validation model is limited by the classical SEFM. The limitation imposed by the classical SEFM results in a sub-ambient pressure close to the trailing edge (see Figure 4(b)). This phenomenon is well known and is the reason for the use of the Gümbel condition in combination with the classical SEFM.[7] For the presented model the top foil folds inwards towards the journal, and thereby reaches an equilibrium position where the air film pressure is very close to the ambient pressure (see Figure 4(a)). This results in the same effect achieved by the Gümbel condition, as can be observed from a good match existing between the two journal orbits.

Numerical investigation: Indirect design of shallow pockets

The numerical investigation examines the dynamic performance of a rotor bearing system where a rigid journal affected by three different levels of unbalance is supported by four different AFBs. The difference between the four AFBs are the support of the top foil as indicated by the four cases shown in Figure 5. Case I is a classical AFB, while for cases II, III and IV the bump foil is removed in a given region spanning 90° circumferentially and with a width of 16 mm symmetrically, placed in an axial direction. This results in a partially supported top foil for cases II, III and IV, hence the structural properties of the top foil carries the load from the aerodynamic pressure in the unsupported area. The rest of the AFB system remains unchanged compared to the system simulated in the validation, where the geometries
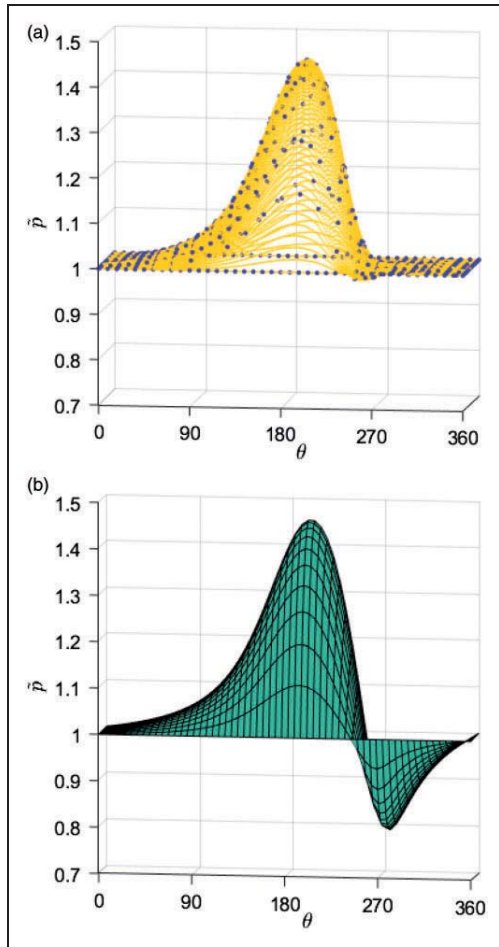
Figure 4. Plot of the pressure profiles calculated with the two AFBs. The presented model uses the 20 first mode shapes in the modal reduction and a mesh of 20×6 elements. The pressure profile from the validation model includes sub-ambient pressure. However, this pressure region is neglected in the calculation of the aerodynamic forces by enforcing the gümbel condition. (a) Pressure profile calculated with the presented model. The blue dots in the figure are the nodal values calculated with the presented model, i.e. not the values from the validation model. (b) Pressure profile calculated with the validation model. The validation model utilises axial symetry, hence the half pressure profile.

and properties are found in Table 1. It is important to highlight that by removing some bumps, a shallow pocket might be created via the sagging effect.

Steady state pressure profile: No unbalance

The initial transient responses of a journal supported by the four cases are shown in Figure 6, with case I in blue, case II in red, case III in yellow and case IV in purple (see Figure 7). The journal without an
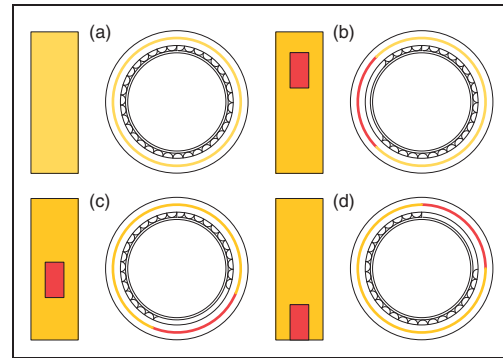
Figure 5. The four cases, which are numerically investigated, are shown with a schematic of the bump foil on the left hand side and a section view of the AFB taken along the axial centre line. The yellow line and area indicates the part where the bump foil supports the top foil, while the red marks the removed bumps. For all cases, the fixed leading edge is located at the top end on the schematics of the bump foil, while the free trailing edge is located at the bottom end. (a) Case I. (b) Case II. (c) Case III. (d) Case IV.
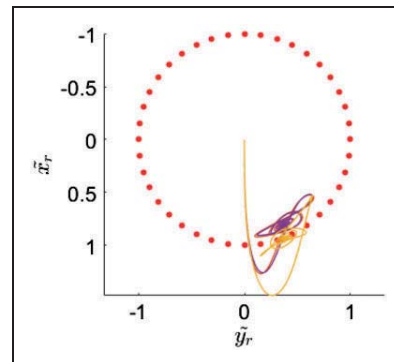
Figure 6. The initial 0.22 s of the orbit for a journal support by the four cases of AFBs. The rotation speed is 12,000 r/min, and the journal is dropped from the centre of the bearing. The orbit colour for each of the cases are: I is blue, II is red, III is yellow and IV is purple (see Figure 7).

unbalance is spinning at 12,000 r/min and is dropped from the centre of the AFB. The four orbits are plotted in the same figure, but since cases I, II and IV are very similar it is only possible to distinguish two orbits. Case III differs from the other orbits by having a bigger maximum deflection during the transient response and a lower equilibrium point, i.e. cases I, II and IV are located at $x \approx 0.81$ and $y \approx 0.37$, while case III is located at $x \approx 0.94$ and $y \approx 0.38$. This is as a result of the reduced support stiffness due to the removed bumps in the high pressure region.

In Figure 8 the pressure profile at equilibrium is shown for all cases. The blue dots are the nodal values, the yellow area corresponds to the supported

part of the top foil, while the red area is the unsupported part. All the pressure profiles have a similar shape, although a slightly wider peak is observed for case III in both circumferential and axial directions.
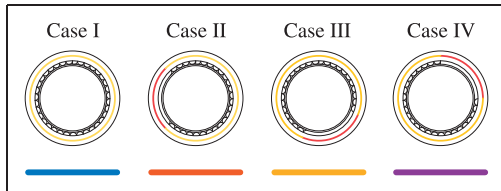

Figure 7. The colours used in the plot of the journal orbits, i.e. Figures 6, 11 and 15.

This pressure peak is also lower in magnitude when compared with cases I, II and IV.

The thickness of the air film for all four cases is shown in Figure 9, while the top foil deflections are shown in Figure 10. The colour coding corresponds to that of the pressure profile, i.e. blue dots are nodal values, the yellow area is the supported part of the top foil and the red area is the unsupported part. The black line in the plots of the top foil deflections is the surface of the journal, i.e. the vertical distance between the black line and the deflected top foil is the thickness of the air film. The z–axis in the plots of the top foil deflection has been inverted, i.e. a deflection into the bump foil corresponds to a positive downward movement, while a deflection in towards the journal corresponds to a negative upward movement.
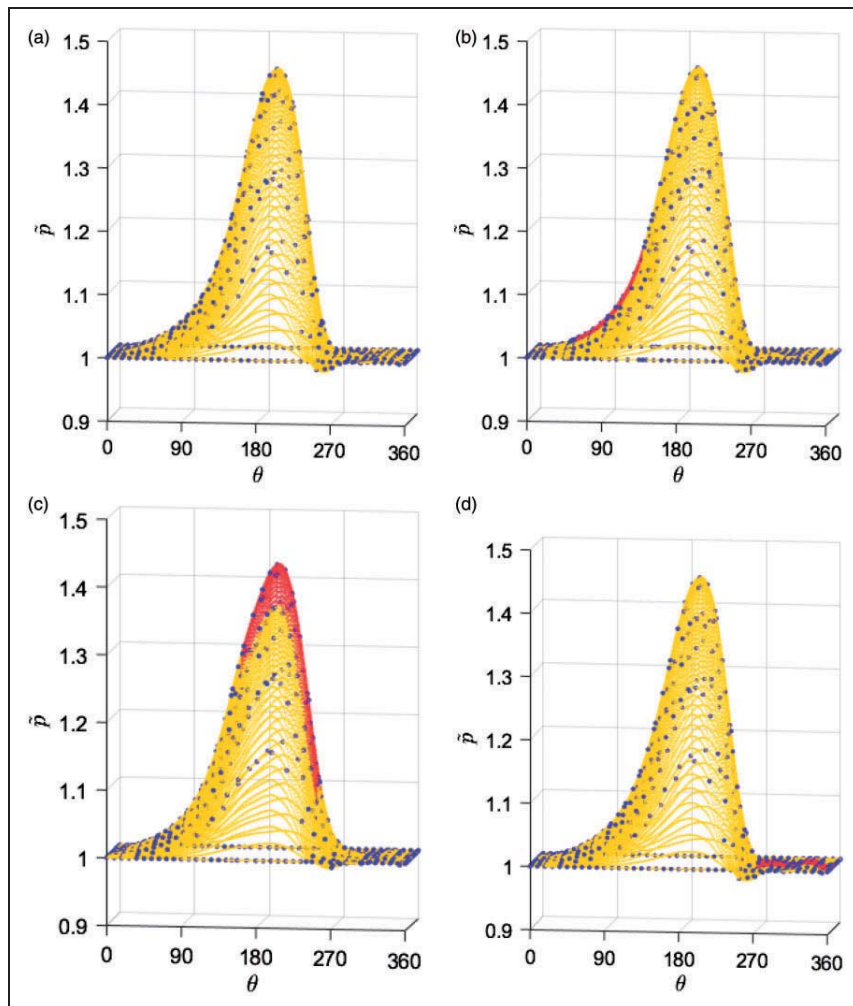
Figure 8. The pressure profile at equilibrium for the journal without an unbalance and where it is rotating at 12,000 r/min. The blue dots are the nodal values, the yellow area is the supported part of the top foil, while the red area is the unsupported part. (a) Case I (similar to Figure 4(a)). (b) Case II. (c) Case III. (d) Case IV.
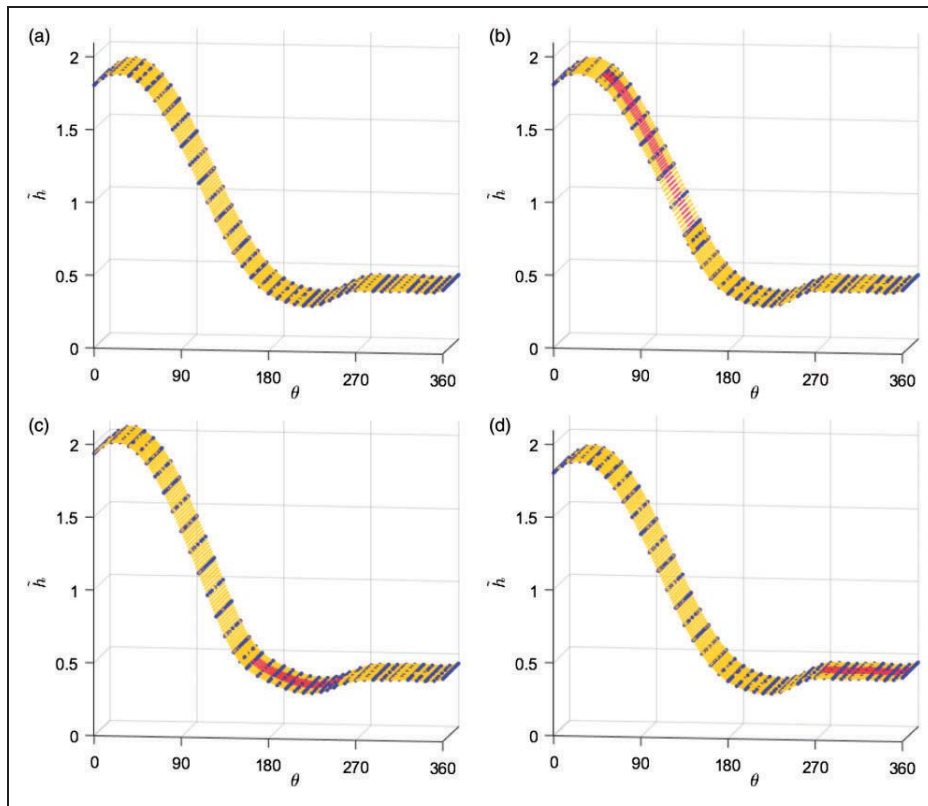
Figure 9. The thickness of the air film at equilibrium for a journal with no unbalance running at 12,000 r/min. The blue dots are the nodal values, the yellow area is the supported part of the top foil, while the red area is the unsupported part. (a) Case I. (b) Case II. (c) Case III. (d) Case IV.

For cases I, II and IV the air film thicknesses are similar. The air film thickness changes along the circumferential direction, while remaining unchanged in the axial direction. The thickness decreases from the leading edge at 0° until approximately 220°, where it then increases slightly until 270°, remaining constant until the trailing edge at 360°. For case III the air film thickness differs slightly in the circumferential direction in its unsupported region. The thickness of the air film changes less in the circumferential direction in the unsupported region, hence it remains almost constant. The most visible difference between cases I, II, IV and case III is, besides the aforementioned shape, the maximum thickness of the air film, which is located close to the fixed leading edge in all cases. The larger thickness of case III is a result of the equilibrium point being located further down in the AFB in comparison to the three other cases.

Looking at the deflection of the top foils, similar trends are seen as in the thickness of the air film, i.e. cases I, II and IV resemble each other, while case III differs. One difference is, however, detected for case II in its unsupported part of the top foil in comparison to cases I and IV. The top foil deflects further outward. This does, however, not affect the air film

thickness, since the additional deflection of the top foil in case II is much smaller than the overall air film thickness in the unsupported area. For case III, the sagging of the top foil is clearly visible by in the unsupported area. The additional deflection of the top foil forms a shallow pocket allowing the journal surface to settle further away from the bearing centre. For all cases, the inward deflection of the top foil towards the journal is easily seen in the region close to the free trailing edge, i.e. the top foil deflections follow the surface of the journal.

Rotor response: 5 g·mm unbalance

Transient responses of a rigid journal with a 5 g·mm unbalance, supported by an AFB, have been simulated for the four cases described above and for the rotational speed ranging from 6000 until the rotational speed where large sub-harmonic vibrations hinder the computation of the response. The steady state responses for the nine selected rotation speeds are shown in Figure 11. At each rotational speed the journal orbits for the four cases are plotted together, i.e. case I is depicted in blue, case II in red, case III in yellow and case IV in purple (see Figure 7). For a
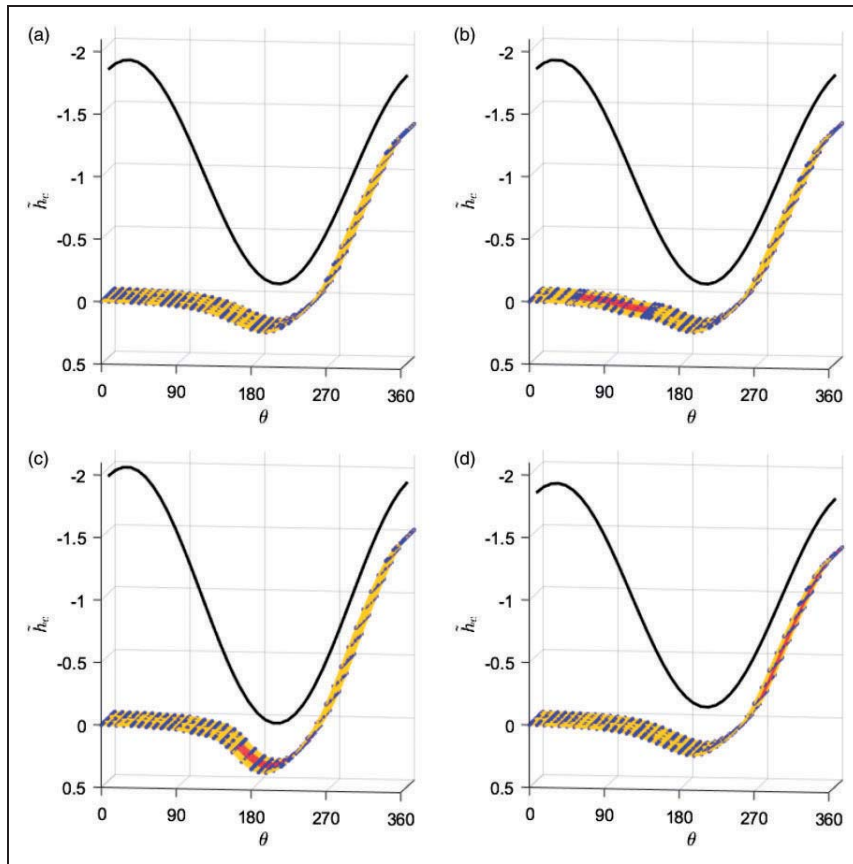
Figure 10. The deflection of the top foil at equilibrium for a journal with no unbalance running at 12,000 r/min. The blue dots are the nodal values, the yellow area is the supported part of the top foil, while the red area is the unsupported part. The black line is the surface of the journal. The thickness of the air film is given as the vertical distance between the deflected top foil and the journal. (a) Case I. (b) Case II. (c) Case III. (d) Case IV.

small journal unbalance the trend for the four cases is the same as for the previous simulations with no unbalance. In figure 11, only two journal orbits are clearly visible, since the response for cases I, II and IV are very similar. Only case III differs, with the journal orbit being located further down in the AFB. For all cases, the journal orbit starts towards the bottom of the AFB, and moves upwards as the rotational speed is increased. The shape of the journal orbit starts out as an ellipse with the direction, resulting from the foci alignment, being turned 30° relative to the y-direction. As the rotational speed increases, the resultant direction of the ellipse foci first turns counter clockwise until aligned with the x-direction, and then the shape of the journal orbit changes from an ellipse into a circle.

The steady state part of the transient response has been transformed into a frequency domain by performing a fast Fourier transformation (FFT) on 1.5 s of the steady state response with a sampling frequency of 5,000 Hz. A modulus of the FFT in the

x- and y-directions for each individual rotational speed has been calculated and normalised with respect to the modulus of the synchronous vibration. All normalised FFTs are summarised in a waterfall diagram for each case, as shown in Figure 12. It is important to highlight that only the synchronous frequency is observed in the waterfall diagrams.

In Figure 13, a waterfall diagram is shown for the initial 0.22 s of the transient response, i.e. the drop from the centre position and onwards. The waterfall diagram is calculated in the same way as the previous waterfall diagrams, hence the magnitudes are normalised with respect to the synchronous frequency. In Figure 13, a sub-harmonic frequency can be observed. This frequency increases slightly from approximately 80 Hz at 8,000 r/min to around 100 Hz at 20,000 r/min.

Rotor response: 20 g·mm unbalance

Figure 14 shows four different waterfall diagrams for a rigid journal with a 20 g·mm unbalanced load
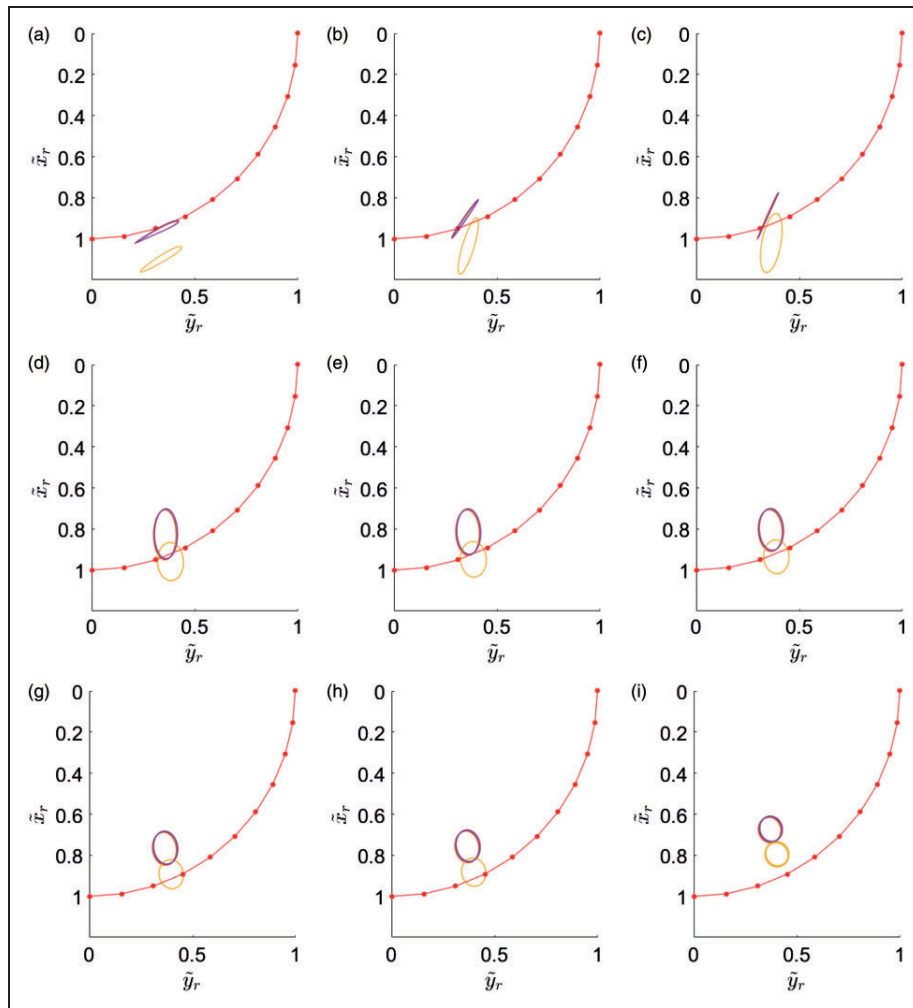
Figure 11. Selected journal orbits for all cases plotted on top of each other at varies of rotational speeds. The journal unbalance is 5 g·mm. The orbit colour for each of the cases are: I is blue, II is red, III is yellow and IV is purple (see Figure 7). (a) 6000 r/min. (b) 8000 r/min. (c) 8500 r/min. (d) 11,000 r/min. (e) 11,500 r/min. (f) 12,000 r/min. (g) 14,000 r/min. (h) 14,500 r/min. (i) 19,500 r/min.

supported by the cases of AFBs described in Table 2 and Figure 5. The waterfall diagrams are calculated in the same manner as for the 5 g·mm unbalance diagrams, and the simulated rotation speeds range from 6000 r/min until the rotational speed where the appearing sub-harmonic vibrations hinder the computation.

In Figure 14, sub-harmonic vibrations are clearly visible in the waterfall diagrams for cases I, II and IV. The sub-harmonic vibrations are caused by non-linear phenomena related to the air film. For all three cases, two types of sub-harmonic vibrations can be distinguished. The first type appears at half of the synchronous frequency, with an onset speed of approximately 8500 r/min and a maximum amplitude close to 10,000 r/min. It fades away at around 11,500 r/min. This half whirl frequency is well

known in the literature.[43] The second type of sub-harmonic vibrations covers a broader range in the frequency spectrum, although there are two dominating frequencies located symmetrically above and below the half synchronous frequency. The onset speed belonging to the second type is approximately 12,000 r/min, i.e. just after the first type has faded out. For cases I and II the vibration continues to grow in magnitude until the rotational speed reaches around 14,000 r/min. Case IV has a maximum amplitude at 13,500 r/min. For cases I, II and IV the second type of sub-harmonic frequency disappears at 14,500 r/min. It can be observed how the span between the two dominating sub-harmonic frequencies increases with rotational speed. The upper frequency follows the increase in rotational speed, while the lower frequency only
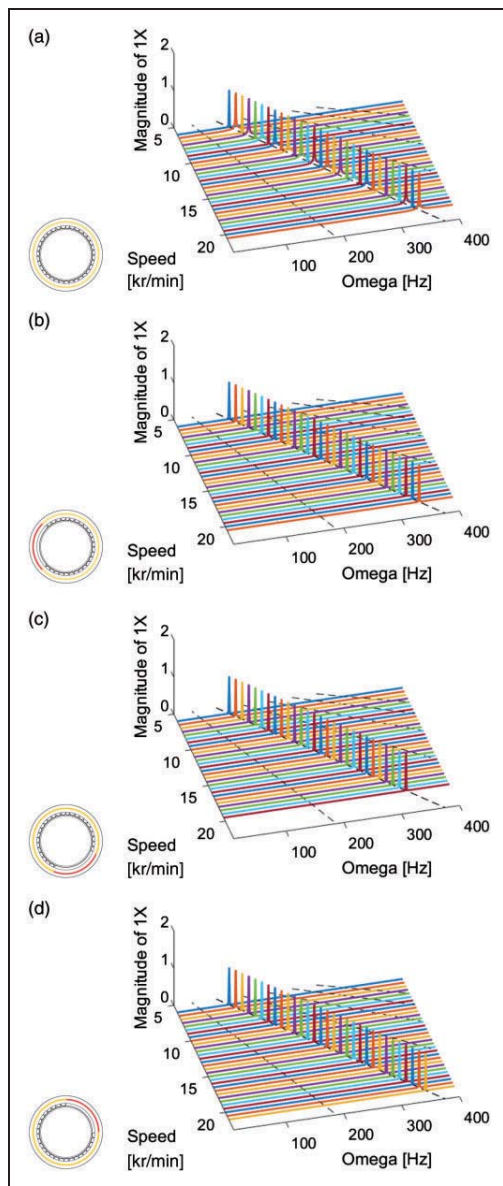
Figure 12. The modulus of FFTs in the x- and y-direction at steady state with a 5 g·mm unbalance. The sampling period is 1.5 seconds and the sampling frequency is 5000 Hz. The colours distinguish the different rotation speeds. (a) Case I. (b) Case II. (c) Case III. (d) Case IV.
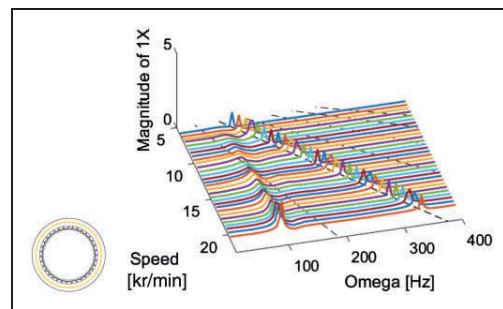

Figure 13. The modulus of the FFTs in the x- and y-direction for the first 0.22 s after the drop from the centre with a 5 g·mm unbalance. The increase in magnitude of the sub-harmonic frequency for an increasing rotational speed originates partly from a larger orbit amplitude and partly from a prolonged run–in time before the steady state is reached. The sampling frequency is 5000 Hz. The colours distinguish the different rotation speeds.

journal orbits of the same rotational speed are plotted together with case I coloured in blue, case II in red, case III in yellow and case IV in purple (see Figure 7). The nine speeds are selected based on the waterfall diagrams and the appearance of the sub-harmonic vibrations observed for cases I, II and IV. The first rotational speed is the slowest one used, i.e. 6000 r/min. The second is the rotational speed just before the sub-harmonic vibration is observed, i.e. 8000 r/min, while the third is just after the initialisation of the sub-harmonic vibration, known as the half whirl frequency, i.e. 8500 r/min. The fourth takes place just before the half whirl frequency disappears, i.e. 11,000 r/min. The fifth is the intermediate speed where no sub-harmonic vibration is present, i.e. 11,500 r/min. The sixth rotational speed is the one after the second type of sub-harmonic vibrations are initialised, i.e. 12,000 r/min. At the seventh speed, sub-harmonic vibrations are the biggest for cases I and II, just before all the sub-harmonic frequencies disappear, i.e. 14,000 r/min. The eighth rotational speed marks the end of the sub-harmonic vibration speed range, i.e. 14,500 r/min. Finally, the last rotational speed is the one that appears just before the return of sub-harmonic vibrations, which prevent the rotor orbits to reach steady state, i.e. 19,500 r/min.

The general trend, observed for the journal orbits when they are compared at a given rotational speed, is that cases I, II and IV are similar, while case III differs by being located further down in the AFB. This is the same trend as seen previously. Looking at the journal orbits, in terms of shape and size, case III stands out since it is elliptic or circular in shape for all rotational speeds. The journal orbit at the lowest rotation speed is elliptic with the direction, resulting from the foci alignment, placed at a 30° angle to the y-axis, as seen in Figure 15. This direction turns towards the x-axis as the rotational speed increases, while the
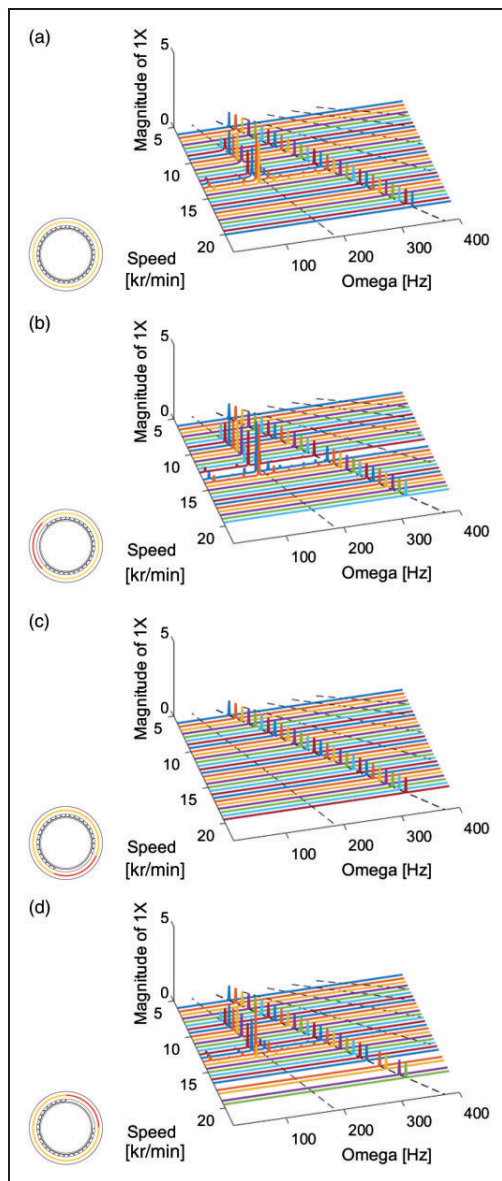
increases slightly. The location of the lower sub-harmonic frequency is slightly higher than the frequency peak found for the AFB system during the initial part of the transient response, shown in Figure 13. For case III it is important to highlight that only the synchronous frequencies are seen.

Figure 15 shows the steady state journal orbits at nine selected rotational speeds for all cases, i.e. the

Figure 14. The modulus of the FFTs in the *x*- and *y*-direction at steady state with 20 g·mm unbalance. The sampling period is 1.5 s and the sampling frequency is 5000 Hz. The colours distinguish the different rotation speeds. (a) Case I. (b) Case II. (c) Case III. (d) Case IV.

size of the ellipses also increases. When the alignment of the foci is overlapped with the *x*-axis, the rotation stops and the shapes of the journal orbit become more circular. For the three other cases the initial orientation, shape and development with rotational speed is similar to case III, with the exception of the ellipse collapse as the rotation speed approaches the initialisation of the half whirl frequency, i.e. 8000 r/min (Figure 15(b)). In the speed range with the half whirl frequency, the journal orbits consist of a double loop, while more

Table 2. Description of the bump foil support for the four cases.

Case number	Description
I	Top foil fully supported
II	Top foil supported from 0° to 45° as well as from 135° to 360°. The unsupported region has a width of 16 mm.
III	Top foil supported from 0° to 157.5° as well as from 247.5° to 360°. The unsupported region has a width of 16 mm.
IV	Top foil supported from 0° to 270°. Then supported region has a width of 16 mm.

complex orbits are observed within the speed range that belongs to the second type of sub-harmonic vibrations. In the last speed range, the largest journal orbit is found at 13,500 r/min for case IV and 14,000 r/min for cases I and II as seen in Figure 15(g). For case III, the largest orbit takes place at 8000 r/min as seen in Figure 15(b), i.e., the rotational speed below the onset speed of the sub-harmonic vibrations found in cases I, II and VI.

Conclusions and future work

The AFB with the bump foil removed from the region where the minimum air film thickness is located, i.e. case III, shows superior steady state behaviour when supporting a journal with a large unbalance (20 g·mm). The sub-harmonic vibrations of the journal supported by an AFB, caused by a large journal unbalance, are eliminated in the entire speed range. This advantage is gained without a loss in performance when supporting a journal with a small unbalance load in comparison to an ordinary AFB. The elimination of the sub-harmonic vibrations is attributed to the shallow pocket, developed in the unsupported region, where the high pressure zone is located in an AFB. When the pressure builds up as the journal approaches the top foil, the lower support stiffness allows for a wider region with a small air film thickness. This widens and lowers the pressure peak and enables a larger minimum air film thickness in comparison to the other cases. This has a positive effect on the performance of the AFB, since the non-linear component of the aerodynamic force gets more pronounced at smaller air film thicknesses resulting in sub-harmonic vibrations.

The possible advantage of removing the bump foil in the aforementioned region is having a more robust AFB with respect to high journal unbalances. The sub-harmonic vibrations found in the steady state response of a journal with a large unbalance supported by an AFB and a fully supported top foil, are effectively eliminated by using an AFB with the partially supported top foil. The journal orbit in the modified AFB is modest in size. One of the drawbacks of removing the bump foil in the region of minimum
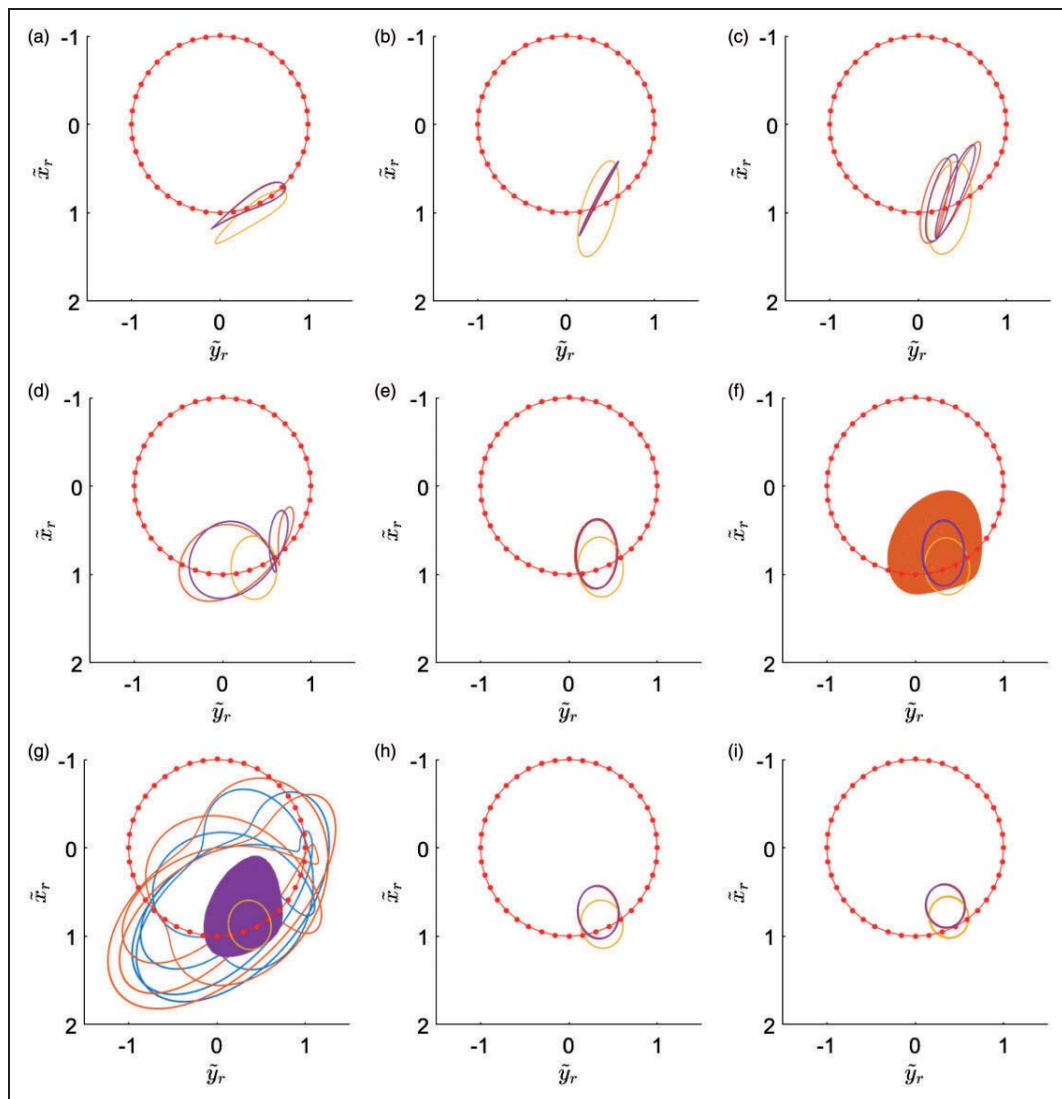
Figure 15. Selected journal orbits for all cases plotted on top of each other at various rotational speeds. The journal unbalance is 20 g·mm. The orbit colour for each of the cases are: I is blue, II is red, III is yellow and IV is purple (see Figure 7). (a) 6000 r/min. (b) 8000 r/min. (c) 8500 r/min. (d) 11,000 r/min. (e) 11,500 r/min. (f) 12,000 r/min. (g) 14,000 r/min. (h) 14,500 r/min. (i) 19,500 r/min.

film thickness is a lowering of the equilibrium position of the journal in the AFB, while the stability threshold is reduced by 500 r/min to 19,500 r/min.

An issue not addressed in the numerical investigation is the mechanical stress in the partially supported top foil. This may be an issue, since a part of the top foil is unsupported and therefore relies on its structural properties to support the load. An investigation of the mechanical stresses in the top foil can whether or not the yield strength will be exceeded.

The shallow pocket found for the AFB is governed by the size and location of the removed bump foil. A parameter study of these design variables can reveal the minimum requirements for the unsupported

area in order to avoid the occurrence of sub-harmonic vibrations.

The equivalent viscous damping used in the SEFM for the bump foil is valid when one vibration frequency is present. This is the case at a low unbalance level; however, at high unbalance levels, multiple vibration frequencies may be present simultaneously. The inclusion of a more advanced bump foil model capable of simulating the dry friction forces in the bump foil contact points will improve the simulations at rotation speeds where multiple frequencies are present. Results from the literature show an optimum point for the stability with respect to the friction coefficient.[16] An AFB model capable of including the dry friction as well as an

unsupported area of top foil will likely be a valuable design tool for the manufacturing of AFBs, supporting their effort to produce faster rotating machinery.

References

1. Agrawal GL. Foil air/gas bearing technology – an overview. In: *International gas turbine & aeroengine congress & exhibition*. Orlando, FL, 2–5 June 1997, ASME-97-GT-347, pp.1–11.
2. Heshmat H. A feasibility study on the use of foil bearings in cryogenic turbopumps. In: *AIAA/SAE/ASME/ASEE 27th joint propulsion conference*, Sacramento, CA, 24–26 June 1991, AIAA-91-2103, pp.1–12.
3. Larsen JS, Hansen AJT and Santos IF. Experimental and theoretical analysis of a rigid rotor supported by air foil bearings. *Mechanics & Industry* 2014; 16(1): 106–118.
4. San Andrés L, Rohmer M and Park S. Failure of a test rig operating with pressurized gas bearings: A lesson on humidity. *Proceedings of ASME Turbo Expo 2015: Turbine Technical Conference and Exposition*, 15–19 June 2015, ASME-GT2015-42556. Montréal: ASME, p.10.
5. Walowit JA and Anno JN. *Modern developments in lubrication mechanics*. London: Applied Science Publishers, 1975.
6. Heshmat H, Shapiro W and Gray S. Development of foil journal bearings for high load capacity and high speed whirl stability. *J Lubric Tech* 1982; 104(2): 149–156.
7. Heshmat H, Walowit JA and Pinkus O. Analysis of gas-lubricated foil journal bearings. *J Lubric Tech* 1983; 105: 647–655.
8. Hamrock BJ, Schmid SR and Jacobsen BO. *Fundamentals of fluid film lubrication*. 2nd ed. New York: Marcel Dekker, Inc., 2004.
9. Ku CPR and Heshmat H. Compliant foil bearing structural stiffness analysis: Part 1 – theoretical model including strip and variable bump foil geometry. *J Tribol* 1992; 114: 394–400.
10. Ku CPR and Heshmat H. Compliant foil bearing structural stiffness analysis – part II: Experimental investigation. *J Tribol* 1993; 115(3): 364–369.
11. Heshmat H and Ku CPR. Structural damping of self-acting compliant foil journal bearings. *J Tribol* 1994; 116: 76–82.
12. Rubio D and San Andrés L. Bump-type foil bearing structural stiffness: Experiments and predictions. *J Eng Gas Turb Power* 2006; 128(3): 653–660.
13. Balducchi F, Arghir M and Gaudillere S. Experimental analysis of the unbalance response of rigid rotors supported on aerodynamic foil bearings. In: *Proceedings of ASME turbo expo 2014*, 16–20 June 2014, ASME-GT2014-25552. Düsseldorf, Germany: ASME.
14. Larsen JS, Varela AC and Santos IF. Numerical and experimental investigation of bump foil mechanical behaviour. *Tribol Int* 2014; 74: 46–56.
15. Kim TH, Lee J and Kim YM. Static structural characterization of multilayer gas foil journal bearings. In: *Proceedings of ASME Turbo Expo 2015: Turbine Technical Conference and Exposition*, 15–19 June 2015 ASME-GT2015-43959. Montréal: ASME.
16. Le Lez S, Arghir M and Frêne J. Nonlinear numerical prediction of gas foil bearing stability and unbalanced response. *J Eng Gas Turb Power* 2009; 131(1): 01253-1–12.
17. San Andrés L, Rubio D and Kim TH. Rotordynamic performance of a rotor supported on bump type foil gas bearings: Experiments and predictions. *J Eng Gas Turb Power* 2007; 129(3): 850–857.
18. Arghir M, Le Lez S and Frene J. Finite-volume solution of the compressible Reynolds equation: Linear and non-linear analysis of gas bearings. *Proc Inst Mech Eng J J Eng Tribol* 2006; 220(7): 617–627.
19. Pham HM and Bonello P. Efficient techniques for the computation of the nonlinear dynamics of a foil–air bearing rotor system. In: *Proceedings of ASME Turbo Expo 2013: Turbine Technical Conference and Exposition*, 3–7 June 2013, San Antonio, Texas, USA ASME-GT2013-94389.
20. Bonello P and Pham HM. The efficient computation of the nonlinear dynamic response of a foil air bearing rotor system. *J Sound Vib* 2014; 333(15): 3459–3478.
21. Bonello P and Pham HM. Nonlinear dynamic analysis of high speed oil–free turbomachinery with focus on stability and self–excited vibration. *J Tribol* 2014; 136: 041705-1–10.
22. Larsen JS and Santos IF. On the nonlinear steady–state response of rigid rotors supported by air foil bearings – theory and experiments. *J Sound Vib* 2015; 346: 284–297.
23. Carpino M and Talmage G. A fully coupled finite element formulation for elastically supported foil journal bearings. *Tribol T* 2003; 46(4): 560–565.
24. San Andrés L and Kim TH. Improvements to the analysis of gas foil bearings: Integration of top foil 1D and 2D structural models. In: *ASME turbo expo 2007: Power for land, sea and air*. ASME-GT2007-27249, 14–17 May 2007, pp.779–789.
25. San Andrés L and Kim TH. Analysis of gas foil bearings integrating FE top foil models. *Tribol Int* 2009; 42(1): 111–120.
26. Temis YM, Temis MY and Meshcheryakov AB. Gas–dynamic foil bearing model. *J Frict Wear* 2011; 32(3): 212–220.
27. Xu F, Liu Z, Zhang G, et al. Hydrodynamic analysis of compliant foil bearings with modified top foil model. In: *Proceedings of ASME turbo expo 2011*, Vancouver, British Columbia, Canada, 6–10 June 2011, ASME-GT2011-46018, pp.1–10.

28. Xu F, Liu Z, Zhang G, et al. Effects of shear stiffness in top foil structure on gas foil bearing performance based on thick plate theory. *Proc Inst Mech Eng J J Eng Tribol* 2013; 227(7): 761–776.

29. Larsen JS and Santos IF. Efficient solution of the nonlinear Reynolds equation for compressible fluid using the finite element method. *J Braz Soc Mech Sci* 2014; 37. DOI: 10.1007/s40430-014-0220-5.

30. Song JH and Kim D. Foil gas bearing with compression springs: Analyses and experiments. *J Tribol* 2007; 129(3): 628–639.

31. Yu H, Shuangtao C, Rugang C, et al. Numerical study on foil journal bearings with protuberant foil structure. *Tribol Int* 2011; 44(9): 1061–1070.

32. San Andrés L and Chirathadam TA. Performance characteristics of metal mesh foil bearings: Predictions versus measurements. *J Eng Gas Turb Power* 2013; 135(12): 122503-1–8.

33. Chen S, Hou Y, Niu L, et al. Study on double–layer protuberant gas foil journal bearings with different foil layers arrangement. *J Adv Mech Des Syst* 2015; 9(2): 1–12.

34. Kim D. Parametric studies on static and dynamic performance of air foil bearings with different top foil geometries and bump stiffness distributions. *J Tribol* 2007; 129(2): 354–364.

35. Kim TH and San Andrés L. Effects of a mechanical preload on the dynamic force response of gas foil bearings: Measurements and model predictions. *Tribol Trans* 2009; 52(4): 569–580.

36. San Andrés L and Norsworthy J. Structural and rotordynamic force coefficients of a shimmed bump foil bearing: An assessment of a simple engineering practice. *J Eng Gas Turb Power* 2015; 138(1): 012505-1–8.

37. Panda S and Natarajan R. Analysis of laminated composite shell structures by finite element method. *Comput Struct* 1981; 14(3–4): 225–230.

38. Larsen JS, Nielsen BB and Santos IF. On the numerical simulation of nonlinear transient behavior of compliant air foil bearings. In: *SIRM 2015 – 11th international conference on vibrations in rotating machines*, Magdeburg, Germany, 23–25 February 2015, Paper-ID 39, pp.1–12.

39. Cook RD, Malkus DS, Plesha ME, et al. *Concepts and applications of finite element analysis*. 4th ed. Hoboken, New Jersey: John Wiley & Sons. Inc., 2002.

40. Harrison WJ. The hydrodynamical theory of lubrication with special reference to air as a lubricant. *Transactions Cambridge Philosophical Society* 1913; 22: 34–54.

41. Heshmat H, Walowit JA and Pinkus O. Analysis of gas lubricated compliant thrust bearings. *J Lubric Tech* 1983; 105: 638–646.

42. Inman DJ. *Engineering vibration*. 2nd ed. Upper Saddle River, New Jersey: Prentice–Hall, Inc., 2001.

43. Powell JW. A review of progress in gas lubrication. *Reviews of Physics in Technology* 1970; 1(2): 96–129.

Appendix 1

Convergence study of the required number of mode shapes used in the modal reduction

In an effort to reduce the number of top foil variables, thereby increasing the computational efficiency,
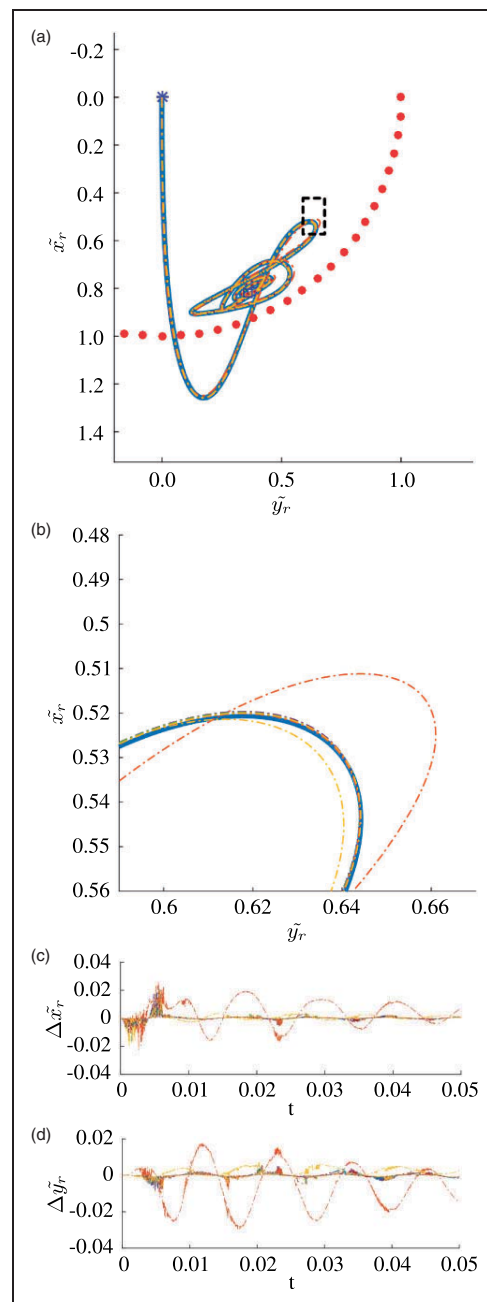

Figure 16. Plot of the journal orbit, with 10 different number of mode shapes used in the mode shape reduction. In all simulations a 40×13 mesh has been used. The number of mode shapes used in the modal reduction ranges from the first five to the first 70, i.e. 5, 10, 15, 20, 25, 30, 35, 40, 45 and 70 with an interval of five. The thick blue line is the baseline simulation in which the first 70 mode shapes have been used in the mode shape reduction. (a) The journal orbit inside the air foil bearing. (b) Zoom of the top left hand loop of the journal orbit. (c) Deviations of the movements in the *x*-direction. (d) Deviations of the movements in the *y*-direction.
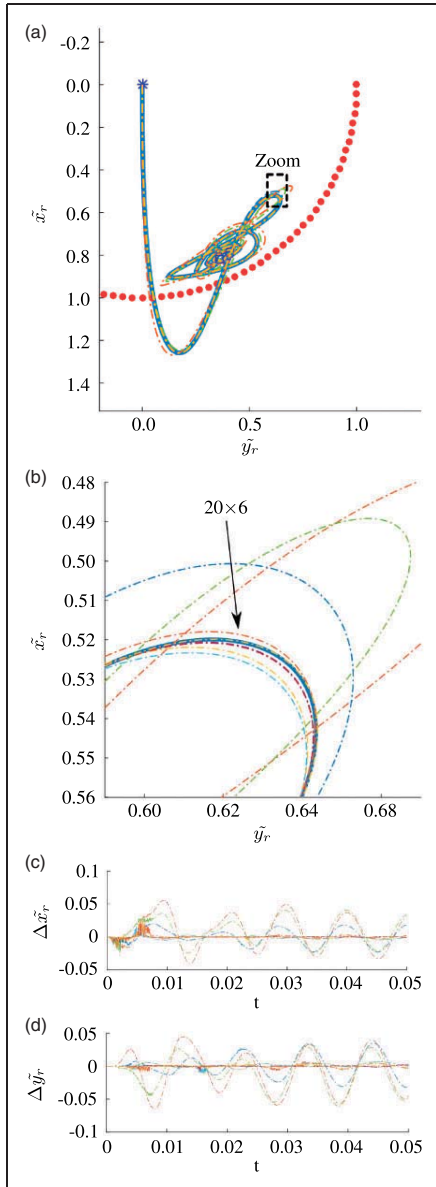
Figure 17. Plot of the journal orbit with ten different refinements of meshes all using 20 mode shapes in the modal reduction. The finest mesh, 70×22, is used as the baseline in the calculation of the derivations. The meshes used are as listed: 8×3, 8×5, 10×3, 16×6, 16×10, 20×6, 32×12, 32×20 and 40×13. (a) The journal orbit inside the air foil bearing. (b) Zoom of the top left hand loop of the journal orbit. (c) Deviations of the movements in the x-direction. (d) Deviations of the movements in the y-direction.

a modal reduction has been proposed. The modal reduction restricts the movement of the top foil to the selected mode shapes, hence an investigation has been performed in order to find the number of mode shapes required to ensure the correct deformation of the top foil. In Figure 16(a) 10 simulations of the transient responses for a journal supported by an AFB are shown. All 10 simulations are computed considering a fine mesh of 40×13 elements, while the number of mode shapes used in the modal reduction vary in the ranges of the first five to the first 70, i.e. 5, 10, 15, 20, 25, 30, 35, 40, 45 and 70. The transient response marked with a thick blue line is calculated utilising the first 70 mode shapes, and serves as a baseline. In Figure 16(b) a zoom of the top right hand curve of the journal orbits is shown, while in Figure 16(c) and (d) deviations between the baseline simulation and the remaining nine simulations are shown. The high frequency deviations seen in Figure 16(c) and (d) are impact vibrations when the top foil and the bump foil re–establish contact after separation due to sub-ambient pressures. In figure 16 the journal orbit from the simulations with five and 10 mode shapes stick out, while the simulation with the first 15 mode shapes is close to the baseline. The difference between the simulation utilising the first 20 mode shapes and the baseline is less than 0.5% when the impact vibrations are neglected. In the following simulations the first 20 mode shapes will be used in the reduced model.

Appendix 2

Convergence study of the required refinement of the mesh

Ten simulations of the transient responses of a journal supported by an air foil bearing are shown in Figure 17 with an increasing refinement of the mesh. The different meshes used in the simulations range from a coarse mesh: 8×3 to a fine mesh: 70×22, i.e. 8×3, 8×5, 10×3, 16×6, 16×10, 20×6, 32×12, 32×20, 40×13 and 70×22. In all of the simulations the first 20 mode shapes have been used in the modal reduction. The finest mesh with 70×22 elements is used as the baseline, and it is marked with a thick blue line. In Figure 17(b) a zoom of the top right hand curve of the journal orbits is shown, while in Figure 17(c) and (d) the derivations between the baseline simulation and the nine others are shown. For many of the coarse meshes the deviations are pronounced, but for a 20×6 mesh the deviation between the simulated orbit and the baseline is deemed acceptably small, without resulting in too high a computational cost.